

https://dspace.org/

Synthesis and characterization of single-walled carbon nanotubes by dual laser vaporization

Moodley, Mathew Kisten

2011-03-07
http://hdl.handle.net/10539/9107

Downloaded from a DSpace repository. https://dspace.org/

Synthesis and Characterization of Single-Walled Carbon Nanotubes by Dual Laser Vaporization

Mathew Kisten Moodley
Supervisor: Professor Neil J. Coville

7 December 2010

Declaration

I declare that this thesis is my own, unaided work. It is being submitted for the degree of Doctor of Philosophy in the University of the Witwatersrand, Johannesburg. It has not been submitted before for any degree or examination in any other University

Mathew Kisten Moodley

Abstract

A singular feature of research in carbon nanotubes which sets it apart from many other similar material systems, is the wide field of promising applications ranging from molecular electronics and quantum computing to materials science and medicine. Fundamental studies of the nanotubes unusual properties combined with an arsenal of potential applications and cross-cutting collaborations between scientists and technologist from different disciplines, gave birth to what we now know as nanoscience and nanotechnology.

However, there are several serious outstanding issues relating to carbon nanotubes which has limited its full potential. The main issue is the inability to synthesize single-walled carbon nanotubes (SWCNTs) with a well-defined atomic (n,m) structure, which is a critical parameter in determining whether the SWCNT is metallic or semi-conducting in nature. Under-pinning the lack of controlled synthesis, is a lack of the understanding of the growth mechanism leading to the nucleation and growth of carbon nanotubes.

In this dissertation, the laser-furnace method was used to study the synthesis of SWCNTs. The investigations revolved around varying process parameters such as gas pressure, gas flow rate, furnace temperature and catalyst composition. A study was made on the effect of varying these parameters on the synthesis of SWCNTs. To quantify these effects, the as-prepared material was characterized by Raman spectroscopy, photoluminescence spectroscopy and electron microscopy.

It was found that the variation of the argon gas pressure and flow rate influenced the quantity (in terms of mass collected) and quality (in terms of I_D/I_G (or I_D/I_{D*}) values) of as-prepared SWCNTs since these parameters affected the plasma dynamics. Low flow rates and low pressures, reduced the cross section for collisions between plasma constituents, in particular between C_2 and the metal catalysts which affected the probability of nucleation and growth of SWCNTs. The temperature, was found to be the critical process parameter in the nucleation and growth of SWCNTs. It was found that as the synthesis temperature was increased from 1073 K to 1373 K, the RBM intensities of Raman spectra increased indicating an increase in the nucleation and growth of SWCNTs. This correlated with the lowering of I_D/I_G (or I_D/I_{D*})

values with increasing temperature. Overall, it was found that an argon pressure of 500 Torr, flow rate of 100 sccm and temperature of 1373 K, produced SWCNTs at a rate of 80 mg/h with the highest quality and the lowest I_D/I_G (or I_D/I_{D*}) value of 0.02 (0.25).

The catalyst composition was changed by adding Fe, in steps of 0.5%. A shift to lower wavenumbers of the RBM spectrum was noted which pointed to the synthesis of nanotubes with larger diameters. This was attributed to an increase in the lattice parameter of the catalyst involved. However, continuously adding Fe to the catalyst saw a significant drop in RBM intensities and hence SWCNT content. We propose that this is due to an increase of FeCo alloy content in the target which was found to be detrimental to the synthesis process.

It was found that with increasing synthesis temperature, the photoluminescence (PL) intensities of the SWCNTs decreased. This was contrary to Raman spectroscopy results. It was concluded that as the synthesis temperature was increased from 1073 K to 1373 K, the laser-furnace method promotes the nucleation of metallic SWCNTs. The presence of metallic-SWCNTs are known to suppress PL emissions from semi-conducting SWCNTs. This showed that by controlling the synthesis temperature, either semiconducting-SWCNT or metallic-SWCNT could be promoted.

To investigate nucleation and growth of SWCNTs, *in situ* optical emission spectroscopy (OES) was used to evaluate the temporal and spatial dynamics of C_2, electron density (N_e) and electron temperature (T_e). It was found that as the furnace temperature was increased from 1073 K to 1373 K in targets which contained catalysts,the concentration and lifetime of C_2 in the plasma plume increased. Raman measurements on material collected from single-shot *in situ* OES measurements showed an increase in Raman RBM intensities and a corresponding decrease in I_D/I_G (or I_D/I_{D*}) values with increasing synthesis temperatures. This showed a direct correspondence between C_2 lifetime and nucleation and growth of SWCNTs. In the absence of catalysts, C_2 formed small graphene sheets or amorphous clusters.

Contour plots of the N_e and T_e showed a number of hot spots or local maxima which increased in number with increasing temperature. We attribute the appearance of hot spots to the energy released when C_2 was systematically consumed during the nucleation and growth of SWCNTs. Under the same ex-

perimental conditions, the ablation of a target containing no catalysts showed no hot spots in either of the N_e or T_e maps and produced no SWCNTs. Therefore, we attribute the appearance of hot spots as a direct consequence of the nucleation and growth of SWCNTs.

Dedication

This work is dedicated to my parents, Kisten and Kala Moodley and to my wife, Loshini and daughter, Michaela Devani.

Acknowledgements

It has been a long journey and I have many to thank who have assisted me in completing the arduous task of completing a PhD.

I would like to thank the organization for which I have been working for the past 10 years, the Council for Scientific and Industrial Research (CSIR) for supporting my research in single-walled carbon nanotubes since 2003. In terms of the infrastructure that was developed over the years to do such sophisticated research and the human resources that was made available, such a project, even today would not have been possible at any other institution in South Africa or the Southern Hemisphere for that matter. For such work, requires the support of senior managers who make the strategic decision to support it. In this regard, I would like to single out the following people, whom I thank: Dr. Philemon Mjwara (CSIR, DST), Mr. Henry Tromp (former NLC), Mr. Hardus Greyling (CSIR), Dr. Thulani Dlamini (CSIR) and Dr. Suprakas Sinha Ray (CSIR)

Throughout my career at the CSIR, I had the privilege of working with highly skilled people, in particularly, at the National Laser Centre (NLC). During the early stages of my research on carbon nanotubes, the following people assisted at various times: Ameeth Sharma, Henk van Wyk, Sisa Pityana, Chris Kruger, Corrie van der Westhuizen, Otto Hamilcik, Bafan Moyo, Thomas du Plooy, Marthinus Kruger, Hansi Pretorius, Kuben Naidoo and Andrew Forbes.

I also thank former students of mine who have assisted me in my laboratory during various times: David Motaung, Patrick Sibiya, Thlogi Matlhoko, Sreejarani Pillai and Manikandan Elayaperumal.

I also thank colleagues at the National Centre for Nano-Structured Materials (NCNSM): Gerald Malgas, Manfred Scriba, Lucky Sikhwivhilu and Thembela Hillie.

Outside the working environment, I thank the following family and close friends for assistance and encouragement: Kisten Moodley, Kala Moodley, Loshini Moodley, Michaela Moodley, Luchelle Moodley, Sathie Pillay, Nundhi

Pillay, Shaun Pillay, Dino Ramanundh, Kershnee Govender, Ameeth Sharma, Sisa Pityana, Venantzio Mzenda, Ramu Rangasamy, Calvin Govender, Siva Venkataraman, Srinivasu Vallabhapurapu, Mr Naidu, Vijay Naidu, Somnath Bhattacharyya, Sharfuddin Sayed, Ramesh Bharuthram and Krish Bharuth-Ram.

I also acknowledge Dr. Malik Maaza who introduced me to pursue the research topic of synthesizing nanotubes by using lasers.

I also acknowledge the support of the Department of Science and Technology (DST) who have provided dedicated funding towards the NCNSM which enabled my laboratory to be equiped with state of the art equipment and making the reserach presented in this dissertation possible.

I also thank the School of Physics, University of the Witwatersrand for their support.

Finally, I thank my supervisor Professor Neil J. Coville who accepted me as his student during a period of uncertainty. His availability, support, guidance, character, honesty and academic integrity is an example for all to follow.

Publications

Publications in peer review journals relating to this work.

1. M.K Moodley, N.J Covillec, B.C Hollowayd and M. Maaza, Synthesis of single-walled carbon nanotubes by dual laser vaporization. South African Journal of Science 102 (2006) 364

2. D.E. Motaung, M.K. Moodley, E. Manikandan and N.J. Coville, In situ optical emission study on the role of C_2 in the synthesis of singlewalled carbon nanotubes, Journal of Applied Physics 107 (2010) 044308

3. M.K. Moodley and N.J. Coville. Experimental evidence for the early nucleation of single-walled carbon nanotubes, Chemical Physics Letters 498 (2010) 140

Contents

1 An Introduction to Carbon fullerenes **1**

1.1 The Discovery of carbon fullerenes 1
1.2 A brief synopsis of carbon nanotube research 4
1.3 Motivation for this dissertation 6
1.4 Research Questions 7
1.5 Plan of dissertation 8

2 Single-Walled Carbon Nanotubes **10**

2.1 Elemental Carbon 10
2.2 Carbon vapour molecules 11
2.3 Major allotropes of carbon 12
2.3.1 Graphite 12
2.3.2 Diamond 14
2.3.3 Fullerenes 15
2.3.4 Carbon nanotubes 17
2.4 Physical description of single-walled carbon nanotubes 17
2.5 Methods for the synthesis of SWCNTs 21
2.5.1 Arc discharge 21
2.5.2 CVD 22
2.5.3 Laser ablation synthesis 24
2.6 Growth mechanisms 26
2.7 Properties of SWCNTs 28
2.7.1 General properties 28
2.7.2 Electronic and optical properties 29
2.7.3 Mechanical properties 30
2.7.4 Reactivity 30
2.8 Application of carbon to advanced technological devices 31
2.8.1 Field emission-based devices 31
2.8.2 Single-Walled Carbon Nanotube Transistors 33
2.8.3 Single-walled carbon nanotube thin film transistors (TFT) 33
2.8.4 SWCNT thin films for sensing 36

2.8.5 Purification and processing of SWCNTs 37
2.8.6 Purification by centrifugation 38
2.8.7 Sorting SWCNTs by density gradient ultracentrifugation 39

3 Characterization of Single-walled carbon nanotubes 41
3.1 Introduction 41
3.2 Raman Spectroscopy 42
3.2.1 Raman Scattering in SWCNTs 44
3.2.2 The radial breathing mode (RBM) 47
3.2.3 G-Band 49
3.2.4 D-Band 53
3.2.5 D*-Band 55
3.2.6 Intermediate Frequency Modes 56
3.2.7 Two-phonon modes 56
3.2.8 The assignment of chiral indices (n,m) to SWCNTs . . . 56
3.3 Photoluminescence of SWCNTs 61
3.4 Electron microscopy 65
3.4.1 Scanning electron microscopy (SEM) 65
3.4.2 Transmission electron microscopy (TEM) 68

4 Laser synthesis of single-walled carbon nanotubes: Theory and Experimental 72
4.1 Introduction to lasers in materials synthesis 72
4.2 Operating principles of a laser 73
4.3 Some properties of pulsed laser Gaussian beams 79
4.3.1 Gaussian beams 80
4.4 Laser induced thermal processes in materials 82
4.4.1 Surface heating 82
4.4.2 Removal of target material by ablation 83
4.5 Synthesis of single-walled carbon nanotubes 85
4.5.1 Self assembly of vaporized carbon 85
4.6 Experimental Design for the laser synthesis of SWCNTs 87
4.6.1 Apparatus 87
4.6.2 Description of the experimental layout 88
4.6.3 Measurement of laser parameters 92
4.6.4 Preparation of laser ablated targets 92
4.6.5 Furnace and argon gas flow conditions 94
4.6.6 System in operation 94
4.7 Summary of the synthesis of as-prepared materials 97

4.7.1 Key to sample labelling 97
4.8 Characterization Instrumentation and sample preparation 104
4.8.1 Raman Spectroscopy 104
4.8.2 Photoluminescence spectroscopy 105
4.8.3 SEM and TEM sample preparation 106

5 Laser synthesis of single-walled carbon nanotubes: Raman, photoluminescence and electron microscopy 107
5.1 Raman spectroscopic analysis of SWCNTs 107
5.1.1 Generalized Raman analysis of as-prepared SWCNTs . . 107
5.1.2 Detailed analysis of various Raman modes of as-prepared samples 121
5.1.3 Analysis of Radial Breath Modes (RBM) 121
5.1.4 Analysis of D and G bands 125
5.2 Photoluminescence spectroscopy of SWCNTs 149
5.2.1 Photoluminescence of samples prepared with Target A . 150
5.2.2 Photoluminescence spectra of samples prepared with Target D 153
5.2.3 Photoluminescence spectra of samples prepared with Target E 153
5.2.4 Photoluminescence spectra of samples prepared with Target F 153
5.2.5 Photoluminescence spectra of samples prepared with Target G 154
5.3 Electron Microscopy studies on the as-prepared SWCNTs 159
5.3.1 Scanning electron microscopy (SEM) 159
5.3.2 Transmission electron microscopy (TEM) 161
5.4 Discussions 167
5.4.1 Raman Spectroscopy 167
5.4.2 Photoluminescence spectroscopy 174

6 Optical Emission Spectroscopy (OES) studies applied to Carbon Nanotube Synthesis 177
6.1 Introduction 177
6.2 Characterization of laser induced plasmas by OES 179
6.2.1 Spectral emission from a laser induced plasma 179
6.2.2 Theoretical Models for the Plasma 181
6.2.3 Measurement of Plasma Parameters 183
6.3 Dominant optical emission bands of carbon 187

6.4 Experimental set-up and parameters for *in situ* OES measurements . . . 187
6.5 Results . . . 193
6.5.1 Characterization of as-prepared materials by single-pulse laser ablation . . . 193
6.5.2 The temporal and spatial dynamics of C_2 . . . 196
6.5.3 The temporal and spatial dynamics of the electron density 199
6.5.4 The temporal and spatial dynamics of electron temperature . . . 202
6.6 Discussion and conclusions . . . 202
6.6.1 Growth model . . . 206

7 Conclusions and Recommendations 208
7.1 Conclusions . . . 208
7.2 Recommendations for future work . . . 211

List of Figures

1.1 Time-of-flight mass spectra of laser ablated graphite recorded by Heath, a student in Richards Smalley's laboratory. Under optimum synthesis conditions, C_{60} and C_{70} molecules dominate. Taken Ref. [2] 2

1.2 TEM images of graphitic tubules as observed by S. Iijima. Note only multi-walled nanotubes were observed. Taken from Ref. [4]. 3

1.3 TEM observation by L.V. Radushkevich and V.M. Lukyanovich who published their findings in 1952 in Ref. [5]. 4

2.1 Vapor pressure of C molecules as function of pressure and temperature. Taken from Ref. [29] 13

2.2 The crystal structure of graphite showing the ABAB stacking sequence and unit. Taken from Ref. [29]. 14

2.3 A schemtaic of the diamond structure. Taken from Ref. [29]. . . 15

2.4 Fullerenes are a familiy of geodesic molecules which are very stable. Twelve pentagons are required in any fullerence molcule to close into a geodesic structure. They may may not be spherically symmetric as $C_{60.}$ (a) C_{60} , (b) C_{100} and (c) C_{320}. MKMoodley 2010© 16

2.5 Schematics and accompanying TEM images of a (a) SWCNT, (b) DWCNT and (c) MWCNT. MKMoodley 2010© 18

2.6 How a graphene sheet could be rolled to form (a) zig-zag nanotubes, (b) chiral nanotubes and (c) armchair. MKMoodley 2010© 19

2.7 A schematic showing how a vector $\vec{C}_h$ could be used to define all SWCNTs. MKMoodley 2010© 20

2.8 A schematic of an electric-arc reactor used to synthesize SWCNTs. Taken from Ref. [11]. 22

2.9 Schematic of CVD apparatus's commonly used to grow SWCNTs (a) typical CVD, (b) HiPCo method and (c) plasma enhanced CVD. Taken from Ref. [44] 23

2.10 Schematic of experiments involving the use of lasers to synthesize SWCNTs for (a) Typical laser-furnace set-up, (b) the use of a high power free electron laser at JFEL and (c) use of a continuous CO_2 laser. Taken from Refs. [11, 44]. 25
2.11 S-L-V model where SWCNT precipitate from the solid phase on catalyst particles. Taken from Ref. [49] 27
2.12 S-L-V mechanism put forward by Kautara et. al. showing that the growth of SWCNT is preceded by fullerene like seed. Taken from Ref. [51]. 28
2.13 A schematic of how a modern TV screen based on the use of CNTs looks inside. (a) Cross-section showing the CNT field emiiter and (b) A SEM of the front of the field emitter. Taken from Ref. [11]. 32
2.14 Top-gated carbon nanotube transistor. (a) A schematic of a top-gated structure for field-effect transistor (FET) and (b) Typical measured output characteristics of drains current I_{ds} versus drain voltage (V_{ds}) of a single nanotube p-type FET. Taken from Ref. [60]. 34
2.15 (a) Schematic view of a flexible SWCNT-TFT , (b) circuit diagram, and c) static transfer characteristics of an inverter composed of two p-channel SWNT TFTs on a PI substrate. PU, polyurethane; PAA, polyamic acid. In c), the dashed line represents a circuit simulation result. d) Optical image of a flexible SWNT integrated circuit chip bonded to a curved surface. Taken from Ref. [26]. 35
2.16 Relative change in capacitance versus time for a SWCNT chemtransistor in response to exposed to doses of N,N-dimethylformamide (DMF) at various concentrations. Taken from Ref. [62]. 36
2.17 A SWCNT based sensor built to measure dimethyl methylphosphonate (DMMP) by monitoring relative changes in conductance. Taken from Ref. [26]. 37
2.18 A Schematic of the resuspension-centrifugation-decantation cycle for removal of CNPs and purification of SWCNTs Taken from Haddon et al. [67]. 38
2.19 SC encapsulated, CoMoCAT-grown SWNTs the separation by DGU. On the left, the separation shows that the formation of coloured bands pointing monodisperse SWCNTs. Absorption spectra are shown on the right. Adapted from Hersam et al. [68] 40

3.1 Jablonkski energy diagram depicting electronic transitions of several processes in an excited atom resulting in the emission of photons of different energies. Taken from Ref. [74]. 44
3.2 A schematic of the Raman scattering process. The dashed lines are virtual states while the solid lines represent real electronic transition levels (a) Stokes scattering where a phonon is emitted (b) Anti-stokes scattering where a phonon is absorbed (c) Resonant Raman scattering occurs when the incident or emitted photon matches a real electronic transition, and the Raman effect is enhanced by several orders of magnitude. From this, the optical transition energy could be determined. Adapted from Ref. Reich et al. [146]. 45
3.3 A typical Raman spectrum of as-prepared SWCNTs. The major Raman bands are depicted. Plotted data are from this study. . . 46
3.4 A schematic model of a (9,7) SWCNT showing the direction of symmteric vibrations resulting in what is known as the radial breathing mode. Analysis of which is correlated to the tubes diameter. MK Moodley 2010© 47
3.5 Resonant Raman spectra of HiPco SWCNT samples excited by a tuneable laser. Taken from Bronikowski et al. Ref. [83]. 49
3.6 Resonant raman imaging of individual SWCNTs measured by Telg et al. [85]. 50
3.7 A laser prepared sample, from this study, excited by 647 nm and 488 nm lasers showing the Raman spectrum SWCNTs bundles and the spiltting of the G bands (a) metallic nanotubes (b) semi-conducting. 51
3.8 A schematic of a (10,10) armchair SWCNT showing vibrational A_{1g} mode. The vibrations are parallel to the C-C bond. MK-Moodley 2010© 51
3.9 A schematic of a (10,10) armchair SWCNT showing vibrational E_{1g} mode. The vibrations are perpendicular to the C-C bond. MK Moodley 2010© 52
3.10 RBM band G nad spectra of individual isolated semi-conducting nanotubes. The diameter dependence of the G^- peak position is noticeable. The peak position of the G^+ show little or no depedence when comared ot the RBM features. From Jorio et al. [90]. 53

3.11 A plot of the frequency position of the G^- and G^+ bands of individual metallic and semiconducting SWCNTs vs $1/d_t$. The plot shows that there is a diameter dependence of the nanotube with the G^- band. Taken from Jorio et al. [90]. 54
3.12 The Kataura plot illustrating that the diameter or the ϖ_{RBM} of the nanotube is not sufficient to determine the chiral index (n,m) with certainty. 58
3.13 Calculated theortical Kataura plot of nanotube transitions energies E_{ii} vs diameter in Å. The grey symbols respresent semiconducting tubes, closed circles ($v = -1$), open circles ($v = +1$). Balck filled circles represent metallic tubes ($v = 0$). Lines connecting the circles represent a branch with $2n + m =$ constant. Taken from Ref. [78]. 59
3.14 A super-imposed plot of experimental E_{ii} values and theoretical values vs nanotube diameter, $1/\varpi_{RBM}$. This is the manner in which the assignement of (n,m) chiral indices are made. For semiconducting tubes, open and closed symbols indicate tubes with $v = +1$ and $v = -1$, respectively. Gray symbols (right and top axes) are theoretical values from Figure 3.13 from Telg et al. [115]. 60
3.15 A graphene sheet labelled with chiral indices (n,m). By rolling the sheet in the direction of the wrapping vector or chiral vector will determine the chirality type of the nanotube formed. The chiral angle,a (from 0^0 to 30^0) is measured between the vector and the zig-zag plane from Bachilo et al. [116]. 62
3.16 A Schematic illustrating the density of states (DOS) for SWCNT. Solid arrows depict the optical excitation and emission transitions while dashed arrows denote nonradiative relaxation of the electron, in the conduction band, and a hole, in the valence band before emission. From Ref Bachilo et al. [116]. . . . 63
3.17 (A) A photoluminescence spectrum of suspended SWCNTs in a solution of SDS in D_2O. The peaks corresponds to unique chiral SWCNTs (B) A plot of spectral peak positions taken from (A) revealing a particular pattern (C) A plot of the measured ratio's of excitation to emission frequencies (D) A plot of computed E_{22}/E_{11} energy ratios versus excitation wavelengths. Blue symbols are $|n - m| \bmod 3 = 1$; red symbols are for $|n - m| \bmod 3 = 2$. 64

3.18 (a) A photoluminescence spectrum of a laser synthesized sample dispersed and suspended in D_2O containing 2% by weight of sodium cholate and (b) a plot of the diameter vs chiral angle. Data in both of these plots (a) and (b) are from this study. . . . 66
3.19 Schematic showing the interaction of an electron beam with a sample in the SEM configuration. Taken from Ref. [120]. 67
3.20 A sample, from this study shows a FE SEM image of as-prepared material containg SWCNT taken at 6 kV accelerationg voltage. The white spots are either Ni or Y metal catalyst particles. . . . 68
3.21 A schematic showing the operating principle of a TEM (a) bright image mode and (b) dark field image mode. Taken from Ref. [120]. 69
3.22 The contrast transfer function (CTF) is used to evaluate the capabilities of a TEM instrument. Taken from Ref. [121]. 70

4.1 A schematic of the Bohr model of the atom to aid in the understanding of excitation and emission of radiation. Figure adapted from Ref. [125]. 73
4.2 A schematic showing the processes involved in a lasing medium when excitated by an external source. A modified figure adapted from Ref. [125]. 76
4.3 A schematic showing how stimulated emission takes place in a laser resonator. Figure adapted from Ref. [125]. 77
4.4 A schematic of a 4-level lasing medium such as Nd:YAG. Figure adapted from Ref. [125]. 78
4.5 A schematic of showing the basic components which make up the laser resonator. A "lasing" such a Nd:YAG rod is located between a high reflecting mirror (HRM) and a output coupling mirror (OCM). Adapted from Ref. [127]. 78
4.6 Focussing of a circular Gaussian beam using a thin convex lens of focal length f. Modified and adapted from Ref. [128]. 81
4.7 Experimental layout to synthesize SWCNTs by the laser-furnace method. 91
4.8 Photograph showing the target correctly postioned in the centre of the furnace, 20 mm from the end of the inner quartz flow tube. 95
4.9 The back-end of the quartz tube showing the clamping of the target, support rod and connection to the vacuum system. . . . 95
4.10 The front-end of the quartz showing the Brewster window from the side and the inlet argon gas connection. 96

4.11 SWCNT material synthesized in the hot zone. The material was carried to the back and condensed on cooler sections of the quartz tube and appeared like a matt black deposit. This material was collected over a period of 30 minutes. 98
4.12 A removed vacuum flange exposing as-prepared SWCNT. . . . 98
4.13 A typical sample of as-prepared material scrapped off the insides of the quartz tube and collected in a petri dish. 99

5.1 The mass of material collected after the ablation of Target A in the laser synthesis method of synthesizing SWCNTs at a furnace temperature of 1273 K. 110
5.2 Raman spectra of samples collected at the back-end (A12P5F2A) and centre (A12P5F2B) of the furnace. The I_D/I_{D^*} and I_D/I_G ratio's of 0.22 and 0.05 for material from A versus 0.44 and 0.11 for material collected from B were observed. Clearly, the material collected at A was superior in quality to material collected at B. 113
5.3 Raman spectra of as-prepared material synthesized by ablating Target A at a fixed furnace temperature of 1073 K. 115
5.4 Raman spectra of as-prepared material synthesized by ablating Target A at a fixed furnace temperature of 1173 K. 116
5.5 Raman spectra of as-prepared material synthesized by ablating Target A at a fixed furnace temperature of 1273 K. 117
5.6 Raman spectra of as-prepared material synthesized by ablating Target A at a fixed furnace temperature of 1373 K. 118
5.7 Raman spectra of as-prepared material synthesized by ablating Target B at a fixed flow rate and pressure of 200 sccm and 400 Torr of argon gas. (a) 1073 K, (b) 1173 K, (c) 1273 K and (d) 1373 K. 127
5.8 Raman spectra of as-prepared material synthesized by ablating Target D at a fixed flow rate and pressure of 200 sccm and 400 Torr of argon gas. (a) 1073 K, (b) 1273 K, (c) 1373 K. 128
5.9 Raman spectra of as-prepared material synthesized by ablating Target E at a fixed flow rate and pressure of 200 sccm and 400 Torr of argon gas. (a) 1073 K, (b) 1173 K, (c) 1273 K and (d) 1373 K. 129

5.10 Raman spectra of as-prepared material synthesized by ablating Target F at a fixed flow rate and pressure of 200 sccm and 400 Torr of argon gas. (a) 1073 K, (b) 1173 K, (c) 1273 K and (d) 1373 K. 130
5.11 Raman spectra of as-prepared material synthesized by ablating Target G at a fixed flow rate and pressure of 200 sccm and 400 Torr of argon gas. (a) 1073 K, (b) 1173 K, (c) 1273 K and (d) 1373 K. 131
5.12 Lorentzian fits of the RBM bands of as-prepared SWCNT material obtained by ablating Target A at a furnace temperature of 1073 K. 132
5.13 Lorentzian fits of the RBM bands of as-prepared SWCNT material obtained by ablating Target A at a furnace temperature of 1173 K. 133
5.14 Lorentzian fits of the RBM bands of as-prepared SWCNT material obtained by ablating Target A at a furnace temperature of 1273 K. 134
5.15 Lorentzian fits of the RBM bands of as-prepared SWCNT material obtained by ablating Target A at a furnace temperature of 1373 K. 135
5.16 Lorentzian fits of the RBM bands of as-prepared SWCNT material obtained by ablating Target D at a furnace temperature of 1273 K. 136
5.17 Lorentzian fits of the RBM bands of as-prepared SWCNT material obtained by ablating Target D at a furnace temperature of 1373 K. 137
5.18 Lorentzian fits of the RBM bands of as-prepared SWCNT material obtained by ablating Target E at a furnace temperature of 1273 K. 138
5.19 Lorentzian fits of the RBM bands of as-prepared SWCNT material obtained by ablating Target E at a furnace temperature of 1373 K. 139
5.20 Lorentzian fits of the RBM bands of as-prepared SWCNT material obtained by ablating Target F at a furnace temperature of 1273 K. 140
5.21 Lorentzian fits of the RBM bands of as-prepared SWCNT material obtained by ablating Target F at a furnace temperature of 1373 K. 141

5.22 Lorentzian fits of the RBM bands of as-prepared SWCNT material obtained by ablating Target G at a furnace temperature of 1273 K. 142
5.23 Lorentzian fits of the RBM bands of as-prepared SWCNT material obtained by ablating Target G at a furnace temperature of 1373 K. 143
5.24 Raman spectra showing D and G bands of material synthesized by using Target A at an argon pressure of 400 Torr and flow rate of 200 SCCM. 144
5.25 A comparison of raw Raman spectra of the D-G bands when excited at 488 and 647 nm. A significant drop in the intensities of the peaks was observed with increasing Fe concentration. . . 145
5.26 A comparison of normalized Raman spectra of the D-G bands when excited by 488 and 647 nm laser excitations. A significant drop in the intensities was observed with increasing Fe concentration. However, no significant change in peaks positions were found. 146
5.27 Raman spectra of the D* band. The peak postion of the D* band showed a clear dependence on the laser excitation energy for all samples. 148
5.28 A comparison between experimental and predicted Raman peak positions for ϖ_D and ϖ_{D^*}. 149
5.29 Photoluminescence spectra of samples obtained by ablating Target A at (a) 1073 K, (b) 1173 K, (c) 1273 K and (d) 1373 K. . . 151
5.30 Spectral plots of SWCNTs diameters versus chiral angle of samples obtained by ablating Target A at (a) 1073 K, (b) 1173 K, (c) 1273 K and (d) 1373 K. 152
5.31 PL plots for (a)D12P4F2 and (b)D13P4F2. SWCNT diameter vs chiral angles plots are shown for (c) D12P4F2 and (d) D13P4F2.155
5.32 PL plots for (a)E12P4F2 and (b)E13P4F2. SWCNT diameter vs chiral angles plots are shown for (c) E12P4F2 and (d) E13P4F2.156
5.33 PL plots for (a)F12P4F2 and (b)F13P4F2. SWCNT diameter vs chiral angles plots are shown for (c) F12P4F2 and (d) F13P4F2.157
5.34 PL plots for (a)G12P4F2 and (b)G13P4F2. SWCNT diameter vs chiral angles plots are shown for (c) G12P4F2 and (d) G13P4F2.158

5.35 SEM images of as-prepared materials synthesized by the laser process under various conditions (a) no catalyst was used, producing amorphous carbon (b) A10P1F1, low temperature, low Ar gas pressure and low flow rate (c) A12P4F2 as-prepared SWCNTs under ideal conditions (d) dried solution of A12P4F2 sonicated in ethanol 160
5.36 SEM of a dried thin film of SWCNT wrapped in 2% sodium cholate solution on top of a holey carbon TEM grid . Tubular structures appear white in contrast due to charging effects. . . . 162
5.37 SEM of a dried thin film of SWCNT wrapped in 2% sodium cholate solution on top of a holey carbon TEM grid which underwent further heat treatment at 180 ^0C to remove surfactant. Nanotube strands were clearly visible between cracks of the holey carbon film. 162
5.38 A zoomed SEM image of Figure 3.36, showing SWCNT bundles The surfactant "pulled up" at both ends between the crack to reveal the SWCNT bundle. 163
5.39 TEM images of sample A12P4F2 under increasing magnification from (a) to (d). 164
5.40 A broken end of a SWCNT bundle (A12P4F2) exposing the open ends of individual SWCNTs bonded together in a bundle by van der Waals forces. 165
5.41 A TEM image of sample A10P4F2 showing a high concentration of graphitic ribbons. 165
5.42 A TEM image of a region of sample A10P4F2 showing graphitic ribbons and SWCNTs. The high disorder band in the Raman spectrum of the sample could be attributed to the large concentration of these graphitic ribbons which are made of a few layers of graphene. 166
5.43 A TEM image of sample A12P4F1. Spot analysis at 2 regions A and B were made. The nanotube diameter at A was determined to be 1.219 nm while the layers surrounding the catalyst particle at B was found to correspond to that of graphite. 166
5.44 Graphical plots of the defect concentration as a function of Fe concentration and synthesis temperature (a) I_D/I_G (b) I_D/I_{D*}. . 170
5.45 A comparison of Raman spectra obtainned from as-prepared materials and samples prepared for PL measurements shown in (a-d) and fitted Raman spectra of PL samples shown in (e-h) . . 176

6.1 Low-lying electronic states of C_2.The direction of arrows indicates emission or absorption. Taken from Tanabashi et al. [181]. 188
6.2 Examples of the (a) C_2 Swan band system and (b) The C_2 Deslandres D' Azambuja system. Taken from Vivien et al. [180]. 189
6.3 Experimental setup for OES measurements and laser single-shot synthesis of SWCNTs. 192
6.4 A schematic showing a closeup of the laser impinging on the target resulting in the generation of the plasma from which optical emissions were collected. MKMoodley 2010© 194
6.5 Raman spectra of as-prepared material obtained for single laser shot experiments at (a) Target A, 1073 K, (b) Target A, 1173 K, (c) Target A, 1273 K and (d) graphite, 1273 K. 195
6.6 A sample of an OES spectrum recorded at a delay time of 1800 ns when a single laser shot was fired at Target A using a furnace temeprature of 1273 K. The gate-width on the DDG was 500 ns. 196
6.7 A sample of an C_2 Swan bands recorded at a delay time of 1800 ns when a single laser shot was fired at Target A at a furnace temeprature of 1273 K. The gate-width on the DDG was 500 ns. The vibrational bands (0,0), (1,1) and (2,2) and the associated peak emissions were clearly visible. 197
6.8 Plots of the temporal and spatial dynamics of C_2 Swan (0, 0) band. (a) Target A at 1073 K, (b) Target A at 1173 K, (c) Target A at 1273 K and (d) graphite at 1273 K. 198
6.9 A contour plot of the temporal and spatial dynamics of C_2 Swan (0, 0) band. (a) Target A at 1073 K, (b) Target A at 1173 K, (c) Target A at 1273 K and (d) graphite at 1273 K. (e) Target A at 1273 K extended to 10 μs (f) Target A at 1173 K extended to 10 μs. 200
6.10 Plots of the spatial dynamics of electron density, N_e of (a) Target A at 1073 K, (b) Target A at 1173 K, (c) Target A at 1273 K and (d) graphite at 1273 K. A number of local maxima appearing as hot spots, shown by white arrows, increase with increasing furnace temperature. 201
6.11 Plots of the spatial dynamics of electron temperature, T_e of (a) Target A at 1073 K, (b) Target A at 1173 K, (c) Target A at 1273 K and (d) graphite at 1273 K. A number of local maxima appearing as hot spots, shown by white arrows, increased with increasing furnace temperature. 203

List of Tables

2.1 Table 2.1: Electronic structure of carbon and common transitional metals that are used as catalysts in the synthesis of single-walled carbon nanotubes 11
2.2 The heat of formation of carbon molecules. Taken from Ref[xxx] 12

4.1 Laser specifications and beam properties at the laser exit aperture 87
4.2 A summary of measured values of laser parameters used in this study. 92
4.3 Chemical composition of graphite-metal catalyst targets used in this study. 93
4.4 Experimental conditions under which the graphite composite target was ablated. 94
4.5 A summary of as-prepared material synthesized using Target A. 100
4.6 A summary of as-prepared material synthesized using Target B. 101
4.7 A summary of as-prepared material synthesized using Target C. 101
4.8 A summary of as-prepared material synthesized using Target D. 102
4.9 A summary of as-prepared material synthesized using Target E. 102
4.10 A summary of as-prepared material synthesized using Target F. 103
4.11 A summary of as-prepared material synthesized using Target G. 103
4.12 A summary of Raman excitation wavelengths and their corresponding phonton energies. 105
4.13 A summary of the Nanolog experimental parameters under which PL measurements were made. 106

5.1 Defect evaluation of as-prepared samples synthesized at different process conditions from Target A. 111
5.2 Defect evaluation of as-prepared samples synthesized at different process conditions from Target B. 119
5.3 Defect evaluation of as-prepared samples synthesized at different process conditions from Target D. 119

5.4 Defect evaluation of as-prepared samples synthesized at different process conditions from Target E. 120
5.5 Defect evaluation of as-prepared samples synthesized at different process conditions from Target F. 120
5.6 Defect evaluation of as-prepared samples synthesized at different process conditions from Target G. 120
5.7 The set of samples which had been subjected to detailed evaluation to determine the effect variation of process parameters on the types of SWCNTs that were synthesized. 121
5.8 A summary of the SWCNTs detected in all material samples synthesized from Target A. Possible (n,m) assignment are shown for individual SWCNTs represented by Lorentzian line-shape fits. Peaks which appear in bold are those which were dominant in the RBM spectra. Some peaks could not be identified. 124

6.1 Experimental parameters under which OES measurements were investigated. 190
6.2 Laser parameters under which OES of in situ SWCNT synthesis were investigated. 191
6.3 Emission line parameters of CII lines taken from NIST [178]. . . 203

Chapter 1

An Introduction to Carbon fullerenes

1.1 The Discovery of carbon fullerenes

Carbon has been known since prehistoric times as soot and charcoal. The recognition of it being a unique element came only in the late eighteenth century. In 1779 C.W. Scheele showed that graphite was composed of carbon while in 1796 T. Tennant measured the amount of CO_2 gas produced when diamond was burnt. This showed that diamond was composed entirely of carbon [1]. In the late 20th century, and in pursuit of an understanding of the nature of the universe and the origins of life, scientists embarked on the study of cosmic spectral emissions emanating from stars. Since carbon was known as a fundamental building block of organic matter, it became important to learn about the precursors to the organic compounds leading to the formation of living matter. Thus, the detection of linear chains of carbon based molecules became an important area of research. Harold W. Kroto then at the University of Sussex was involved in this type of spectroscopic study of long chain organic molecules. In 1985, Robert Curl who was based at Rice University introduced Richard Smalley to Kroto. Richard Smalley had developed a laser-based apparatus to study cluster formation by time of flight mass spectrometry (TOFMS). A collaboration between the three, led to the study of cluster formation by laser ablating of carbon. Time of flight mass spectra of the ablated graphite material [2, 3], shown in Figure 1.1, revealed that clusters of 60 and 70 carbon atoms were favoured when the graphite was ablated. Clusters with 60 atoms were about nine times more abundant than clusters of 70 atoms. Chemical and physical tests on this material showed that it was not reactive and very stable when heated to high temperatures.

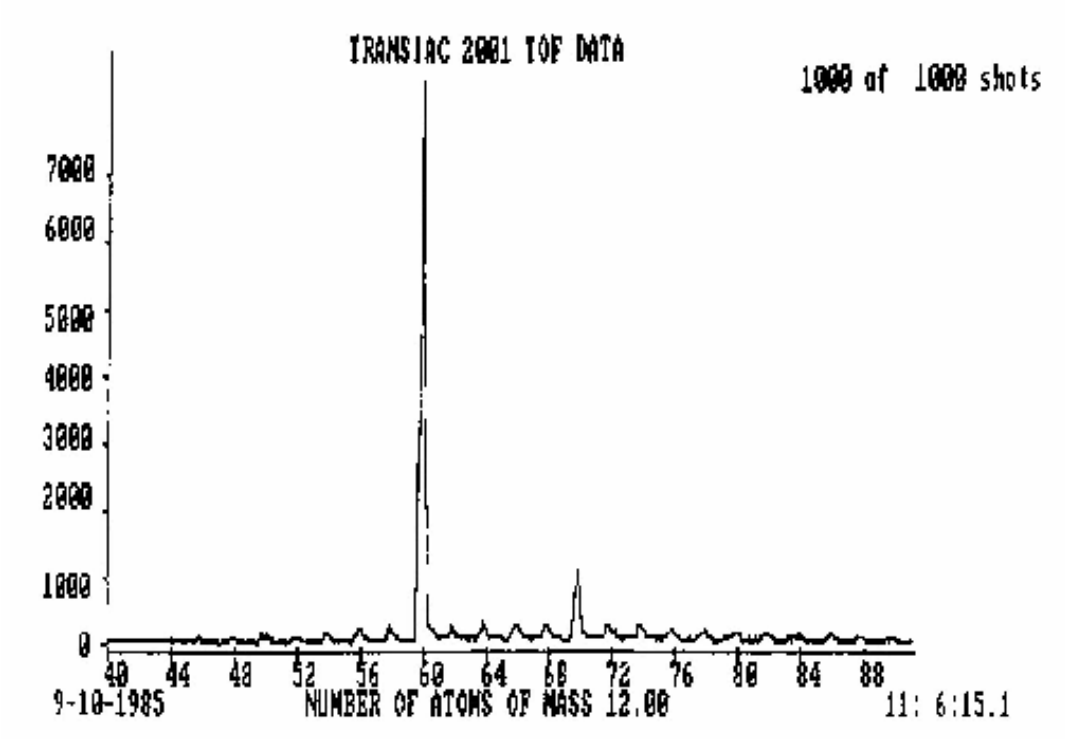


Figure 1.1: Time-of-flight mass spectra of laser ablated graphite recorded by Heath, a student in Richards Smalley's laboratory. Under optimum synthesis conditions, C_{60} and C_{70} molecules dominate. Taken Ref. [2]

In trying to deduce its shape, a geometry based on geodesic domes, developed by American architect R. Buckminster Fuller, was proposed. With this in mind, the group proposed a caged structure consisting of 20 hexagons and 12 pentagons, a shape identical to a soccer ball. The curvature of the structure was generated by the presence of pentagons. For this work they were awarded the Nobel prize in 1996 [2, 3].

The discovery of C_{60} spurred a huge interest in materials science due to the possibility of using the material in advanced technology devices. In 1991, Sumio Iijima of NEC who was interested in forming endohedrals (C_{60} structure incorporating metals), commenced experiments by using an arc-discharge apparatus by applying a voltage to induce an arc between graphite rods. Before arcing, a hole was drilled into one of the graphite electrodes and transition metals where inserted into the hole. The experiments were done in an helium gas chamber. Transmission electron microscopy analysis of the soot, shown in Figure 1.2, showed that instead of finding the expected endohedrals, concentric tubules which we now refer to as multi-walled carbon nanotubes were found. The publication of this result in the journal, Nature, made Iijima famous [4] and revitalized research in fullerene type materials.

However, even though Iijima received credit for the discovery of nanotubes,

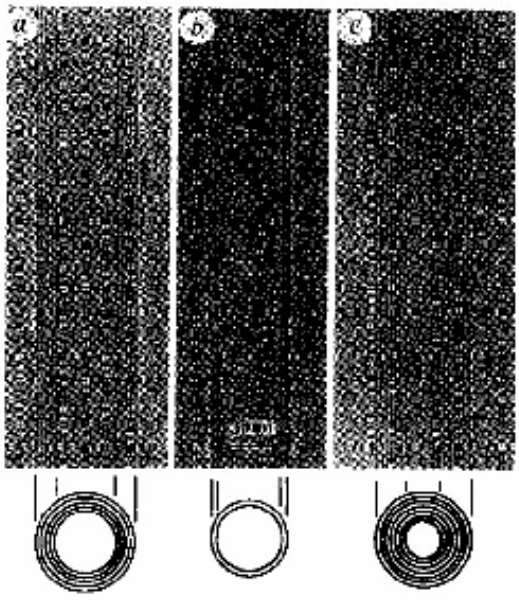


Figure 1.2: TEM images of graphitic tubules as observed by S. Iijima. Note only multi-walled nanotubes were observed. Taken from Ref. [4].

he was not the first to have synthesized nor the first to have published such findings in open literature. That credit goes to two Russian scientists, L.V. Radushkevich and V.M. Lukyanovich who published their findings in 1952 in the Russian journal [5]. Figure 1.3 shows TEM images scanned from their publication.

Due to the political conflict between the West and the Soviet Union during this time, most Soviet research findings were unknown to the rest of the world. There were also much work done by M. Hillert and N. Lange [6] on carbon structures exhibiting the concentric texture whose findings were debated for some time up to the 1970's until TEMs achieved better resolution [7]. A report by A. Oberlin, M. Endo and T. Koyama [8] in 1976 showed tubes in TEM micrographs with a diameter of 5 nm. Thus, Iijima cannot be given credit for the discovery of the nanotubes, he was the first to define the structure as being composed of rolled up sheets of graphite that formed a seamless tube and suggested that these structures was "elongated" fullerenes. It was this work which initiated an avalanche of research in the field of carbon nanotubes. Because of their size, the study and applications of carbon nanotubes have since formed the cornerstone of what we now know as nanoscience and nanotechnology.

The planting of the seeds of nanoscience and nanotechnology can be attributed to the American physicist Richard Feynman (1908-1988). In 1959, he gave a speech entitled "*There's Plenty of Room at the Bottom: An invitation to enter a New Field in Physics*"[9]. In it, he posed a question as to whether it

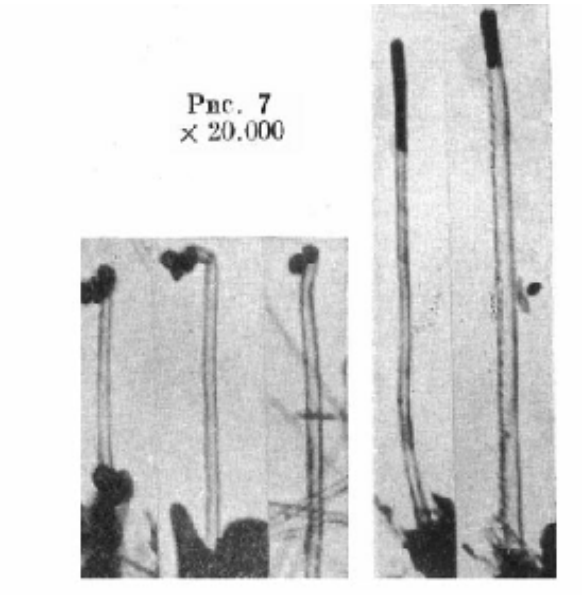


Figure 1.3: TEM observation by L.V. Radushkevich and V.M. Lukyanovich who published their findings in 1952 in Ref. [5].

was possible to compress all the information contained in 24 volumes of Encyclopaedia Britannica, all the books of Library of Congress, the British Museum Library and the National Library of France, totalling 24 million books onto the head of a pin. In principle, he deduced that it was not inconceivable. Hence, it was at this public lecture where the concept of miniaturization was born. The ability to look at and manipulate atoms, creating legible writing at the atomic scale so that an entire volume of information could be fitted on a pin head and then duplicating this stored information by creating templates by physical evaporation was proposed. However, the limitation to do this was the lack of technology at the time i.e., there were no powerful electron microscopes to view atoms. It was because of this need to miniaturize, that he called on physicists to develop better electron microscopes.

Since the "re-discovery" of carbon nanotubes in the early 1990's, the many wonderful properties of carbon nanotubes and the possible devices which exploit the properties of the nanotubes have been demonstrated in many laboratories worldwide.

1.2 A brief synopsis of carbon nanotube research

The rejuvenation of carbon research and in particular tubular fullerene's (carbon nanotubes) can attributed to Sumio Iijima's letter to Nature in 1991 [4].

Following Iijima's paper, the next major event in the history was the discovery of single-walled nanotubes (SWCNTs) in 1993 [10]. These were initially produced using arc-evaporation. Interestingly, a revisit of samples on which the 1991 Iijima paper was based, also revealed SWCNT in that sample [11]. In 1995, the Smalley group at Rice University, used laser-furnace method to produce high quality single-walled tubes [12] and in 1996 developed a method to produce SWCNTs catalytically [13]. This was an important development since large quantities could be synthesized by this method. A number of methods for the bulk synthesis of SWCNTs have since been developed, patented and commercialized. Most notable are the methods with acronyms HiPco [14] and CoMoCAT [15]. However, the commercial price of SWCNTs still remain high ($750/gram in 2010) [16]. It is important to note that the quality of single-walled carbon nanotubes produced using catalytic processes are similar to those made using the arc- or laser–furnace methods. A huge amount of research has been done on the growth of vertical arrays of multi-walled tubes on substrates, following the pioneering work of Zhifeng Ren and colleagues in 1998 [17]. The primary aim of this work was to manufacture field emission display devices, although it is not clear whether this has led to any commercial products as yet. A field emission display based on carbon nanotubes was promised by the electronic giant Samsung but this device has not as yet made it to the market. Another important application was the directed growth of SWCNTs across substrates, to produce nanoscale circuits, pioneered by Hongjie Dai's group (a former member of Smalley's group). They showed in a 2001 paper that this could be achieved using electric fields and in 2004, they used catalytic growth to integrate nanotube transistors into a silicon circuit [18].

The study and exploitation of the electronic properties of SWCNTs has been a driving force in nanotube research and has largely relied on theory followed by experiment. Theoretical papers on the electronic properties of tubular fullerenes were published by Dresselhaus's MIT group before Iijima announced the synthesis of SWCNTs in 1993 [19]. Further work by this group demonstrated that electronic properties were a function of both tube structure and diameter and that SWCNTs could be either semiconducting or metallic depending on their size and structure [20].

Other significant achievements in SWCNT research include the construction in 2001 of a SWCNT-based single-electron transistor which operated at room temperature and of a logic gate based on a single nanotube bundle [21]. While most of these types of devices have been demonstrated, reliable methods of scaling up production to produce reliable devices based on well defined nanotubes is not available and is currently under development [22].

Recent research has suggested that single layer graphene offers a better prospect than nanotubes for the construction of nanoscale devices [23]. Graphene is certainly a fascinating and important material but its use in nanoelectronics is still at a very early stage of development and a reliable synthesis of graphene has still to be achieved.

An obvious application of nanotubes is to exploit their excellent mechanical properties[11]. The Young's modulus was found to close to 1 TPa [11], making it one of the stiffest materials known. Their high tensile strength was measured at 63 GPa which is about 50 times higher than steel [24]. The extraordinary mechanical properties of carbon nanotubes have prompted a major research effort into the production of nanotube-containing composite materials. More recently, significant progress has been made in dispersing nanotubes homogeneously in a variety of matrices, and achieving good bonding between the tubes and the matrix. As a result, several groups have produced nanotube/polymer composites with impressive mechanical properties [25].

The production of better nanotube-containing composites has been enhanced by progress in nanotube functionalization, and in the understanding of the chemistry of nanotubes. In particular, the purification of nanotubes has been an intensive area of research [21]. The functionalization of nanotubes (the attachment of chemical groups to the outside of nanotubes) and on research of filling the tubes [11].

The application of nanotubes as AFM tips is an important growth area. Many groups have demonstrated that nanotubes have significant advantages over conventional silicon or silicon nitride AFM probes [24] and AFM tips based on nanotubes are now commercially available. An area with great commercial potential, is the use of nanotubes as sensors [26, 24]. The use of nanotubes in bio-sensors is also attracting a major research effort. Both bulk amounts of nanotubes and individual tubes can be used in this way, and the prospects for commercial exploitation appear to be good.

1.3 Motivation for this dissertation

In 2006, a study by Michael Banks [27] based at the Max Planck Institute for Solid-State Physics in Stuttgart, Germany found that carbon nanotubes was the hottest topic being studied by scientists. This topic was followed by nanowires, quantum dots, fullerenes, giant magnetoresistance, M-theory and quantum computation. He determined this by combining the *h-index* which is a measure of a scientists research productivity and how long a certain topic continues to be investigated. In 2008, a report in *Materials Today* [28] on the

Top Ten most advances in materials science listed carbon nanotubes at number 8 in the list, lower on the list than one would have expected, given the intensity of the research area. Even though advances in its study have been made, there still remains much to understand in their synthesis, purification, large-scale production, and assembly into devices. Compounding these problems is the frustrating inability to manufacture uniform samples of nanotubes with the same properties [22].

It is well known that SWCNTs form by self-assembly, leading to the formation of an assortment of semiconducting, metallic and chiral nanotubes. Furthermore the mechanism as to how nanotubes grow is as yet not understood. Without such an understanding there is little hope of developing mastery on preparing nanotubes with defined structures, or for the bulk synthesis of high-quality nanotubes. Although progress has been made, the growth mechanisms of both single-walled and multi-walled nanotubes remain controversial. We know how to make single-electron transistors from individual carbon nanotubes, but it is still not known how to prepare nanotubes with a defined structure!

1.4 Research Questions

The key questions in current single-walled carbon nanotube research is to explain how they grow, when they grow or nucleate and how we can control their growth. In this dissertation, an investigation of these questions is pursued in order to achieve a better understanding of the problem and to contribute to the body of knowledge that would eventually unravel the mysteries surrounding the controlled growth of single-walled carbon nanotubes. To do this, the laser-furnace method to synthesize SWCNTs has been employed [12]. Briefly, a material target containing graphite and a small percentage of transition metal catalysts have been used. The target was then ablated. The ablated material self-assembled during the evolution of the plasma plume and condensed in the cooler regions. It is this material which is rich in SWCNTs. In order to develop a picture of how nanotubes are formed and which nanotubes are formed, a parametric investigation was undertaken which involved changing the furnace temperature, target composition and the pressure and flow rate of argon gas used in the synthesis experiments. In this way, conditions were found which appeared to discriminate between the type of nanotubes which could be synthesized by applying Raman and photoluminescence spectroscopies. Furthermore, the conventional experimental setup was modified to allow optical access to the laser induced plasma. Optical emissions from the carbon species

within the plasma was temporally and spatially investigated. The results of these experiments were used to calculate the temporal and spatial changes to the electron density and electron temperature which are important parameters in a laser induced plasma. Furthermore, the temporal and spatial changes of C_2, an important precursor to the nucleation and growth of SWCNTs, was investigated.

1.5 Plan of dissertation

In Chapter 1, the background to the nature of the dissertation is provided and includes a motivation for the research undertaken based on research questions formulated as a result of a lack of understanding relating to the controlled growth of single-walled carbon nanotubes.

In Chapter 2, single-walled carbon nanotubes as another form of carbon is discussed, including its physical description, methods of synthesis, its growth mechanisms, physical properties and potential applications which has made carbon nanotubes one of the most researched material in the last two decades.

In Chapter 3, methods of characterizing single-walled carbon nanotubes are discussed. While there are many analytical methods employed to investigate carbon nanotube properties, in this dissertation, the focus was on applying Raman spectroscopy, photoluminescence spectroscopy and electron microscopy. These methods have been the most widely used techniques to distinguish between nanotube types. Details of these analytical methods and how they can be used to distinguish between nanotubes are discussed.

In Chapter 4, background information on laser and laser-material interaction are discussed. Also included in this chapter, are the description of the experimental methods and experimental layout employed to synthesize single-walled carbon nanotubes.

In Chapter 5, results and discussions of the experiment to synthesize nanotubes are presented. A major component of this chapter, are the results and discussion of the characterization of the as-prepared using Raman spectroscopy, photoluminescence spectroscopy and electron microscopy on as-prepared material. It concludes with a proposed growth of single-walled carbon nanotubes synthesized by the laser-furnace method.

Chapter 6 is devoted entirely to the application of *in situ* optical emission spectroscopy to investigate the laser induced plasma properties during the synthesis of single-walled carbon nanotubes. In this chapter, measurements of the temporal and spatial dynamics of C_2, electron density and electron temperature were made and correlated to the nucleation and growth of single-

walled carbon nanotubes.

In Chapter 7, we conclude the research undertaken and propose future research that could extend the scope of the present study.

Chapter 2

Single-Walled Carbon Nanotubes

2.1 Elemental Carbon

Carbon is the sixth element of the Periodic Table of Elements consisting currently of 116 elements. Carbon has historically two naturally occurring allotropes, namely diamond and graphite, whilst lonsdalite, fullerenes and carbon nanotubes have been artificially formed either in laboratories or by meteor impact. These materials are called allotropes because while they are composed entirely of carbon, their crystal structures are different. The ability of an element to have several stable crystal variants of itself is not unique to carbon. Elements in the Group 14 column of the periodic table have similar capabilities. However, the uniqueness of carbon lies in the fact that the properties of its polymorphs are extraordinarily different from one another. Diamond is transparent in the visible spectrum and is the hardest material known to mankind while graphite is opaque and its surface is lubricating. In recent times a new allotrope called carbon nanotubes has become a major focus in scientific and engineering research. It too has extraordinary properties that are different to diamond and graphite.

Besides bonding to itself in repetitive fashion, carbon has a rich chemistry with many elements of the periodic table forming an extraordinary number of compounds. In particular, the chemistry of carbon bonding with hydrogen, oxygen, nitrogen etc. is the branch of chemistry known as organic chemistry. Such is the bonding capability of carbon, that more carbon compounds exist than the compounds of all other elements put together [29].

What makes carbon so unique? It is the purpose of this section to bring into perspective and explain why and how carbon is able and can form crys-

Element, symbol	Atomic number, Z	Electronic structure
carbon, C	6	$1s^2 2s^2 2p^2$
nickel, Ni	28	$[Ar]3d^8 4s^2$
cobalt, Co	27	$[Ar]3d^7 4s^2$
iron, Fe	26	$[Ar]3d^6 4s^2$
yttrium, Y	39	$[Kr]4d^2 5s^2$

Table 2.1: Table 2.1: Electronic structure of carbon and common transitional metals that are used as catalysts in the synthesis of single-walled carbon nanotubes

talline allotropes such as graphite, diamond, lonsdalite, fullerenes and carbon nanotubes.

The carbon atom in its natural state has six electrons orbiting the nucleus (Bohr Model) which consist of 6 protons and 6 neutrons resulting in an overall electronic charge of zero. The wave-nature of electrons associated with the nucleus was put forward by Erwin Schroedinger (1887-1961) who proposed that the electrons where confined to particular energy levels, called orbitals. These energy levels are well defined. Only certain energy levels are allowed [30]. The electronic structure of carbon and common transition metals used in the synthesis of carbon nanotubes is shown in Table 2.1

2.2 Carbon vapour molecules

At high temperature, carbon vaporizes to form a gas. This gas is a mixture of carbon ions or radicals, single carbon atoms and diatomic and polyatomic molecules, that is, molecules. These gaseous constituents are usually designated as C_1, C_2, C_3 etc.. The understanding of the composition and behavior of these carbon vapors, the accurate measurement of their heat of formation, and the precise determination of their ratio are essential if the heat of formation of organic compounds is to be calculated, i.e., the energies of all bonds involving carbon.

The vaporization of carbon occurs during the ablation of carbon. The rate of ablation is related to the composition of the carbon vapor formed during laser ablation and to the heat of formation of the various carbon-vapor species and their evaporation coefficients. Mass-spectrographic measurements of the energy required to vaporize graphite to the monoatomic gas C, is 710.51 $kJ.mol^{-1}$. Values for the heat of formation of other molecular vapor species of carbon shown in Table 2.2 were taken from Ref. [31].

C_1, C_2, and particularly C_3 are the dominant species in the equilibrium vapor in the temperature range of 2400 - 4500 K as shown in the Arrhenius

Molecule	Heat of formation (KJ/mole)
C_2	823
C_3	786
C_4	1005
C_5	1004
C_6	1199

Table 2.2: The heat of formation of carbon molecules. Taken from Ref[xxx]

plot of the partial pressure of these species in Fig. 2.1 [32]. The contribution of C_6 and larger molecules to the vapor pressure is small and generally, these species are unstable or short lived [33]. The general structure of these carbon molecules is believed to contain double bonds, :C=C::::C=C: (the so-called cumulene structure) which have delocalized bonding and an axial symmetry.

2.3 Major allotropes of carbon

The chemistry of carbon is extremely rich due the different bonding configurations that enables it to bond covalently with itself and other elements. By bonding to itself, carbon has the softest material in graphite, and the hardest naturally occurring material, in diamond. In recent years, due to the attraction of the discovery of the fullerene (1985) and carbon nanotubes (1991), the field of carbon and its allotropes have vastly increased. Here, we focus on four, of these allotropes i.e., graphite, diamond, fullerenes and carbon nanotubes.

2.3.1 Graphite

The origin of the word "graphite" is the Greek word "graphein" which means "to write". In the 18th century, it was demonstrated that graphite actually is an allotrope of carbon. Strictly speaking, the term "graphite" by itself describes an ideal material with a perfect graphite structure with no defects. However, the term "graphitic carbons" is used to describe, materials consisting of carbon with the graphite structure, but with a number of structural defects, or "non-graphitic carbons". These materials consist of carbon atoms with the planar hexagonal networks of the graphite structure, but lacking the crystallographic order in the c direction [29].

Graphite is composed of series of stacked parallel layer planes as shown schematically in Figure 2.2, with trigonal sp^2 bonding. Within each layer plane, the carbon atom is bonded to three others, forming a series of continuous hexagons in what can be considered as an essentially infinite two-dimensional molecule. The bond is covalent and has a short length (0.141 nm) and high

pressure C.png

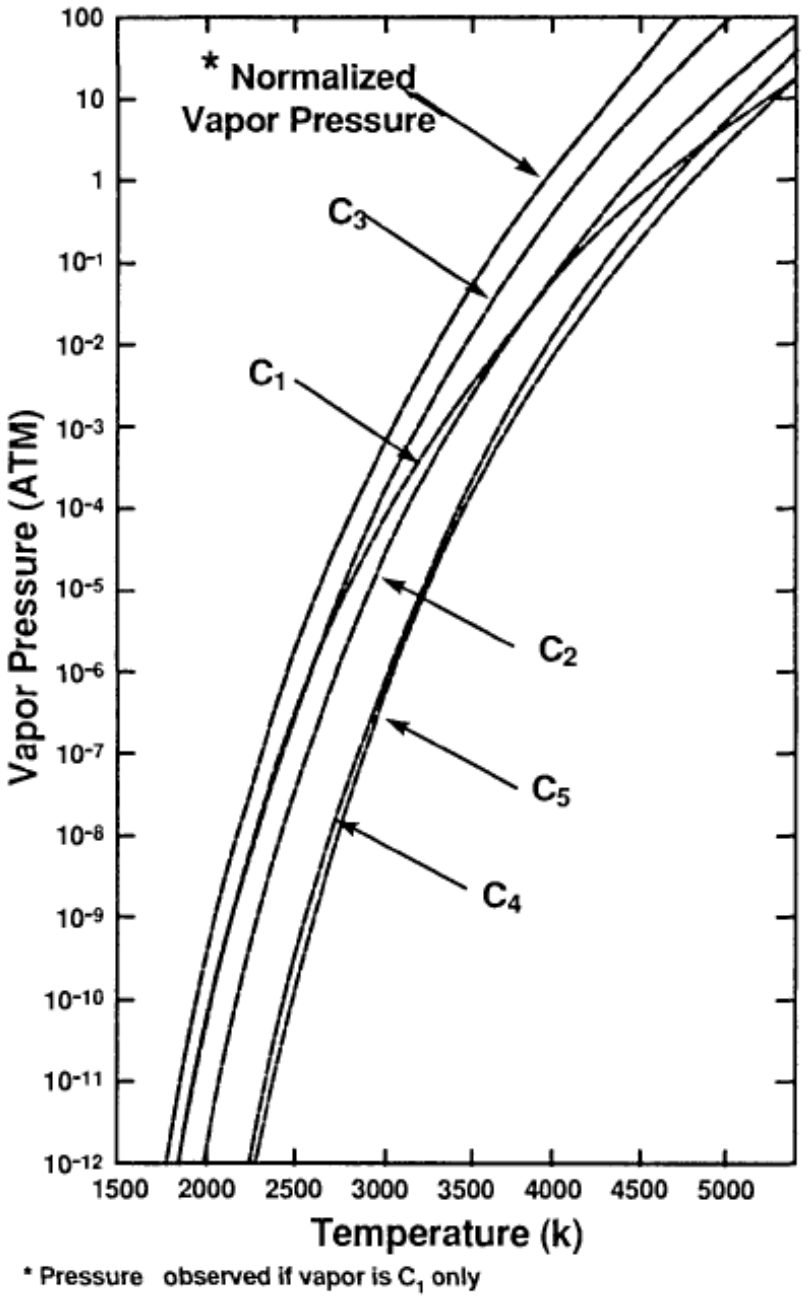


Figure 2.1: Vapor pressure of C molecules as function of pressure and temperature. Taken from Ref. [29]

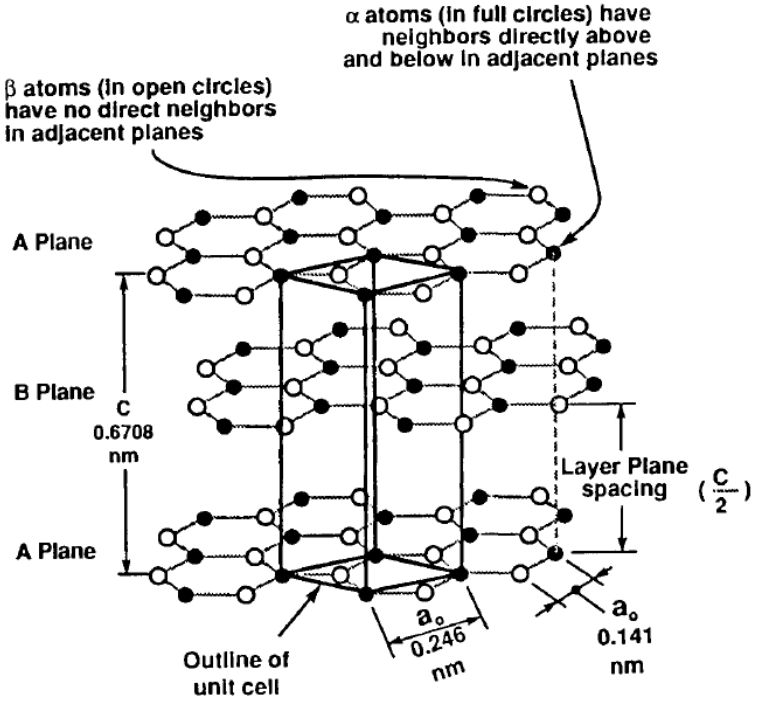


Figure 2.2: The crystal structure of graphite showing the ABAB stacking sequence and unit. Taken from Ref. [29].

strength (524 kJ/mole). The hybridized fourth valence electron is paired with another delocalized electron of the adjacent plane by a much weaker van der Waals bond (a secondary bond arising from structural polarization) of only 7 kJ/mol (pi bond).

Carbon is the only element to have this particular layered hexagonal structure. The spacing between the layer planes is relatively large (0.335 nm) or more than twice the spacing between atoms within the basal plane and approximately twice the van der Waals radius of carbon. The stacking of these layer planes of carbon can occur in two slightly different ways: a hexagonal, stacking sequence ABABABA etc. and a rhombohedral, stacking sequence ABCABCABC etc.

2.3.2 Diamond

Diamond has been in use since ancient times. The name diamond is derived from the ancient Greek (adámas) which mean, unalterable and/or unbreakable. In 1772, Antoine Lavoisier used a lens to concentrate the rays of the sun on a diamond in an atmosphere of oxygen, and showed that the only product of the combustion was carbon dioxide, proving that diamond is composed of only carbon. Later in 1797, Smithson Tennant repeated and expanded on the

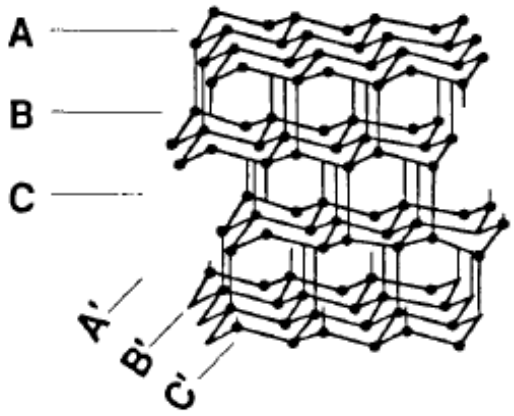


Figure 2.3: A schemtaic of the diamond structure. Taken from Ref. [29].

experiment. By demonstrating that burning either diamond or graphite (charcoal) released the same amount of gas, he established the chemical equivalence of these substances [1].

A diamond is a transparent crystal made of tetrahedrally bonded carbon atoms (sp^3) that crystallizes with a diamond lattice. Diamonds have been adapted for many uses because of the material's exceptional physical characteristics. Most notable are its extreme hardness and thermal conductivity (900–2320 $W{\cdot}m^{-1}{\cdot}K^{-1}$) as well as wide bandgap. (5.5 eV) and high optical dispersion. Above 1700 ^{0}C, in a vacuum or oxygen-free atmosphere, diamond converts to graphite; in air, transformation starts at $\sim$700 ^{0}C. Naturally occurring diamonds have a density ranging from 3.15–3.53 g/cm^3, with pure diamond being close to 3.52 g/cm^3. Despite the hardness of diamond, the chemical bonds that hold the carbon atoms in diamond together are weaker than those that hold together the carbon atoms in graphite. The difference is that in diamonds, the bonds form an inflexible three-dimensional lattice [34].

The cubic structure of diamond can be visualized as a stacking of puckered infinite layers of the {111} planes, or as two face-centered interpenetrating cubic lattices, one with origin at 0, 0, 0, and the other at 1/4, 1/4, 1/4, with parallel axes, as shown in Figure 2.3. The stacking sequence of the {111} planes is ABCABC, so that every third layer is identical.

2.3.3 Fullerenes

The recent discovery of a family of large, solid carbon molecules with great stability, the so-called "fullerenes", has considerably extended the scope and variety of carbon molecules known to exist before 1985. The fullerenes can be considered as another major allotrope of carbon.

Unlike graphite or diamond, the fullerenes are not a single material, but

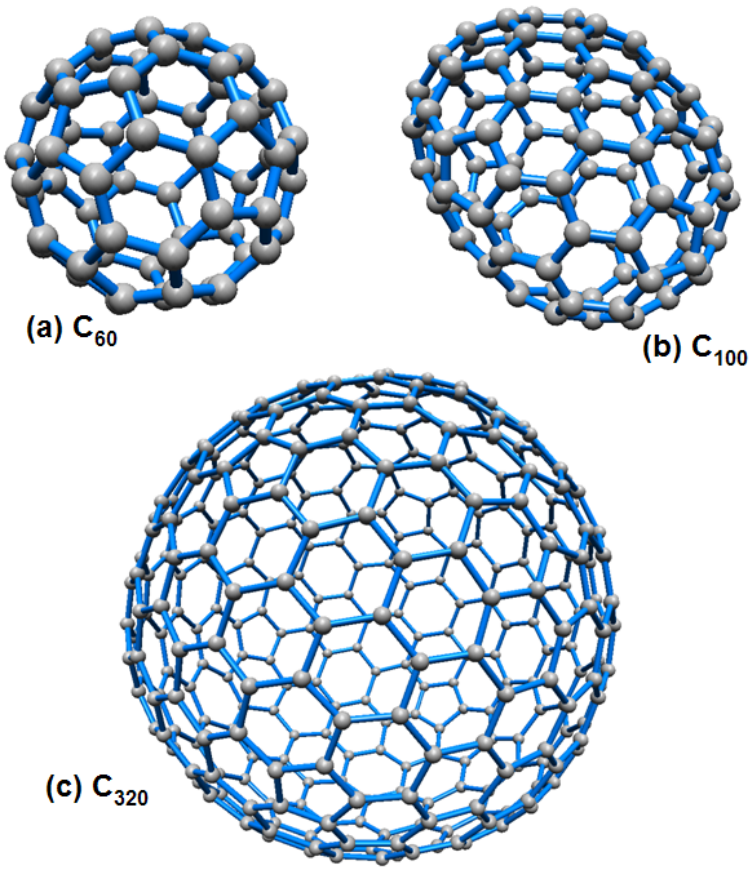


Figure 2.4: Fullerenes are a familiy of geodesic molecules which are very stable. Twelve pentagons are required in any fullerence molcule to close into a geodesic structure. They may may not be spherically symmetric as $C_{60.}$ (a) C_{60} , (b) C_{100} and (c) C_{320}. MKMoodley 2010©

a family of molecular, geodesic structures in the form of cage-like spheroids, consisting of a network of five-membered rings (pentagons) and six-membered rings (hexagons). In order to close the structure into a spheroid, these geodesic structures must have exactly twelve pentagons, but they can have a variable number of hexagons (m). They have the general composition: C_{20+2m}. Such an even-numbered distribution is unique to the element carbon. Figure 2.4 shows a schematic of three different fullerene molecules.

In order to account for the bonding of the carbon atoms in a fullerene molecule, the hybridization must be a modification of the sp^3 hybridization of diamond and sp^2 hybridization of graphite. Thus, the $\sigma-$ orbitals no longer contain only σorbital character and the $\pi-$orbitals no longer consist purely of πorbital character.

2.3.4 Carbon nanotubes

Carbon nanotubes (CNTs; also known as buckytubes) are allotropes of carbon with a cylindrical nanostructure. These cylindrical carbon molecules have novel properties that make them potentially useful in many applications in nanotechnology, electronics, optics and other fields of materials science. They exhibit extraordinary strength and unique electrical properties, and are efficient thermal conductors. The ends of a nanotube can be capped with a hemisphere of the buckyball structure. Like their fullerene cousins, the single-walled (SWCNT), double-walled (DWCNT) and multi-walled (MWCNT) carbon nanotubes.

The nature of bonding in a nanotube is described by orbital hybridization. The chemical bonding of nanotubes is composed entirely of sp^2 bonds, similar to those of graphite. This bonding structure, which is stronger than the sp^3 bonds found in diamonds, provides the molecules with their unique strength. Nanotubes naturally align themselves into "ropes" held together by Van der Waals forces. Figure 2.5 shows the schematics and accompanying TEM images of a (a) SWCNT, (b) DWCNT and (c) MWCNT. In recent years there has been a proliferation of research on SWCNTs resulting in numerous excellent texts and reviews on the subject. For completeness of this dissertation, some information on SWCNTs is given.

2.4 Physical description of single-walled carbon nanotubes

To imagine a single-wall carbon nanotube (SWCNT), consider a perfect graphene sheet of sp^2-hybridized carbon atoms arranged in hexagons and rolled into a cylinder so that the hexagonal rings connect coherently. The tips of the tube can be are sealed by two caps, each cap being a hemi-fullerene of the appropriate diameter.

Geometrically, there is no restriction to the diameters of a tube. However, calculations have shown that collapsing a single-wall tube into a flattened two-layer ribbon is energetically more favorable than maintaining the tubular morphology beyond a diameter value of ≈ 2.5 nm [35]. On the other hand, it is easy to grasp intuitively that the shorter the radius of curvature, the higher the stress and the energetic cost to maintaining a tubular structure. However, SWCNTs with diameters as low as 0.4 nm have been synthesized successfully [36]. A suitable energetic compromise is therefore reached for tubes with diameters

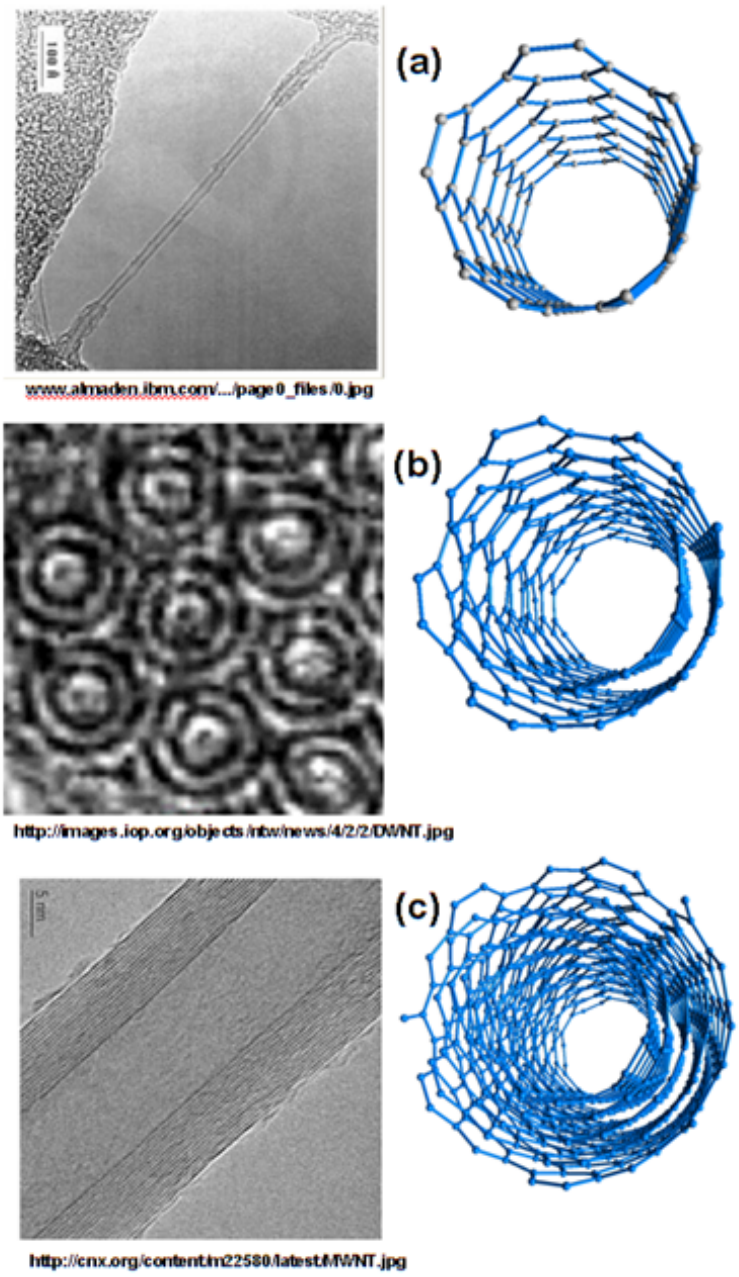


Figure 2.5: Schematics and accompanying TEM images of a (a) SWCNT, (b) DWCNT and (c) MWCNT. MKMoodley 2010©

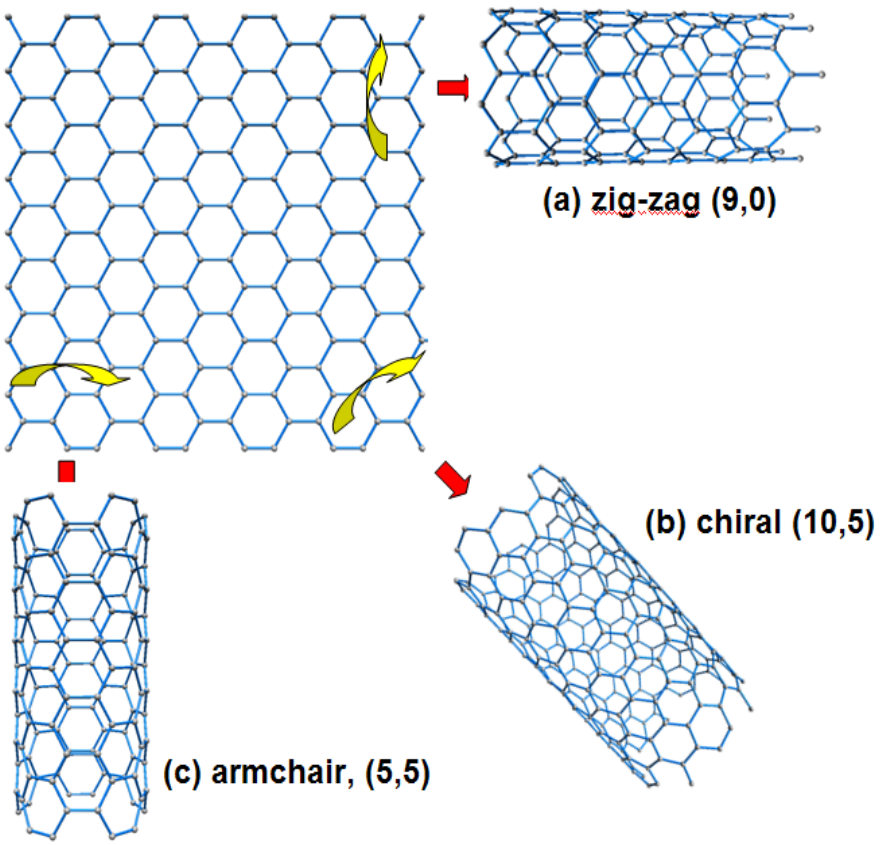


Figure 2.6: How a graphene sheet could be rolled to form (a) zig-zag nanotubes, (b) chiral nanotubes and (c) armchair. MKMoodley 2010©

of $\approx$ 1.3 nm, the most frequent diameter encountered, regardless of the synthesis technique. There is no such restriction on the nanotube length, which only depends on the limitations of the preparation method and the specific conditions used for the synthesis (thermal gradients, residence time, and so on). Experimental data are consistent with these statements, since SWCNTs wider than 2.5 nm are only rarely reported in the literature. These features make single-wall carbon nanotubes a unique example of single molecules with huge aspect ratio's.

As illustrated in Figure 2.6, there are many ways to roll a sheet of graphene into a single-wall nanotube. Some of the resulting nanotubes possess planes of symmetry both parallel and perpendicular to the nanotube axis (such as the SWCNTs generated in Figure 2.6a and 2.6c), while others do not, such as that of Figure 2.6b. Similar to the terms used for molecules, the latter are commonly called "chiral" nanotubes, since they are unable to be superimposed on their own image in a mirror.

The word "helical" is however sometimes also preferred. The various ways to roll graphene into tubes can be defined by the vector of helicity $\vec{C}_h$, and the angle of helicity θ, as shown in Figure 2.7. From Figure 2.7:

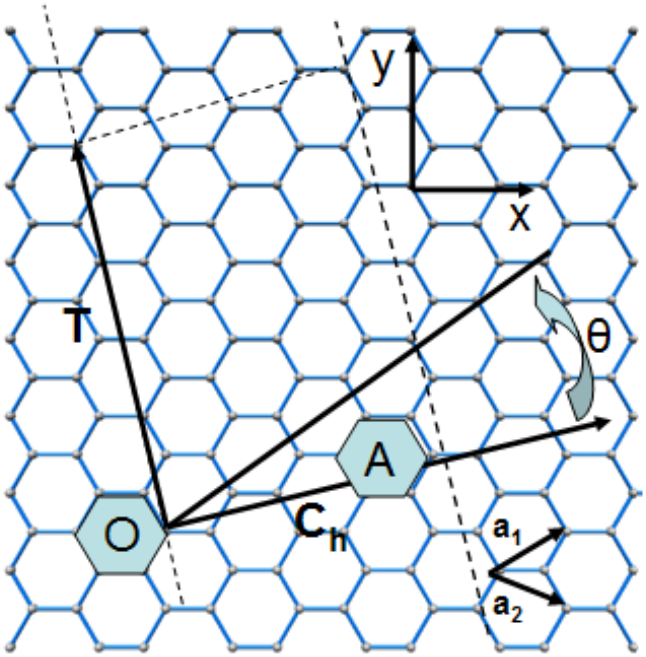


Figure 2.7: A schematic showing how a vector $\vec{C}_h$ could be used to define all SWCNTs. MKMoodley 2010©

$$OA = \vec{C}_h = n\mathbf{a}_1 + m\mathbf{a}_2 \text{ with} \tag{2.1}$$

$$\begin{aligned} \mathbf{a}_1 &= \frac{a\sqrt{3}}{2}\mathbf{x} + \frac{a}{2}\mathbf{y} \text{ and } \mathbf{a}_2 = \frac{a\sqrt{3}}{2}\mathbf{x} - \frac{a}{2}\mathbf{y} \text{ where } a = 2.46\mathring{A} \text{ and} \\ \cos\theta &= \frac{2n+m}{2\sqrt{n^2+m^2+nm}} \end{aligned} \tag{2.2}$$

where n and m are the integers of the vector OA. The unit vectors are $\mathbf{a}_1$ and $\mathbf{a}_2$. The vector of helicity $\vec{C}_h(= OA)$ is perpendicular to the tube axis, while the angle of helicity θ is taken with respect to the so-called zig-zag axis: the vector of helicity that results in nanotubes of the "zig-zag" type. The diameter D of the corresponding nanotube is related to $\vec{C}_h$ by the relation:

$$D = \frac{\left|\vec{C}_h\right|}{\pi} = \frac{a_{cc}\sqrt{3(n^2+m^2+nm)}}{\pi} \tag{2.3}$$

where $1.41\mathring{A}$ (graphite) $\leq a_{c=c} \leq 1.44\mathring{A}$ (C_{60}). The C-C bond length is actually elongated by the curvature imposed by the structure; the average bond length in the C_{60} fullerene molecule is a reasonable upper limit, while the bond length in flat graphene in genuine graphite is the lower limit (corresponding to an infinite radius of curvature). Since $\vec{C}_h$, θ, and D are all expressed as a

function of the integers n and m, they are sufficient to define every SWCNT by denoting them as (n, m). The values of n and m for a given SWCNT can simply be obtained by counting the number of hexagons that separate the extremities of the $\vec{C}_h$vector following the unit vector $\mathbf{a}_1$ first and then $\mathbf{a}_2$ [37].

In the example, of the schematic shown in Figure 2.7, the SWCNT that is obtained by rolling the graphene sheet so that the two shaded aromatic cycles can be superimposed exactly is a (4,2) chiral nanotube. Similarly, SWCNTs from Figures 2.6a to 2.6c are (9,0), (5,5), and (10,5) nanotubes respectively. These illustrate examples of zig-zag type SWCNTs (with an angle of helicity $= 0^0$), armchair-type SWCNTs (with an angle of helicity of 30^0) and chiral SWCNTs, respectively. This also illustrates why the term "chiral" is sometimes inappropriate and should preferably be replaced with the word "helical".

Armchair (n, n) nanotubes, although definitely achiral from the standpoint of symmetry, exhibit a nonzero "chiral angle". "Zig-zag" and "armchair" qualifications for achiral nanotubes refer to the way that the carbon atoms are displayed at the edge of the nanotube cross-section (Figure. 2.6a and 2.6c).

Generally speaking, it is clear from Figures 2.6a and 2.7 that having the vector of helicity perpendicular to any of the three overall C=C bond directions, will provide zig-zag type SWCNTs, denoted $(n, 0)$, while having the vector of helicity parallel to one of the three C=C bond directions will provide armchair type SWCNTs, denoted (n, n). On the other hand, because of the sixfold symmetry of the graphene sheet, the angle of helicity, θ , for the chiral (n, m) nanotubes is such that $0 < \theta < 30^0$.

2.5 Methods for the synthesis of SWCNTs

There are numerous reviews and books in which the synthesis of carbon nanotubes have been described [11, 24, 38, 39, 40]. While there have been a plethora of methods used to synthesize carbon nanotubes, this section only highlights the most common methods used to synthesize SWCNTs. Whether the synthesis of SWCNTs occurs near the focus of a high-powered laser, or between two arcing graphite electrodes, in a hot furnace full of hydrocarbon gas, or even in the middle of a flame, the common factors and basic prerequisites are an active catalyst, a source of carbon, and adequate energy.

2.5.1 Arc discharge

Arc discharge was the first recognized method for producing both SWCNTs and MWCNTs, and has been optimized to be able to produce gram quantities

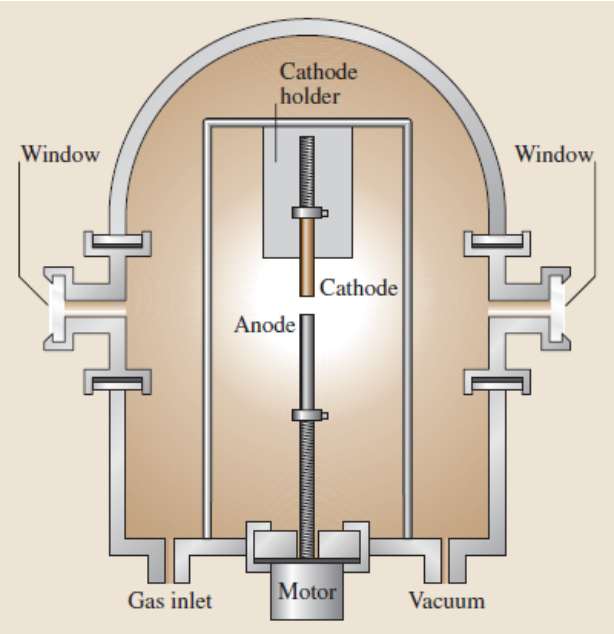


Figure 2.8: A schematic of an electric-arc reactor used to synthesize SWCNTs. Taken from Ref. [11].

of the material. Arc-discharge synthesis use a low-voltage (∼12 to 25 V), and high-current (50 to 120 amps) power supply such as an arc welder. An arc is generated across a 1-mm gap between two graphite electrodes 5 to 20 mm in diameter. An inert gas such as He or Ar is used as the atmosphere for the reaction, at a pressure of 100 to 1000 Torr. Iijima produced the first MWCNTs by this method [4]. He found that nanotubes formed on the cathode, along with soot and fullerenes. Iijima and Ichihashi [10] and Bethune et al. [41] were the first to report on the production of SWCNTs. Figure 2.8 [11] shows a schematics of an arc-discharge apparatus.

Both Iijima and Bethune found that SWCNTs could only be formed by adding metal catalyst's to the anode. Iijima used an Fe:C anode in a methane:argon environment, while Bethune utilized a Co:C anode in a He environment. Currently, most experiments utilizing this method employ an Ar:He gas mixture. By tailoring the Ar:He gas ratio, the diameter of the SWCNTs formed can be controlled [42].

Several metal catalyst compositions produce SWCNTs, but the most favoured is a Y:Ni mixture that has been shown to yield up to 90% SWCNTs, with an average diameter of 1.2 to 1.4 nm [43].

2.5.2 CVD

Chemical vapour deposition is a method in which thermal energy provided by a furnace or a plasma source is used to dissociate an organic gas or vaporize an

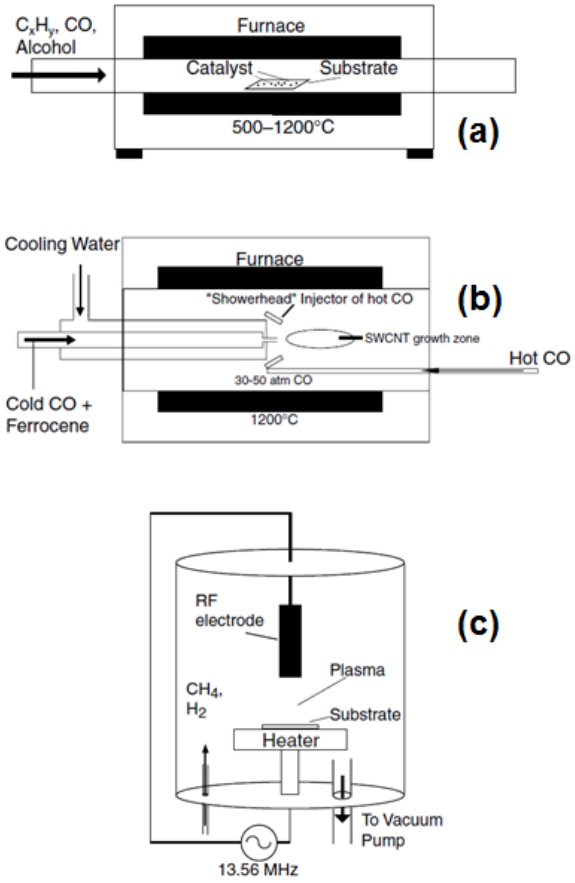


Figure 2.9: Schematic of CVD apparatus's commonly used to grow SWCNTs (a) typical CVD, (b) HiPCo method and (c) plasma enhanced CVD. Taken from Ref. [44]

organic chemical rich in carbon. In the CVD method, metals such as Ni, Fe or Co etc. are used as catalysts. Mo and Ru are sometimes added as promoters to the catalyst to render the feedstock more active for the formation of CNTs.

In 1996 a CO-based CVD process to produce SWCNTs was developed [13] that popularized the CVD method to produce SWCNTs. The CVD process encompasses a wide range of synthesis techniques, from the gram-quantity bulk formation of nanotube material to the formation of individual aligned SWCNTs on SiO_2 substrates. Figure 2.9(a)-(c) shows a typical schematic of an experimental setup for a CVD process [44]. In Figure 2.9(a), well aligned SWCNT can be grown. This method is particular good for use in advanced electronic applications were the properties of SWCNTs can be exploited [22].

Patented methods for producing SWCNTs in large quantities such as the HiPco (high pressure disproportion of CO)[14] are shown in Figure 2.9(b). A combination of a plasma source and CVD, called plasma enhanced CVD (PECVD) (Figure 2.9(c) is also a very good method for growing aligned SW-

CNT for advanced electronic applications [21].

2.5.3 Laser ablation synthesis

The first laser was built in 1960. Thereafter, physicists immediately made use of it as a means of concentrating/depositing large quantities of energy inside a very small volume in a relatively short time span. During the interaction between the laser beam and a material, numerous phenomena occur and each of these processes are sensitive to parameters such as the characteristics of the laser beam, the incoming power density, the nature of the target. Depending on the laser power incident on the target, the material can heat up, melt or vaporize. While a laser was successfully used to synthesize fullerene-related structures for the very first time in 1985 [2], the synthesis of SWCNTs by laser ablation took another ten years of research [12].

Two types of laser devices are currently utilized for carbon nanotube production: lasers operating in pulsed mode and lasers operating in continuous mode. The latter generally provide a smaller fluency at the target surface. An example of the layout of a laser ablation device is given in Figure 2.10(a). A graphite pellet containing the catalyst is placed in the middle of a quartz tube filled with inert gas and placed in an oven maintained at a temperature of 1200 ^0C [12]. The focussed laser beam vaporizes the target surface. The vaporized carbon species, are swept along by a flow of neutral gas, and are then deposited as soot at different regions within the reaction zone.

Due to the high quality of SWCNTs produced by the laser method, Jefferson's Laboratory's Free Electron Laser (JFEL) was also applied to the synthesis method. The schematic of the equipment used is shown in Figure 2.10(b). Ultrafast femtosecond pulses from the JFEL at a rate of 75 MHz was used to synthesize SWCNTs. A jet of re-heated argon gas "blows" away plasma plumes generated by the JFEL. Typical laser wavelengths employed are 3000 nm and the targets are similar to those used in the traditional laser method. With JFEL, about 45 g/h of SWCNTs can be produced [45]. Nevertheless, it is a very expensive system to operate.

In Figure 2.10(c), a schematic of an experimental set-up in which a continuous wave CO_2 ($\lambda = 10.6$ μm) laser is employed is shown. The power can be varied from 100 W to 1600 W. The temperature of the target is measured with an optical pyrometer, and these measurements are used to regulate the laser power to maintain a constant vaporization temperature. The gas, heated by contact with the target, acts as a local furnace and creates an extended hot zone, making an external furnace unnecessary. The gas is extracted through

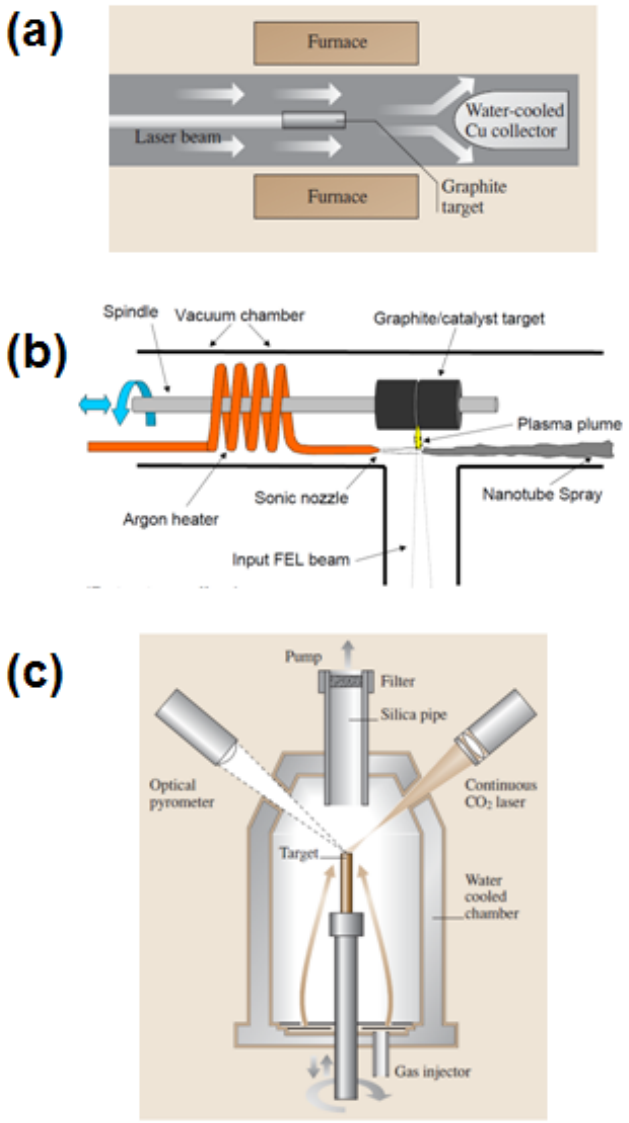


Figure 2.10: Schematic of experiments involving the use of lasers to synthesize SWCNTs for (a) Typical laser-furnace set-up, (b) the use of a high power free electron laser at JFEL and (c) use of a continuous CO_2 laser. Taken from Refs. [11, 44].

a silica pipe, and the solid products formed are carried away by the gas flow through the pipe and collected on a filter [46].

2.6 Growth mechanisms

The mechanisms by which carbon nanotubes nucleate and grow remain poorly understood. Current knowledge on growth mechanisms indicate that there is no universal mechanism which can explain the growth of SWCNTs in the arc-discharge, laser method and CVD methods i.e. the growth mechanisms appear to be different in each case. In this section, we summarize an excellent review by P.J.F. Harris [39] who proposed an explanation for SWCNT growth in the arc-evaporation and laser-vaporization processes. For growth mechanism's using the CVD methods, see reviews by Mann [44] and Monthioux et al.[11] and references therein.

Mechanisms of single-walled nanotube formation in the arc-evaporation and laser-vaporization processes are similar since both methods use similar starting materials, namely a graphite–metal mixture. Both also involve the vaporization of this mixture followed by condensation in an inert atmosphere. Moreover, the nanotube-containing soot produced by both methods is identical in appearance, containing bundles of SWCNTs together with disordered carbon and metal particles. Therefore, we assume that mechanisms proposed for one process are applicable to both.

It is generally accepted that the mechanism probably involves "root growth" rather than "tip growth". In other words, the tubes grow away from the metal particles, with carbon being continuously supplied to the base. This is supported by the fact that metal particles are not found at the tips of SWCNTs produced by arc-evaporation or laser-vaporization, as would be the case if tip growth had occurred [47]. Also, most of the particles observed in the SWCNT containing soot have diameters much larger than those of the individual tubes. As far as a detailed mechanism is concerned, a theory which has gained wide popularity is the vapour–liquid–solid (VLS) model and assumes that the first stage of nanotube formation involves the simultaneous condensation of carbon and metal atoms from the vapour phase to form a liquid metal carbide particles.

When the particles are supersaturated, solid phase nanotubes begin to grow. A number of detailed modelling studies, for example by Gavillet and colleagues [48] have been carried out, based on this mechanism. However, a number of experimental studies have suggested that SWCNT growth, like MWCNT growth, may involve a solid state transformation, thus casting doubt on

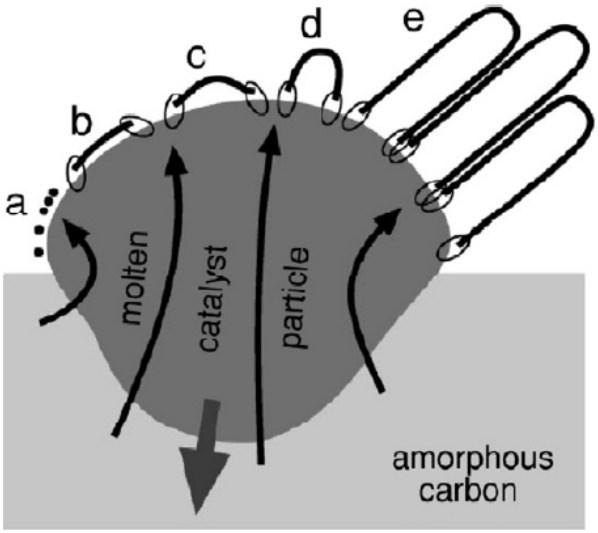


Figure 2.11: S-L-V model where SWCNT precipitate from the solid phase on catalyst particles. Taken from Ref. [49]

the validity of the VLS model [49]. The solid state growth of carbon nanotubes by thermal annealing of mechanically milled graphite powder was claimed as some single-walled nanotubes, as well as multiwalled tubes, were formed. The first unambiguous evidence for solid state growth of single-walled nanotubes was given by Geohegan and colleagues in 2001 [50], which is discussed below. Similar arguments were put forward by Gorbunov [49] and Kataura et al. [51]. Yet, in some of the arguments and experiments, there are contradictions. Figure 2.11 shows a schematic of the proposed model put forward by Gorbunov [49].

The experimental work of the Geohegan, Gorbunov and Kataura groups provides clear evidence that the formation of single-walled nanotubes, like that of multiwalled nanotubes, is a solid state process. The model suggested by Geohegan and colleagues [50] gives a picture of the processes at increasing times from the initial laser vaporization stage. The mechanism is probably broadly correct, but does not include a detailed mechanism for the transformation of solid carbon into nanotubes. The solid–liquid–solid mechanism of Gorbunov et al. [49] assumes that this transformation involves the dissolution of solid carbon in a liquid metal–carbon particle, followed by the precipitation of nanotubes at the surface of the particle. A problem with this theory is that it does not explain the findings of Kataura and colleagues [51].

The Gorbunov theory assumes that the "seeds" for nanotubes form when carbon precipitates out of the carbon–metal particles. This would suggest that nanotubes could be grown from a mixture of metal and any form of carbon,

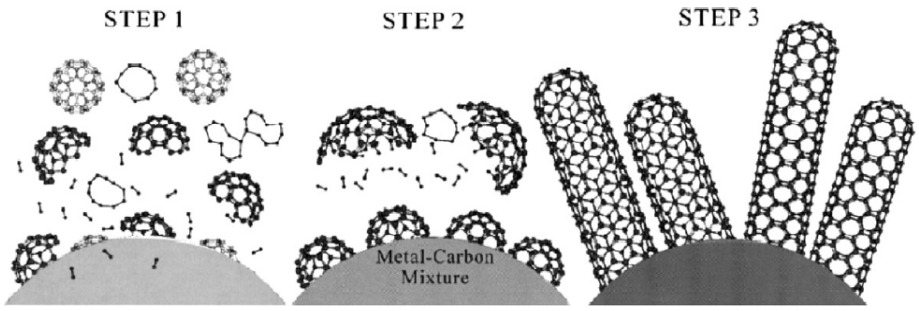


Figure 2.12: S-L-V mechanism put forward by Kautara et. al. showing that the growth of SWCNT is preceded by fullerene like seed. Taken from Ref. [51].

if it is subjected to a suitable heat-treatment. Kataura and colleagues showed that this is not the case: soot which had been prepared at temperatures below about 550 ^{0}C yielded no nanotubes on annealing at 1200 ^{0}C. This suggests that the growth of nanotubes requires the presence of fullerene-like seeds, which are presumably not formed when low oven temperatures are used.

The model put forward by the Kataura group assumes that some fullerene-like carbon fragments remain undissolved in the metal–carbon particles, and are deposited onto the particle surfaces, where they act as the seeds for nanotube growth. This model would seem to offer the best currently available explanation for SWCNT production by the arc and laser methods. A schematic of this model is shown in Figure 2.12.

2.7 Properties of SWCNTs

2.7.1 General properties

The diameters of SWCNTs fall in the nanometer regime, commonly between 0.8 nm to 1.6 nm but can be hundreds of micrometers long. SWCNTs are stable up to 750 ^{0}C in air but may suffer damage before this temperature is reached due to oxidation mechanisms at the atomic scale, as demonstrated by the fact that this is one of the methods of filling SWCNTs with other elements or molecules. They are stable up to between 1500–1800 ^{0}C in an inert atmosphere, beyond which they transform into regular, polyaromatic solids. The properties of a SWCNT, like any molecule, are heavily influenced by the way that its atoms are arranged. The physical and chemical behavior of a SWCNT is therefore related to its unique structural features [11].

2.7.2 Electronic and optical properties

The electronic states in SWCNTs are strongly influenced by their one-dimensional cylindrical structures. One-dimensional sub-bands are formed that have strong singularities in the density of states (Van Hove singularities). By rolling the graphene sheet to form a tube, new periodic boundary conditions are imposed on the electronic wave-functions, which give rise to one dimensional sub-bands. The roll-up vector $\vec{C}_h$ defines the helicity (chirality) and the diameter of the tube, as discussed in earlier sections. The electronic band structure of SWCNTs can be derived from the electronic band structure of graphene by applying the periodic boundary conditions of the tube under consideration.

The conduction and the valence bands of the graphene only touch at six corners (K points) of the Brillouin zone . If one of these sub-bands passes through the K point, the nanotube is metallic; otherwise it is semiconducting. This is a unique property that is not found in any other one-dimensional system. This means that for certain orientations of the honeycomb lattice with respect to the tube axis (chirality), some nanotubes are semiconducting and others are metallic. The band gap for semiconducting tubes is found to be inversely proportional to the tube diameter. As pointed out in section 2.4, knowing (n,m) allows us, in principle, to predict whether the tube is metallic or not. The energy gap decreases for larger tube diameters [37].

The electronic and optical properties of the tubes are considerably influenced by the environment. The electronic transition energies are in the infrared and visible spectral range [21]. The one-dimensional Van Hove singularities have a large influence on the optical properties of SWCNTs. Visible light is selectively and strongly absorbed by SWCNTs. Photoluminescence can be observed in individual SWCNT aqueous suspensions stabilized by the addition of surfactants. Detailed photo-excitation maps provide information about the helicity (chirality)- dependent transition energies and the electronic band structures of SWCNTs. Agglomeration of tubes into ropes or bundles influences the electronic states of SWCNTs. Photoluminescence signals are quenched for agglomerated tubes [52].

SWCNTs are model systems for the study of one dimensional transport in materials. Due to the reduced electron scattering observed for metallic SWCNTs and their stability at high temperatures, SWCNTs can support current densities as high as 109 A.cm^2 which is about three orders of magnitude higher than Cu. Structural defects can, however, lead to quantum interference of the electronic wave function, which localizes the charge carriers in one-dimensional systems and increases resistivity [53].

As a probable consequence of both the small number of defects which contribute by negatively affecting phonon transport and the cylindrical topography, SWCNTs exhibit a large phonon mean free path, which results in a high thermal conductivity. The thermal conductivity of SWCNTs is comparable to that of a single, isolated graphene layer or high purity diamond (6000 $W.m^{-1}K^{-1}$) [54]. Finally, carbon nanotubes may also exhibit positive or negative magnetoresistance depending on the current, the temperature, and the field [11].

2.7.3 Mechanical properties

The tubular, nanomorphology is observed for many two-dimensional solids. Carbon nanotubes are unique due to the particularly strong bonding between the sp^2 carbons bonds of the curved graphene sheet, which is stronger than in diamond where the carbon bonds are sp^3 hybridized. This makes carbon nanotubes particularly stable against deformations.

The tensile strength of SWCNTs can be 20 times that of steel and has been measured as to be as high as 45 GPa [55]. Very high tensile strength values are also expected for ideal (defect-free) MWCNTs, since combining perfect tubes concentrically is not detrimental to the overall tube strength, provided the tube ends are well capped (otherwise, concentric tubes could glide relative to each other, inducing high strain). Tensile strength values as high as 150 GPa have actually been measured for perfect MWCNTs prepared from an electric arc [56].

2.7.4 Reactivity

Unlike graphite, perfect SWCNTs have no, chemically active, dangling bonds. In the case of graphene, the reactions of poly-aromatic solids is known to occur mainly at graphene edges. Although graphene planes are chemically relatively inert, the radius of curvature imposed on the graphene in nanotubes causes the three normally planar C-C bonds formed by sp^2 hybridization, to undergo distortions, resulting in bond angles that are closer to three of the four C-C bonds in diamond. Even though this is not enough to make the carbon atoms chemically reactive, one consequence of this is that either nesting sites are created at the concave surface, or strong physisorption sites are created above each carbon atom of the convex surface, both with a bonding efficiency that increases as the nanotube diameter decreases.

The chemical reactivity of SWCNTs are believed to derive mainly from the caps, since they contain six pentagons each, as opposed to the tube body, which

supposedly only contains hexagons. Indeed, applying oxidizing treatments to carbon nanotubes (air oxidation, wet-chemistry oxidation) selectively opens the nanotube tips [57]. SWCNTs can be opened by oxidation methods and then filled with foreign molecules such as fullerenes. This suggests the occurrence of side defects. The defect sites have been proposed to be due to Stone–Wales mis-arrangements which may occur every 5 nm along the tube length and involves about 2% of the carbon atoms in a regular (10,10) SWCNT [58]. A Stone– Wales defect is formed from four adjacent heterocycles, two pentagons and two heptagons, arranged in pairs opposite each other.

Such a defect, allows localized double bonds to form between the carbon atoms involved in the defect, instead of these electrons participating in the delocalized electron cloud above the graphene as usual. Thus, the defect enhances the chemical reactivity [58]. This means that the overall chemical reactivity of carbon nanotubes should depend strongly on how they are synthesized. For example, SWCNTs prepared by the laser method are believed to contain fewer structural defects than CCVD synthesized SWCNTs, which are more chemically reactive [11].

2.8 Application of carbon to advanced technological devices

A carbon nanotube is inert, has a high aspect ratio and a high tensile strength, has low mass density, high heat conductivity, a large surface area, and a versatile electronic and optical behavior, including high electron conductivity. These properties make them ideal candidates for a large number of applications. The application of carbon nanotubes is therefore a very fast moving field, with new potential applications found every year, even several times per year [11]. Therefore, creating an exhaustive list of these applications is not the aim of this section. Instead, only a few important applications where great impact are possible are highlighted.

2.8.1 Field emission-based devices

In a pioneering work by de Heer et. al. [59], carbon nanotubes were shown to be efficient field emitters. This property is currently being used in several applications, including flat panel displays for television sets and computers. The first prototype of such a display was exhibited by Samsung in 1999. The principle of a field emission-based screen is demonstrated in Figure 2.13 [11]. Briefly, a potential difference is set up between the emitting tips and an extrac-

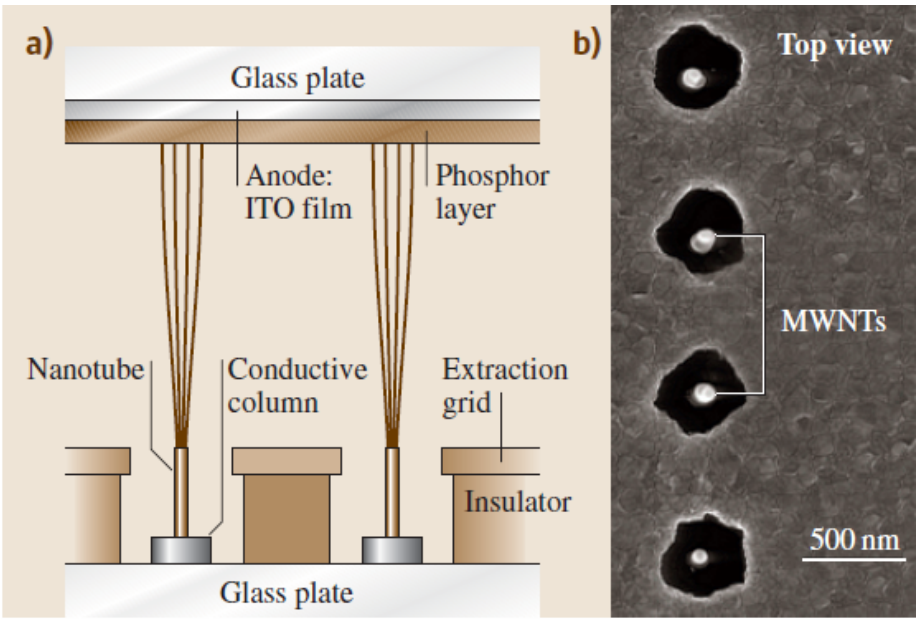


Figure 2.13: A schematic of how a modern TV screen based on the use of CNTs looks inside. (a) Cross-section showing the CNT field emiiter and (b) A SEM of the front of the field emitter. Taken from Ref. [11].

tion grid so that electrons are pulled from the tips onto an electron-sensitive screen layer. Replacing the glass support and protecting the screen using a polymer-based material should even permit the development of flexible screens. Unlike regular (metallic) electron-emitting tips, the structural perfection of carbon nanotubes allows higher electron emission stability, higher mechanical resistance, and longer lifetimes.

Most importantly, the use of CNTs saves energy since the tips operate at a lower heating temperature and require a much lower threshold voltage than in other set-ups. For example, it is possible to produce a current density of 1 mA.cm^{-2} for a threshold voltage of 3V μm with nanotubes, while it requires 20V μm for graphite powder and 100V μm for regular Mo or Si tips. The subsequent reductions in cost and energy consumption are estimated at 1/3 and 1/10 respectively. Generally speaking, the maximum current density that can be obtained ranges from 106 A.cm^{-2} to 108 A.cm^{-2}.

The use of MWCNTs rather than SWCNTs is preferred for many of these applications since MWCNTs emit more electrons when they are used as bunches. Furthermore it is easier to grow MWCNT-like arrays than it is for SWCNT arrays. On the other hand SWCNTs provide a more coherent source, a useful feature for devices such as electron microscopes or X-ray generators. The market associated with this application is huge. With major companies, such as Motorola, NEC, NKK, Samsung, Thales and Toshiba involved. Companies such as Oxford Instruments and Medirad are also commercializing miniature

X-ray generators for medical applications that use nanotube-based cold cathodes developed by Applied Nanotech Inc. [11].

2.8.2 Single-Walled Carbon Nanotube Transistors

One of the most important CNT devices, the CNT-FET, is composed of an individual SWCNT covered by metal electrodes at both ends and by a gate stack made of a metal electrode and a dielectric layer (Figure 2.14) [22]. The first reported CNT-FETs (in 1998) were based on a simple design involving the substrate (typically doped Si covered by a thin dielectric layer) as both device support and gate. Scaling the dimensions of the devices was soon recognized as an essential requirement in order to improve on the device characteristics. This, however, implied that better structures had to be explored, one of which, the top-gated structure having a high-k dielectric layer, is shown in Figure 2.14(a). The electrical characteristics of such a top-gated CNT-FET (see Figure 2.14(b) [60] are similar to those of conventional silicon transistors.

One may ask why carbon nanotubes? The atomic and electronic structures of a CNT provide a number of unique advantages for making a FET channel. First, its small diameter (1–2 nm) allows optimum coupling between the gate and the channel. Second, because the surface of CNTs is atomically smooth and all carbon bonds are satisfied in terms of valence (i.e., no dangling bonds), scattering by surface states or roughness that plague conventional FETs are absent in CNT-FETs.

2.8.3 Single-walled carbon nanotube thin film transistors (TFT)

Despite their outstanding performance, the practical implementation of single CNT-FETs face a number of hurdles. The principal one is the heterogeneity of the as-produced SWCNT mixtures. While synthetic techniques producing narrow distributions of SWCNT diameter and chirality have appeared in recent years and separation techniques have been demonstrated (see Liu and Hersam [61]), large quantities of pure single-type (diameter/chirality) semiconducting nanotubes are not available. This is an important problem, since such quantities are essential for large-scale integration of SWCNT-FETs. A nanotube-based electronic technology that has, to some extent, bypassed the heterogeneity problem is that of SWCNT thin-film transistors (SWCNT-TFTs) [22]. In such a TFT, a film of typically randomly oriented, as-prepared SWCNTs is deposited on an insulator. The electrodes are then patterned on top of it. The result is a channel having properties that are an ensemble average over all

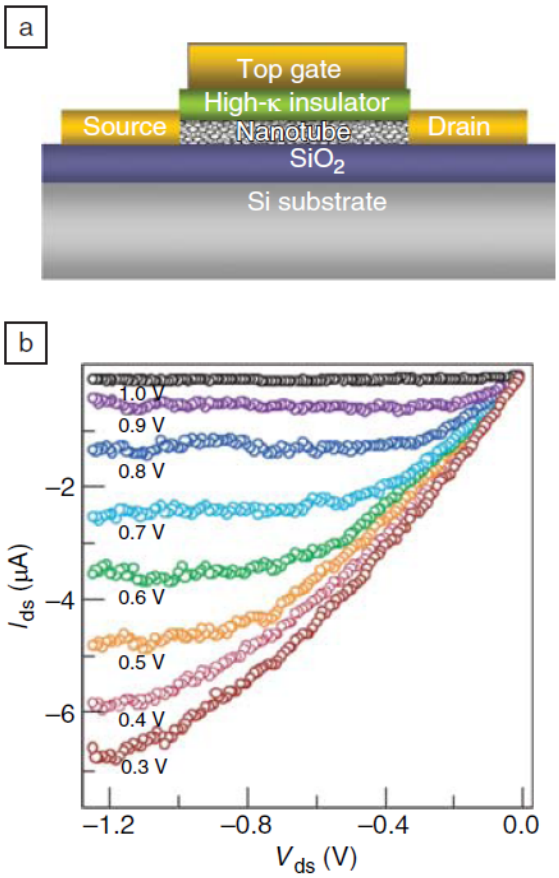


Figure 2.14: Top-gated carbon nanotube transistor. (a) A schematic of a top-gated structure for field-effect transistor (FET) and (b) Typical measured output characteristics of drains current I_{ds} versus drain voltage (V_{ds}) of a single nanotube p-type FET. Taken from Ref. [60].

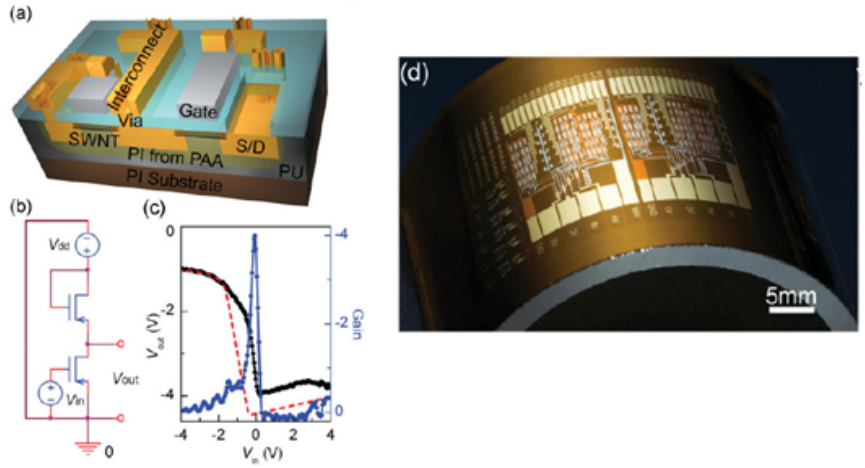


Figure 2.15: (a) Schematic view of a flexible SWCNT-TFT , (b) circuit diagram, and c) static transfer characteristics of an inverter composed of two p-channel SWNT TFTs on a PI substrate. PU, polyurethane; PAA, polyamic acid. In c), the dashed line represents a circuit simulation result. d) Optical image of a flexible SWNT integrated circuit chip bonded to a curved surface. Taken from Ref. [26].

SWCNT species present in the layer. Multiple SWCNTs having multiple tube-tube junctions form the switching channel, and transport involves percolation across SWCNTs having random orientation, chirality, and diameter.

For applications, the presence of metallic SWCNTs in the mixture obviously poses problems, since they tend to short-circuit the FET channels. To avoid this, the device has a generally longer source-drain separation compared to the average length of the SWCNTs. This approach ensures that metallic tubes do not directly bridge the gap between source and drain contacts, and the transport is dominated by percolation through semiconducting SWCNTs. One can optimize the current throughput of the SWCNT-TFT by controlling the SWCNT coverage. The challenge is to achieve the largest coverage of semiconducting SWCNTs, while staying below the threshold for metallic percolation.

In an unsorted mixture of CNTs, the semiconducting SWCNTs outnumber the metallic ones by about a factor of two, which allows for an increase of the SWCNT coverage, enabling improvement of the on-current without affecting the transistor on/off ratio [26]. The performance optimization in this case is a compromise between the on-current and the on/off ratio. The work on SWCNT-TFTs has evolved significantly over recent years, and prototypes clearly demonstrate that it could be applied for making useful, flexible, integrated circuits such as those shown in Figure 2.15 [26].

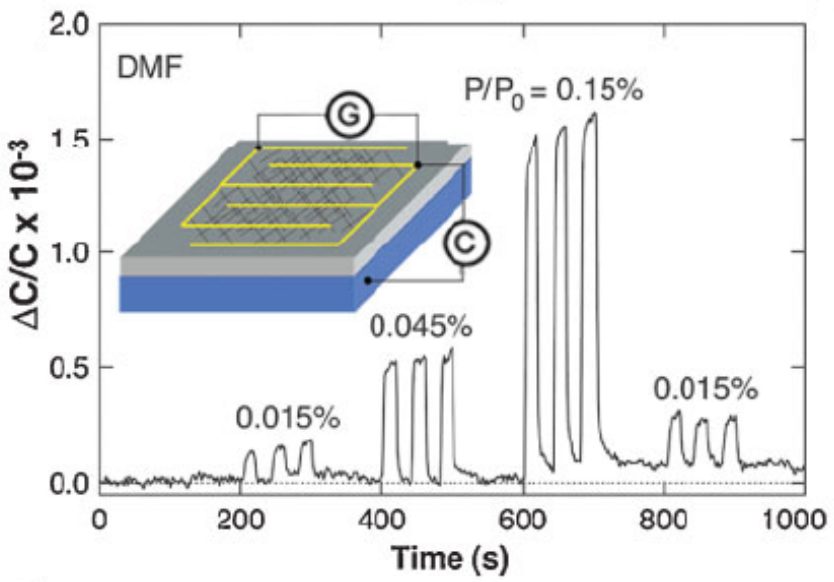


Figure 2.16: Relative change in capacitance versus time for a SWCNT chem-transistor in response to exposed to doses of N,N-dimethylformamide (DMF) at various concentrations. Taken from Ref. [62].

2.8.4 SWCNT thin films for sensing

The electronic properties of SWCNTs are very sensitive to adsorbent and electron charge transfer. Changes in conductivity during charge transfer can be electrically evaluated to correspond to gas concentration for example. In this manner, sensing devices based on SWCNTs can be of interest for detecting toxic chemical vapors to bio-macromolecules. Compared with individual nanotubes, SWCNT thin films can improve the signal-to-noise ratio and thus the detection limit but they can also be used conveniently to build large numbers of identical devices.

Besides monitoring variations in the conductance of SWCNT thin films, sensing can be accomplished by measuring the changes in capacitance between the film and a planar electrode in a chem-capacitor structure. The capacitance response comes from changes in i) the quantum capacitance of SWCNTs, due to the shift of the Fermi level as a result of charge transfer doping associated with adsorbed molecules, and ii) geometrical capacitance, due to the change of dielectric environment of closely surrounding SWCNTs, as a result of both electric-field alignment of dipole moments and field-induced polarizations of adsorbed molecules [62]. Because an AC field is utilized in capacitance measurements, molecules are forced to undergo continuous adsorption–desorption processes. This feature leads to rapid and reversible behavior and is shown in Figure 2.16 [62].

Unlike conductance, the capacitance responses do not require strong in-

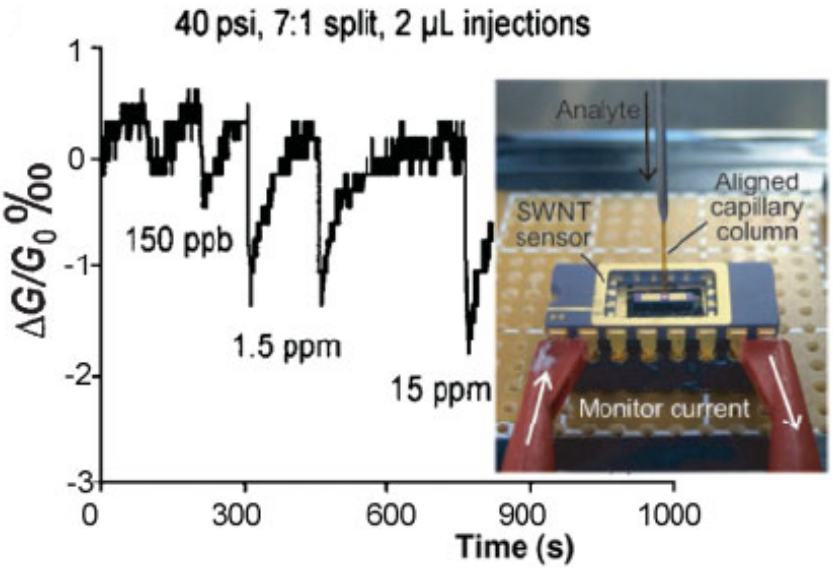


Figure 2.17: A SWCNT based sensor built to measure dimethyl methylphosphonate (DMMP) by monitoring relative changes in conductance. Taken from Ref. [26].

teractions with the absorbed molecules or direct charge transfer, the latter of which is likely to happen only at some finite "active" sites, for example, defect points. The result is an ability to detect over a large range of concentrations [63].

A major disadvantage of SWCNT gas sensors is their lack of specificity. One way to solve this problem is to functionalize SWCNTs with specific receptors for targeted analytes. For instance, decorating SWCNTs with either evaporated or electroplated palladium nanoparticles leads to the formation of a SWCNT chem-resistor specific to CH_4 detection [64]. When exposed to methane, the reversible formation of electron-rich palladium hydride hinders hole transport in p-doped s-SWCNTs, and thus leads to higher resistance. Due to the availability of abundant active sites in SWCNT thin films, these sensors can respond linearly over a wide concentration range, an obvious advantage over previous results from individual-tube devices shown in Figure 2.17 [65]. A major source of interference for this sensor is oxygen, which also reacts with Pd. Additional chemo-selective coatings may help to solve this problem [64].

2.8.5 Purification and processing of SWCNTs

In all advanced applications involving the use of SWCNTs, it is assumed that impurities such as metallic catalysts which are necessary in the synthesis process, are removed. The purification and processing of SWCNTs forms a large component in nanotube research. The core work presented in this disser-

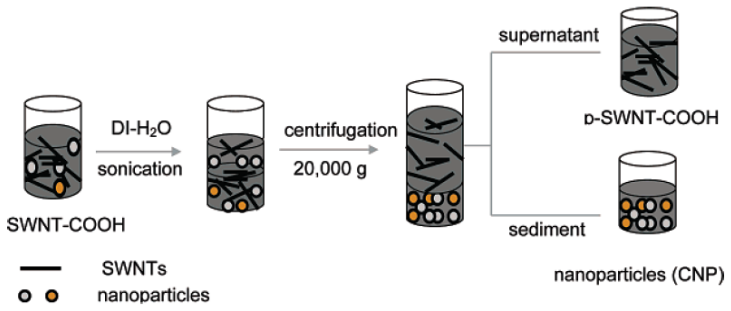


Figure 2.18: A Schematic of the resuspension-centrifugation-decantation cycle for removal of CNPs and purification of SWCNTs Taken from Haddon et al. [67].

tation does not involve any purification or processing. However, it is inevitable, at some stage, that some form of purification and processing would be needed to use the SWCNT in some application such as in a sensing device. In this regard, we present a short review of recent purification methods of sorting inhomogeneous samples containing SWCNTs.

2.8.6 Purification by centrifugation

There are many reports and reviews on the purification of carbon nanotubes. Many of them are complicated and messy. Therefore, methods that ease the purification process are favoured. The use of a centrifuge is one such method. Haddon et al. [66] showed that low-speed centrifugation was effective in removing amorphous carbon (AC). In these experiments, the AC content is preferentially suspended in aqueous dispersions during low-speed centrifugation (2000g), leaving the SWCNTs in the sediment. The effectiveness of this method is based on the $\zeta-$potential, which is an index of the magnitude of the electrostatic interaction between colloidal particles.

The $\zeta-$potential becomes effective after the as-prepared material is treated with acids to oxidize the metallic catalysts which leave a charge on the different components. The suspension in each of these components attain a different $\zeta-$potential and acquire different mobilities due to electrostatic forces. In this way, the use of the centrifuge discriminates between the different components in the suspension. With a high-speed centrifuge, it was found that the supernatant becomes enriched with SWCNT-COOH, while all the remaining impurities form the sediment. Efficiency of purification has been reported to be as high as 90% [67]. Figure 2.18 shows a schematic of the purification process using a centrifuge.

2.8.7 Sorting SWCNTs by density gradient ultracentrifugation

As-prepared SWCNTs vary in their diameter and chiral angle, and these physical variations result in striking changes in their electronic and optical behavior. This has prevented their widespread application in high-performance field-effect transistors, optoelectronic near-infrared emitters detectors, chemical sensors etc. [22]. Thus, efficient methods to sort SWCNT material according to electronic properties will be needed so that large quantities of these nanomaterials can be produced which are monodisperse in their structure and properties.

Hersam et al. [68] developed a general approach for sorting carbon nanotubes by diameter, bandgap. and electronic type (metallic versus semiconducting), using the technique of density-gradient ultracentrifugation (DGU). This method which is scalable, exploits the differences in the buoyant densities (mass per volume) between SWCNTs of different structures. In this technique, purification is induced by ultracentrifugation in a density gradient. In response to the resulting centripetal force, particles sediment towards their respective buoyant densities and spatially separate in the gradient. To do this, as-prepared material is dispersed by sonication in a solution of surfactant such as sodium cholate (SC). Thereafter, this solution is placed on top of an already prepared linear gradient such as OptiPrep® and ultracentrifuge at 250 000g for 12 hours. Figure 2.19 shows a solution of SWCNTs that was ultracentrifuged in a linear gradient. Visually, the separation is made evident by the formation of coloured bands of isolated SWCNTs sorted by diameter and bandgap. Bundles, aggregates and insoluble material sediment to lower positions in the gradient [68].

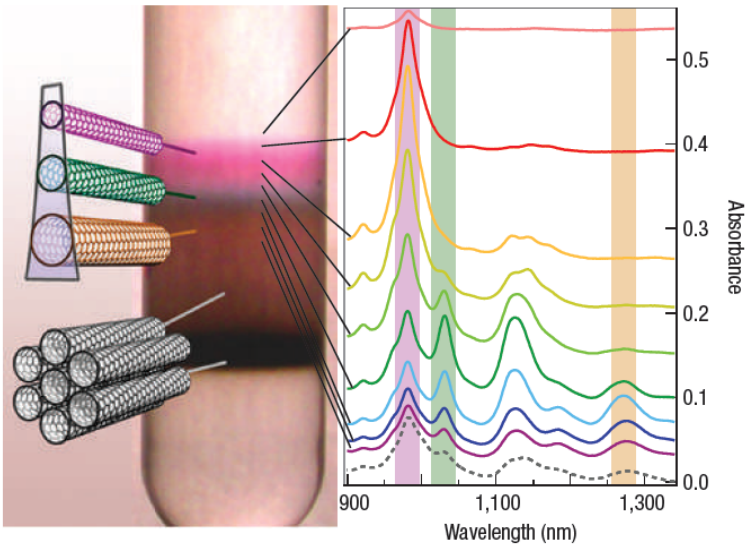


Figure 2.19: SC encapsulated, CoMoCAT-grown SWNTs the separation by DGU. On the left, the separation shows that the formation of coloured bands pointing monodisperse SWCNTs. Absorption spectra are shown on the right. Adapted from Hersam et al. [68]

Chapter 3

Characterization of Single-walled carbon nanotubes

3.1 Introduction

The extraordinary physical properties of single-walled carbon nanotube (SWCNTs) and the exploitation of this material for use in advanced technological devices means that this material has to be properly characterized and exhibit uniform physical characteristics so that it can be used in consumer products. The financial success that can be derived from the exploitation of such products will depend not only on their novelty but more importantly on consistency in performance and long-term reliability. Thus, a complete material characterization will be required before SWCNTs could be used in such products. No single experimental method has been developed to describe a SWCNT completely. Since the discovery of SWCNTs, techniques have been used to describe the properties of SWCNTs and carbon materials such as Raman spectroscopy, IR spectroscopy, UV-VIS absorption spectroscopy, electron microscopies, electron spin resonance, X-Ray diffraction, X-Ray photo-electron spectroscopy, nuclear magnetic resonance, thermal gravimetric methods etc [69, 70]. But, in reference to SWCNTs in particular, a class of characterization methods has been referred to as carbon nanotube metrology [71]. These methods have the ability to distinguish between individual SWCNTs and can be divided into three main groups:

- optical microscopies
- scanning probe microscopies
- electron microscopies

Each method provides a different set of information which contributes to the complete characterization of the material. Under optical we have Raman, photoluminescence and absorption spectroscopies. Under scanning probe microscopies we have atomic force microscopy (AFM) and scanning tunneling microscopy (STM) which are the most widely used methods. Electron microscopies, due to its nature of observing matter which are too small for the optical microscope were the first to observe SWCNTs.

The above techniques provide an array of measurements that allow for a comprehensive description of carbon nanotubes. The key parameters that need to be determined on carbon nanotubes for it to be used in advanced devices are:

- conducting type i.e. either semi or metallic
- the diameter and chirality distribution
- length
- alignment

Methods to remove impurities such as metallic catalyst's, which are remnants from the synthesis process, usually involve the use of acids to oxidize the metals. During the purification process, damage can occur to the nanotubes. Therefore, the nanotube material needs to be continuously monitored to prevent irreparable damage to the nanotubes. In these instances, optical spectroscopy methods are versatile and non-destructive which can be applied to detect the presence of carbon nanotubes, chemical modifications and to identifying the chiral index (n, m).

In this chapter, the optical methods of Raman and photoluminescence spectroscopy to characterize carbon nanotubes are described. These are the two most widely used optical methods currently in use to characterize carbon nanotubes. We also briefly discuss the use of electron microscopy. In this study, as-prepared laser synthesized material that contain SWCNTs was not purified after the synthesis.

3.2 Raman Spectroscopy

Raman spectroscopy is the measurement of the Raman "effect" and is named after Indian Physicist C.V. Raman (born 1888, died 1970) [72]. The "effect" which is the inelastic scattering of light by a molecule or system of molecules was predicted by Russian physicist Adolf Smekal in 1923. However, it was

only in 1928 that experiments performed by Raman and Krishnan, was this effect discovered [73]. In their simple experiment, sunlight was filtered using a coloured glass filter which limited the light to a narrow coloured band and was allowed to fall onto a vessel containing a pure liquid. This filtered light was transmitted through the liquid onto a photographic plate. It was found that in addition to the original transmitted light (Rayleigh scattering), a secondary component was recorded onto the plate which persisted even when another filter was used to cut off the original light. This secondary component had a different and longer wavelength compared to that of the primary filtered scattered light [73]. Raman was awarded the Nobel prize for this work in 1930.

The Raman effect occurs when light impinges upon a molecule and interacts with the electron cloud and the bonds of that molecule. For a spontaneous Raman effect, a photon excites the electron from the ground state to a virtual energy state. When the electron relaxes it emits a photon and it returns to a different rotational or vibrational state. The difference in energy between the original state and this new state leads to a shift in the emitted photon's frequency away from the excitation wavelength.

If the final vibrational state of the molecule is more energetic than the initial state, then the emitted photon will be shifted to a lower frequency in order for the total energy of the system to remain balanced. This shift in frequency is designated as a Stokes shift. If the final vibrational state is less energetic than the initial state, then the emitted photon will be shifted to a higher frequency, and this is designated as an Anti-Stokes shift. Raman scattering is an example of inelastic scattering because of the energy transfer between the photons and the molecules during their interaction. These transitions are depicted graphically in Jablonski energy diagram of Figure 3.1 [74].

A change in the molecular polarization potential — or amount of deformation of the electron cloud — with respect to the vibrational coordinate is required for a molecule to exhibit a Raman effect. The amount of the polarizability change will determine the Raman scattering intensity. The pattern of shifted frequencies is determined by the rotational and vibrational states of the sample. A detailed theoretical description of the Raman effect including the discussion of symmetry and selection rules was developed between 1930-34 by George Placzek and can be found in several reference texts on the subject [74, 75, 76]. Nowadays, lasers are the preferred excitation source and has made Raman spectroscopy very powerful.

Raman spectroscopy is one of the most widely used techniques to characterize carbon nanotubes. The ability of the Raman effect to probe and differ-

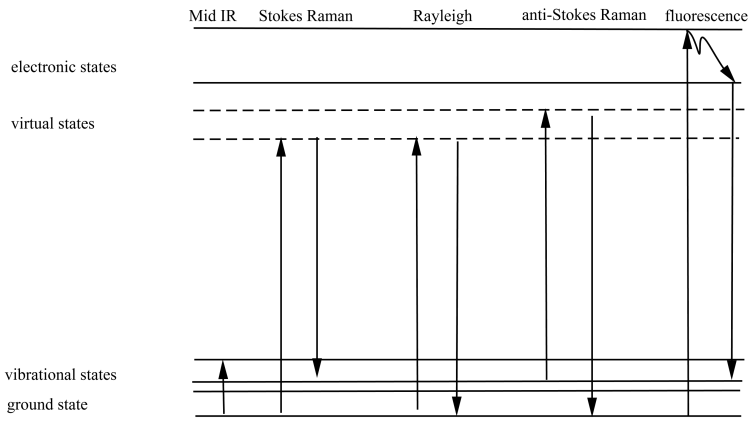


Figure 3.1: Jablonkski energy diagram depicting electronic transitions of several processes in an excited atom resulting in the emission of photons of different energies. Taken from Ref. [74].

entiate between semiconducting and metallic nanotubes is a great advantage of this technique. Sample preparation is not demanding and the method can be performed on individual single tubes and on samples consisting of bundles of nanotubes.

Since, sample preparation is not demanding, the Raman technique is frequently used to characterize nanotubes and to monitor growth conditions. In the subsections below, Raman scattering as applied to the study of carbon nanotubes is described. The background information needed for the characterization of SWCNTs synthesized by the laser-furnace method is also discussed.

3.2.1 Raman Scattering in SWCNTs

Figure 3.2 shows a schematic illustration of the Raman process. Laser produced photons incident on a material sample excites an electron–hole pair in a carbon atom. The electron (or hole) is scattered by emitting or absorbing a phonon, and the electron–hole pair recombines. The difference in energy between the incident and the scattered light corresponds to the energy of the phonon. The phonons that are allowed to participate in this process are selected by the requirements of energy and quasi-momentum conservation:

$$\hbar\varpi_i = \hbar\varpi_s \pm \hbar\varpi_{ph} \tag{3.1}$$

$$\hbar\vec{k}_i = \hbar\vec{k}_s \pm \hbar\vec{q} \tag{3.2}$$

where $\varpi_{i,s}$ are the angular frequencies of the incident and scattered light, respectively and ϖ_{ph} is the phonon frequency, $\hbar = h/2\pi$ where h is Planck's

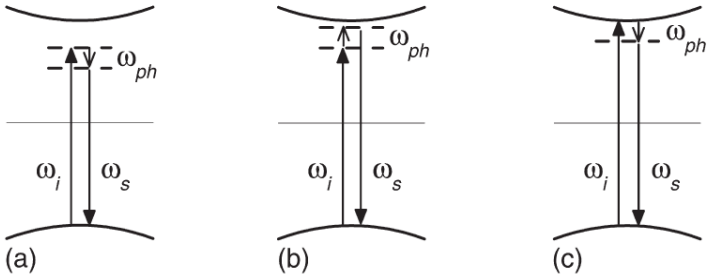


Figure 3.2: A schematic of the Raman scattering process. The dashed lines are virtual states while the solid lines represent real electronic transition levels (a) Stokes scattering where a phonon is emitted (b) Anti-stokes scattering where a phonon is absorbed (c) Resonant Raman scattering occurs when the incident or emitted photon matches a real electronic transition, and the Raman effect is enhanced by several orders of magnitude. From this, the optical transition energy could be determined. Adapted from Ref. Reich et al. [146].

constant, $\vec{k}$ are the photon momenta and q is the phonon quasi-momentum. The plus and minus signs correspond to Stokes (phonon emission, Figure 3.2 (a)) and anti-Stokes scattering (phonon absorption, Figure 3.2 (b)), respectively. The maximum momentum transferred from the incident photons to the phonon in the scattering process is $q \approx 2\vec{k}_i$(backscattering). If the incident light is in the visible range, the photon wave-vector is much smaller than the extension of the Brillouin zone in a crystal structure with a lattice constant of a few angstroms and only phonons close to the zone center, $q \approx 0$ can be probed in first-order Raman scattering.

Higher-order Raman scattering may be used to probe phonons in the entire Brillouin zone. Selection rules based on the symmetry of the system and the scattering geometry further restrict the phonon modes that can be observed in a Raman experiment [77]. Since in Raman scattering measurements, only the difference between the incoming and outgoing photon energies are measured, the choice of laser excitation wavelength is not critical and is relatively independent of the sample type. However, if the energy of the incoming or outgoing photons matches a real transition in the electronic structure of the material, the Raman signal is resonantly enhanced as shown in Figure 3.2 (c). By recording the Raman intensity as a function of excitation energy, a resonance profile could be obtained.

By applying a special fitting function to this profile, a parameter could be extracted which equals to the optical transition energies. From this, resonance effect, the chiral index (n,m) of carbon nanotubes could be assigned. Therefore in order to obtain a good resonance profile, the sample needs to be subjected to a tunable Raman excitation laser. Only in this way, will the chiral indices

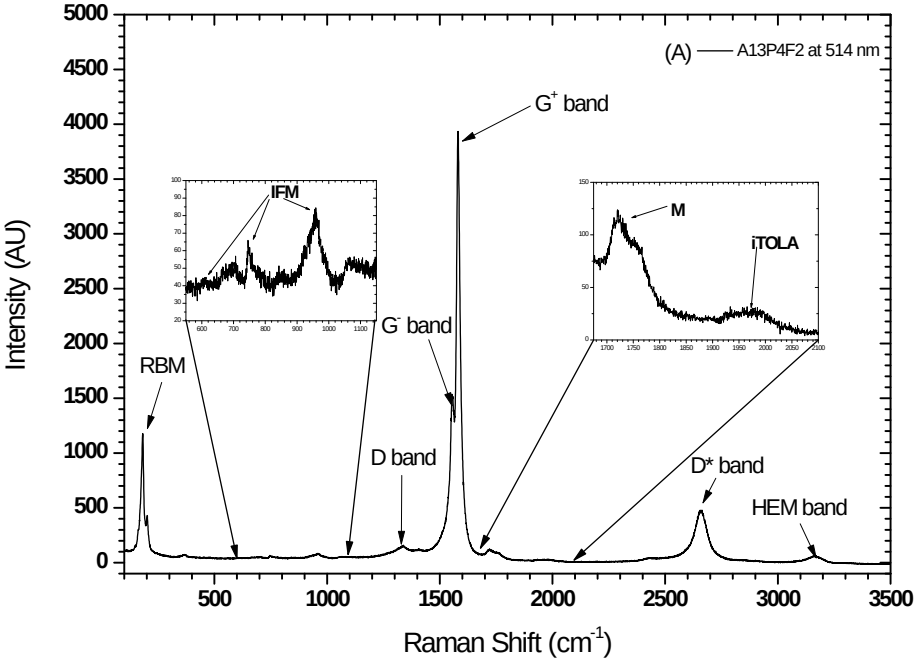


Figure 3.3: A typical Raman spectrum of as-prepared SWCNTs. The major Raman bands are depicted. Plotted data are from this study.

be determined with reasonable accuracy. This will be explained in more detail in later subsections.

Figure 3.3 shows a typical Raman spectrum measurement made on a film of as-prepared SWCNTs from this study. This sample consisted of individual and bundles of SWCNTs together with metal catalysts and amorphous carbon. The first-order and second-order features are visible in the spectrum. In a typical analysis, first order features usually suffice but for more detailed analysis, it is necessary to study all features of the spectrum which improves the physical description and understanding of phonon processes in SWCNTs. The following are significant features of the Raman spectrum of SWCNTs [37, 78]. The inserts in Figure 3.3 show more detailed features:

- radial breathing mode (RBM) , ∼100-400 cm^{-1}
- disorder or defect induced band (D), ∼1250-1400 cm^{-1}
- graphitic like band (G), ∼1550-1600 cm^{-1}
- D* band- over tone of D-band ∼2700 cm^{-1}
- Intermediate frequency modes (IFM) between 600-1100 cm^{-1}
- M and iTOLA bands between 1700-2000 cm^{-1}

The above feature are discussed in more detail.

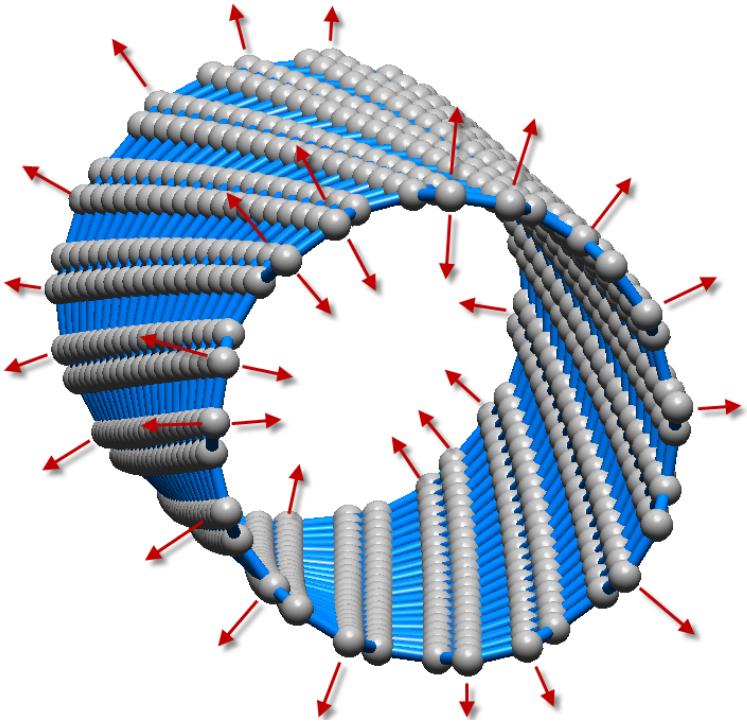


Figure 3.4: A schematic model of a (9,7) SWCNT showing the direction of symmteric vibrations resulting in what is known as the radial breathing mode. Analysis of which is correlated to the tubes diameter. MK Moodley 2010©

3.2.2 The radial breathing mode (RBM)

The radial breathing mode is a totally symmetric vibrational mode associated with the vibration of carbon atoms in a radial direction in relation to the nanotube axis [37]. Figure 3.4 shows a schematic model of a (9,7) SWCNT with red arrows pointing outward and inward depicting symmetric vibrations perpendicular to the nanotube axis. Theoretical and experimental results show that the RBM frequency, ϖ_{RBM} is inversely proportional to the nanotube diameter, following the equation, $\varpi_{RBM} = \mathrm{A/d}_t + \mathrm{B}$ [79]. The parameters A and B are determined experimentally and different values have been obtained for samples prepared by different synthesis methods.

This has posed problems in adopting a accepted standard set of parameters for device applications. However, the growth of individual SWCNTs by the "super growth method" [80], has allowed the research community to adopt parameters that can be used as a benchmark.

From the Raman analysis of these samples, a value of A= 227 and B= 0 was adopted [81], so that the relation of RBM frequency, ϖ_{RBM} is related to the diameter d_t of the nanotubes as:

$$\varpi_{RBM} = \frac{227}{d_t} \tag{3.3}$$

The authors concluded that all other nanotube samples obtained from various synthesis methods and measurement conditions were "up shifted" from this value. This relation, is in agreement with calculations using the velocity of sound in graphite and has $\varpi_{RBM} \rightarrow 0$ as $d_t \longrightarrow \infty$ i.e. an unwrapped graphene sheet. All the RBM results in the literature are upshifted from the pristine values due to van der Waals interaction with the environment, such as nanotube-nanotube interactions in bundles, nanotube-substrate, nanotube-surfactant etc. and can be generally described by:

$$\varpi_{RBM}^{Lit.} = \frac{227}{d_t}\sqrt{1 + C.d_t^2} \tag{3.4}$$

where $C = [6(1-\nu^2)/Eh][K/s_0^2] = 0.05786$ nm^{-2}, where K is the van der Waals interaction strength, s_o is the equilibrium separation between the SWCNT wall and the environment shell, v is the Poisson's ratio, E is Young's modulus and h is the thickness of the shell [81]. For $d_t < 1.2$ nm, where curvature effects become important, the environmental effect depends more critically on the specific sample with the observed environmental-induced upshifts ranging from 1 to 10 cm^{-1} [81].

The dependence on the nanotube diameter in eqn. 3.4 is clear. This explains why this region of a spectrum is commonly used in the characterization of the diameter distribution in SWCNTs. The Raman intensity for the RBM is strongly enhanced when the incident or scattered light is in resonance with an excitonic transition according to [82]:

$$I(E_L) = \left(\frac{Mc}{\hbar\varpi_{RBM}}\right)\left|\frac{1}{(E_l - E_{ii} - i\gamma/2)} - \frac{1}{(E_l - \hbar\varpi_{RBM} - E_{ii} - i\gamma/2)}\right|^2 \tag{3.5}$$

where $I(E_{l)}$ is the intensity of the Raman resonance profile, E_l is the laser energy, E_{ii} the energy of the allowed optical transition, and γ is the lifetime broadening of the intermediate electronic states. Mc contains all matrix elements and remaining factors. Thus, the Raman spectra of the RBMs for a sample composed of an ensemble of different nanotube chiralities is strongly dependent on E_l because for each value of E_l, the optical transition energies E_{ii} for different SWCNTs are in resonance i.e. when $E_l = E_{ii}$, the intensity of the RBM for these nanotubes is resonantly enhanced.

In Figures 3.5, RBM spectra of SWCNTs dispersed in sodium dodecyl sulphate (SDS) aqueous solution obtained by using different laser excitation energies E_l [83]. The sample consisted of dispersed individual SWCNTs produced by the high pressure dissociation of carbon monoxide (HiPco) process

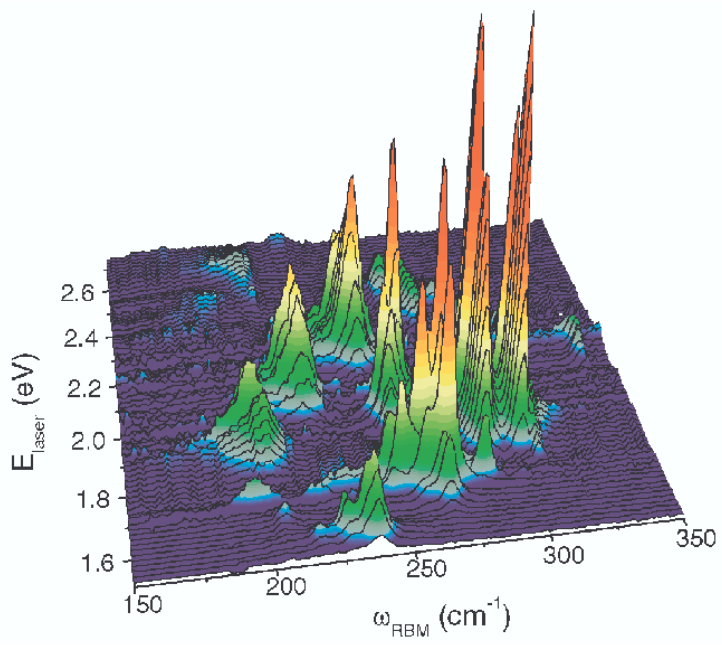


Figure 3.5: Resonant Raman spectra of HiPco SWCNT samples excited by a tuneable laser. Taken from Bronikowski et al. Ref. [83].

[84]. Such a plot is referred to as a Raman map. A map can only be achieved with a tunable laser system in which the laser excitation is changed by small increments, so that the sample is be "swept" over a large laser excitation range. In doing so, SWCNTs with different E_{ii} values are be brought into resonance. By using equations 3.3-3.5, the diameter distribution of individual wrapped tubes can be determined.

The strong resonance enhancement in the RBM Raman spectra makes it possible to observe the Raman spectrum of one single nanotube when the energy of the incident or the scattered light is in resonance with the energy of an optical transition in the nanotube. The observation of the RBMs for single nanotubes combined with a Kataura plot (see below) allows the (n, m) assignment for the nanotubes can be determined. Figure 3.6 shows resonant Raman imaging of isolated individual SWCNTs prepared by the HiPco method [85].

3.2.3 G-Band

The graphite-like band (G-band) in carbon nanotubes is directly related to the G-band in graphite that is identified with an in-plane tangential optical phonon involving the stretching of the bond between the two atoms in the graphene unit cell. While the G-band in graphite exhibits a single Lorentzian feature of E_{2g} symmetry at $\sim$1582 cm^{-1}, the G-band of carbon nanotubes

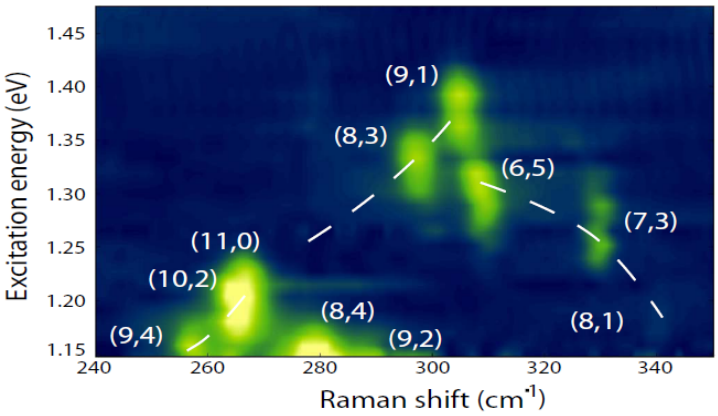


Figure 3.6: Resonant raman imaging of individual SWCNTs measured by Telg et al. [85].

is composed of several peaks originating from the quantum confinement of the wave-vector along the SWCNT circumferential direction, and the folding of the graphite Brillouin zone into the SWCNT Brillouin zone. The G-band of a chiral (a-chiral) SWCNT is composed of phonon modes of symmetries $A(A_{1g})$, $E_1(E_{1g})$ and $E_2(E_{2g})$ originating from a first-order Raman process. Two phonons of each symmetry are both predicted [86] and observed [87] meaning that the spectra around the G-band should be fitted by six Lorentzian lines corresponding to each phonon process. Figure3.7(a,b) shows the G-band Raman spectra of metallic and semiconducting SWCNTs. The G-band band is split into two main features, the so-called G^- and G^+ components, and are observed with frequencies at ∼1530 and ∼1580 cm^{-1} for metallic natured nanotubes and ∼1550 and ∼1580 cm^{-1} for semi-conducting type nanotubes.

These two features are associated, respectively, with vibrations of the carbon atoms along the circumferential direction, (transverse optical phonon (TO)) and along the nanotube axis (longitudinal optical phonon (LO)).

These are seen more clearly in Figures 3.8 and 3.9. While there are six vibrational modes, it is only the A_{1g} and E_{1g} modes which are most intense. The G^- feature is strongly sensitive to whether the nanotube is metallic or semiconducting, showing a Breit–Wigner–Fano (BWF) lineshape in the case of metallic nanotubes, as described in references [88, 89] and mathematically described by:

$$I(\varpi) = I_0 \frac{[1 + (\varpi - \varpi_{BWF})/q\Gamma]^2}{1 + [(\varpi - \varpi_{BWF})/]^2} \tag{3.6}$$

where q represents the asymmetry of the line shape of the G^-feature exhibited by metallic nanotubes while ϖ_{BWF}, I_0 and Γ are fitting parameters of

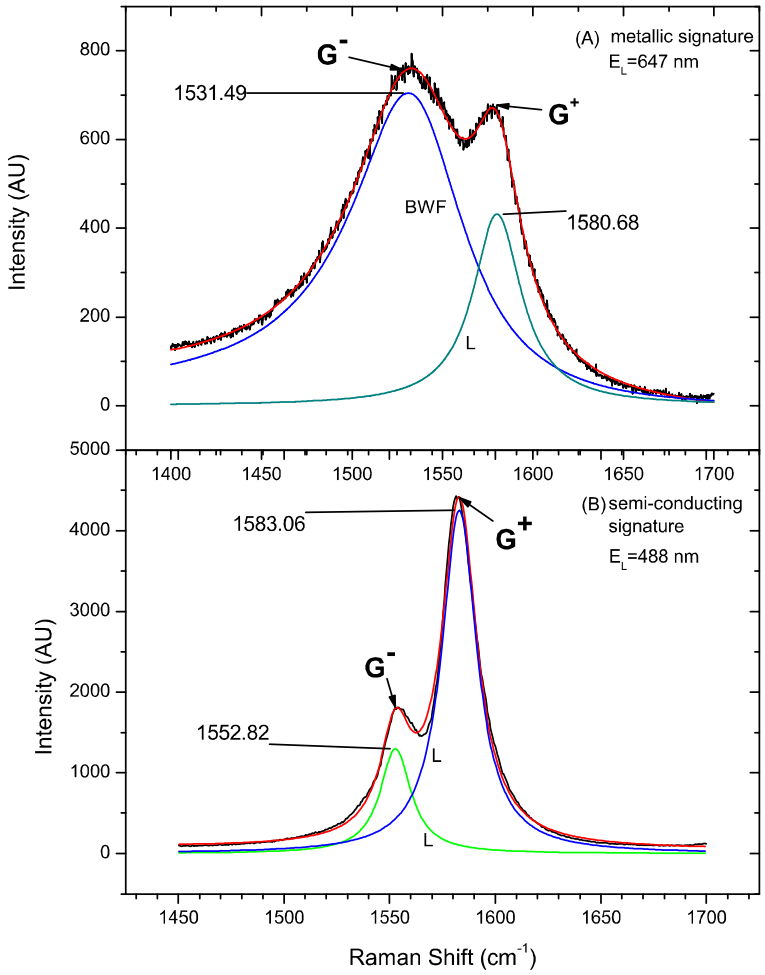


Figure 3.7: A laser prepared sample, from this study, excited by 647 nm and 488 nm lasers showing the Raman spectrum SWCNTs bundles and the spiltting of the G bands (a) metallic nanotubes (b) semi-conducting.

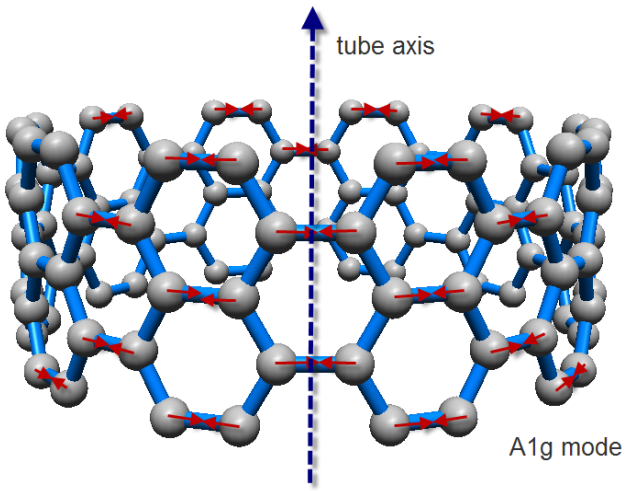


Figure 3.8: A schematic of a (10,10) armchair SWCNT showing vibrational A_{1g} mode. The vibrations are parallel to the C-C bond. MKMoodley 2010©

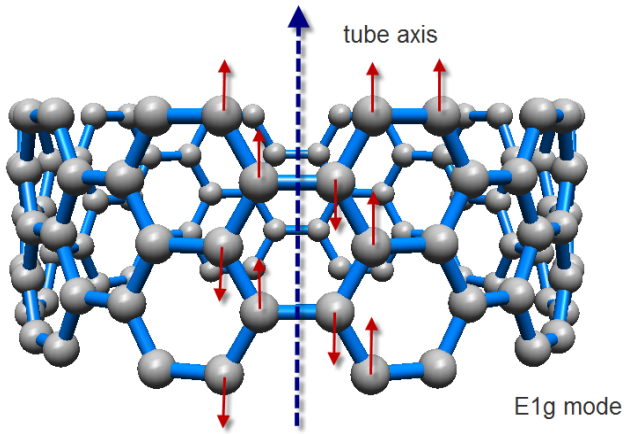


Figure 3.9: A schematic of a (10,10) armchair SWCNT showing vibrational E_{1g} mode. The vibrations are perpendicular to the C-C bond. MK Moodley 2010©

the central frequency, intensity and the broadening factor respectively. The BWF signal appears only when the electronic density of states at the Fermi energy, E_F has a finite value. Therefore, the BWF line-shape appears only in metallic SWCNTs and graphite intercalation compounds [37].

The diameter dependence of the frequencies of the G^+ and G^- features are obtained from measurements of the RBM and G-band spectra shown Figure 3.10 [90]. Such measurements reveal that the frequency of the G^+ feature is both diameter and chiral-angle independent, while the G^- feature shows a dependence on the nanotube diameter. The frequencies of the G^- and G^+ features are plotted in Figure 3.11 as a function of $1/d_t$ for 46 isolated semiconducting (solid circles) and 16 isolated metallic (open circles) SWCNTs. The frequency of the G^- feature can be well fitted with the equation:

$$\varpi_{G^-} = \varpi_{G^+} - C/d_t^2 \tag{3.7}$$

with the constants $\varpi_{G^+} = 1591$ cm^{-1} and C = 47.7 (79.5) cm^{-1}nm^2 for semiconducting (metallic) SWCNTs [90].

While, a single BWF line-shape was used to fit the spectra in Figure 3.7(a), this had been done to illustrate its application. Due to the diameter dependence of the G^-, the fitting of a single BWF can be only applied to individual and isolated SWCNTs. In this dissertation, we have analyzed bundles and not individual nanotubes. The fitting of multiple BWF lines is not practical since the sample is of mixed distribution of metallic and semi-conducting tubes.

For a-chiral (i.e. zigzag and armchair) SWCNTs, the atomic vibrating direction of the A_{1g} mode is parallel to the C-C bond, while the atomic vibrating direction of the E_{1g} mode is perpendicular to the C-C bond (see Figures 3.8

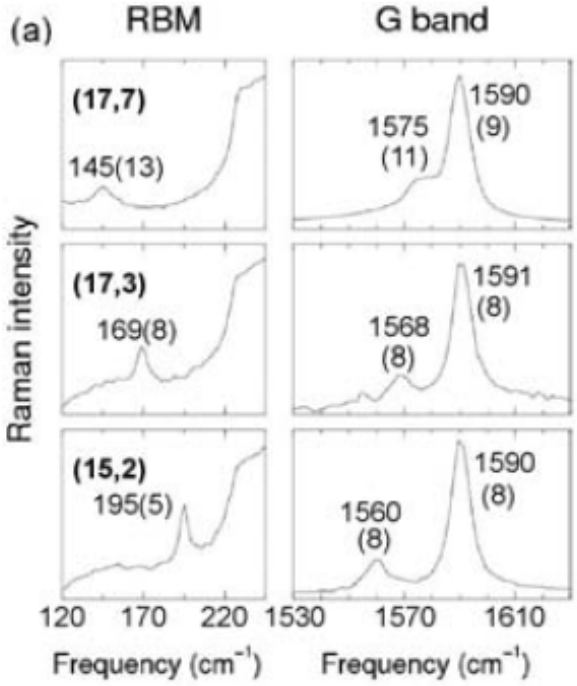


Figure 3.10: RBM band G nad spectra of individual isolated semi-conducting nanotubes. The diameter dependence of the G^- peak position is noticeable. The peak position of the G^+ show little or no depedence when comared ot the RBM features. From Jorio et al. [90].

and 3.9). According to the results obtained by Kahn and Lu [91], G^+ corresponds to the E1g mode for zigzag tubes but to the A1g mode for armchair tubes, while G^- corresponds to the A_{1g} mode for zigzag tubes but to the E_{1g} mode for armchair tubes.

However, Jorio et. al. [87] showed that G^+ corresponds to the A_{1g} mode for zigzag tubes and to the E_{1g} mode for armchair tubes, while G^- corresponds to the E_{1g} mode for zigzag tubes and to the A_{1g} mode for armchair tubes. These differences in the assignment of the phonon modes for metallic and semi-conducting nanotubes is still under debate and the reader is referred to references [92, 93, 94, 95] for more information.

3.2.4 D-Band

In the second-order Raman spectral features, it is possible to probe features identified with phonons associated with interior points in the Brillouin zone because the selection rules for the second-order features are relaxed with respect to the first-order features. The most common example of a second-order feature in the Raman spectra of carbon nanotubes, is the disorder-induced D-band, observed in the ∼1260–1400 cm^{-1} region (see Figure 3.3).

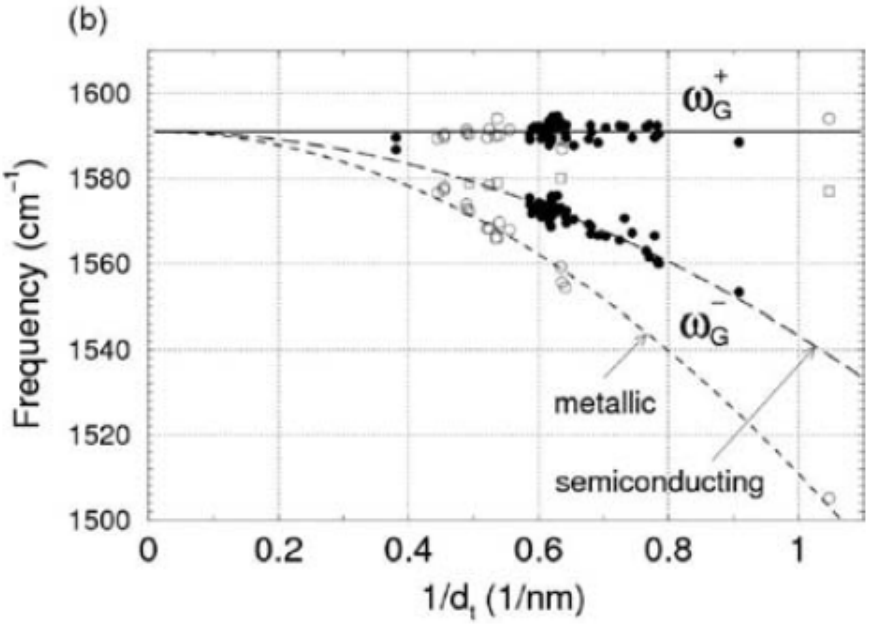


Figure 3.11: A plot of the frequency position of the G^- and G^+ bands of individual metallic and semiconducting SWCNTs vs $1/d_t$. The plot shows that there is a diameter dependence of the nanotube with the G^- band. Taken from Jorio et al. [90].

The D-band, common to all sp^2-hybridized disordered carbon materials, originates from phonons close to the K point of the graphite Brillouin zone, and becomes active in carbon nanotubes due to the presence of defects, such as impurities or missing atoms, finite-size effects and molecules linked to the nanotube sidewalls. In graphite, the frequency of this band shows a strong linear dependence on the excitation laser energy, presenting a dispersion $\Delta\varpi_D/\Delta E_L$ $\sim$53 cm^{-1}/eV. The strong E_L dependence is caused by a softening of the LO phonons near the K(K') point due to the electron–phonon coupling [37].

The dispersive behavior of this band has been explained by a double-resonance process involving a phonon and a defect [96]. In this process an electron–hole pair is created when the incident photon is absorbed. After that, the electron is scattered by a phonon (or a defect) with wave-vector q and scattered back by a defect (or phonon) with wave-vector $-q$, recombining with the hole and emitting a scattered photon. The E_L dependence of the D-band has been largely investigated for both bundled and isolated carbon nanotube samples. In both cases, a dispersion in ϖ_D as a function of E_L has been observed, but, with some marked differences.

In the case of bundled carbon nanotube samples, it has been observed for a given value of E_L that the D-band frequency is always smaller by about $\sim$20 cm^{-1}, as compared with other sp^2 carbon materials. The ϖ_D for SWCNT

bundles is observed to follow the relation $\varpi_D = 1210 + 53E_L$, with ϖ_D in cm^{-1} and E_L in eV [97]. For bundled nanotubes an oscillation is observed in the E_L dependence of ϖ_D. Such an oscillation is not observed for other sp^2 carbon materials. For a given E_L, the different isolated SWCNTs exhibit different ϖ_D values, because the double-resonance condition must be satisfied for each tube. It is also observed for isolated nanotubes that ϖ_D decreases with decreasing nanotube diameter [88].

Thus, the D-band spectra observed for a sample composed of an ensemble of nanotubes is a sum of different features originating from different (n,m) species of nanotubes and for resonances with different E_{ii}, which together give rise to the oscillatory behavior.

3.2.5 D*-Band

The D*-band at around 2700 cm^{-1}, seen in Figure 3.3, is the most intense feature in the second-order Raman spectra of SWCNTs. It is the overtone of the D band and its frequency is $2\varpi_D$. While the D-band originates from a double-resonance process involving a phonon and a defect, the D*peak is an interaction between two phonons and it is the second phonon which is responsible for the momentum conservation in the double-resonance process. In contrast to what happens in graphene, where the D* band is a single Lorentzian feature, in isolated SWCNTs, two features are sometimes observed in the D* band [98].

The presence of two peaks in the D* band of a single nanotube indicates a resonance with two different van Hove singularities, one in (space), resonant with the incident photon of energy E_L and another in resonance with the scattered photon $E_L \pm E'_G$. The signals + and − corresponds to the anti-Stokes and Stokes processes, respectively. The two peaks observed in the D* band are associated with phonons corresponding to the wave-vectors $q_i = 2k_i$ where i represents the i^{th} optical transition energy E_{ii}.

In the case of semiconducting nanotubes where the resonance occurs with the optical transition energies E^S_{33} and E^S_{44}, the difference in the phonon wave-vectors is $q_4 - q_3 \simeq 4d_t/3$. Thus, the two different features observed in the D* band are related to phonons with different wave-vectors in the phonon dispersion around the K point. In the case of metallic nanotubes, the two peaks observed in the D* band originate from the splitting in the van Hove singularities caused by the trigonal warping effect [99, 100].

The electron wave-vector, and consequently also the phonon wavevectors, for the two resonance states, in this case, show almost the same magnitude but

opposite signs in the wavevector relative to the K point. Thus, the two peaks observed in the D* band are caused by an anisotropy of the phonon dispersion around the K point, known as the phonon trigonal warping effect [101].

3.2.6 Intermediate Frequency Modes

In the spectral range between the RBM and the D-band, some low-intensity spectral features called the intermediate-frequency modes (IFMs) can be seen in the insert of Figure 3.3. It was observed that these modes exhibit a strong dependence on the laser excitation energy, and a dispersion of their frequency with E_L [37]. However, the dispersive behavior is not monotonic, as observed for many features in graphite-like materials due to energy-selective double-resonance Raman-scattering processes, but occurs in "steps". This effect is referred to as a "step-like dispersive behavior" [102]. Due to limitation on the number of laser excitations, this "step-like" features was not observed. Many features of the IFM and its response to laser excitation remain unexplained. In this dissertation, the investigation of IFMs were not made.

3.2.7 Two-phonon modes

Two-phonon modes present in the Raman spectra of carbon nanotubes show very low intensity response but nevertheless shed light on the vibrational properties. One such mode is the M-band observed at $\sim$1750 cm^{-1}, and is assigned as an overtone of the out-of-plane (oTO) phonon in graphite. The M-band is composed of a non-dispersive M^+ feature associated with an intravalley q = 0 scattering process, and an M^- feature associated with an intervalley q = 2k process, that exhibits a small negative dispersion of -23 cm^{-1}/eV. Another low-intensity second-order feature is observed at $\sim$1900 cm-1. This band, shows a very large dispersion ($\sim$200 cm^{-1}/eV) in its frequency as E_L is changed and has been assigned as a combination of the iTO + LA phonons in graphite [103]. These modes are usually strong when using FT-Raman at E_L = 1.16 eV. The study and understanding of these intensity of these and other double-resonance features is ongoing.

3.2.8 The assignment of chiral indices (n,m) to SWCNTs

The ultimate in the characterization of SWCNTs is to assign the chirality index to individual nanotubes. This is important since it physically describes

the nanotube completely. It is from this assignment that one would be able to distinguish between:

- a semi-conducting or metallic nanotube
- truly metallic armchair nanotubes (n,n) and quasi-metallic tubes that exhibit a small gap in the electronic band structure
- chiral and a-chiral nanotubes
- the optical band gap of semi-conducting nanotubes

3.2.8.1 RBM and the diameter of SWCNTs

The origin and meaning of the RBM bands was discussed in Section 3.2.2. In Chapter 2 we showed that the diameter d_t of a nanotube with chiral index (n,m) is given as:

$$d_t = \frac{a_0}{\pi}\sqrt{n^2 + nm + m^2} \tag{3.8}$$

where $a_0 = 2.461$ Å is the in-plane lattice constant of graphite. From eqn. 3.4 it was that ϖ_{RBM} is given by:

$$\varpi_{RBM} = \frac{227}{d_t} \text{ and } \varpi^{Lit.}_{RBM} = \frac{227}{d_t}\sqrt{1 + C.d_t^2} \tag{3.9}$$

While the above equation enables us to determine estimates of the nanotube diameters, knowledge of the ϖ_{RBM} is not by itself sufficient to determine the chiral index (n,m). This is because in a wide ensemble of nanotubes, the difference ϖ_{RBM} frequencies of tubes can be low as 2 cm^{-1}. This means that the Raman spectra must be of high resolution to resolve the difference between nanotubes of diameters which are very close to each other, yet may have different chiralities. Figure 3.12 shows a "Kataura Plot" which is a plot of the nanotube optical transition energies vs the nanotube diameter. By drawing a vertical line, one can deduce that there are many nanotubes of different chiralities which intersect this line. By zooming in (Figure 3.13), this is shown more clearly. This reinforces the point, that the ϖ_{RBM} value is not sufficient to determine a nanotubes chirality.

3.2.8.2 Optical transition energies: Kataura Plot

In addition to the ϖ_{RBM} we need to determine the optical transition energies of each nanotube that is contained in the sample. The optical transition energies can be determined by resonant Raman spectroscopy. The SWCNT electronic

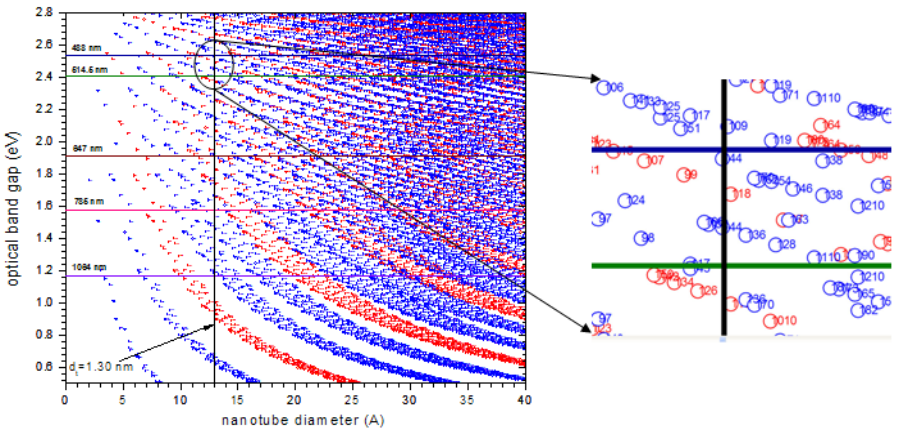


Figure 3.12: The Kataura plot illustrating that the diameter or the ϖ_{RBM} of the nanotube is not sufficient to determine the chiral index (n,m) with certainty.

bandgap. can be classified into three families defined in terms of the indices so that:

$$\nu = (n-m) \bmod 3 \rightarrow \nu = +1 \text{ and } v = -1 \quad (3.10)$$

$$\text{(are semiconducting nanotubes)} \quad (3.11)$$

$$v = 0 \text{ (nanotubes are metallic nanotubes)}$$

By plotting the transition energies E_{ii} for all nanotubes as a function of their diameter, a Kataura plot is obtained [104]. Figure 3.12 shows a theoretical Kataura plot for all possible tubes in the diameter range from d = 0 to 40 Å. A Kataura plot with a shorter diameter range is shown in Figures 3.13(a,b). The energy range covers the first and second transitions of semiconducting tubes (gray symbols, E_{11}^S and E_{22}^S), and the first transition of metallic nanotubes (black symbols, E_{11}^M). Except for armchair tubes, the metallic E_{11}^M is split into a lower-energy and a higher-energy transition.

Although there is an overall 1/d dependence, the transition energies show systematic deviations, forming V-shaped branching. Each of these branches is defined by a constant value $2n + m$ of its constituent nanotubes. For E_{11}^M, the upper and lower "V" branches are the split transitions and belong to the same (n, m) tubes. The innermost tube is always an armchair nanotube (no splitting).

The outermost tube is a zigzag (n ,0) or an (n,1) tube. The V-shaped patterns in the semiconducting transitions are formed each by a $v = +1$ and a $v = -1$ branch, where in the first transitions E_{11}^S the $v = -1$ branch is higher

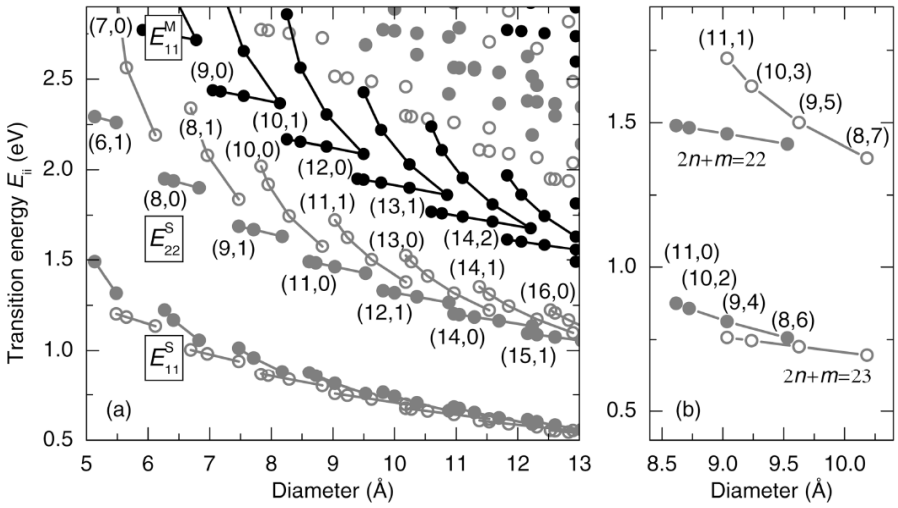


Figure 3.13: Calculated theortical Kataura plot of nanotube transitions energies E_{ii} vs diameter in Å. The grey symbols respresent semiconducting tubes, closed circles ($v = -1$), open circles ($v = +1$). Balck filled circles represent metallic tubes ($v = 0$). Lines connecting the circles represent a branch with $2n + m =$ constant. Taken from Ref. [78].

in energy than the $v = +1$ branch, and vice versa in E^S_{22}. The outermost positions are zigzag or close - to - zigzag tubes, and at the inner positions are close - to armchair tubes. The chiral indices of neighboring tubes in a branch are given by:

$$(n', m') = (n - 1, m + 2) \tag{3.12}$$

The (n,m) assignment obtained by any optical method involves a comparison between experimentally obtained E_{ii} values and a calculated Kataura plot. There are many different methods to calculate a Kataura plot. . The methods of obtaining a Kataura plot are:

- Zone folding from tight-binding models [105, 106, 107, 108].
- Non-orthogonal tight-binding mode [109].
- First-principles calculations [110, 111, 112].
- Empirical relations [113, 114].

For more information the reader is requested to refer to the references provided above.

3.2.8.3 (n,m) Assignment from the experimental Kataura Plot

Assuming that the transition energy E_{ii} of the ensemble's of nanotubes in the sample, has been obtained by a full resonance profile from fitting eqn. 3.5, the approximate nanotube diameter from the RBM frequency ϖ_{RBM} can be obtained from Equation 3.3 or 3.4. We can convert the RBM frequencies, ϖ_{RBM}, into $1/\varpi_{RBM}$, to sidestep the need to know the constants in eqn. 3.4. By doing this we an experimental Kataura plot of E_{ii} vs $1/\varpi_{RBM}$ such as that by reference [115] was obtained.

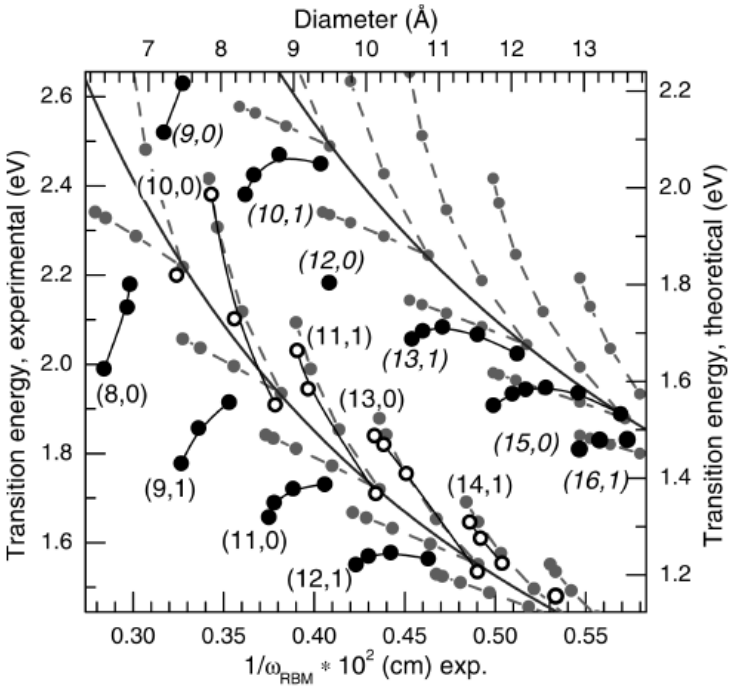


Figure 3.14: A super-imposed plot of experimental E_{ii} values and theoretical values vs nanotube diameter, $1/\varpi_{RBM}$. This is the manner in which the assignement of (n,m) chiral indices are made. For semiconducting tubes, open and closed symbols indicate tubes with $v = +1$ and $v = -1$, respectively. Gray symbols (right and top axes) are theoretical values from Figure 3.13 from Telg et al. [115].

To assign the chiral index (n, m) to each data point in the experimental plot, it must be matched to a point in the theoretical plot. To match the experimental and theoretical plots for a definitive assignment, it is necessary shift both axes of the theoretical plot to match the experimental plot. These shifts account for differences in the real nanotubes and theoretical estimation obtained from the model. On the energy axis, the shifts account for the shortcomings of the theoretical model due to the many-body effects and the curvature of the nanotube while the stretching on the diameter axis corresponds to the differences in the constants used to estimate the nanotubes

diameter.

Finally, to determine and assign chirality indices (n, m) from resonant Raman spectroscopy it is necessary to have:

- a theoretical Kataura plot. This is available from various sources.
- an experimental Kataura plot. For this, the sample needs to be completely characterized by extracting full resonant Raman profiles of the unknown sample either in bundles or surfactant wrapped individually dispersed nanotubes using a tunable Raman laser. Typically between 10-15 laser excitations would be needed.
- Both theoretical and experimental plots are matched from which assignments could be made.

In the research presented in this dissertation, it was not possible to obtain an experimental Kataura plot due to the non-availability of a tunable Raman laser and therefore the nanotubes contained in the laser prepared samples could not be assigned chiral indices purely from Raman spectroscopy alone.

3.3 Photoluminescence of SWCNTs

The first report of the application of the photoluminescence (PL) technique to the study of SWCNTs dates back to 2002 [52]. In the intervening half-decade there has been tremendous progress in this area. This has included many fundamental studies of SWCNT PL as a basic characterization tool. The term "photoluminescence" describes any process in which light is absorbed by a medium to generate an excited state, and then re-emission of light of lower frequency upon recombination to a ground state.

In the current accepted picture of PL in SWCNT, electron-hole pairs are created in the form of excitons, which are subsequently annihilated with the emission of photons. As previously mentioned in earlier sections and chapters, SWCNTs have a huge potential of being applied in technological advanced applications. A major obstacle to such efforts has been the diversity of tube diameters, chiral angles, lengths and aggregation in nanotube samples obtained from current synthesis techniques. PL has become an important tool in measuring a fraction of the total population where this fraction represent all semi-conducting tubes. The seminal paper by Bachilo et al. [116], laid the ground work for use of PL to determine chiral indices (n, m) of semiconducting nanotubes and became the basis on which the software program called Nanosizser® [117]. The discussion below is a synopsis of that paper.

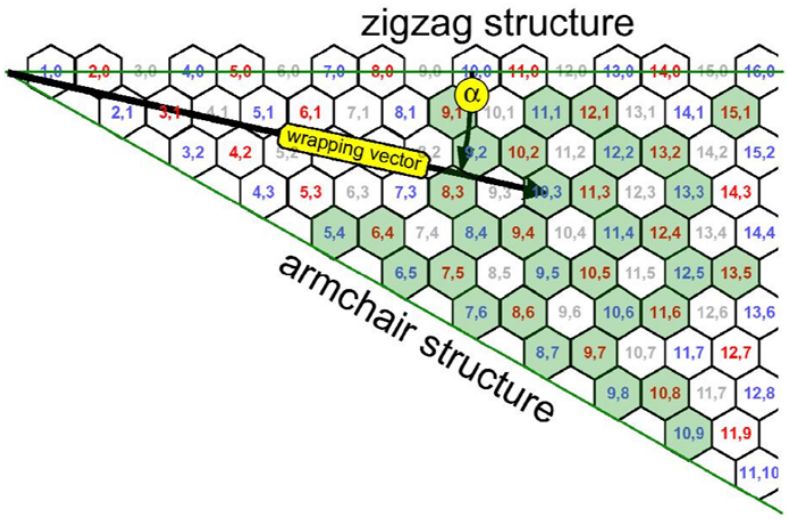


Figure 3.15: A graphene sheet labelled with chiral indices (n,m). By rolling the sheet in the direction of the wrapping vector or chiral vector will determine the chirality type of the nanotube formed. The chiral angle,a (from 0^0 to 30^0) is measured between the vector and the zig-zag plane from Bachilo et al. [116].

Figure 3.15 illustrates how each SWCNT structure is indexed by two integers (n,m), with the length, L, defined as, $L = \pi d_t$ and d_t is the nanotube diameter. The chiral angle is α of that tube's roll-up vector on a graphene sheet. Structures having $|n - m| \mod 3 = 0$ are metals or semimetals and will not fluoresce and will therefore not appear in PL spectrum. Figure 3.16 shows the qualitative pattern of sharp van Hove peaks, which arise from quasi–one dimensionality, predicted for electronic state densities of semiconducting SWCNTs. As shown in the figure, light absorption at photon energy E_{22} is followed by fluorescence emission near E_{11}. The values of E_{11} and E_{22} will vary with the nanotube structure [118].

Sample preparation for photoluminescence measurements is not straight forward (see experimental section). Individually suspended nanotubes wrapped by surfactant are excited selectively by a double excitation monochromator incremented in steps from 300 to 900 nm. Prior to each increment, an emission spectrum emanating from the sample is collected and spatially resolved by a spectrograph. This spatially resolved spectrum is detected by a liquid nitrogen detector from which a 3-D spectrum called a contour plot is extracted (Figure 3.17(a-d).

The area enclosed by the white oval drawn in Fig. 3.17a highlights a region showing peaks, arising from the transitions shown in Figure 3.17b emanating from various semiconducting nanotubes of different chiralities of which there are many. Additional peaks at shorter excitation wavelengths are attributed

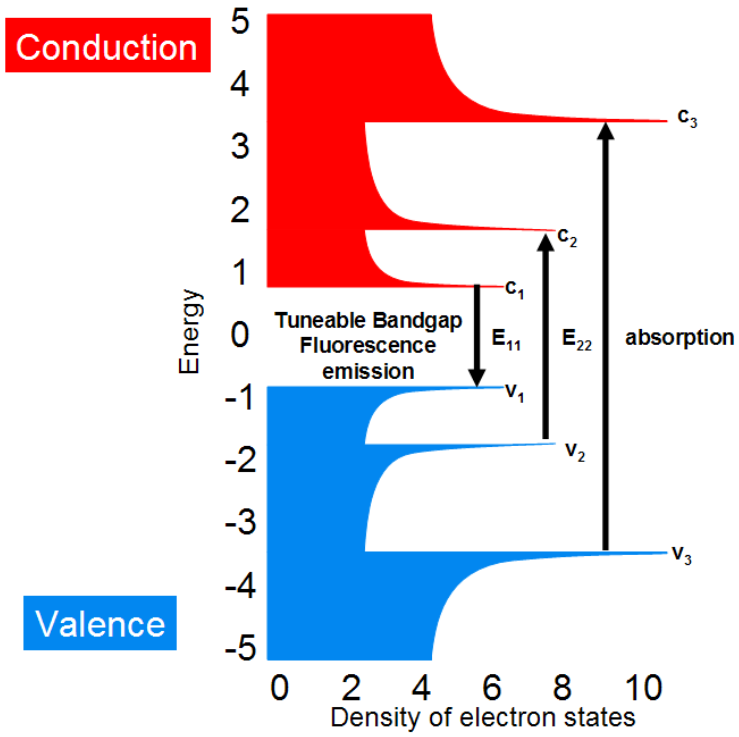


Figure 3.16: A Schematic illustrating the density of states (DOS) for SWCNT. Solid arrows depict the optical excitation and emission transitions while dashed arrows denote nonradiative relaxation of the electron, in the conduction band, and a hole, in the valence band before emission. From Ref Bachilo et al. [116].

to a $v_{33} \rightarrow c_{33}$ excitation followed by a $v_1 \rightarrow c_1$ emission in the same set of nanotubes (Figure 3.17). Between these two branches of peaks lies a region that shows very low emission intensity but with strong absorption.

This region can attributed to the presence of metallic and semimetallic nanotubes in the sample, which are expected to absorb between the semiconductors' $v_2 \rightarrow c_2$ and $v_3 \rightarrow c_3$ branches and not to emit measurable luminescence. Several of the features outside the circled region at longer excitation wavelengths are due to $v_1 \rightarrow c_1$ vibrionic bands (electronic transitions with vibrational excitation). The coordinates of each peak in the region of interest give the $v_2 \rightarrow c_2$ optical excitation energy equal to $E_{22} = hc/\lambda_{22} = hc\bar{v}_{22}$ and the corresponding a $c_1 \rightarrow v_1$ emission energy is $E_{11} = hc\bar{v}_{11}$for a single semiconducting nanotube species where h is the Planck's constant, c is the speed of light, λ is photon wavelength, and $\bar{v}$ is the photon frequency in wave numbers, cm^{-1}.

The main objective is to identify the specific (n,m) nanotube structure that corresponds to each observed spectral peak. To do this, the 3D excitation-emission-intensity map is combined with resonant Raman spectroscopy as discussed in some detail in the previous section. The wave number position for

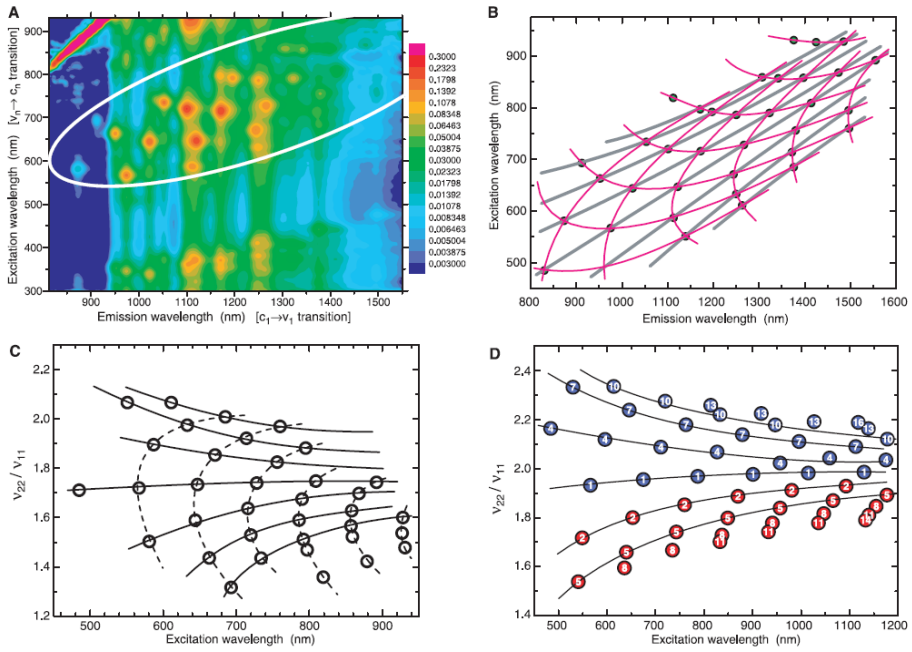


Figure 3.17: (A) A photoluminescence spectrum of suspended SWCNTs in a solution of SDS in D_2O. The peaks corresponds to unique chiral SWCNTs (B) A plot of spectral peak positions taken from (A) revealing a particular pattern (C) A plot of the measured ratio's of excitation to emission frequencies (D) A plot of computed E_{22}/E_{11} energy ratios versus excitation wavelengths. Blue symbols are $|n-m| \bmod 3 = 1$; red symbols are for $|n-m| \bmod 3 = 2$.

each peak gives the transition energy and this is correlated with the diameter relationship of eq. 3.3 to obtain (n,m) values using curve fitting procedures.

However, the variation of transition energies with diameter and chirality are also of substantial interest for understanding nanotube electronic states and excitations. The simplest theoretical treatments predict that the optical transition wavelengths of semiconducting nanotubes depends linearly on diameter according to the relations:

$$\lambda_{11} = \frac{hcd_t}{2a_{cc}\gamma_0} \text{ and } \lambda_{22} = \frac{hcd_t}{4a_{cc}\gamma_0} \tag{3.13}$$

where d_t is the tube diameter, a_{cc} is the C-C bond distance and γ_0 is the interaction energy between neighbouring C atoms [119]. By combining empirical expressions for the linear undeviated wavelengths i.e., when there are no differences between model and observation, and with that when there are deviations, we obtain the following equations for first and second van Hove optical transition frequencies of SWCNTs as a function of their diameter (in nm) and chiral angle:

$$\bar{v}_{11} = \frac{1 \times 10^7 cm^{-1}}{157.5 + 1066.9 d_t} + \frac{A_1 \cos(3\alpha)}{d_t^2} \text{ and } \bar{v}_{22} = \frac{1 \times 10^7 cm^{-1}}{145.6 + 575.7 d_t} + \frac{A_1 \cos(3\alpha)}{d_t^2} \tag{3.14}$$

with $A_1 = -710$ cm^{-1} for $|n-m| \bmod 3 = 1$ or $A_1 = 369$ cm^{-1} for $|n-m| \bmod 3 = 2$; $A_2 = 1375$ cm^{-1} for $|n-m| \bmod 3 = 1$ or $A_2 = -1475$ cm^{-1} for$|n-m| \bmod 3 = 2$. Application of the above equations in combination with an excitation-emission spectrum such as that of Figure 3.17a, are used to determine the chiral indices of semiconducting nanotube species. These formulae and constants are incorporated into the Fluorescence Nanosizer [117] software which is used determine by fitting the experimentally obtained excitation-emission spectrum the chiral index of each peak in the spectrum. Further to this, the chiral angle α, population intensity of each chiral family is also calculated. Figure 3.18a show a sample spectrum that is fitted using the above equations and shows the chiral labelling of the peaks. Figure 3.18b shows a plot of chiral angle vs nanotube diameter vs population intensity of the sample sample. The larger the closed circles implies higher population of that nanotube. The peak positions and (n, m) values are assigned with the aid of a library of (n, m) values. In some instances, fitted peaks have no assigned values since they do not appear in the library. These libraries are at present, still under development.

3.4 Electron microscopy

3.4.1 Scanning electron microscopy (SEM)

SEM is the most widely used electron microscopic technique because of versatility and ease of use. Samples can be quickly analyzed since sample preparation need not be elaborate. Accelerating voltages up to 30 kV are available which means a very wide range of magnification is possible, enabling very good resolution. SEMs analysis can yield image resolutions in the range of 0.6 nm but these resolutions are only possible for metallic samples.

Sample size is not a limitation in a SEM and samples as large 6" silicon wafers can be put directly in a modern machine. Modern advanced SEMs utilize field emission gun sources, called FE SEM. These sources provide a high density of electrons and result in images with excellent resolution. There have been numerous advances in various aspects of SEM hardware such as lenses, detectors and digital image acquisition. These advances in hardware, coupled with advances in other areas of instrumentation such as power supplies

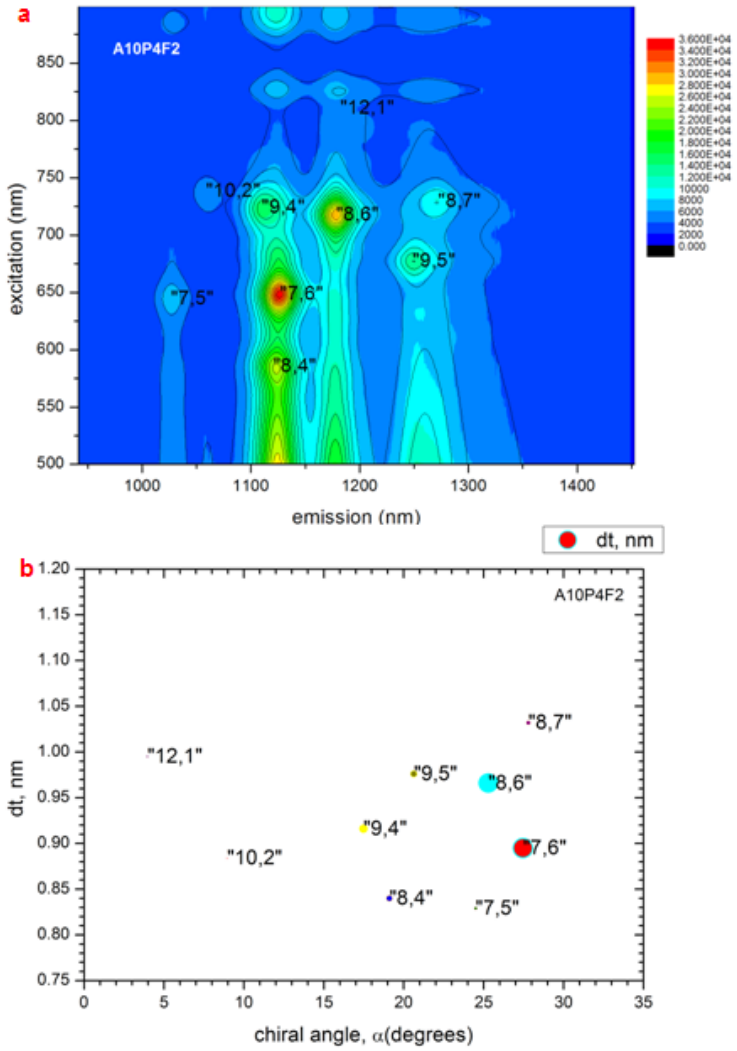


Figure 3.18: (a) A photoluminescence spectrum of a laser synthesized sample dispersed and suspended in D_2O containing 2% by weight of sodium cholate and (b) a plot of the diameter vs chiral angle. Data in both of these plots (a) and (b) are from this study.

and high vacuum instrumentation have now made it possible to acquire SEM images from almost any object, including wet biological samples. Low voltage SEM is another new development.

The extreme surface sensitivity of this technique is a result of the reduced interaction volume. This allows the measurement of images with nanometer scale resolution with less than 1 kV accelerating voltage. At these low energies, charging is not an issue and it is possible to measure images without conductive coatings. The electron energy can be reduced further by applying a negative potential on the sample and in this way, the beam energy can be reduced to below 100 eV [120]. This also makes ultra low voltage SEM (ULV-SEM) possible. This is an extremely surface-sensitive and avoids beam-

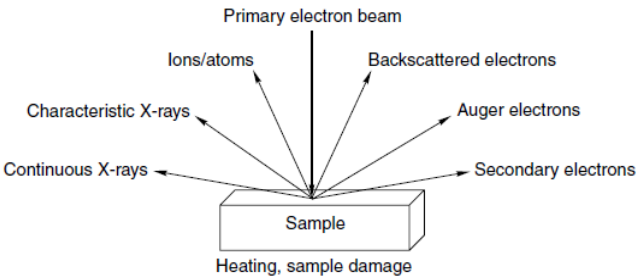


Figure 3.19: Schematic showing the interaction of an electron beam with a sample in the SEM configuration. Taken from Ref. [120].

induced damage at surfaces. In the case of carbon nanotubes, no conductive coating on a sample is required.

When an electron beam interacts with matter, several processes occur. These result in particle or photon emission processes which are summarized in Figure 3.19. The electron emission processes include elastic and inelastic scattering, and the emission of secondary electrons and Aüger electrons. Inelastic scattering occurs as the beam interacts with the sample and electronic excitations of the constituent atoms can occur. These excitations can lead to valence and core electron excitations and emissions. The core hole that is created, may get filled by de-exciting electrons resulting in the emission of X-rays. The de-excitation can also result in electron ejection, called Aüger emission. In addition, collision of the primary beam can also lead to excitations of lattice vibrations. All these electrons can be used to gather microscopic information on the sample. In addition, the data can also be used to obtain chemical or compositional information as in the case of Aüger electrons or structural information as in the case of backscattered electrons. In a normal SEM image, only secondary electrons are detected.

In this dissertation only images due to secondary electrons were captured. Figure 3.20 shows a sample SEM image of an as-prepared SWCNT material. Only bundles are visible. Generally with current SEMs, it is not possible to resolve individual SWCNTs. Since, the amount of secondary electrons produced from a low atomic number element such as carbon is not sufficient to resolve the nanotubes with diameter of less than ± 1 nm.

However, high resolution SEM is now a routine analytical tool. This technique provides an important high throughput characterization tool since "seeing is believing". It is important to know the dimensions of the structures fabricated and the materials prepared when characterizing device structures. Thus a SEM has become an indispensable tool in nanometrology [120].

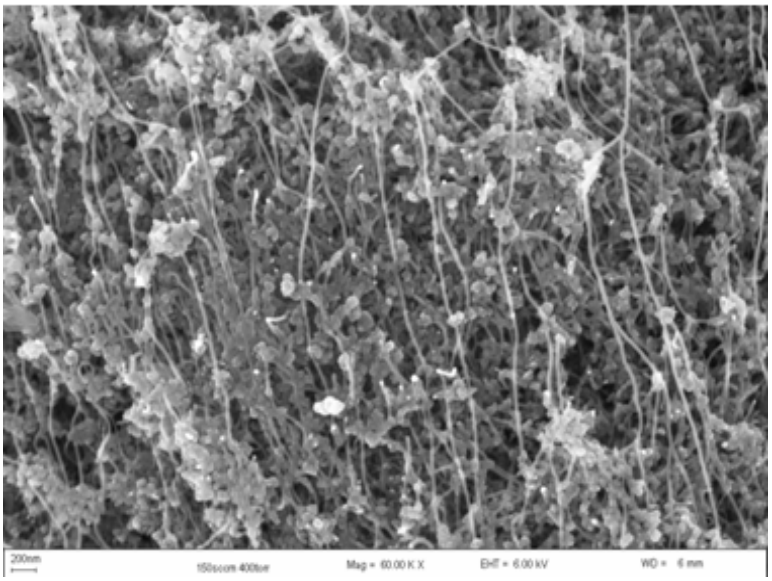


Figure 3.20: A sample, from this study shows a FE SEM image of as-prepared material containg SWCNT taken at 6 kV accelerationg voltage. The white spots are either Ni or Y metal catalyst particles.

3.4.2 Transmission electron microscopy (TEM)

Among the various analytical techniques that have been used to study carbon nanotubes, it was in a transmission electron microscopy (TEM) were carbon nanotubes were discovered by Iijima [4] in 1991. Compared to SEM, a TEM principal of operation is different. TEM requires a dedicated and expertly trained materials scientist to operate the TEM to its full potential. In TEM, the transmitted electrons are used to create an image of the sample. Scattering occurs when the electron beam interacts with matter. Scattering can be elastic (no energy change) or inelastic (energy change). Elastic scattering can be both coherent and incoherent (with and without phase relationship). Elastic scattering occurring from well-ordered arrangements of atoms as in a crystal, results in coherent scattering, giving spot patterns. This can be in the form of rings in the case of a polycrystalline material. However, inelastic scattering also occurs, which also gives regular patterns as in the case of Kikuchi patterns [121]. Inelastic processes give characteristic absorption or emission, specific to the compound or element or chemical structure. Because of all these diverse processes, a transmission electron microscope is akin to a complete laboratory.

There are two main mechanisms of determining contrast in an image. In the first, the transmitted and scattered beams can be recombined at the image plane, thus preserving their amplitudes and phases. This results in the phase contrast image of the object. An amplitude contrast image can be obtained by eliminating the diffracted beams. This is achieved by placing suitable aper-

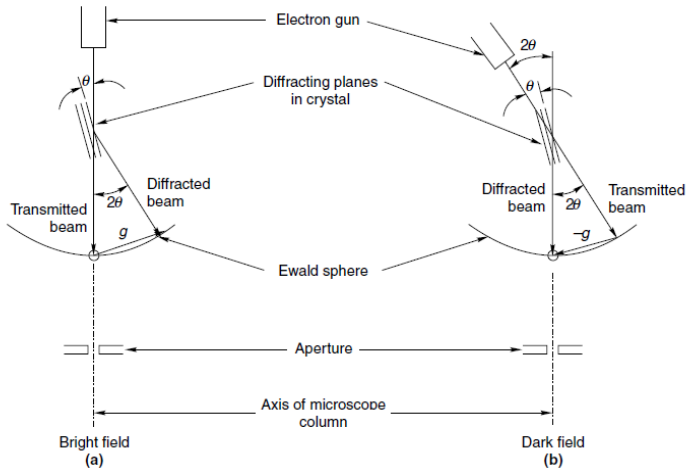


Figure 3.21: A schematic showing the operating principle of a TEM (a) bright image mode and (b) dark field image mode. Taken from Ref. [120].

tures below the back focal plane of the objective lens. This image is called the bright field image. In the second method, all other beams except the particular diffracted beam of interest are excluded. The image obtained using this method, is called the dark field image as shown in the schematic of Figure 3.21 [120].

TEMs with resolving powers in the vicinity of 1 Å are now common. As a result, high resolution TEM (HR TEM), is one of the most essential tools of nanoscience. Interaction of the electrons with the sample produces elastic and inelastic scattering. Most of the studies are done with the elastically scattered electrons which form the bright field image. The inelastically scattered electrons are used for electron energy loss spectroscopy as well as for energy filtered imaging. Electrons emerging from the sample, after a series of interactions with the atoms of the target material, have to be transferred to the viewing screen to form an image. This is influenced by the transfer characteristics of the objective lens. A parameter which can be used to understand the transfer properties is the phase contrast transfer function (CTF). This function modulates the amplitudes and phases that form the electron diffraction pattern in the back focal plane of the objective lens. The function is given as [121]:

$$T(k) = -\sin\left[\frac{\pi}{2}C_s\lambda^3k^4 + \pi\Delta f\lambda k^2\right] \tag{3.15}$$

where, C_s is the spherical aberration coefficient, λ, the wavelength of the beam, Δf , the defocus value and k is the spatial frequency. Defocus setting (with reference to the Gaussian focus) in the electron microscope determines the shape of the CTF. This is given in Angstrom units, Å. In the electron

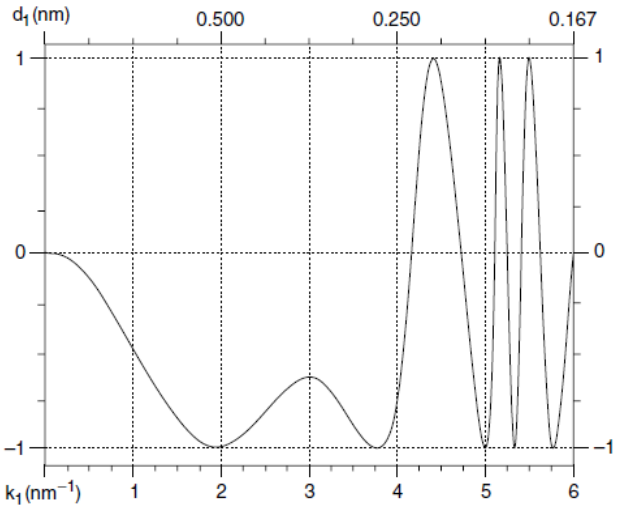


Figure 3.22: The contrast transfer function (CTF) is used to evaluate the capabilities of a TEM instrument. Taken from Ref. [121].

optical convention, over-focus implies negative defocus values, while under-focus (the only useful range) implies positive defocus values. The CTF of a 200 keV microscope will look like the one shown in Figure 3.22 [121]. The general characteristic to be noted is its oscillatory nature. When it is negative, we have a positive phase contrast and atoms will appear dark on a bright background. When it is positive, a negative phase contrast occurs, and atoms will appear bright on a dark background. When it is equal to zero, there is no contrast or information transfer. CTF can continue forever but it is modified by functions known as 'envelope functions' and eventually dies off.

In any instrument, the most important aspect is the resolution. This is the ability of the instrument to discriminate between two closely lying objects. As the wavelength of electrons is in the picometer range, it is only natural to expect a resolution of that order. However, this is not the case. This is because of the fact that electron lenses have aberrations and also due to the fact that it is impossible to get a coherent electron beam. We can express the resolution R as [121]:

$$R \approx d\alpha C_s^{1/4} \lambda^{3/4} \tag{3.16}$$

The interpretable resolution, or the structural or point resolution is the first zero crossover of the CTF at the optimum defocus. This can be given as $\sim 0.66(C_s\lambda^3)^{1/4}$. C_s increases with electron beam energy, but the point resolution improves with acceleration voltage as λ is reduced. As C_s goes from 0.3 mm for 100 keV to 1.5 mm for 1 MeV[120], the resolution changes from 0.25 to 0.12 nm. In view of the increasing cost of the instrument at larger acceleration

voltages and the resulting damage of the material under investigation at larger acceleration voltages, it is more advisable to use intermediate energy ranges.

Chapter 4

Laser synthesis of single-walled carbon nanotubes: Theory and Experimental

4.1 Introduction to lasers in materials synthesis

The word "laser", an acronym for *(L)ight (A)mplification by (S)timulated (E)mission of (R)adiation,* was first coined by Columbia University student Gordon Gould who was working on his doctoral thesis in the late 1950's. The claim to who first developed the concept of the laser was hotly debated for half a century between Charles Townes and Arthur Schawlow of Bell Labs and Gordon Gould. The concept of the laser followed the discovery of its microwave counterpart, named the MASER. The discovery, of the maser device, was made in 1953 by Charles Townes. However, continuous output power of the device was not possible. In 1955, a group of scientists working independently in the former Soviet Union, Nikolay Basov and Aleksander Prokhorov solved the problems experienced by the Bell labs group to produce a continuous maser output. For this work, Charles Townes, Nikolay Basov and Alexander Prokhorov received the Noble Prize in Physics in 1964 [122].

Consumed by the patent filing applications by Bells Labs and Gordon Gould for various rights to the laser design, it was Theodore H. Maiman who in 1960 became the first to construct a functioning laser based on the ruby crystal. Since then, there have been many laser developments with lasers being produced using gases, solid state crystal materials and diode lasers fabricated from semiconducting materials. Furthermore, besides different optical wave-

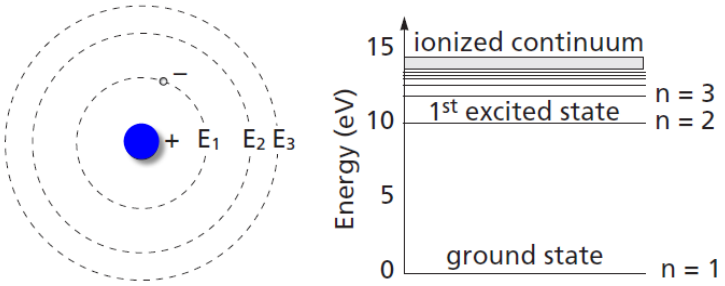


Figure 4.1: A schematic of the Bohr model of the atom to aid in the understanding of excitation and emission of radiation. Figure adapted from Ref. [125].

lengths, laser are also capable of producing continuous wave (CW) and pulsed laser beams. In pulsed laser systems, the time period of a pulse can vary from milliseconds (10^{-3} s) to a few femtoseconds (10^{-15} s). This large variation in the temporal profile, during which energy is transmitted, makes the laser a extremely important tool to study the basic interactions in materials. The construction of high energy, tunable wavelength and short pulsed laser systems, has found its use in fundamental particles physics and in modern fusion research [123]. The basics of how a laser operates and its interaction with a material will be discussed in the following subsections.

4.2 Operating principles of a laser

To understand the laser, one needs to understand the meaning of the terms in the acronym LASER. The term "light" is generally accepted to be electromagnetic radiation ranging from 1 nm to 1000 μm in wavelength. The visible spectrum, ranges from approximately 400 to 700 nm i.e. from the violet to the red. The wavelength range from 700 nm to 10 μm is considered the near infrared (NIR) region, and anything beyond that is the far infrared (FIR) region. Conversely, 200 to 400 nm is called ultraviolet (UV) radiation; below 200 nm is the deep ultraviolet (DUV) radiation.

To understand the concept of stimulated emission, we can use the simple Bohr model of the atom, proposed by Niels Bohr in 1913. Figure 4.1 shows a schematic of the Bohr model of the atom in which electrons orbit the nucleus of an atom. Unlike earlier "planetary" models, the Bohr atom has a limited number of fixed orbits that are available to the electrons. Under the right

circumstances an electron can move from its ground state having lowest-energy to a higher (excited) state, or it can decay from a higher state to a lower state; but it cannot be found between these states. The allowed energy states are called "quantum" states and are referred to by the principal "quantum numbers" 1, 2, 3, etc. The quantum states are represented by an energy-level diagram.

For an electron to jump to a higher quantum state, the atom must receive energy from an external source. This can happen through many possible mechanisms such as inelastic or semi-elastic collisions with other atoms and absorption of energy in the form of electromagnetic radiation (e.g., light). Likewise, when an electron drops from a higher state to a lower state, the atom must give off energy, either as kinetic activity (nonradiative transitions) or as electromagnetic radiation (radiative transitions). For the remainder of this discussion, we will consider only radiative transitions i.e. involving light. Light is made up of photons which exhibit both particle-like and wave-like properties. Each photon has an intrinsic energy determined by the equation [124]:

$$E = h\nu \tag{4.1}$$

where ν is the frequency of the light and h is Planck's constant where the frequency and wavelength are related by the equation:

$$c = \nu\lambda \tag{4.2}$$

and c is the speed of light in vacuum and λ its wavelength. Combining these we can write the energy of the photon as being:

$$E = \frac{hc}{\lambda} \tag{4.3}$$

Therefore, it is evident from this equation that the longer the wavelength of the light, the lower the energy of the photon; consequently, ultraviolet light is much more "energetic" than infrared light. In the Bohr atom: for an atom to absorb light i.e., for the light energy to cause an electron to move from a lower energy state E_n to a higher energy state E_m, the energy of a single photon must equal, almost exactly, the energy difference between the two states. Too much energy or too little energy and the photon will not be absorbed. Consequently, the wavelength of that photon must be:

$$\lambda = \frac{hc}{\Delta E} \text{ where } \Delta E = E_m - E_n \tag{4.4}$$

Similarly, when an electron decays to a lower energy level in a radiative

transition, the photon of light given off by the atom must also have an energy equal to the energy difference between the two states. In general, when an electron is in an excited energy state, it must eventually decay to a lower level, giving off a photon of radiation. This event is called "spontaneous emission," and the photon is emitted in a random direction and with a random phase. The average time it takes for the electron to decay is called the time constant for spontaneous emission, and is represented by τ.

On the other hand, if an electron is in energy state E_2, and its decay path is to E_1, but before it has a chance to spontaneously decay, a photon passes by whose energy is approximately E_2-E_1, then there is a probability that the passing photon will cause the electron to decay in such a manner that a photon is emitted at exactly the same wavelength, in exactly the same direction, and with exactly the same phase as the passing photon. This process is called "stimulated emission." Absorption, spontaneous emission, and stimulated emission are illustrated in Figure 4.2

Now consider the group of atoms shown in Figure 4.3 [125]. All begin in exactly the same excited state, and most are effectively within the stimulation range of a passing photon. We also will assume that its lifetime is very long, and that the probability for stimulated emission is 100 percent. The incoming (stimulating) photon interacts with the first atom, causing stimulated emission of a coherent photon; these two photons then interact with the next two atoms in line and the result is four coherent photons. At the end of the process, we will have eleven coherent photons, all with identical phases and all traveling in the same direction. In other words, the initial photon has been "amplified" by a factor of eleven (one photon resulting in eleven, as depicted in Fig. 4.3). Note that the energy required to excite these atoms is provided by some external energy source which is usually referred to as the "pump" source such as a pulsed flash-lamp.

In any real population of atoms, the probability for stimulated emission is quite small. Furthermore, not all of the atoms are usually in an excited state; in fact, the opposite is true. Boltzmann's principle, states that, when a collection of atoms is at thermal equilibrium, the relative population of any two energy levels is given by:

$$\frac{N_2}{N_1} = \exp\left[-\frac{E_2 - E_1}{kT}\right] \tag{4.5}$$

where N_2 and N_1 are the populations of the upper and lower energy states, respectively, T is the equilibrium temperature, and k is Boltzmann's constant. Substituting $h\nu$ for $E_2 - E_1$ yields:

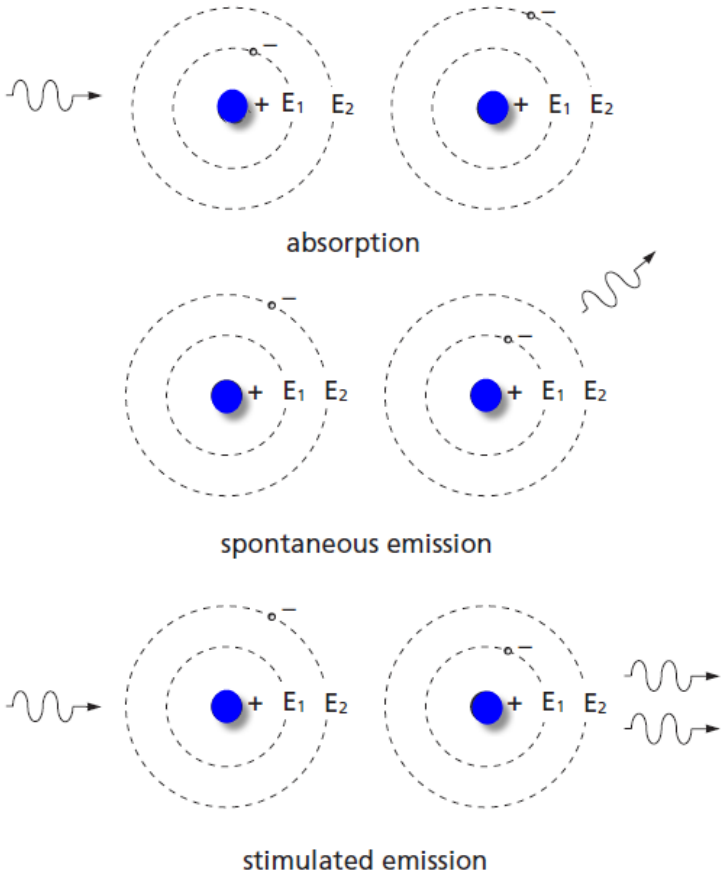


Figure 4.2: A schematic showing the processes involved in a lasing medium when excited by an external source. A modified figure adapted from Ref. [125].

$$\Delta E \equiv N_1 - N_2 = (1 - e^{\frac{h\nu}{kT}})N_1 \tag{4.6}$$

Under normal conditions, the majority of the atoms in the population will always be in the lower energy levels than in the upper one's. Since the probability for an individual atom to absorb a photon is the same as the probability for an excited atom to emit a photon via stimulated emission, the collection of atoms, the majority of which will be in the ground state, will result in the total system to be a net absorber and not a net emitter. Therefore, amplification will not be possible. Consequently, to make a laser, we must therefore create a "population inversion."

Atomic energy states are much more complex than indicated by the description above. There are many more atomic energy levels, and once excited, each one would have its own time decay constants. The four-level energy di-

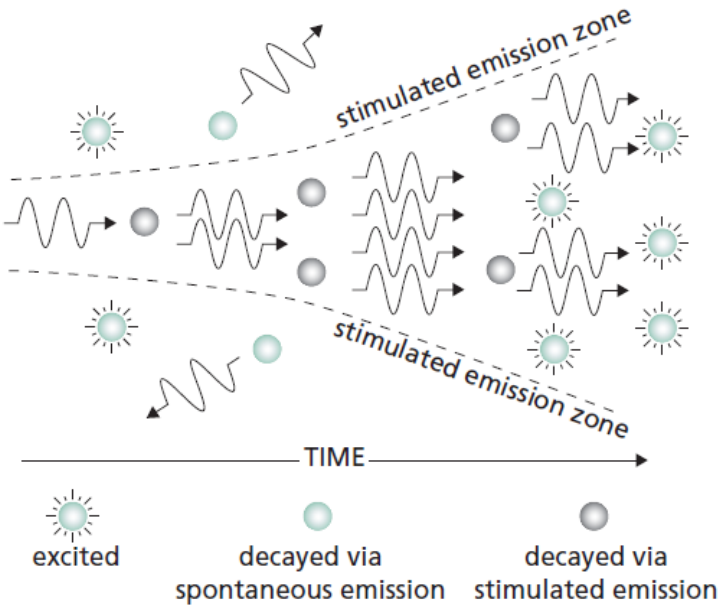


Figure 4.3: A schematic showing how stimulated emission takes place in a laser resonator. Figure adapted from Ref. [125].

agram shown in Figure 4.4 is representative of a laser material such as that of a Nd:YAG. The electrons are pumped (excited) into an upper level E_4 by some mechanism for such as, a collision with another atom or absorption of high-energy radiation. It then decays to E_3, followed by to E_2, and finally to the ground state E_1. If we assume that the time it takes to decay from E_2 to E_1 is much longer than the time it takes to decay from E_3 to E_2 then in a large population of atoms, at equilibrium and with a continuous pumping process, a population inversion will occur between the E_3 and E_2 energy states. Thus, a photon entering the population will be amplified coherently.

Although with a population inversion we have the ability to amplify a signal via stimulated emission, the overall single-pass gain is quite small, and most of the excited atoms in the population emit spontaneously and do not contribute to the overall output. To turn this system into a laser, we need a positive feedback mechanism that will cause the majority of the atoms in the population to contribute to the coherent output. This is achieved by means of a resonator, a system of mirrors that reflects undesirable (off-axis) photons out of the system and reflects the desirable (on-axis) photons back into the excited population where they can continue to be amplified.

Now consider the laser system shown in Figure 4.5. The lasing medium is pumped continuously, by an external light source, such as a bank of flash-lamps, to create a population inversion at the lasing wavelength. As the excited

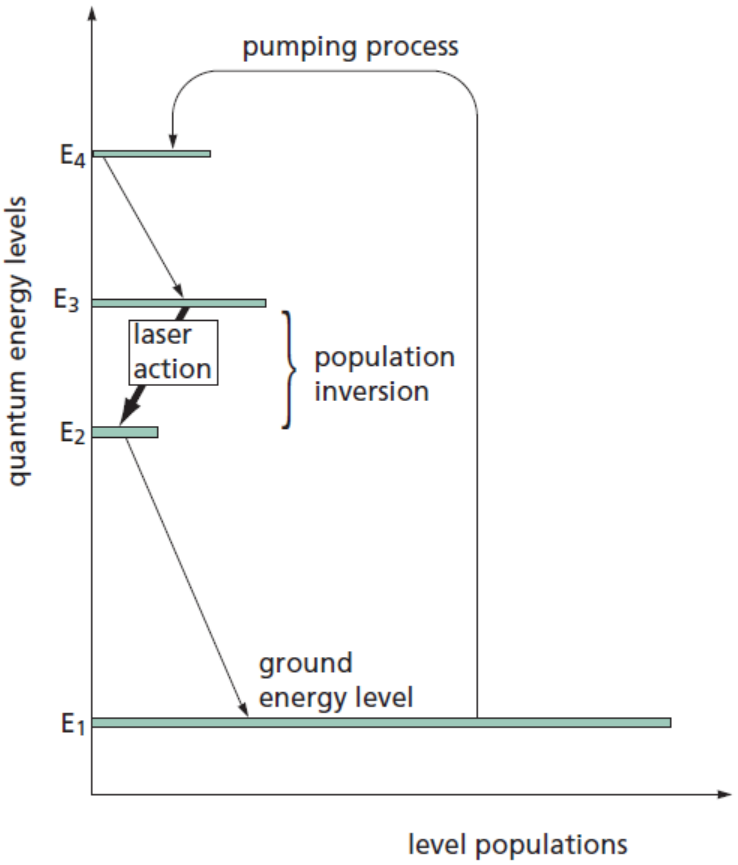


Figure 4.4: A schematic of a 4-level lasing medium such as Nd:YAG. Figure adapted from Ref. [125].

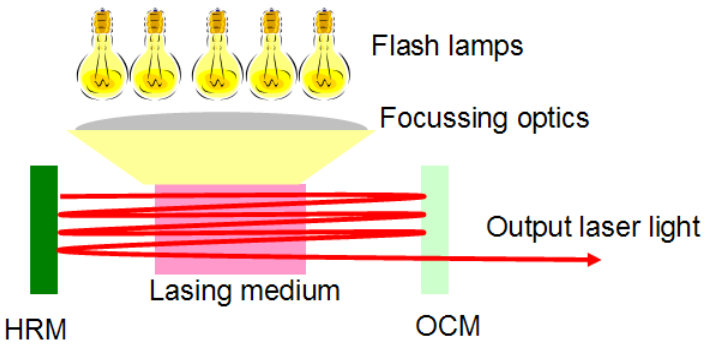


Figure 4.5: A schematic of showing the basic components which make up the laser resonator. A "lasing" such a Nd:YAG rod is located between a high reflecting mirror (HRM) and a output coupling mirror (OCM). Adapted from Ref. [127].

atoms start to decay, they emit photons spontaneously in all directions. Some of the photons travel along the axis of the lasing medium, but most of the photons are directed out the sides. The photons traveling along the axis have an opportunity to stimulate atoms they encounter to emit photons, but the ones radiating out the sides do not. Furthermore, the photons traveling parallel to the axis will be reflected back into the lasing medium and be given the opportunity to stimulate more excited atoms. As the on-axis photons are reflected back and forth interacting with more and more atoms, spontaneous emission decreases, stimulated emission along the axis predominates, and we have a laser.

Finally, the light exits the system, by employing one of the mirrors to highly reflect at the lasing wavelength called the high reflector (HR) and another mirror which is partially transmitting at the lasing wavelength, called an out coupling mirror (OCM) that couples small percentage of the circulating photons externally. The amount of coupling depends on the characteristics of the laser system and varies from a fraction of a percent for helium neon lasers to 50 percent or more for high-power lasers [126, 127].

4.3 Some properties of pulsed laser Gaussian beams

Different applications require laser beams of different pulse duration and output power. Lasers employed for materials processing or synthesis, range from those with a high peak power and extremely short pulse duration to lasers with high-energy continuous-wave output. Many pulsed laser ablation experiments, such as in pulsed laser deposition, prefer excimer lasers (usually KrF at $\lambda = 248$ nm, but also XeCl at $\lambda = 308$ nm and ArF at $\lambda = 193$ nm) with pulse durations in the range 20–30 ns, maximum pulse energies in the range of 0.25–1 J, and pulse repetition rates typically between 5–300 Hz. Peak power's as high as 10^{10} W.cm^{-2} are achievable, which make the excimer laser a successful tool for initiating photo-chemical and/or photo-thermal ablation. Except for materials synthesis or ablative experiments, the excimer laser is not commonly used. The Nd:YAG (neodymium doped yttrium aluminium garnet, Nd:$Y_3Al_5O_{12}$) laser is a more versatile laser and depending on its configuration can be used in many scientific applications requiring a coherent light source. When pulsed and in free running mode, it provides pulse widths of about 200μs. When Q-switched (an internal resonator mechanism to store laser energy and release it quickly), it can provide pulses in the region of between 5-30 ns. With pulse energies

of in the region of 1 J per pulse, peak power intensities can be 10^{10} W.cm^{-2}. Furthermore, combined with harmonic solid state crystals, the common laser wavelength output of 1064 nm can be frequency doubled to 532 nm; frequency tripled to 355 nm and even quadrupled to 255 nm. With pulse repetition rates of 10-30 Hz, this provides sufficient laser power for most laser material processing needs.

4.3.1 Gaussian beams

The spatial profile of a laser beam at the laser exit aperture is determined by the geometry of the laser cavity. When the cross section of the cavity is symmetrical as in the case of cylindrically or rectangular shaped cavities, the spatial profiles become simple. Transverse electromagnetic modes (TEMs) are characterized by TEM$_{mn}$, where m and n indicate the number of modes in two orthogonal directions. The mode of highest symmetry is the TEM$_{00}$ mode. This is a completely spherical beam. In the discussions which follow, only the TEM$_{00}$ mode will be discussed. For a more authoritative treatment of laser beam modes, refer to to the text by Siegman [127]. Of importance to laser beams and beam delivery, is how quickly the beam diverges after exiting the laser. For definition purposes, we define the distance over which the laser diameter increases by a factor $\sqrt{2}$, as z_R. This is known as the Rayleigh length. ω_0 is the diameter of the laser beam at the laser exit aperture (as is the case for the laser used in this study) and is also known as the waist of the laser beam, i.e. the minimum diameter the beam can attain in its propagation. For a TEM$_{00}$ (Gaussian) laser beam that is propagating in the z-direction, with wavelength λ and in a medium of refractive index n and with a circular profile, the spot size ω will change with z as [128]:

$$\omega(z) = \omega_0^2 \left(1 + \frac{z^2}{z_R^2}\right) \text{ and } z_R = \frac{\pi \omega_0^2 n}{\lambda} \tag{4.7}$$

The laser energy contained in a single laser pulse has a Gaussian intensity distribution. It is given by [128]:

$$I(r,t) = I_{pk}(t) \exp\left(-\frac{2r^2}{\omega}\right) \tag{4.8}$$

where ω is the radius of the laser beam at the point where the intensity drops by a factor of $1/e^2$ with respect to the peak intensity I_{pk}, at $r = 0$, were r is the radial coordinate. For pulsed laser beams, we define the pulse fluence or fluence, F, as the pulse energy divided by an area corresponding to a circular disk of radius ω:

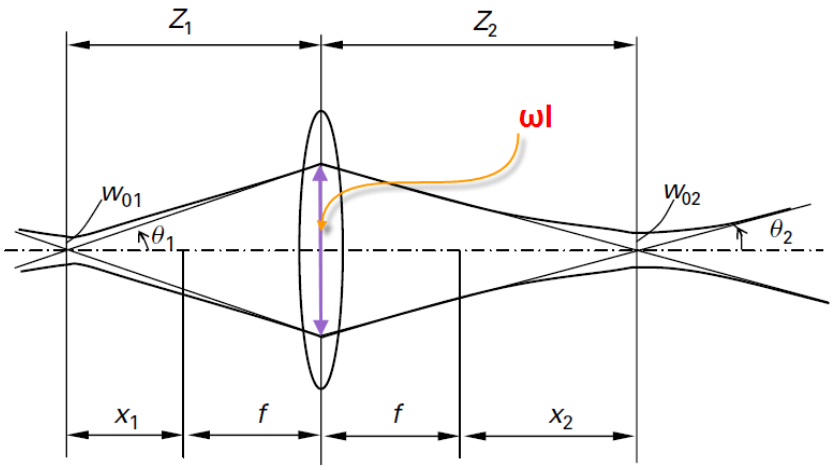


Figure 4.6: Focussing of a circular Gaussian beam using a thin convex lens of focal length f. Modified and adapted from Ref. [128].

$$F = \frac{E_{pulse}}{\pi\omega^2} \tag{4.9}$$

To achieve high peak power intensities, it is necessary in most materials processing or synthesis environment to focus the laser beam onto the target zone which contains the source material which needs to be vaporized. This is generally accomplished by the use of thin optical lenses. Figure 4.6 shows a ray diagram of transmitted laser light and the use of a lens to focus the laser beam. In this figure, the laser beam moves from left to right and the natural waist ω_{01} of the laser beam is positioned at the exit window of the laser.

Let f be the focal length of the lens. If the incoming beam's half-divergence angle is θ_1, and it is assumed that the beam waist ω_{01} is formed at a distance z_1 from the lens, with $x_1 = Z_1 - f$. The focused beam's focal waist ω_{02} is formed at a distance Z_2 ahead of the lens with $x_2 = Z_2 - f$, and the half-divergence angle is θ_2. Assuming that the beam size, ω_l can be measured at the position of the lens, then it can be shown from geometrical optical analysis [129] that ω_{02} which is the diameter at the target is:

$$\omega_{02} \cong \frac{f\lambda}{\pi\omega_l} = \frac{2\lambda}{\pi}\frac{f}{2\omega_l} \tag{4.10}$$

As a further approximation, the diameter, ω_0 at the focus can be approximated as $\sim 2\lambda$ or 2 μm [128] for the laser beam at 1064 nm and 1 μm when the beam is at 532 nm.

4.4 Laser induced thermal processes in materials

4.4.1 Surface heating

Classical continuum transport models are often used effectively to describe laser interactions with materials where nonequilibrium processes are not dominant. In this study, we assume local thermodynamic equilibrium (LTE) and that macroscopic transport laws are operative. Fourier heat conduction model is sufficiently to modeling nanosecond or longer-duration pulsed-laser heating of materials. Here only a brief discussion and summary of the formulation of relevant formulae on thermal processes taking place in laser-materials interactions are presented. For a more detailed treatise see texts on the subject by Grigoropoulos [128] and/or Miller and Haglund [130]. For nanosecond or longer-duration laser pulses, when the electrons and the lattice are at thermal equilibrium, it is characterized by a common temperature, T. The transient temperature field can then be calculated by solving the heat-conduction equation [128]:

$$\rho C_p(T)\frac{\partial T}{\partial t} = \nabla \cdot (K(T)\nabla T) + Q_{ab}(x, y, z, t) \tag{4.11}$$

where ρ, C_p, K, and T represent density, specific heat for constant pressure, thermal conductivity, and temperature, respectively. For a laser beam incident on the surface, z = 0, of a bulk substrate of thickness d and initial temperature T_0, the initial condition for the heat-transfer problem is $T(t = 0) = T_0$ and the boundary conditions are [128]:

$$\begin{aligned} K\tfrac{\partial T}{\partial t}\,|_{z=0} \quad &= h_{con,u}(T(x, y, 0, t) - T_\infty) \\ &+\varepsilon_{em,u}\sigma_{SB}(T(x, y, 0, t)^4 - T_\infty^4) \\ \text{and } K\tfrac{\partial T}{\partial t}\,|_{z=d} \quad &= h_{con,L}(T(x, y, d, t) - T_\infty) \\ &+\varepsilon_{em,L}\sigma_{SB}(T(x, y, d, t)^4 - T_\infty^4) \end{aligned} \tag{4.12}$$

In the above, $h_{conv,u}$ and $h_{conv,L}$ are the coefficients for linear convective heat transfer from the top and bottom surfaces of the sample, $\varepsilon_{em,u}$ and $\varepsilon_{em,L}$ are the corresponding emissivities, σ_{SB} is the Stefan–Boltzmann constant, and T_∞ is the ambient temperature. The thermal-diffusion penetration depth into the material is given by $d_{th} = \sqrt{\alpha t_{pulse}}$, where α is the thermal diffusivity, $\alpha = \frac{K}{\rho C_p}$, and t_{pulse} is the pulse duration. For $d_{th} \ll d$, the target material can be considered semi-infinite. If $d_{abs}/d_{th} \ll 1$, the absorption of laser radiation is essentially a skin surface phenomenon, which is a valid approximation for metals irradiated by laser pulses of duration longer than nanoseconds. If the

absorption coefficient is weak and $d_{abs}/d_{th} \gg 1$, radiation penetrates deeper into the material, giving rise to shallower thermal gradients and a more uniform temperature field. An important assumption is that absorption coefficient and surface reflectivity during the laser pulse is constant [128].

If a Gaussian laser beam is considered, the heat flow is essentially perpendicular to the target surface if the beam radius is much greater than the thermal penetration depth, i.e. $w \gg \sqrt{\alpha t_{pulse}}$. In the other extreme case, if $w \ll \sqrt{\alpha t_{pulse}}$, the laser heat source may be considered as a point source and the isotherms are concentric hemispherical surfaces [128]:

$$T(r,0,t) = \frac{(1-R)w^2}{\rho C_p \sqrt{\pi\alpha}} \int_0^t \frac{I(t')}{(t-t')^2\left[4\alpha(t-t')+w^2\right]} \exp\left(-\frac{r^2}{4\alpha(t-t')+w^2}\right) dt' \tag{4.13}$$

However, for an estimate, the following relation is used in later sections to determine the rise in temperature of the target when it is impacted by laser pulses:

$$T \approx \frac{(1-R)E_{pulse}}{\rho C_p V_{HAZ}} \tag{4.14}$$

where E_{pulse} is the pulse energy and V_{HAZ} is an estimate of the heat-affected material volume [128]:

$$V_{HAZ} = \begin{cases} \pi w^2 \sqrt{\alpha t_{pulse}} & if \quad w \gg \sqrt{\alpha t_{pulse}} \\ \frac{4}{3}\pi(\alpha t_{pulse})^{3/2} & if \quad w \ll \sqrt{\alpha t_{pulse}} \end{cases} \tag{4.15}$$

4.4.2 Removal of target material by ablation

There are several ablative mechanisms by which material, either atomic or bulk, can be released from the surface of the target. References to "thermal" or "photothermal" ablation generally embrace a model in which laser light is converted to lattice vibrational energy before bond breaking liberates atomic material from the bulk surface. Thermal mechanisms are distinct from a "photochemical" or "electronic" processes. In the case of laser-induced plasma's, electronic excitations dominate. These are faster and lead directly to bond breaking before an electronic to vibrational energy transfer has a chance to occur. Both thermal and electronic sputtering mechanisms lead to the liberation of atomic-size material from the surface. This is distinct from two other ablation mechanisms, identified in the literature as "hydrodynamical" and "exfoliation," which introduce bulk material into the ablation plume.

The hydrodynamical mechanism is ascribed to the liberation of micrometer-

sized droplets, following motion in the molten phase. Exfoliation refers to an erosive-like mechanism by which material is removed from the surface in solid flakes. Separation of flakes from the surface is thought to occur through energy-absorbing defects in the material. It should be pointed out that these mechanisms are not necessarily distinguishable in a specific laser-ablation system, in which more than one mechanism can occur, either simultaneously or in different phases of the ablation process, depending upon the range of the laser parameters [130]. For nanosecond laser ablative sources, the classical picture of thermal vaporization is sufficient as a first approximation. It does not however, provide a full description of the processes taking place.

Experimentally, it is usually easier to achieve vaporization than to control melting without significant material loss to the vapor phase. For moderate laser intensities, the laser-induced peak target surface temperature is below the thermodynamic critical point, and a sharp interface separates the vapor from the liquid phase. Both the sensible heat, which is the energy that leads to a temperature change, and the latent heat of melting are typically much smaller than the latent heat of vaporization, implying that evaporation is dominant in the energy balance. For a surface absorber, $d_{abs} = 1/\gamma \ll \sqrt{\alpha t_{pulse}}$, simple energy-balance considerations give the following estimate for the material-removal depth, d_{abl} [128]:

$$d_{abl} = \frac{(1-R)(F-F_{sh}) - q_{loss}}{\rho C_p (T_{bp} - T_0) + L_{sl} + L_{lv}} \tag{4.16}$$

where F_{sh} represents the fluence loss due to plasma shielding. This estimate is appropriate for short pulses, since conduction losses become more significant for longer pulses. For laser energy intensities $I < 10^8$ W.cm^{-2}, energy absorption by the evaporated particles is insignificant, so the vapor phase may be considered transparent. According to the thermal surface-vaporization picture, the material-removal rate is limited by the surface temperature. Neglecting recondensation of vapor onto the surface, the rate of evaporation from the liquid surface, j_{ev}, can be described using kinetic theory [128]:

$$j_{ev} = N_l \left(\frac{k_B T_l}{2\pi m_a}\right)^{1/2} \exp\left(-\frac{L_{lv}}{k_B T_l}\right) - \upsilon_s N_v \left(\frac{k_B T_v}{2\pi m_a}\right)^{1/2} \tag{4.17}$$

where N_l and N_v are the numbers of atoms per unit volume for liquid and vapor, L_{lv} and T_v are the latent heat of vaporization and temperature of vapor, m_a is the atomic mass, and k_B is the Boltzmann constant. The first term on the right represents the evaporation rate from the liquid surface at temperature T_l. The second term represents a damping of this evaporation rate due to the return of liquid molecules to the liquid surface. The parameter υ_s, called the

sticking coefficient, represents the probability that a vapor atom returning to the liquid surface is finally adsorbed on the liquid surface.

The total ablation depth, d_{abl}, due to surface evaporation is [128]:

$$d_{abl} = \int_0^\infty j_{ev} m_a \rho dt \tag{4.18}$$

During the first stage of interaction between the laser pulse and the solid material, part of the laser energy is reflected at the surface and part of the energy is absorbed within a short penetration depth in the material. The energy absorbed is subsequently transferred deeper into the interior of the target by heat conduction. At a later stage, if the amount of laser energy is large enough (depending upon the pulse length, intensity profile, wavelength, and thermal and radiative properties of the target material), melting occurs and vaporization follows. The velocity of the liberated material can be estimated from:

$$v = \sqrt{\frac{2\eta kT}{M}} \tag{4.19}$$

where η is the number of internal degree's of freedom which can vary between 2.53 and 3.28, M is the atomic mass of the species ejected and T is the temperature [131].

The vapor generated can be ionized, creating a high-density plasma that further absorbs the incident laser light. Effects of this laser-plasma shielding have been shown via the simplified one-dimensional model of Lunney et. al. [132]. Of interest are the descriptions of the vaporization and ionization processes (beyond the scope of the dissertation). The material which constitutes the plasma and the light emissions as a result of recombination processes taking place when the plasma condenses is described in the Chapter 6.

4.5 Synthesis of single-walled carbon nanotubes

4.5.1 Self assembly of vaporized carbon

The common factor in all known methods of synthesizing carbon nanotubes introduced briefly in Chapter 2, is that carbon is in the form of vapour or in the gaseous dissociated phase prior to the formation of caged carbon fullerenes such as C_{60}, multi-walled carbon nanotubes (MWCNTs) or single-walled carbon nanotubes (SWCNTs). In the chemical deposition process, the carbon source is an organic gas such as acetylene, methane, ethanol vapour, camphor vapour etc. In the heated furnace, these chemical gases or vapours undergo thermal

decomposition into smaller carbon chains, trimers, dimers or elemental carbon with sp, sp^2 or sp^3 forms of hybridized carbon. When they condense under certain conditions e.g. in the presence of metallic catalyst, MWCNTs and/or SWCNTs are nucleated.

In the laser ablation method or arc-discharge method, graphite is the source of the carbon. The graphite needs to be vaporized by intense laser pulses or continuous addition of energy to dissociate the very strong sp^2 bonds between carbon atoms in the graphene plane. The graphene planes are held together by weak van der Waals forces. A pulsed laser is used to "break-up" the graphite into smaller clusters such as C_2. Prior to using a laser to synthesize SWCNTs, Smalley used the laser to vaporize graphite to study carbon cluster formations. The discovery of C_{60} was an outcome of this study [2]. The study revealed, that in order to promote cluster formation, graphite must be vaporized and allowed to condense or self-assemble. A material called endohedral fullerenes which were was C_{60} molecules into which metals were imbedded was predicted to be of technological importance, became a major focus of research [133]. In studies to make endo-fullerenes, a small percentage of metals was mixed with graphite and ablated in the hope the metals could find their way in to the caged- self assembled C_{60}. TEM analysis of material synthesized in this way showed ropes of tubular graphene instead of endohedrals. This lead to the study of SWCNTs [12].

The unique properties and applications of SWCNTs have been described in Chapter 2. Experimental methods used to characterize SWCNTs have been presented in Chapter 3.

An unsolved problem, that has plagued SWCNTs since their discovery, is the production of a wide variety of nanotubes which are present in any as-prepared sample irrespective of which synthesis route is employed. This is not conducive for appplication in electronic devices which demand single-type nanotubes. While, enormous progress in synthesis has been made, a complete understanding of the catalytic growth of SWCNTs remains unresolved [21]. To a certain extent, this is a consequence of the fact that the abundance and properties of SWCNTs are sensitive to the many process variables. These include the composition of the target source material, synthesis parameters, and the inconsistent approach of characterizing SWCNTs [134, 135].

It is widely accepted that the synthesis of SWCNTs is a multistep process that involves the atomization of the starting material, nucleation, and growth stages. Although expensive to operate, a better management and study of the growth conditions is possible using a laser-furnace method to synthesize SWCNTs. In this study, the method to synthesize SWCNTs using a laser is

SpectraPro Quanta Ray Nd:YAG	**1064 nm**	**532 nm**
Pulse energy (mJ)	250	450
Average power at 30 Hz (W)	7.5	13.5
Pulse width (ns)	10	8
Beam divergence (mrad)	<1	<1
TEM mode	TEM_{00}	TEM_{00}

Table 4.1: Laser specifications and beam properties at the laser exit aperture

described. In particular, a dual laser configuration was utilized in this study whereby pulses of 1064 nm and 532 nm were combined, to ablate a graphite composite target with various compositions under different operational conditions. It was shown that even though the self-assembly of particular SWCNTs could not be achieved, the self assembly of families of particular nanotubes was favoured by the adjustment of process parameters.

4.6 Experimental Design for the laser synthesis of SWCNTs

4.6.1 Apparatus

Initially, the assembly of the apparatus to synthesize SWCNTs was closely guided by the early reports of Guo et al. [12], Arepalli et al. [136] and Puretzsky et al. [137]. During the period 2003-2010, various configurations and types of equipment were used to synthesize SWCNTs. Key parts of the equipment are discussed below:

4.6.1.1 Laser

A SpectraPro Quanta Ray 290E-30 pulsed Q-switched Nd:YAG laser operated at a pulse repetition frequency of 30 Hz or in single shot mode for OES plasma studies was used. The fundamental wavelength was 1064 nm. The laser was also frequency doubled to produce 532 nm pulses separated temporarily by about 50 ns from fundamental operating wavelength. Detailed specifications are shown in Table 4.1.

4.6.1.2 Furnace

The laser ablation occurs in a sealed quartz tube placed in a tube furnace. The furnace was 1.2 m long, of the hinged type and manufactured by Carbolite. It accommodated a quartz tube of 50 mm outside diameter (OD). It had

three proportion integral derivative(PID) controlled temperature zones divided equally over length of the furnace. These zones could be operated independently. The design was such that it ensured a uniform temperature for a total length of 1.1 m with a small drop in temperature at both ends of the tube. The furnace in operation was stable between 873 and 1373 K. In all experiments, the furnace was operated between 1073K and 1373 K in increments of 100 K. The hinged tube design allowed for faster cool-down times and made *in situ* OES measurements possible.

4.6.1.3 Pressure, Mass Flow control and vacuum systems

A standard rotary pump (Balzer) was used to evacuate the system to a base pressure of 10^{-2} mbar. Thereafter it was filled with high purity argon 5.0 gas. While the vacuum pump was in operation, argon gas flow and pressure were set and kept constant to specified values. This was accomplished by using a MKS 273 controller with a MKS 640 pressure transducer and a Mass Flo® device.

4.6.1.4 Optical and mechanical components

A set of specially coated optical mirrors were used steer the laser beams from the laser towards the location of the target in the furnace. The laser mirrors were 50.6 mm in diameter and were manufactured by Newport using BK7 glass. Some mirrors had optical coatings that were only reflective at 45^0 for 532 nm or 1064 nm or could reflect both wavelengths equally. Special mirrors with dielectric coatings were used to combine 532 and 1064 nm beams from different optical paths. The coatings on all the mirrors could withstand a high laser damage threshold ($>$10 J.cm^{-2}) to prevent optical damage.

4.6.2 Description of the experimental layout

Figure 4.7 shows a schematic of the experimental layout employed to synthesize SWCNTs. Both the laser and furnace were installed on purpose built tables to accommodate an optical breadboard. The optical tables are sandwiched 5 mm stainless steel plates with honeycomb internal structure which keeps the vibrations to a minimum which is an important feature in any laser-optical experiment. These breadboards were supplied with holes threaded for M6 bolts and which were spaced 25 mm apart. This made it easier to bolt down opto-mechanical components to ensure that the laser optical beam path was kept aligned at all times. The furnace and laser were positioned parallel and adjacent to each other to keep the optical beam path of the laser beams entering

the furnace as short as possible. A set of laser mirrors with anti-reflective (AR) coatings for 532 nm and 1064 nm laser pulses was utilized to steer the laser beams towards the centre of the furnace. In all instances, these mirrors were designed for 45^0 reflection and were carefully positioned with respect to the incident laser pulses.

Due to laser safety precautions which are customary when a Class 4 pulsed infrared Nd:YAG laser is utilized, an alignment laser was utilized to correctly position the laser mirrors. Firstly, the alignment laser itself was positioned parallel to the main laser. Secondly, the alignment laser was "coupled" to the main laser in a such a way that it was made collinear with the pulsed lasers beams of the main Nd:YAG laser. This meant that the path taken by the alignment laser was the same as that of the pulsed lasers. This alignment procedure was done with pulsed Nd:YAG laser operating in very low energy mode. Safety wise, this was very important since the IR laser beam is invisible to the naked eye and its positional status needs to be known at all times. Thereafter, all optics and positioning of the target in the furnace was accomplished using the alignment laser. An internal second harmonic generator converted the fundamental wavelength from 1064 nm to 532 nm via a non-linear optical process. Not all of the 1064 nm pulse energy was converted. The depleted fundamental beam was still significant in energy and therefore, useful and was transmitted out of the laser through the 1064 nm exit aperture shown by the red line in Figure 4.7. The new 532 nm laser pulses, shown by the green line, took a slightly longer optical path but eventually became collinear with the 1064 nm beam with the use of dielectric mirrors, which are labelled DM in Figure 4.7.

The combined beams were steered towards a motorized mirror that was highly reflective for 1064 nm + 532 nm beams. These mirrors directed the beam into the vacuum sealed quartz tube. The quartz tube was supported horizontally in the furnace. The longitudinal axis of the 50 mm OD quartz tube was collinear with the incoming laser pulses. The laser pulses entered the quartz tube via a window with a specially designed opto-mechanical mount machined out aluminium at Brewster's angle, which was approximately 54^0 to the vertical. To this part, a 50 mm diameter, 3 mm thick quartz window was fitted. This window had dual AR coatings for 532 nm + 1064 nm. The intention of having the entrance at Brewster's angles, was to minimize reflections at the window interface [138]. At both ends of the quartz tube, Atomate® vacuum fittings were used. These provided a very good vacuum seal.

A second, smaller quartz tube was mounted coaxially inside the first quartz tube. This tube served the purpose of being a gas flow tube and allowed a

more laminar gas flow than would have been possible if no flow tube had been utilized. The flow tube had an inner diameter of 24 mm and was supported by graphite rings. The target was positioned towards the centre of the furnace by a stainless steel 6.3 mm tube and faced the incoming laser pulses. This tube extended from the back of the larger quartz tube and was supported by a graphite bar through which a hole was drilled for the target holder tube to pass through. The distance between the end of the flow tube and the target surface was 20 mm. The diameter of the target was 20 mm and of length 20 mm. Therefore, it was slightly smaller than the inside diameter of the flow tube. The argon gas acted as a buffer and aided in plasma confinement which improved the conditions under which self-assembly of carbon atoms into SWCNTs was favored. The second function of the gas was to carry the SWCNTs to the rear of the quartz tube where they would condense on cooler regions.

A gas connection to allow the in-flow and out-flow of argon gas was fitted to the front-end and back-end of the quartz tube respectively. The flow and pressure of the argon gas was controlled by an MKS Type 247 system consisting of a Mass-Flo® and an MKS Type 640 transducer, respectively. To produce as-prepared material containing significant amounts of SWCNTs, the laser was allowed to raster the target surface for about 30 min. by means of motion controlled steering mirrors. These mirrors were positioned just before the entrance of the quartz tube. After each run, and after the system had cooled down, the material for sample characterization was scrapped off the inside back-end of the quartz tube.

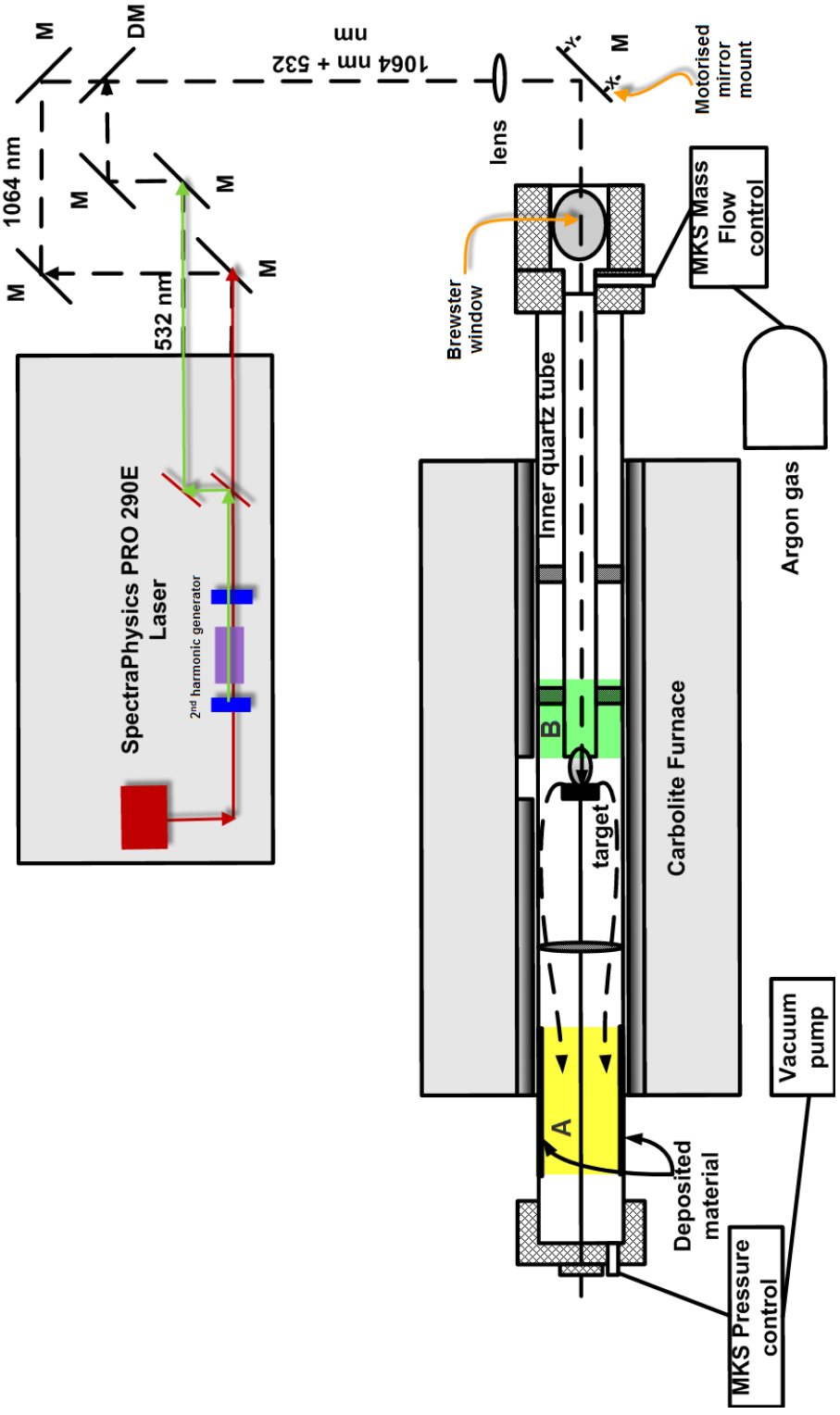


Figure 4.7: Experimental layout to synthesize SWCNTs by the laser-furnace method.

SpectraPro Quanta Ray Nd:YAG	**1064 nm**	**532 nm**
Pulse energy (mJ)	250	450
Average power at 30 Hz (W)	7.5	13.5
Pulse width (ns)	10	8
Spot size, focussed, with lens f_L=1500 mm	3	2
beam size (mm)	8	8
Eneregy fluence, focussed beam ($J.cm^{-2}$)	3.5	14
Energy fluence, unfocussed ($J.cm^{-2}$)	0.5	0.9
Peak power density, focussed ($MW.cm^{-2}$)	355	1.8×10^3
Peak power density, unfocussed($MW.cm^{-2}$)	50	112
Beam divergence (mrad)	<1	<1
TEM mode	TEM_{00}	TEM_{00}

Table 4.2: A summary of measured values of laser parameters used in this study.

4.6.3 Measurement of laser parameters

Prior to any synthesis experiments, laser parameters which play an important role in the laser ablation process were measured and are shown in Table 4.2.

1. Pulse laser energy (mJ), was measured with a Newport 818E-20-50F energy head coupled to a Newport 1918-C optical meter.

2. Average power (W), was measured with a Newport 818P–050-50 power head coupled to a Newport 1918-C optical meter.

3. Pulse width (ns) and delay for the 532 nm and the 1064 nm pulsed beams, were measured with a New Focus model 1621 VIS and model 1623 IR photodetectors respectively and was connected to a Tektronix DPO7104 1 GHz oscilloscope.

4. Laser beam spot size and TEM mode were estimated from ZAP–IT® paper at 86% ($1/e^2$) for both 532 nm and 1064 nm. Values are provided for focussed and unfocused beams. Ideally those should have been measured with a CCD camera but this was unavailable.

4.6.4 Preparation of laser ablated targets

For SWCNT synthesis, targets were fabricated from graphite and a small percentage of metallic catalysts. The efficiency of the synthesis is dependent on the type of metal catalyst chosen [134, 135], the quantities and the catalyst size the correctly chosen catalysts [139, 140].

Target label	**Graphite content at.%**	**Catalyst content at.%**
A	98	1%Ni:1%Co
B	98	1%Ni:1%Fe
C	98	1%Co:1%Fe
D	97.5	1%Ni:1%Co:0.5%Fe
E	97	1%Ni:1%Co:1%Fe
F	96.5	1%Ni:1%Co:1.5%Fe
G	96	1%Ni:1%Co:2%Fe
H	95	4%Ni:1%Y

Table 4.3: Chemical composition of graphite-metal catalyst targets used in this study.

From literature, the percentage of total catalyst contribution should not exceed 10% and is generally kept below 5%. Excessive use of catalyst makes the purification process difficult as the catalysts need to be removed for applications in advanced electronics [21]. It is known that the use of bimetallic catalysts produce higher yields. In this study, four different catalysts were utilized, all of which were transition metals. To make a durable target that holds together during ablation in the furnace at high temperature, a proprietary product called Dylon® cement was used. This cement was used as the bonding agent which when cured, resulted in a complete carbon bonded structure. Since it is proprietary, no detailed composition was given. However, from the chemical user datasheet indicated that by curing the target at 750^0C, results in a 23% loss in mass. Therefore, this was taken into account when the quantities needed to give a final composition was determined. Since the effect of target composition on the synthesis process was being investigated, it was important to have the recipe correct. In Appendix A, a recipe to synthesize a target to give a final ratio of 98%C:1%Ni:1%Co is given. The same method was used in all target preparations. Once the correct mixture was prepared, the target was pressed in a piston and sleeve apparatus. The piston and sleeve was bolted tight and cured at 403 K in a vacuum oven for 12 h. Thereafter, the unit was allowed to cool. The sleeve was removed and the hard target was forced out of the piston. Thereafter, the target was fixed to a 6.4 mm diameter stainless steel tube and positioned at the center of a larger quartz tube as previously described. The target was baked at 1273 K for 4 hours to allow out-gassing of all unwanted chemicals so that a final target composition was achieved viz. 98% C:1% Ni:1% Co. Table 4.3 provides details of the target compositions used in the study.

Target label	Temperature (K)	Pressure (Torr)	Ar flow rate (SCCM)
A	1073, 1173, 1273, 1373	100, 400, 500	100, 200, 300
B	1073, 1173, 1273, 1373	400	200
C	1073, 1173, 1273, 1373	400	200
D	1073, 1173, 1273, 1373	400	200
E	1073, 1173, 1273, 1373	400	200
F	1073, 1173, 1273, 1373	400	200
G	1073, 1173, 1273, 1373	400	200
H	1073, 1173, 1273, 1373	400	200

Table 4.4: Experimental conditions under which the graphite composite target was ablated.

4.6.5 Furnace and argon gas flow conditions

The furnace temperature plays an important role in the nucleation of the nanotubes since all nucleation process are driven by energetics of pre-cursors [39, 134]. The pressure and flow of argon gas influences the plasma dynamics and may influence the nucleation of different types of nanotube families. Table 4.4 list the conditions under which the targets shown in Table 4.3 were ablated.

4.6.6 System in operation

Figure 4.8 shows a photograph of the mounted target positioned at the centre of the furnace. The support rod was able to slide back and forth so that the target could be correctly positioned 20 mm from the end of inner quartz flow tube. The He-Ne laser was also used to ensure that the target was centred. At the front-end of the outer quartz tube, the inner quartz tube was carefully fed through and was supported by graphite rings. Next, the Brewster window was carefully fitted and clamped and the inlet argon gas was connected. This is shown in Figure 4.10. With the target correctly positioned, the nut securing the support rod at the back of the vacuum flange, seen in Figure 4.9, was tightened and connected to the vacuum system to pump down the entire quartz tube to a base pressure of 10^{-2} mbar using the Balzer rotary vein pump.

Once the system had been pumped down, the furnace was closed and switched on. Whenever a new target was used, it had to be completely outgassed of all impurities such as NO_2, CH_4, H_2 and other gaseous compounds of sulphur due the product Dylon® cement. To do this, the outgassing proceeded with the vacuum pump on, but performed in a flow of argon gas, to remove outgassed products faster. The temperature was slowly ramped in steps of 100 K up to operating temperature and then held for 30 minutes for each setting. This allowed the outgassing to proceed in a carefully controlled

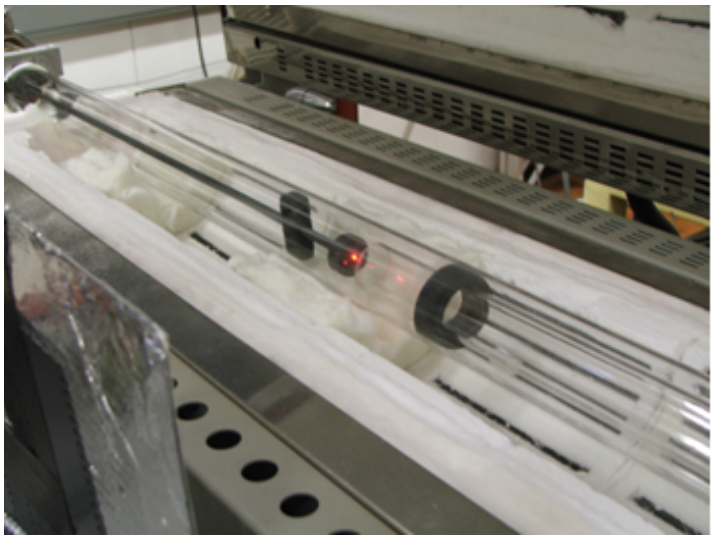


Figure 4.8: Photograph showing the target correctly postioned in the centre of the furnace, 20 mm from the end of the inner quartz flow tube.

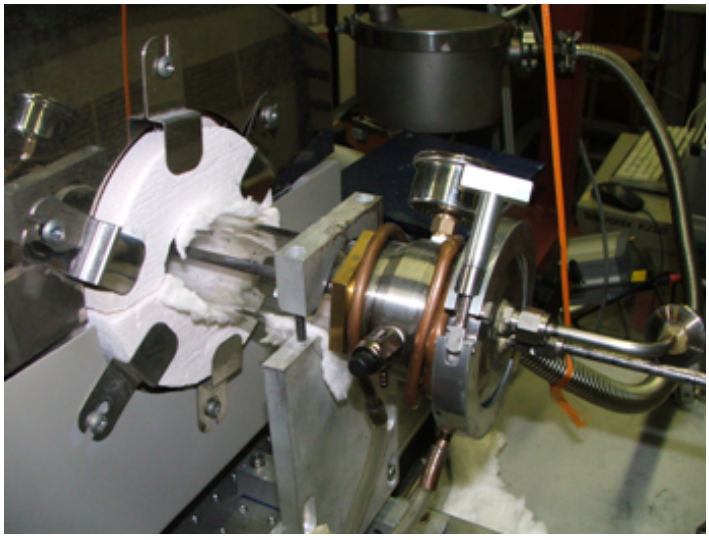


Figure 4.9: The back-end of the quartz tube showing the clamping of the target, support rod and connection to the vacuum system.

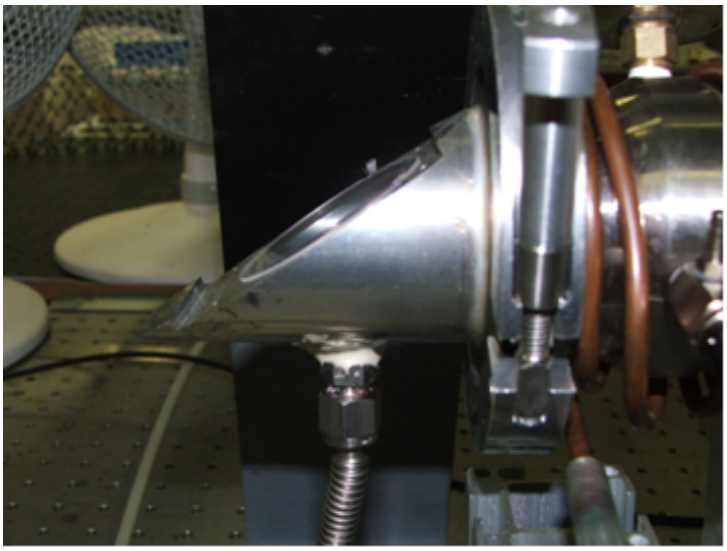


Figure 4.10: The front-end of the quartz showing the Brewster window from the side and the inlet argon gas connection.

manner. If this was not strictly followed, the target would have shattered due to excessive and sudden outgassing.

Generally, a new target would need approximately 6 hours of outgassing before it could be used. After this period, the MKS gas and pressure was set for operating conditions shown in Table 4.4. During this time, the laser was switched on, with only the flash lamps being fired. This was to get the lamps and Nd:YAG laser rods warmed up to operating temperature. Twenty minutes of warming up was sufficient to warm up the system. Thereafter, the laser was operated in free running mode for a further 20 minutes i.e. not Q-switched. Once the system was ready to start ablating the target, the pressure and flow settings was double-checked. The alignment of the laser entering the furnace was double-checked by operating the laser at reduced energy.

A small software program written in Labview was used to control the motion of the beam steering windows which allowed the target to be scanned. Once the motion of the mirrors was started, the laser was switched to full power. For safety reasons, it was important to ensure that the entire system was constantly monitored at all times. Typical laser runs were of 30 minutes duration. The following were constantly monitored during operation:

- pressure: an increasing pressure in the system could be attributed to a leak, a damaged laser entrance window or a clogged vacuum system. A drop in pressure may be caused by a depleted gas supply.
- furnace temperature.
- unusual noise that increased in pitch was normally associated with in-

creasing damage on the laser entrance window.

It was important to have the entire gas line from the quartz tube to the vacuum pump, including the MKS mass flow and pressure transducers frequently cleaned. It was found that very good quality nanotubes could escape the quartz tube and clog the system. In an attempt to solve the problem, a cold trap with a cellulose filter was inserted into the cold trap connected to the vacuum pump line, at the back-end of the quartz tube. This reduced the problem but did not completely eliminate it. The material trapped on this filter was off high quality and therefore was very useful.

After 30 minutes of continuous ablation, the laser was stopped and the furnace switched off. Figure 4.11 shows the deposit of as-prepared SWCNT deposits on the inside of the quartz tube. Material synthesized in the hot zone was carried to the back-end were it condensed on the cooler sections of the quartz tube. After the furnace had cooled to room temperature, the vacuum flange holding the target support rod at the back-end of the quartz tube was carefully removed. Figure 4.12 shows the removal of the flange exposing the as-prepared material. At this stage the use of surgical powder free gloves and a face mask was mandatory.

The black deposited material was removed by scrapping off by using a rod to which a 3 mm Teflon disc of diameter 40 mm was attached. In this way, it was easy to remove material from the inside wall of the quartz tube. Figure 4.13 shows a typic sample of material that was collected from the synthesis process.

4.7 Summary of the synthesis of as-prepared materials

4.7.1 Key to sample labelling

Due to the extensive number of samples and the different experimental conditions under which the samples were prepared, it was necessary to have an identification key which enabled an easy way of identifying the conditions under which the sample was prepared. The following identification key was adopted which incorporated important parameters such as: target description, furnace temperature, argon gas pressure, argon gas flow, and the position at which the sample was extracted. Example: A12P4F2A

- The first label was an alphabet and corresponded to the label of the target in Table 4.3.

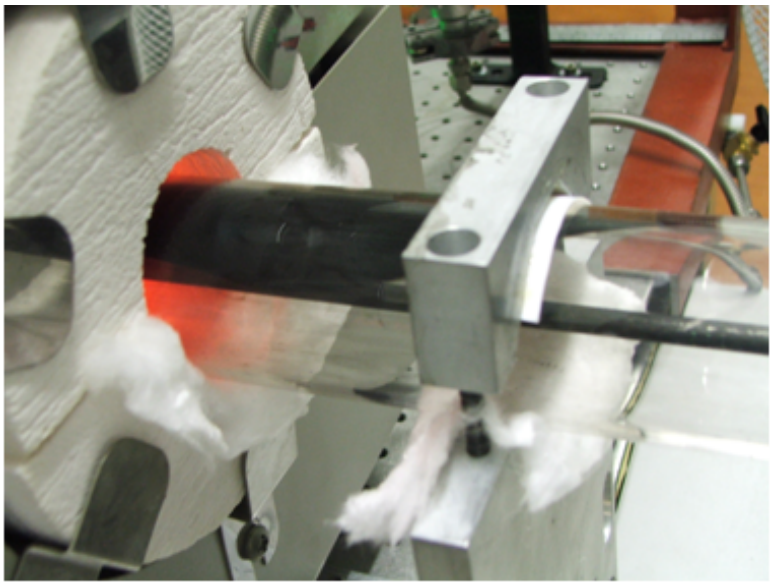


Figure 4.11: SWCNT material synthesized in the hot zone. The material was carried to the back and condensed on cooler sections of the quartz tube and appeared like a matt black deposit. This material was collected over a period of 30 minutes.

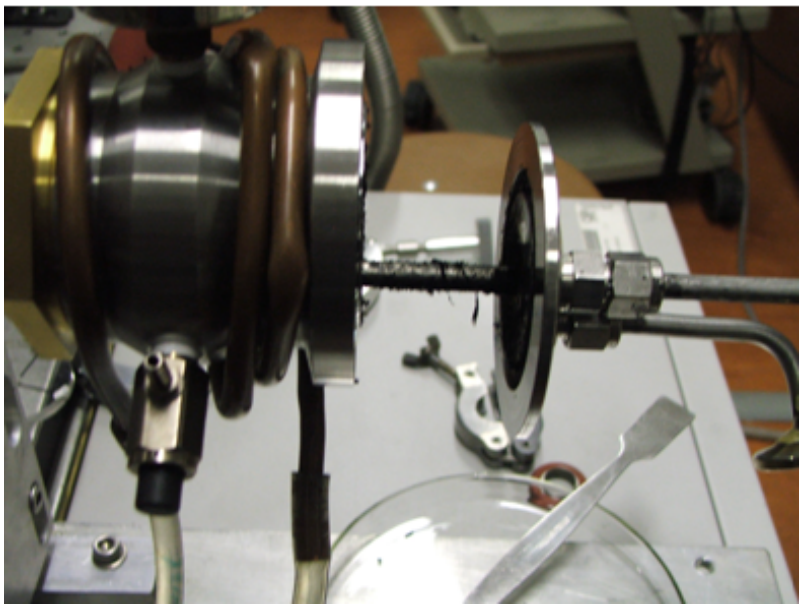


Figure 4.12: A removed vacuum flange exposing as-prepared SWCNT.

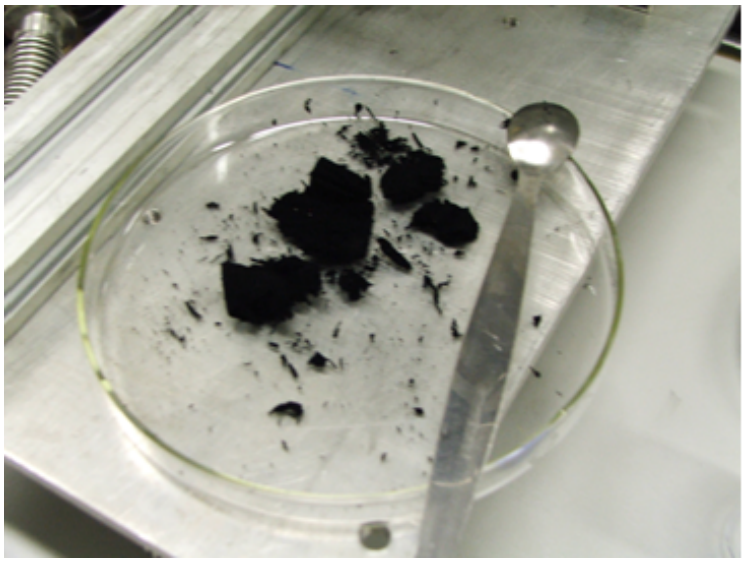


Figure 4.13: A typical sample of as-prepared material scrapped off the insides of the quartz tube and collected in a petri dish.

- The second two numbers were the first 2 digits of the furnace temperature used in the synthesis.
- The alphabet, P, implied the pressure followed by a number which was the first digit of the gas pressure selected in the synthesis.
- The alphabet, F, implied the gas flow and was followed by a number which was the first digit of the gas pressure selected in the synthesis.
- The last letter referred to the sample collected at the back-end of the quartz tube, A, and the sample collected from the inside of the inner flow tube, just in front of the target which was B. See Figure 4.7.

Tables 5.1-5.7 tabulate the quantities and conditions under which as-prepared materials were synthesized by dual laser ablation of targets listed in Table 4.3.

Target A		**Temperature**	**1073 K**		**1173 K**		**1273 K**		**1373 K**
			Mass		**Mass**		**Mass**		**Mass**
Pressure (Torr)	**Flow (SCCM)**	**Sample**	**(mg)**	**Sample**	**(mg)**	**Sample**	**(mg)**	**Sample**	**(mg)**
500	100	A10P5F1A	30	A11P5F1A	34.5	A12P5F1A	36.4	A13P5F1A	27.3
		A10P5F1B	10	A11P5F1A	20.7	A12P5F1B	47	A13P5F1B	30.3
	200	A10P5F2A	65.9	A11P5F2A	69.6	A12P5F2A	53.6	A13P5F2A	55
		A10P5F2B	12.6	A11P5F2B	25	A12P5F2B	44	A13P5F2B	28
	300	A10P5F3A	74.6	A11P5F3A	82.4	A12P5F3A	65.9	A13P5F3A	61.4
		A10P5F3B	17	A11P5F3B	18.7	A12P5F3B	27.3	A13P5F3B	14.1
400	100	A10P4F1A	33	A11P4F1A	28.3	A12P4F1A	37.1	A13P4F1A	36.6
		A10P4F1A	22	A11P4F1B	31.7	A12P4F1B	39.5	A13P4F1B	41.5
	200	A10P4F2A	65.6	A11P4F2A	55.2	A12P4F2A	63	A13P4F2A	50.5
		A10P4F2B	18.1	A11P4F2B	25	A12P4F2B	51	A13P4F2B	29.5
	300	A10P4F3A	74.1	A11P4F3A	74.1	A12P4F3A	59.1	A13P4F3A	53.6
		A10P4F3B	12.9	A11P4F3B	11.6	A12P4F3B	21	A13P4F3B	20.3
100	100	A10P5F1A	66.6	A11P5F1A	88.7	A12P5F1A	32.6	A13P5F1A	41.6
		A10P5F1B	37.8	A11P5F1B	29.7	A12P5F1B	70	A13P5F1B	51.1
	200	A10P5F2A	87.8	A11P5F2A	79.1	A12P5F2A	41	A13P5F2A	47.4
		A10P5F2B	25.4	A11P5F2B	51.3	A12P5F2B	41.2	A13P5F2B	53.1
	300	A10P5F3A	64	A11P5F3A	7	A12P5F3A	23	A13P5F3A	33.4
		A10P5F3B	17	A11P5F3B	3.6	A12P5F3B	17	A13P5F3B	12

Table 4.5: A summary of as-prepared material synthesized using Target A.

Target B		**Temperature**	**1073 K**		**1173 K**		**1273 K**		**1373 K**
			Mass		**Mass**		**Mass**		**Mass**
Pressure (Torr)	**Flow (SCCM)**	**Sample**	**(mg)**	**Sample**	**(mg)**	**Sample**	**(mg)**	**Sample**	**(mg)**
400	200	B10P4F2A	59	B11P4F2A	41.1	B12P4F2A	60	B13P4F2A	46
		B10P4F2B	19.5	B11P4F2B	61.5	B12P4F2B	28	B13P4F2B	28.3

Table 4.6: A summary of as-prepared material synthesized using Target B.

Target C		**Temperature**	**1073 K**		**1173 K**		**1273 K**		**1373 K**
			Mass		**Mass**		**Mass**		**Mass**
Pressure (Torr)	**Flow (SCCM)**	**Sample**	**(mg)**	**Sample**	**(mg)**	**Sample**	**(mg)**	**Sample**	**(mg)**
400	200	C10P4F2A	68.7						
500				C11P5F2A	38				

Table 4.7: A summary of as-prepared material synthesized using Target C.

Target D		**Temperature**	**1073 K**		**1173 K**		**1273 K**		**1373 K**
			Mass		**Mass**		**Mass**		**Mass**
Pressure (Torr)	**Flow (SCCM)**	**Sample**	**(mg)**	**Sample**	**(mg)**	**Sample**	**(mg)**	**Sample**	**(mg)**
400	200	D10P4F2A	72.6	D11P4F2A	64.7	D12P4F2A	48.5	D13P4F2A	67
		D10P4F2B	14.5	D11P4F2B	100	D12P4F2B	85	D13P4F2B	55

Table 4.8: A summary of as-prepared material synthesized using Target D.

Target E		**Temperature**	**1073 K**		**1173 K**		**1273 K**		**1373 K**
			Mass		**Mass**		**Mass**		**Mass**
Pressure (Torr)	**Flow (SCCM)**	**Sample**	**(mg)**	**Sample**	**(mg)**	**Sample**	**(mg)**	**Sample**	**(mg)**
400	200	E10P4F2A	56.1	E11P4F2A	43.4	E12P4F2A	55.8	E13P4F2A	74
		E10P4F2B	17	E11P4F2B	22	E12P4F2B	41.4	E13P4F2B	25.8

Table 4.9: A summary of as-prepared material synthesized using Target E.

Target F		**Temperature**	**1073 K**		**1173 K**		**1273 K**		**1373 K**
			Mass		**Mass**		**Mass**		**Mass**
Pressure (Torr)	**Flow (SCCM)**	**Sample**	**(mg)**	**Sample**	**(mg)**	**Sample**	**(mg)**	**Sample**	**(mg)**
400	200	F10P4F2A	55.7	F11P4F2A	44.9	F12P4F2A	51.0	F13P4F2A	54.6
		F10P4F2B	20.3	F11P4F2B	25.4	F12P4F2B	25.5	F13P4F2B	39.0

Table 4.10: A summary of as-prepared material synthesized using Target F.

Target G		**Temperature**	**1073 K**		**1173 K**		**1273 K**		**1373 K**
			Mass		**Mass**		**Mass**		**Mass**
Pressure (Torr)	**Flow (SCCM)**	**Sample**	**(mg)**	**Sample**	**(mg)**	**Sample**	**(mg)**	**Sample**	**(mg)**
400	200	G10P4F2A	56.3	G11P4F2A	46.0	G12P4F2A	55.1	G13P4F2A	50.5
		G10P4F2B	18.0	G11P4F2B	26.2	G12P4F2B	24.9	G13P4F2B	23.6

Table 4.11: A summary of as-prepared material synthesized using Target G.

4.8 Characterization Instrumentation and sample preparation

4.8.1 Raman Spectroscopy

As-prepared materials synthesized by the laser exhibited different textures. These varied from powder like appearances to a rubbery and fibre like texture. For an accurate assessment and comparison of the Raman features and hence, to deduce the physical nature of the as-prepared material, it was necessary to prepare all samples for analysis in exactly the same way i.e. to create a standard. During the period of this study, progress were being made by the international community in defining and adopting a standard. The method discussed here is nevertheless consistent with methods utilized by other research groups [134].

Since a micro-Raman spectroscope was used, the material for analysis had to be placed on a standard microscope glass slide. Due to the varying texture and the need for multiple spot analysis, it was found be best to prepare a thin film of the as-prepared material on the microscope slide. To do this, 5 mg of the as-prepared material was sonicated for 2 minutes in 5 ml of laboratory grade ethanol using a Heilscher UP400S horn sonicator which was operated at 100 W electrical power. A few drops of this solution was placed on a glass slide and allowed to dry to produce a thin film about 20 mm in diameter.

The instrument utilized for micro-Raman spectroscopy was a Jobin Yvon HR 800 VIS-NIR-IR Raman spectrometer equipped with an Olympus BX41 microscope. The system was equipped with two detectors; a CCD detector for use with lasers excitations in the UV-VIS-NIR range and a liquid nitrogen cooled InGaAs detector which was designed for use with IR lasers. Five laser lines from 3 lasers were available for Raman analysis. An Ar-Krypton ion laser generated tunable lasers emissions and was optimized to deliver 488 nm (blue), 514.5 nm (green) and 647 nm (red) laser lines. The second laser was a laser-diode device which produced 785 nm laser emission and the third was a diode pumped solid state laser emitting at 1064 nm. All three lasers were purposely built for Raman spectroscopic analysis i.e. they possessed narrow line-width emissions. For general Raman analysis, all samples were subjected to 514.5 nm (green) excitation lasers. When the chiral distributions of SWCNTs were investigated, specific samples were subjected to 5 laser excitations since different nanotube diameters are brought into resonance by different laser excitations [37]. The laser power at the sample for each of the lasers was adjusted to about 1.5 mW. However, the 1064 nm laser required about 15 mW

Raman excitation laser wavelength, $\lambda(nm)$	**Raman excitation laser photon energy,** $E(eV)$
1064	1.165
785	1.579
647	1.916
514.5	2.41
488	2.541

Table 4.12: A summary of Raman excitation wavelengths and their corresponding phonton energies.

power for carbon nanotube analysis. The laser spot sizes on the sample was about 150 μm in diameter. In Table 4.12, Raman laser wavelengths in nm and their corresponding laser photon energy in eV are shown.

4.8.2 Photoluminescence spectroscopy

Photoluminescence spectroscopy (PL) was used to investigate the population and chiralities of semi-conducting single-wall carbon nanotubes. The principles of PL were discussed in Chapter 3. Due to the nature of the as-prepared materials, the nanotubes aggregate during synthesis and also nucleate as bundles on metallic catalysts. Furthermore, there are a lot impurities such as residual catalysts and other forms of carbonaceous material which suppress PL. For PL it was absolutely necessary to have the tubes as individual strands in suspension so as enhance the PL emissions. SWCNTs once separated into individual single tubes in solution, tend to aggregate again. To prevent this, a surfactant such as sodium cholate (NaC) was used. NaC wraps around the nanotubes and keeps them apart. To prepare a suspension of SWCNTs, about 10 mg of as-prepared material was heavy sonicated with a Heilscher UP400S sonicator at 400 W electrical power in 15 ml of 2% solution of sodium cholate and D_2O (heavy water) for 20 minutes. To prevent excessive heating and damage to the nanotubes during sonication, the vessel was placed in a water chiller which was operated at 12^0C. D_2O was used instead of common H_2O since H_2O absorbs PL emissions from the SWCNTs when PL emissions are longer that 1350 nm [52].

To remove bundled SWCNTs and other impurities, the sonicated solution was ultracentrifuged at 286 000g for 4 hours. Thereafter, the upper 2/3rds of the supernatant was carefully decanted and the remaining liquid and residue was discarded. The supernatant appeared light grey in colour and it was this fluid which was used for PL measurements.

The instrument that was used for PL experiments was a Horib Jobin Yvon

Nanolog PL instrument Parameters	**Condition**
Light source	450 W Xe source
excitation wavelength scan range, λ_{ex}	500-900 nm
excitation wavelength scan step, $\Delta\lambda_{ex}$	3 nm
emission wavelength center, λ_{emc}	1200 nm
emission wavelength range, $\Delta\lambda_{em}$	900-1550 nm
detector	InGaAs array, LN cooled
detector integration time/$\Delta\lambda_{ex}$	15 s
HR 320 Spectrograph slit width	14 nm

Table 4.13: A summary of the Nanolog experimental parameters under which PL measurements were made.

NanoLog 3-22-TRIAX which was equipped with a double-grating excitation monochromator plus an imaging spectrograph. Detector was a liquid nitrogen cooled InGaAs array for recording emission from the 850 nm- 1600 nm. The parameters that were used in the PL measurements are shown Table 4.13. A typical PL analysis lasted approximately 45 minutes.

4.8.3 SEM and TEM sample preparation

For scanning electron microscopy (SEM) analysis, a small piece of the as-prepared material was put on carbon tape stuck onto a brass stub. A JEOL F7500 FEG SEM and a LEO 1550 SEM were used for SEM analysis. Typical working distances and operating accelerating voltages for both instruments were very similar i.e. working distances of between 5-6 mm and accelerating voltages between 5-6 kV respectively.

For transmission electron microscopy (TEM), 3 mg of as-prepared material was sonicated in 5 ml in laboratory grade ethanol using the Heilscher UP400S horn sonicator for about a minute. Three drops of this solution was further diluted in 10 ml ethanol. This solution was sonicated again at 400 W power for 2 minutes. A single drop of this solution was put onto a TEM grid followed by drying in air [71]. For TEM measurements, a Phillips CM 200 and JEOL 2100 LaB_6 operated 100 kV was used.

Chapter 5

Laser synthesis of single-walled carbon nanotubes: Raman, photoluminescence and electron microscopy

5.1 Raman spectroscopic analysis of SWCNTs

5.1.1 Generalized Raman analysis of as-prepared SWCNTs

Raman Spectroscopy (RS) is presently the de facto standard in the characterization of SWCNTs. Due to its ease of use, simple sample preparation and the speed of which samples could be evaluated, RS is routinely used to evaluate the effect of process variables when synthesizing SWCNTs. In this RS study, a standard procedure was adopted to initially evaluate all as-prepared materials using the Raman laser excitation wavelength of 514.5 nm (green). At this excitation wavelength, both semi-conducting (s-SWCNTs) and metallic (m-SWCNTs) nanotubes can be brought into resonance or near resonance [115, 141]. Therefore, the use of 514.5 nm excitation can from first analysis determine what effect the variation of process parameters have on the synthesis of different types of SWCNTs. A critical requirement in this study, was the synthesis of SWCNTs of high quality and to evaluate how process parameters can affect the quality and chirality.

To determine the quality of SWCNTs, the ratio of the Raman intensities of the D and D* bands or I_D/I_{D^*}, extracted directly from the Raman plots was evaluated [142]. The D peak appears at around 1250-1350 cm^{-1} while the

D^* peak appears at 2600-2700 cm^{-1}. The lower this ratio, the lower the concentration of defects attributed to disordered carbon atoms within the walls. Contributions from hemisphere's of shortened nanotubes and physical attachments to the side walls also negatively affect this ratio. For longer nanotubes, these contributions from hemispherical ends decrease [37]. Defect concentration are also commonly represented by the ratio of the D and G bands of the Raman spectra or I_D/I_G [143] and hence results for this evaluation are also presented.

5.1.1.1 Target A (98%C:1%Ni:1%Co)

Figure 5.1 shows a plot of the mass of the as-prepared material collected for the different process conditions. Material was collected at two zones, the back-end(A) (highlighted yellow in Fig 4.7) and from the centre (B) (highlighted green in Fig. 4.7) of the quartz tube. After the system had cooled to room temperature, the material was scrapped off from the both zones (A and B). It was observed that at low pressure and low flow rates, more material was collected at B, while at higher pressure and higher flow rates, more material was collected at A. There were significant differences in the nature of the material collected at A and B. The material collected at zone A had a"spongy" texture and came off as a film while the material at zone B was more "powder like" i.e. fine loose particles.

The Raman spectra of material collected at A and B were also very different. Figure 5.2 shows Raman spectra of material collected at A (A12P5F2A) and B (A12P4F2B). Applying the ratio's of the Raman intensities I_D/I_{D^*} and I_D/I_G to both of these samples showed that the defect concentrations of the sample at B was twice that of at A. Furthermore, the length of the nanotubes which are proportional to the intensity of the G peak [144] show that the tubes at A were about 10 times longer. Hence, the Raman measurements were consistent with their physical appearance. As a result of this, and given the objective to synthesize and characterize defect free SWCNTs material useful for technological applications, material collected from region B was set aside for future investigations.

Figures 5.3-6 show Raman spectra of materials synthesized from Target A under conditions outlined in Table 4.1 covering the spectral region 100-3500 cm^{-1}. A summary of the defect ratio for material synthesized from Target A is shown in Table 5.1. From a visual inspection of the Raman spectra taken as a function of temperature, it was clear that the intensity of the signature peaks of SWCNTs i.e. RBM bands and G^+, increased with temperature and that there was a corresponding decrease in the defect ratio's. This means that

the nucleation and growth of SWCNT was thermally driven and promoted at higher furnace temperatures.

At any set temperature, the I_D/I_{D^*} or I_D/I_G ratio were observed to vary with argon gas flow and pressure. However, the flow rate appeared to be the more critical process parameter. At a lower flow rate of 100 sccm, appeared to almost always produce SWCNTs with the lowest defect concentration where the quality worsened with increasing flow rate. However, at 1073 K, this was not observed. No consistent behavior in I_D/I_{D^*} or I_D/I_G could be deduced. One can speculate that at this temperature, which is the borderline temperature in SWCNT synthesis, the nucleation and growth maybe chaotic.

It appeared that the best sample in terms of quality ($I_D/I_{D^*} = 0.25$, $I_D/I_G = 0.04$) and quantity (41.6 mg) was A13P5F2A. However, at the low flow rates, an equal amount of material was found deposited in zone B. At lower pressure and flow rates, the plasma plume of the ablated material was able to extend further into the inner quartz tube where the material was deposited.

While it has been shown that the higher temperature at 1373 K produced better quality nanotubes, operating the system at 1373 K continuously, had a negative effect on durability of individual components such at the quartz tubes and the mechanical fittings at the ends of the quartz tube when the system was operated for more than 1 hour. Therefore, a compromise, was made in operating the system at 1273 K which enabled longer production runs.

To investigate the effect of changing the target composition on the type of as-prepared material, the system was subsequently operated at a fixed pressure and flow rate. A pressure of 400 Torr and flow rate of 200 sccm was thus chosen for the study which were the conditions that good quality and yield of SWCNTs was obtained.

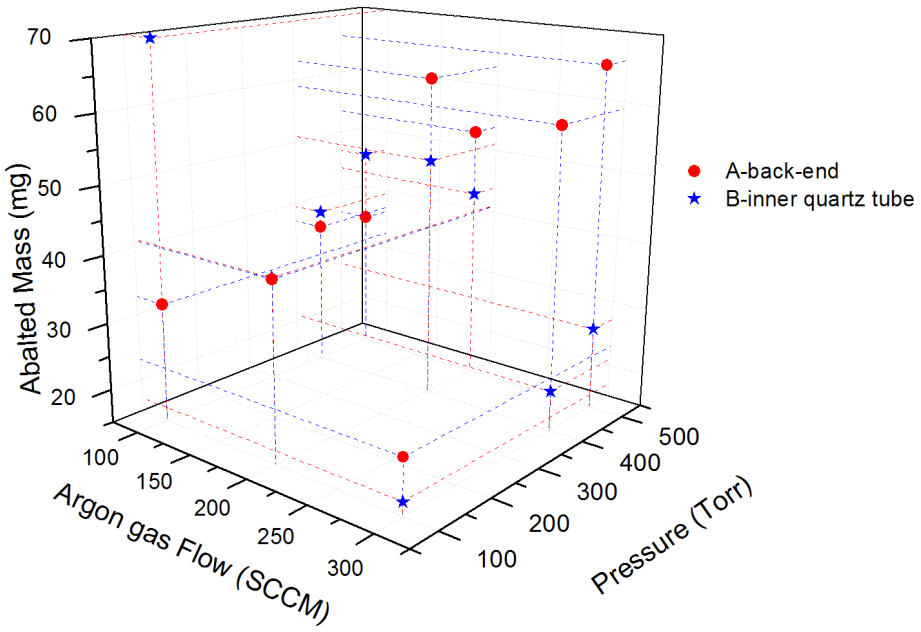


Figure 5.1: The mass of material collected after the ablation of Target A in the laser synthesis method of synthesizing SWCNTs at a furnace temperature of 1273 K.

Target A		**Temp**	**1073 K**			**1173 K**			**1273 K**			**1373 K**	
Pressure	**Flow**		$\frac{I_D}{I_{D*}}$	$\frac{I_D}{I_G}$		$\frac{I_D}{I_{D*}}$	$\frac{I_D}{I_G}$		$\frac{I_D}{I_{D*}}$	$\frac{I_D}{I_G}$		$\frac{I_D}{I_{D*}}$	$\frac{I_D}{I_G}$
Torr	**SCCM**	**Sample**			**Sample**			**Sample**			**Sample**		
500	100	A10P5F1A	1.68	0.82	A11P5F1A	0.51	0.12	A12P5F1A	0.30	0.07	A13P5F1A	0.25	0.02
	200	A10P5F2A	0.85	0.63	A11P5F2A	0.95	0.29	A12P5F2A	0.60	0.17	A13P5F2A	0.85	0.26
	300	A10P5F3A	2.83	0.64	A11P5F3A	0.78	0.27	A12P5F3A	0.78	0.31	A13P5F3A	0.93	0.45
400	100	A10P4F1A	1.85	0.59	A11P4F1A	0.70	0.25	A12P4F1A	0.33	0.06	A13P4F1A	0.29	0.03
	200	A10P4F2A	1.41	0.45	A11P4F2A	0.47	0.10	A12P4F2A	0.74	0.27	A13P4F2A	0.78	0.23
	300	A10P4F3A	1.11	0.39	A11P4F3A	0.70	0.30	A12P4F3A	0.80	0.33	A13P4F3A	0.87	0.33
100	100	A10P1F1A	0.89	0.42	A11P1F1A	0.4	0.08	A12P1F1A	0.34	0.04	A13P1F1A	0.25	0.04
	200	A10P1F2A	0.96	0.17	A11P1F2A	0.72	0.27	A12P1F2A	0.86	0.30	A13P1F2A	0.79	0.27
	300	A10P1F3A	1.15	0.47	A11P1F3A	0.70	0.35	A12P1F3A	0.82	0.33	A13P1F3A	0.93	0.51

Table 5.1: Defect evaluation of as-prepared samples synthesized at different process conditions from Target A.

5.1.1.2 Target B (98% C:1% Ni:1% Fe)

Target B consisted of 98% C, 1% Ni and 1% Fe. Figure 5.7 shows Raman spectra of as-prepared materials obtained by using Target B in the synthesis process. Results for the defect ratios are shown in Table 5.2. As was observed with as-prepared material obtained using Target A, the defect concentration decreased with temperature. However, a distinct difference between the values of the defect ratio's for Target A and B were observed. It appears that at the same flow rate and pressure of argon gas, the replacement of Co by Fe, reduced the defect concentration of as-prepared material dramatically. As an example, at 1073 K, the use of Target A synthesized material with defects ratio's as high as 0.45 but at the same pressure and low rate, the use of Target B showed a defect ratio of 0.14 (I_D/I_G). Lower values were also measured at 1173 K, 1273 and 1373 K. An explanation for this observation will be provided later.

5.1.1.3 Target D (97.5% C:1% Ni:1% Co: 0.5% Fe)

Target D consisted of 97.5% C, 1% Ni, 1%Co and 0.5% Fe. Figure 5.8 shows Raman spectra of as-prepared materials. Results for the defect ratios are shown in Table 5.3. As was observed with as-prepared material obtained from using Targets A and B, the defect concentration decreased with increasing furnace temperature. It appeared that at the same flow rate and pressure of argon gas, the defect ratio's of Target A, B and D all differ. The results obtained from Target D were better than that from Target A but worse than that for Target B.

5.1.1.4 Target E (97% C:1% Ni:1% Co:1% Fe)

Target E consisted of 97% C, 1% Ni, 1% Co and 1% Fe. Figure 5.9 shows Raman spectra of as-prepared materials. Results for the defect ratios are shown in Table 5.4. The defect concentration decreased with temperature. At a temperature of 1073 K, the defects ratio's are smaller than that of material obtained by using Target D, but as the temperature increased, the defect values were greater than those from Target D. In fact at higher temperature, there was a relative increase in defect concentration in comparison with material obtained from using Targets B and D.

5.1.1.5 Target F (96.5% C:1% Ni:1% Co:1.5% Fe)

Target F consisted of 96.5% C, 1% Ni, 1% Co and 1.5% Fe. Figure 5.10 shows Raman spectra of as-prepared materials. Results for the defect ratios are

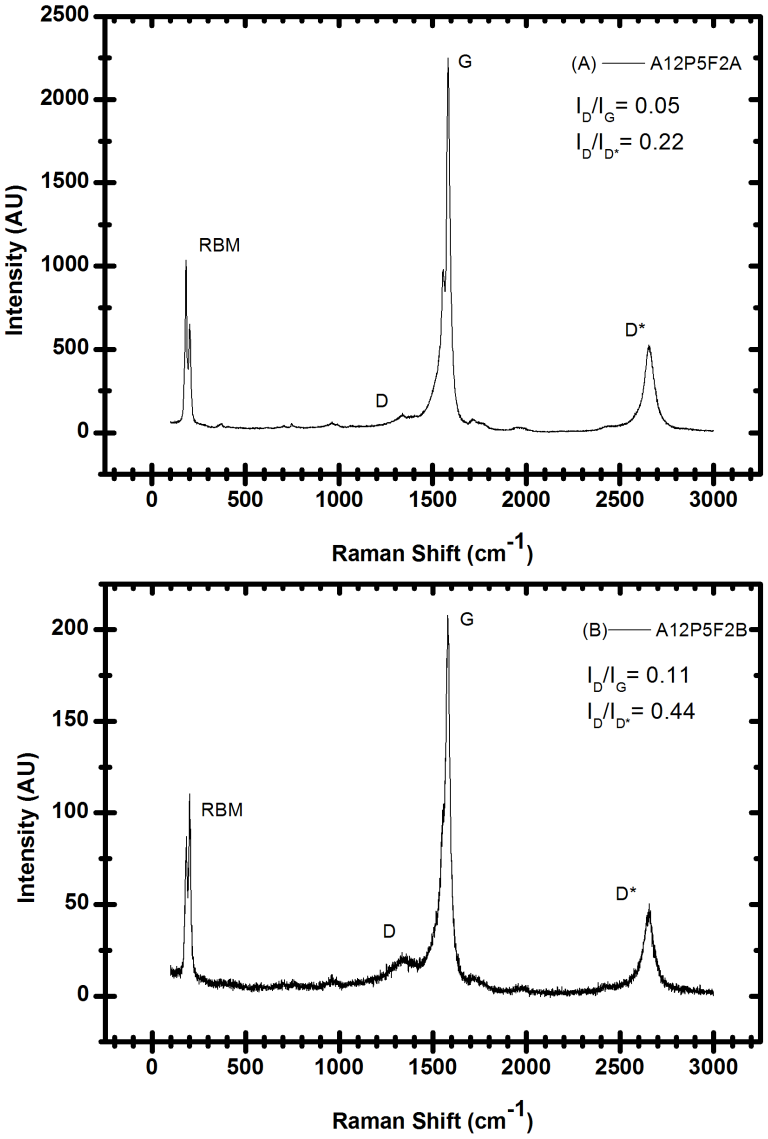


Figure 5.2: Raman spectra of samples collected at the back-end (A12P5F2A) and centre (A12P5F2B) of the furnace. The I_D/I_{D^*} and I_D/I_G ratio's of 0.22 and 0.05 for material from A versus 0.44 and 0.11 for material collected from B were observed. Clearly, the material collected at A was superior in quality to material collected at B.

shown in Table 5.5. As was observed with as-prepared material obtained from other targets; the Fe concentration was increased in the target composition, the defect concentration at 1073 K and 1173 K was lowered relative to targets with smaller Fe concentrations. However, at 1273 K and 1373 K, the defect concentration was seen to increase and appeared to reach defect concentrations similar to those obtained at lower temperatures.

5.1.1.6 Target G (96% C:1% Ni:1% Co:2% Fe)

Target G consisted of 96% C, 1% Ni, 1% Co and 2% Fe. Figure 5.11 shows Raman spectra of as-prepared materials. Results for the defect ratios are shown in Table 5.6. It was observed that with increasing Fe concentration, the defect concentration was lowered yet the defect concentration at high temperature increased. It appeared that the level of defect concentration remained constant throughout the temperature range.

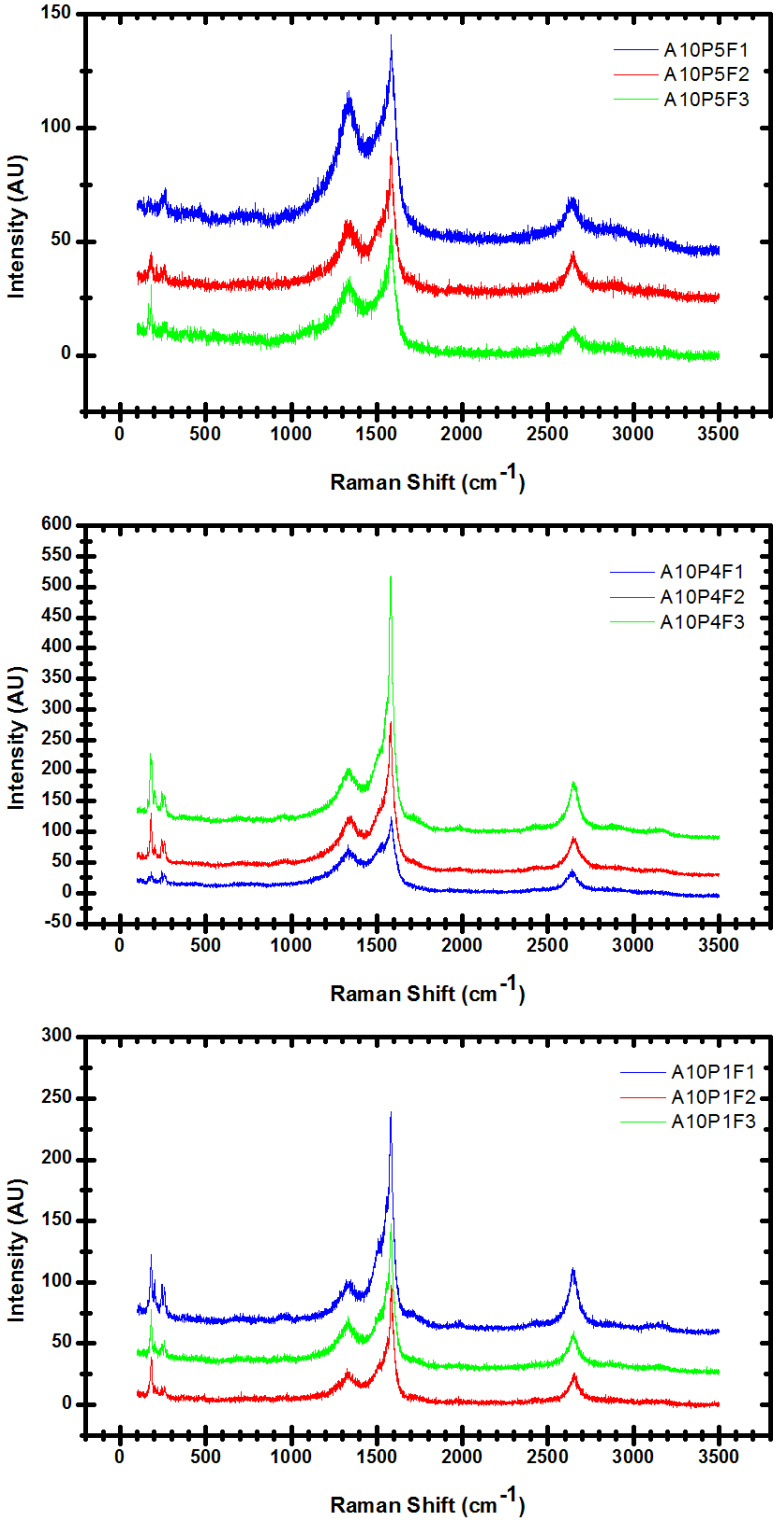


Figure 5.3: Raman spectra of as-prepared material synthesized by ablating Target A at a fixed furnace temperature of 1073 K.

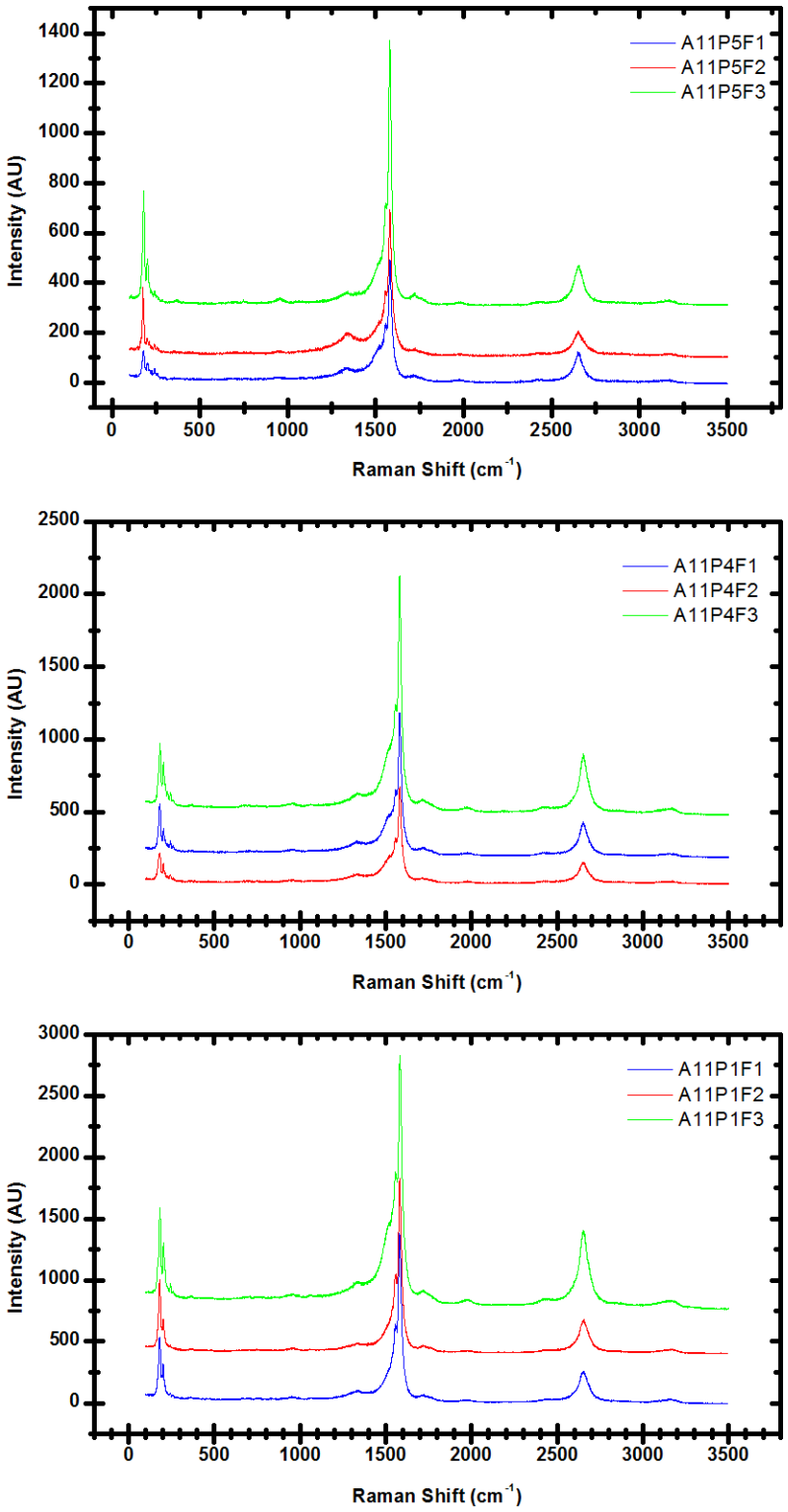


Figure 5.4: Raman spectra of as-prepared material synthesized by ablating Target A at a fixed furnace temperature of 1173 K.

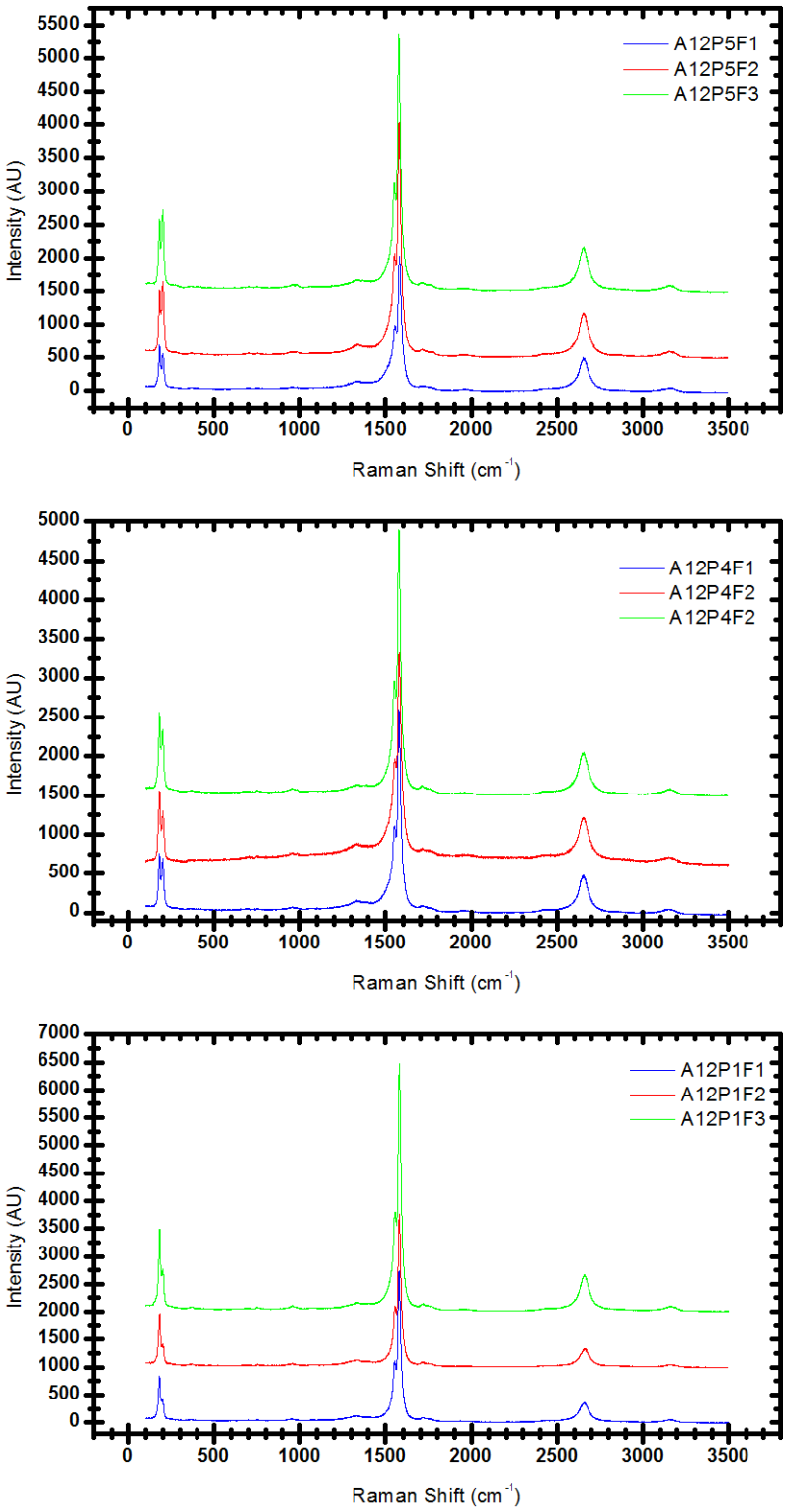


Figure 5.5: Raman spectra of as-prepared material synthesized by ablating Target A at a fixed furnace temperature of 1273 K.

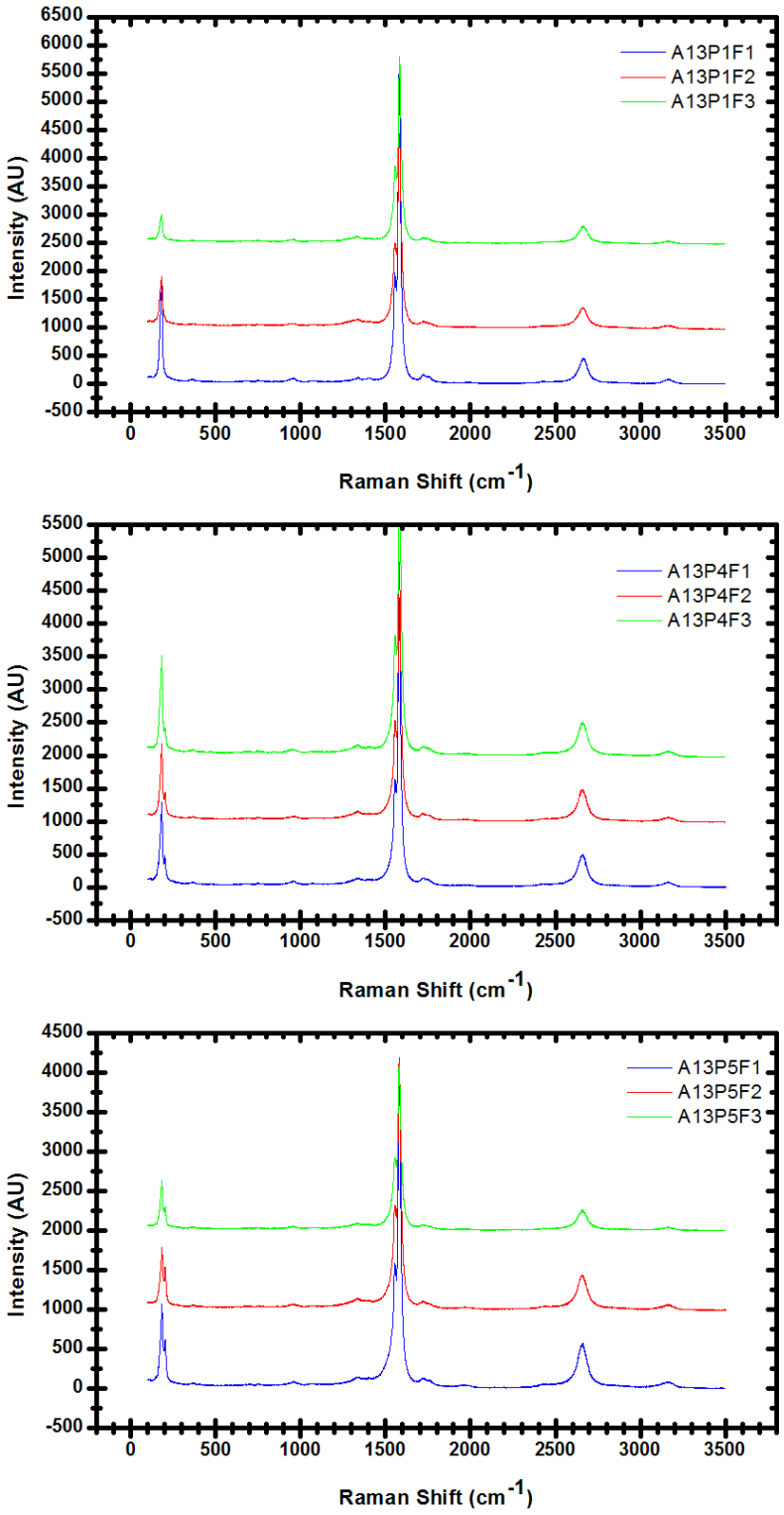


Figure 5.6: Raman spectra of as-prepared material synthesized by ablating Target A at a fixed furnace temperature of 1373 K.

Target B		**Temp**	**1073 K**			**1173 K**			**1273 K**			**1373 K**	
Pressure	**Flow**		$\frac{I_D}{I_{D*}}$	$\frac{I_D}{I_G}$		$\frac{I_D}{I_{D*}}$	$\frac{I_D}{I_G}$		$\frac{I_D}{I_{D*}}$	$\frac{I_D}{I_G}$		$\frac{I_D}{I_{D*}}$	$\frac{I_D}{I_G}$
Torr	**SCCM**	**Sample**			**Sample**			**Sample**			**Sample**		
400	200	B10P4F2A	0.68	0.14	B11P4F2A	0.24	0.04	B12P4F2A	0.19	0.03	B13P4F2A	0.24	0.02

Table 5.2: Defect evaluation of as-prepared samples synthesized at different process conditions from Target B.

Target D		**Temp**	**1073 K**			**1173 K**			**1273 K**			**1373 K**	
Pressure	**Flow**		$\frac{I_D}{I_{D*}}$	$\frac{I_D}{I_G}$		$\frac{I_D}{I_{D*}}$	$\frac{I_D}{I_G}$		$\frac{I_D}{I_{D*}}$	$\frac{I_D}{I_G}$		$\frac{I_D}{I_{D*}}$	$\frac{I_D}{I_G}$
Torr	**SCCM**	**Sample**			**Sample**			**Sample**			**Sample**		
400	200	D10P4F2A	1.72	0.45	————	-	-	D12P4F2A	0.29	0.04	D13P4F2A	0.25	0.03

Table 5.3: Defect evaluation of as-prepared samples synthesized at different process conditions from Target D.

Target E		**Temp**	**1073 K**			**1173 K**			**1273 K**			**1373 K**	
Pressure	**Flow**		$\frac{I_D}{I_{D*}}$	$\frac{I_D}{I_G}$		$\frac{I_D}{I_{D*}}$	$\frac{I_D}{I_G}$		$\frac{I_D}{I_{D*}}$	$\frac{I_D}{I_G}$		$\frac{I_D}{I_{D*}}$	$\frac{I_D}{I_G}$
Torr	**SCCM**	**Sample**			**Sample**			**Sample**			**Sample**		
400	200	E10P4F2A	1.43	0.31	E11P4F2A	0.62	0.06	E12P4F2A	0.60	0.05	E13P4F2A	0.47	0.05

Table 5.4: Defect evaluation of as-prepared samples synthesized at different process conditions from Target E.

Target F		**Temp**	**1073 K**			**1173 K**			**1273 K**			**1373 K**	
Pressure	**Flow**		$\frac{I_D}{I_{D*}}$	$\frac{I_D}{I_G}$		$\frac{I_D}{I_{D*}}$	$\frac{I_D}{I_G}$		$\frac{I_D}{I_{D*}}$	$\frac{I_D}{I_G}$		$\frac{I_D}{I_{D*}}$	$\frac{I_D}{I_G}$
Torr	**SCCM**	**Sample**			**Sample**			**Sample**			**Sample**		
400	200	F10P4F2A	1.09	0.17	F11P4F2A	0.5	0.06	F12P4F2A	0.49	0.06	F13P4F2A	0.76	0.08

Table 5.5: Defect evaluation of as-prepared samples synthesized at different process conditions from Target F.

Target G		**Temp**	**1073 K**			**1173 K**			**1273 K**			**1373 K**	
Pressure	**Flow**		$\frac{I_D}{I_{D*}}$	$\frac{I_D}{I_G}$		$\frac{I_D}{I_{D*}}$	$\frac{I_D}{I_G}$		$\frac{I_D}{I_{D*}}$	$\frac{I_D}{I_G}$		$\frac{I_D}{I_{D*}}$	$\frac{I_D}{I_G}$
Torr	**SCCM**	**Sample**			**Sample**			**Sample**			**Sample**		
400	200	G10P4F2A	0.91	0.10	G11P4F2A	1.27	0.23	G12P4F2A	0.83	0.10	G13P4F2A	0.88	0.09

Table 5.6: Defect evaluation of as-prepared samples synthesized at different process conditions from Target G.

Target Label	Temperature / Target Composition	1073 K	1173 K	1273 K	1373 K
A	1%Ni:1%Co	A10P4F2	A11P4F2	A12P4F2	A13P4F2
D	1%Ni:1%Co:0.5%Fe			D12P4F2	D13P4F2
E	1%Ni:1%Co:1%Fe			E12P4F2	F13P4F2
F	1%Ni:1%Co:1.5%Fe			F12P4F2	F13P4F2
G	1%Ni:1%Co:2%Fe			F12P4F2	F13P4F2

Table 5.7: The set of samples which had been subjected to detailed evaluation to determine the effect variation of process parameters on the types of SWCNTs that were synthesized.

5.1.2 Detailed analysis of various Raman modes of as-prepared samples

Detailed analysis of the most important Raman spectral features of as-prepared materials were shown in Figure 3.3. In particular, the effect of changing the catalyst composition of targets on the diameters of as-prepared SWCNTs were investigated. Furthermore, the influence of furnace temperature on the change in the diameters of the as-prepared material are also reported. Due to the large number of process variables that can influence the results, the argon gas pressure and flow rate was fixed to 400 Torr and 200 sccm respectively. In Table 5.7, the as-prepared samples that were subjected to detailed Raman analysis are shown.

5.1.3 Analysis of Radial Breath Modes (RBM)

The radial breathing mode of SWCNTs lies between 100-400 cm^{-1}. The peaks in this region was deconvoluted by fitting Lorentzian line-shapes, where each line-shape was attributed to radially directed vibrations of a single walled carbon nanotube. The full-width-half-maximum (FWHM) of the Lorentzian line-shape fit typically lies between 3 and 10 cm^{-1} [71, 145]. Here, a value of 4 cm^{-1} was used to fit the spectra. The number of Lorentzian lines fitted to the raw spectra was increased until a chi-square value of 0.99 was attained. From the frequency of these vibrations, the diameter of the nanotube was determined using the established relation [81]:

$$\varpi_{RBM} = \frac{227}{d_t}\sqrt{1 + C_e \cdot d_t^2} \tag{5.1}$$

where ϖ_{RBM} is the Raman RBM frequency in cm^{-1}, d_t is the nanotube diameter in nm. $C_e = 0.056$ is a constant attributed to van der Waals interactions with other nanotubes.

It must be stressed that in this dissertation, the above relation was used as an approximation to determine the nanotube diameters. The above relation was originally derived for nanotubes grown by the "super growth" method but it has proved to be a good approximation for most methods of SWCNT synthesis [146].

To summarize: Lorentzian curves were fitted to all the spectra. Each peak corresponds to a nanotube of a particular diameter. Even though accurate determination of the nanotubes (n, m) assignment could not be made, possible chiral assignments were largely guided by several publications [147, 37, 148, 85]. It was found that Raman peak position in this study were within ± 1 cm^{-1} of the reported RBM positions.

5.1.3.1 RBM analysis of Target A

Figures 5.12-5.15 show Raman spectra of samples obtained by using Target A in the laser-furnace method of synthesizing SWCNTs. It can be noted that the intensity of the RBM bands increase with temperature for the same target and this indicates that the formation of SWCNTs was favoured at higher temperatures. Each of the samples were subjected to five laser excitations, namely, (a) 488 nm, (b) 514.5 nm, (c) 647 nm, (d) 785 nm and (e) 1064 nm to bring into resonance the various nanotubes in the ensemble.

In Figure 5.12(a)-(e), the dominant tube(s) detected in each of the spectra are seen to vary with different laser excitations. At higher synthesis temperatures, as shown in Figures 5.13-15, where the synthesis temperature increased from samples A11P4F2 > A12P4F2 > A13P4F2, the tubes which dominated at the lower temperature were also seen to dominate the Raman spectra in terms of peak intensities of the individual peaks. However, at higher synthesis temperatures, more Lorentzian's curves were required to provide a good fit to the raw spectra. This means that at higher synthesis temperatures there was an increase in the probability of the nucleation of nanotubes with small variations in the nanotubes diameters (because there was no significant broadening in the spectral range) to the ones which were dominant at lower temperatures.

Even though five laser excitations were employed, the photon energy from these lasers do not exactly match an electronic bandgap of a SWCNT. Therefore, to demonstrate how nanotubes are brought "into and out of" resonance, i.e. to find the optimum laser excitation energy which exactly matches a real transition in the electronic structure of the nanotube, a tunable laser would be needed [78]. From the observed spectra, the intensities of the fitted peaks appeared to change with laser excitation. Another important observation was that as the synthesis temperature was increased, the "spread" of the RBM

spectral band decreased i.e. the range of the nanotube diameters was found to decrease.

SWCNTs which were detected from samples obtained using Target A are summarized in Table 5.8. The peak positions in cm^{-1} were extracted from Figures 5.12-5.15. The (n,m) assignments of the peaks also appear as labels on the graphs, adjacent to the peaks. The table of results also indicates whether the nanotube was either metallic or semiconducting. The diameter of the SWCNT, calculated from eqn. 5.1 is also shown. Nanotubes which are highlighted in bold text were found to be dominant in the spectra. Some peaks could not be identified and hence could not be assigned.

5.1.3.2 RBM analysis of as-prepared material using Target D

Figures 5.16-5.17 show Raman spectra of samples obtained by using Target D in the laser-furnace method of synthesizing SWCNTs. Results for material synthesized at 1273 K and 1373 K are presented. An effect of the addition of 0.5% Fe in the RBM bands was observed. When compared to the RBM spectra of A12P4F2, the spectra of D12P4F2 showed the following differences:

- lower RBM intensities for all Raman excitation wavelengths were observed.
- a broadening of the RBM bands was observed
- a distinct shift of the Raman spectrum to lower wavenumbers was observed i.e., nanotubes with larger diameters appeared to have been favoured by the addition of 0.5% Fe
- Fitted peaks point to be more m-SWCNT in nature (Table 5.8)

A similar observation was made when comparing Figures 5.15 and 5.17. Lorentzian fits with lower wavenumbers showed an increase in intensity.

5.1.3.3 RBM analysis of as-prepared material using Target E

Figures 5.18-5.19 show Raman spectra of samples obtained by using Target E in the laser-furnace method of synthesizing SWCNTs. Results for material synthesized at 1273 K and 1373 K are presented. The same RBM changes noted for D12P4F2 and D13P4F2 were also observed for E12P4F2 and E13P4F2. However, the RBM intensities showed a larger drop using 1% Fe rather than 0.5% Fe. This meant that increasing the concentration of Fe had a negative effect on the ability to nucleate SWCNTs.

Detected nanotubes Target A $\varpi_{RBM}(cm^{-1})$	**assignment (n,m)**	**semiconducting (S) or metallic (M)**	d_t(Å)
145	?	?	16.85
150	?	?	16.21
155	?	?	15.61
162	?	?	14.85
170	?	?	14.07
175	**(14,5)**	**M**	**13.63**
179	**(15,3)**	**M**	**14.91**
182	**(16,1)**	**M**	**13.05**
190	**(12,6)**	**M**	**12.46**
195	**(13,4)**	**M**	**12.11**
199	**(12,5)**	**S**	**11.85**
202	**(15,0)**	**M**	**11.66**
204	(9,8)	S	11.53
205	(14,1)	S	11.47
215	(11,5)	M	10.90
216	(9,7)	S	10.85
222	(11,4)	S	10.54
225	(10,5)	S	10.39
230	(8,7)	S	10.15
231	**(11,3)**	**S**	**10.10**
246	(8,6)	S	9.46
252	(7,7)	M	9.22
259	(9,4)	S	8.96
262	**(8,5)**	**M**	**8.85**
264	(7,6)	S	8.78
273	(9,3)	M	8.48
280	(8,4)	S	8.26
289	(10,0)	S	7.99

Table 5.8: A summary of the SWCNTs detected in all material samples synthesized from Target A. Possible (n,m) assignment are shown for individual SWCNTs represented by Lorentzian line-shape fits. Peaks which appear in bold are those which were dominant in the RBM spectra. Some peaks could not be identified.

5.1.3.4 RBM analysis of as-prepared material using Target F

Figures 5.20-5.21 show Raman spectra of samples obtained by using Target F in the laser-furnace method of synthesizing SWCNTs. Results for material synthesized at 1273 K and 1373 K are presented. The same RBM changes noted for Target D and Target E (F12P4F2 and F13P4F2) were also observed for this target. However, the RBM intensities were seen to show an even larger drop in intensity on increasing the Fe content in the targets. For a higher synthesis temperature, the RBM intensity was found to be lower which was unexpected. See Table 5.5.

5.1.3.5 RBM analysis of as-prepared material using Target G

Figures 5.22-5.23 shows Raman spectra of samples obtained by using Target G in the laser-furnace method of synthesizing SWCNTs. Results for material synthesized at 1273 K and 1373 K are presented. The same RBM changes noted for Target D, Target E and Target F were observed in G12P4F2 and G13P4F2. A decrease in RBM intensities with temperature was also observed when comparing samples G12P4F2 and G13P4F2. In fact, 2% Fe addition to a target containing 1% Ni and 1% Co was extremely detrimental to SWCNT synthesis. In comparisons to RBM intensities of samples A12P4F2, RBM intensities of G12P4F2 were an order of magnitude smaller.

5.1.4 Analysis of D and G bands

The nature of the D and G band was discussed in sections 3.24 and 3.23 respectively. Briefly, the D band is associated with disorder while the G band is split into the G^- and G^+ components. The G band is associated with phonon emission due to stretching of the C-C network of a nanotube, parallel to the nanotubes axis [37]. The fitting of Lorentzian's curves to the D and G bands for individual and isolated SWCNT was not possible since all samples were as-prepared and contained bundles and ensembles of nanotubes. Instead, only the peak positions of the D, G^- and G^+ bands was monitored. The evaluation of the I_D /I_G ratio which corresponds to the defect concentration in the SWCNT was reported in section 5.1.1. As in section 5.1.3, evaluated samples are listed in Table 5.7. Figure 5.24 shows the D and G bands subjected to five Raman laser excitations (a) 488 nm, (b) 514.5 nm, (c) 647 nm, (d) 785 nm and (e) 1064 nm. From left to right (Figure 5.24), the following observations were made:

- The G bands were clearly split into G^- and G^+ components.

- On average, the G^+ band appeared at 1582 $\pm$ 5 cm^{-1} and its peak position did not show any laser excitation dependence.
- The position of the G^- peak showed little variation for the same laser excitation for different samples. It showed more sensitivity when the same sample was subjected to different laser excitations.
- At 647 nm, the metallic nature of the SWCNT population was evident and the broadened shape of the G^- peak could be fitted by a BWF line-shape.
- A clear broadening of the spectral area to the low wavelength region of the G^- peak at 1073 K and 1173 K synthesis temperatures was observed. This observation was noted for all Raman laser excitations.
- At the Raman excitation of 647 nm, the synthesis of metallic SWCNTs was favoured at higher temperatures.
- At the Raman excitation of 514.5 nm, the BWF line-shape which is indicative of the presence of m-SWCNTs was more visible at lower synthesis temperatures. With increasing synthesis temperatures, the spectra exhibited a line-shape attributed to s-SWCNTs.

The D band shows a clear dependence on laser excitation. The peak position of the D band shifts to the higher wavenumber region with increasing photon energy. It was observed that the peak position, ϖ_D, remarkably follows the relation $\varpi_D = 1210 + 53 \cdot E_l$, (determined from inspection of a number Raman spectra and laser excitations) taken from reference [144] where E_l is in eV.

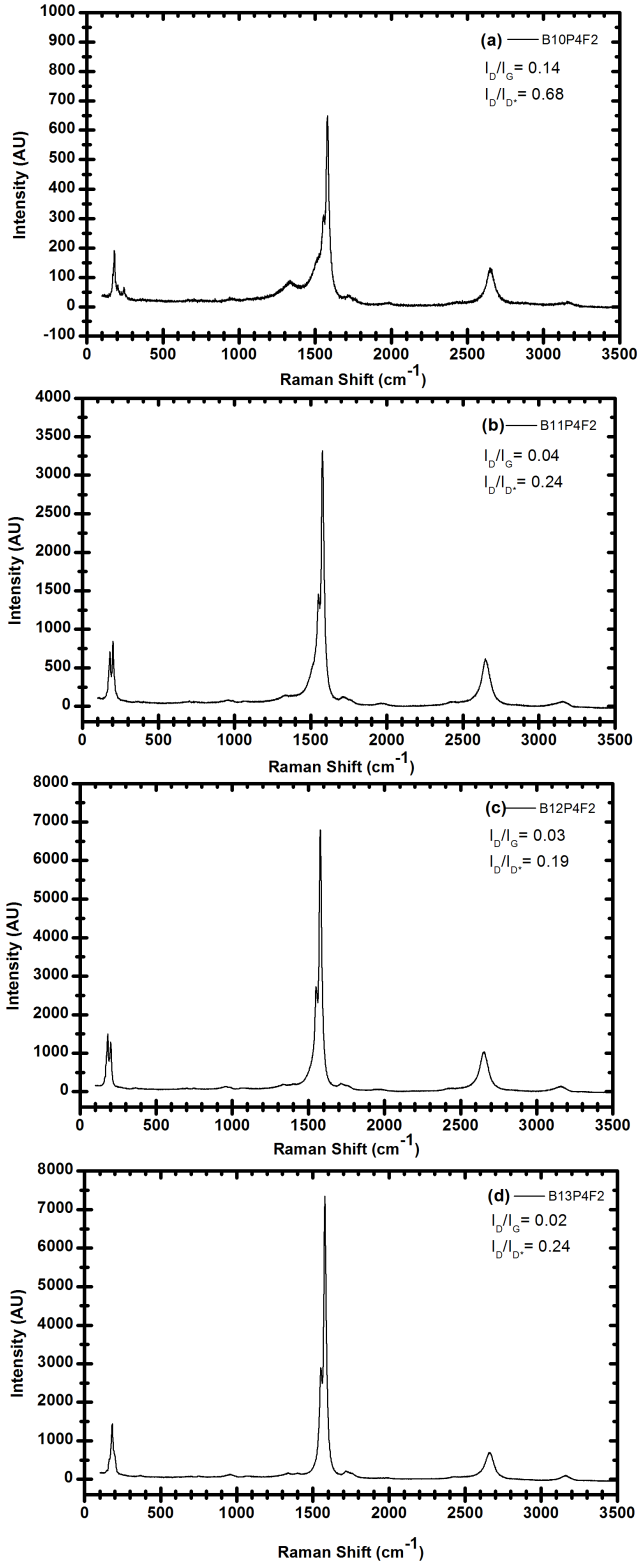


Figure 5.7: Raman spectra of as-prepared material synthesized by ablating Target B at a fixed flow rate and pressure of 200 sccm and 400 Torr of argon gas. (a) 1073 K, (b) 1173 K, (c) 1273 K and (d) 1373 K.

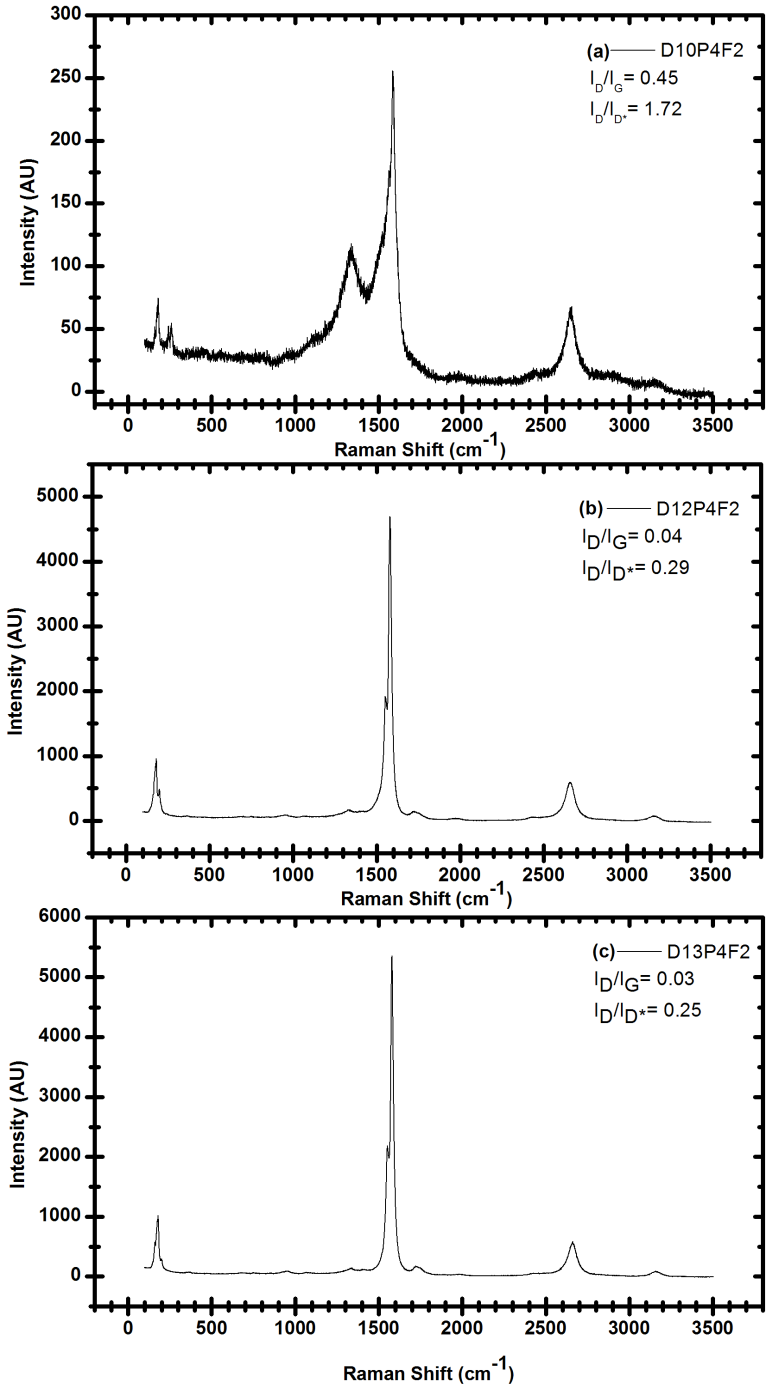


Figure 5.8: Raman spectra of as-prepared material synthesized by ablating Target D at a fixed flow rate and pressure of 200 sccm and 400 Torr of argon gas. (a) 1073 K, (b) 1273 K, (c) 1373 K.

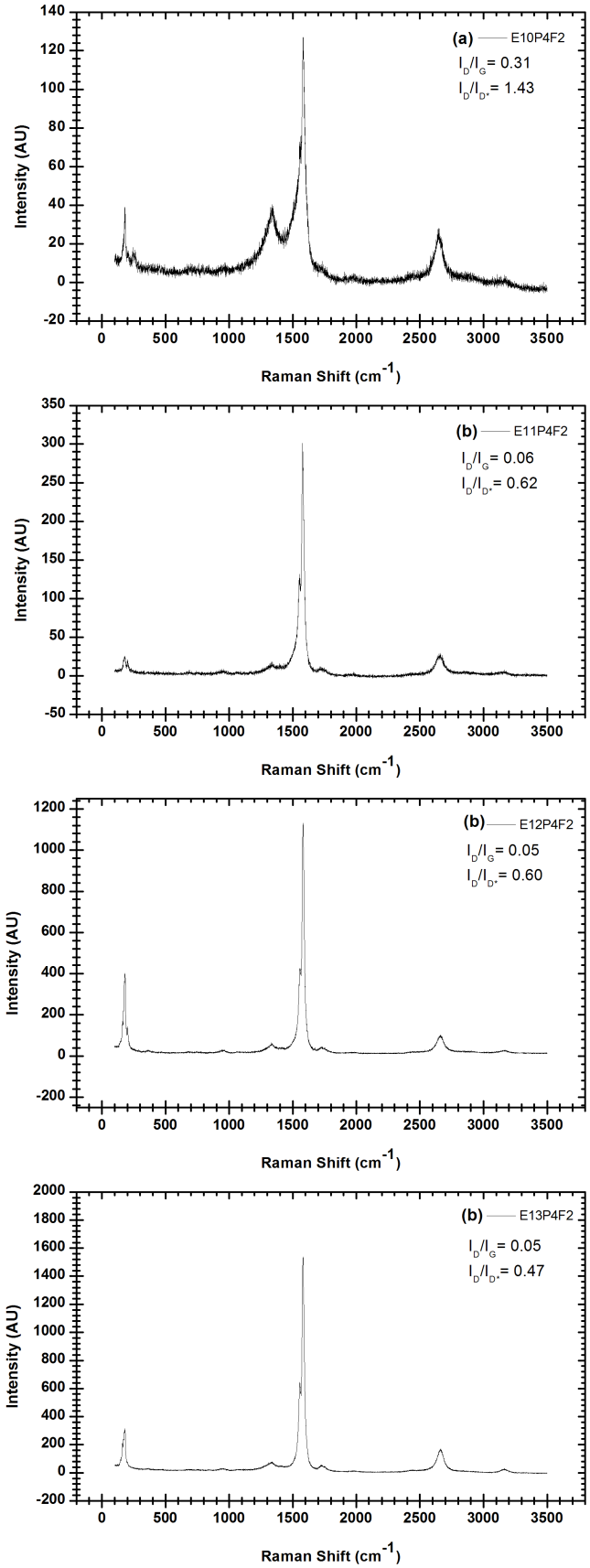


Figure 5.9: Raman spectra of as-prepared material synthesized by ablating Target E at a fixed flow rate and pressure of 200 sccm and 400 Torr of argon gas. (a) 1073 K, (b) 1173 K, (c) 1273 K and (d) 1373 K.

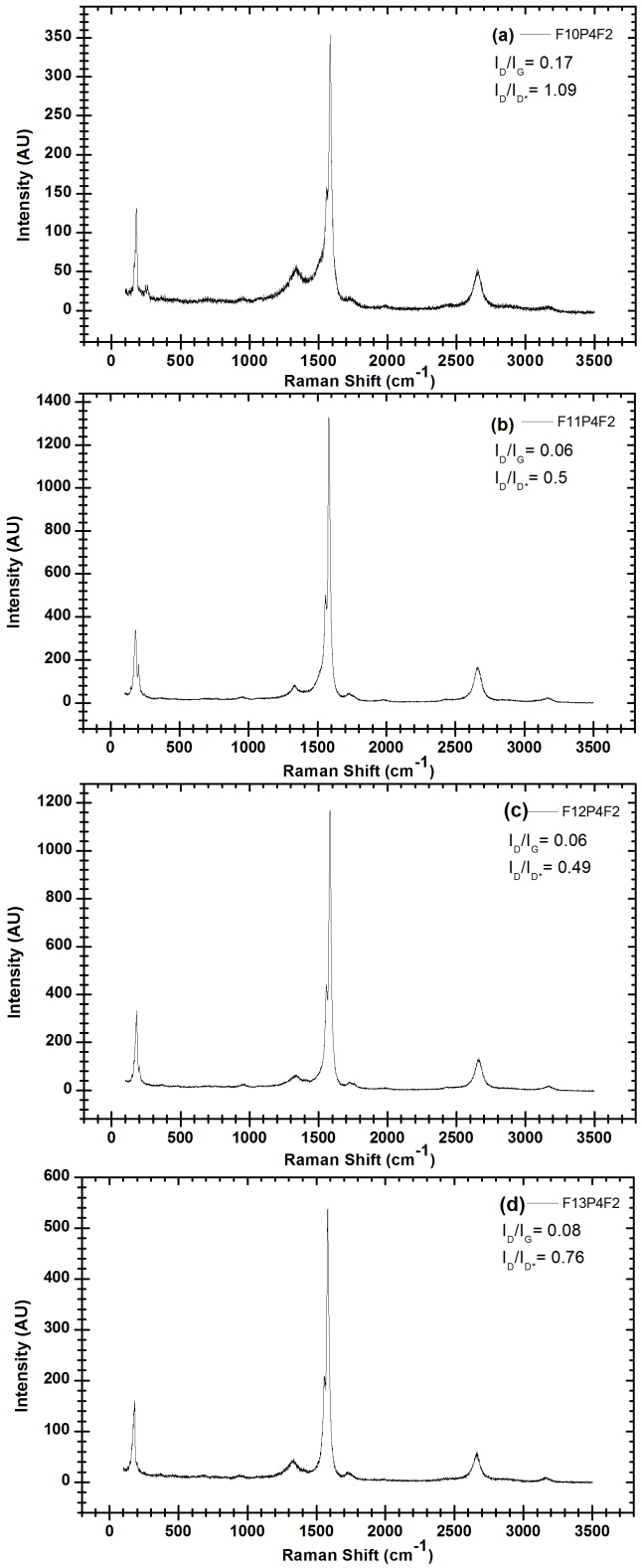


Figure 5.10: Raman spectra of as-prepared material synthesized by ablating Target F at a fixed flow rate and pressure of 200 sccm and 400 Torr of argon gas. (a) 1073 K, (b) 1173 K, (c) 1273 K and (d) 1373 K.

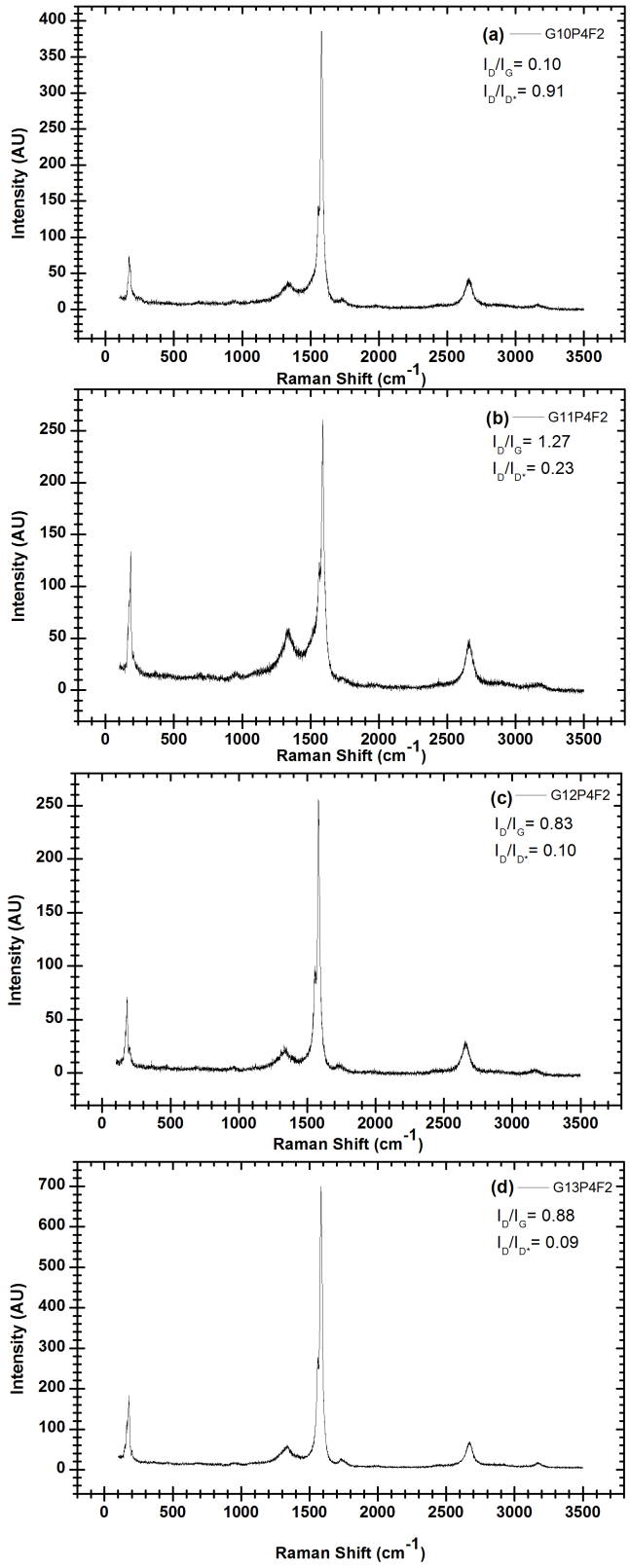


Figure 5.11: Raman spectra of as-prepared material synthesized by ablating Target G at a fixed flow rate and pressure of 200 sccm and 400 Torr of argon gas. (a) 1073 K, (b) 1173 K, (c) 1273 K and (d) 1373 K.

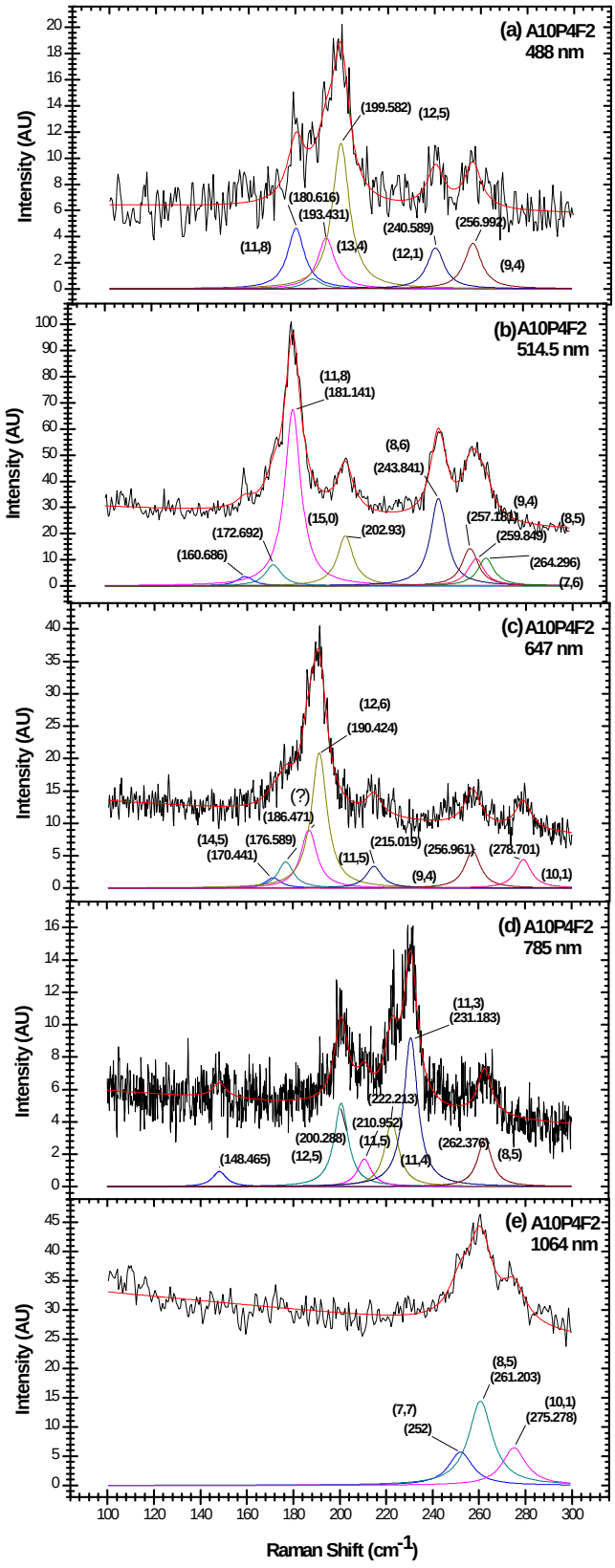


Figure 5.12: Lorentzian fits of the RBM bands of as-prepared SWCNT material obtained by ablating Target A at a furnace temperature of 1073 K.

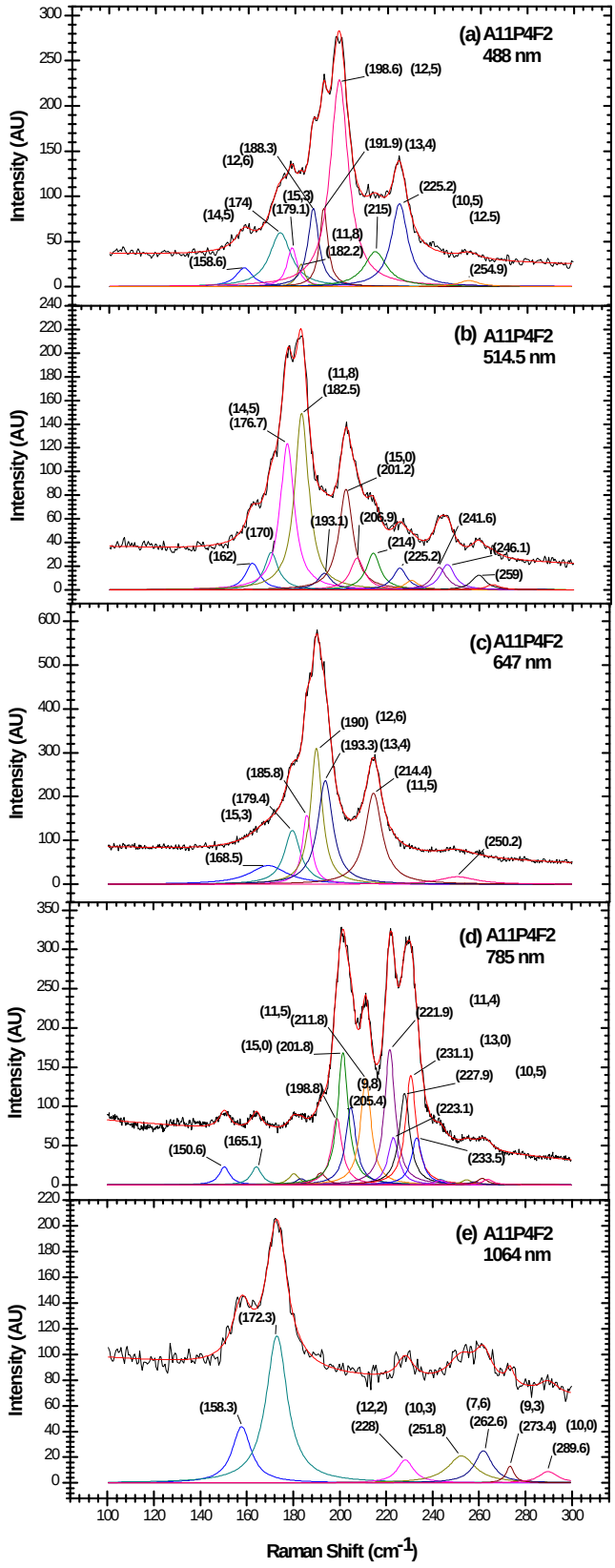


Figure 5.13: Lorentzian fits of the RBM bands of as-prepared SWCNT material obtained by ablating Target A at a furnace temperature of 1173 K.

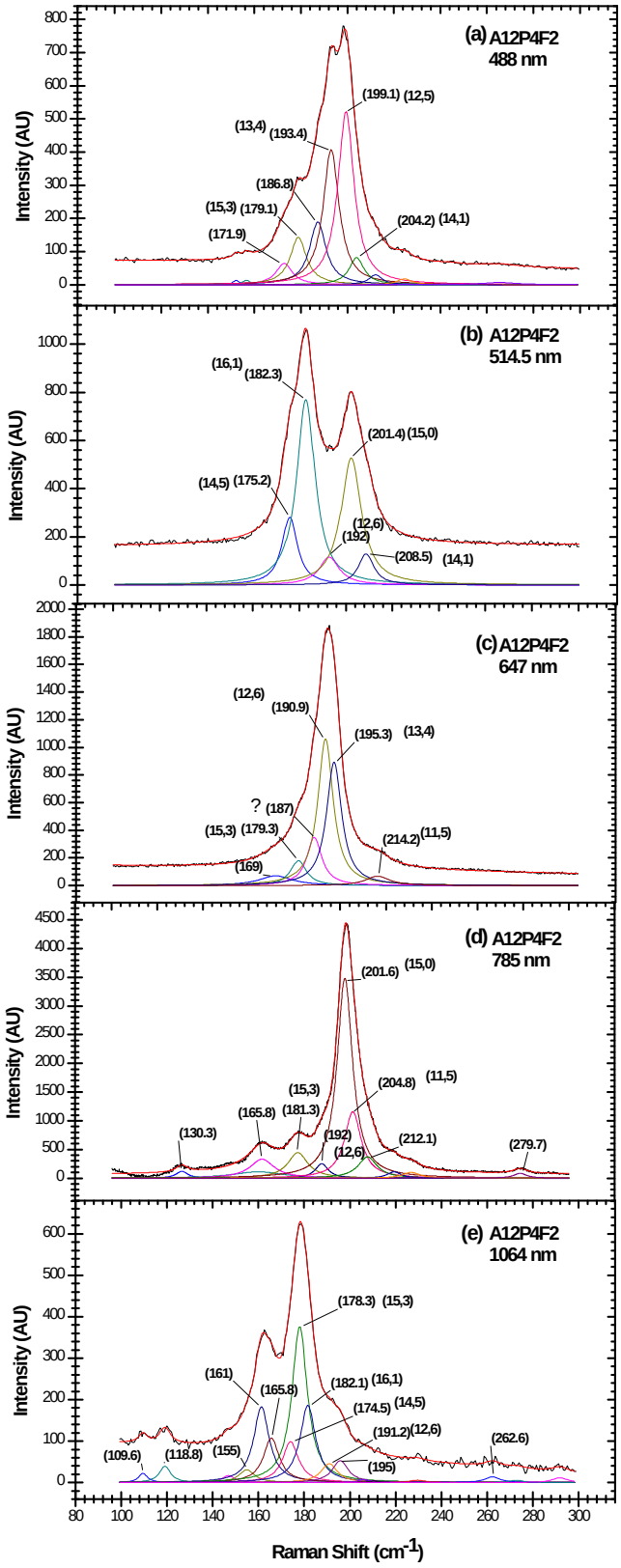


Figure 5.14: Lorentzian fits of the RBM bands of as-prepared SWCNT material obtained by ablating Target A at a furnace temperature of 1273 K.

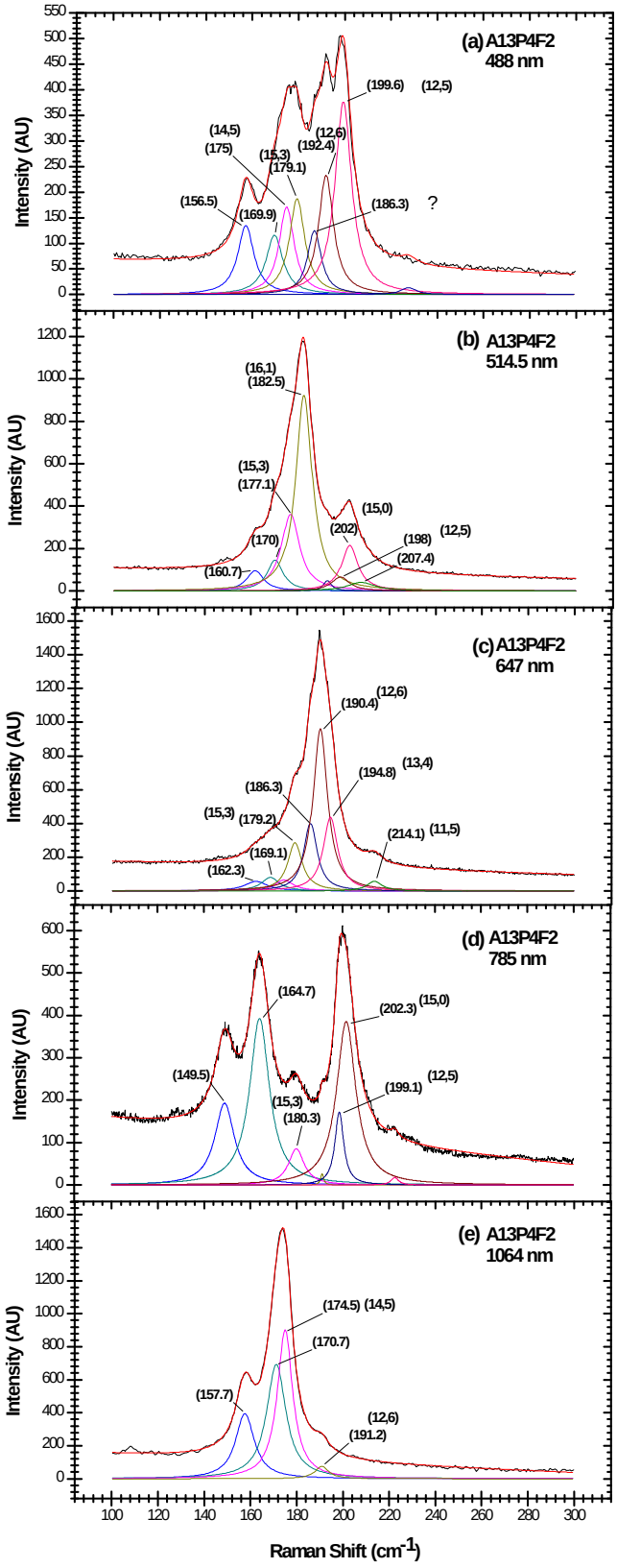


Figure 5.15: Lorentzian fits of the RBM bands of as-prepared SWCNT material obtained by ablating Target A at a furnace temperature of 1373 K.

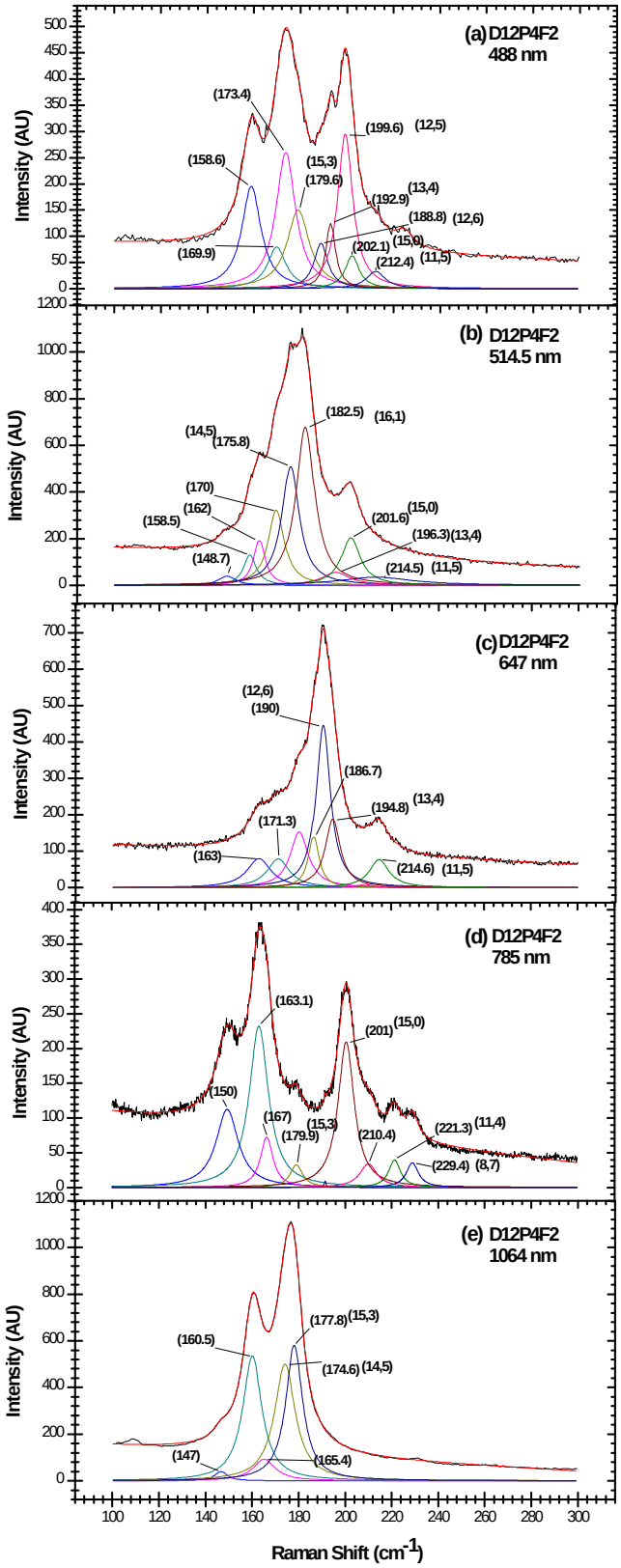


Figure 5.16: Lorentzian fits of the RBM bands of as-prepared SWCNT material obtained by ablating Target D at a furnace temperature of 1273 K.

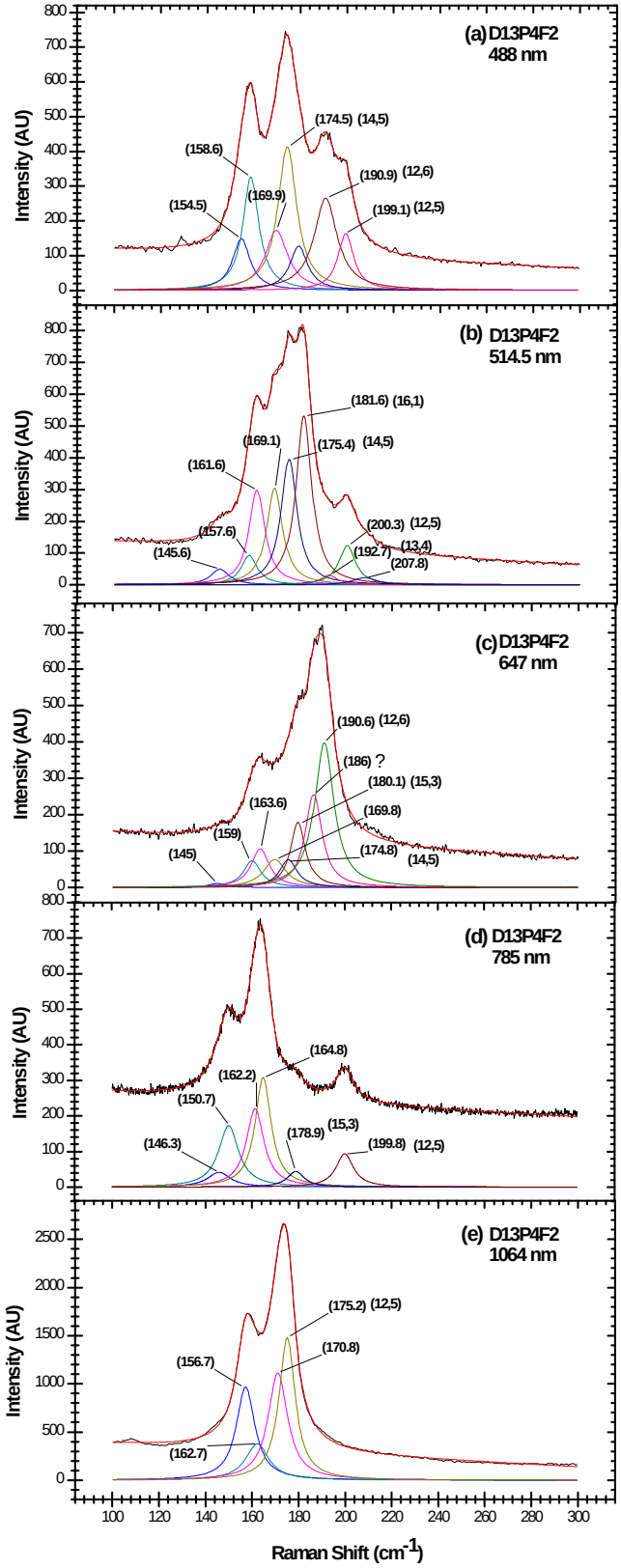


Figure 5.17: Lorentzian fits of the RBM bands of as-prepared SWCNT material obtained by ablating Target D at a furnace temperature of 1373 K.

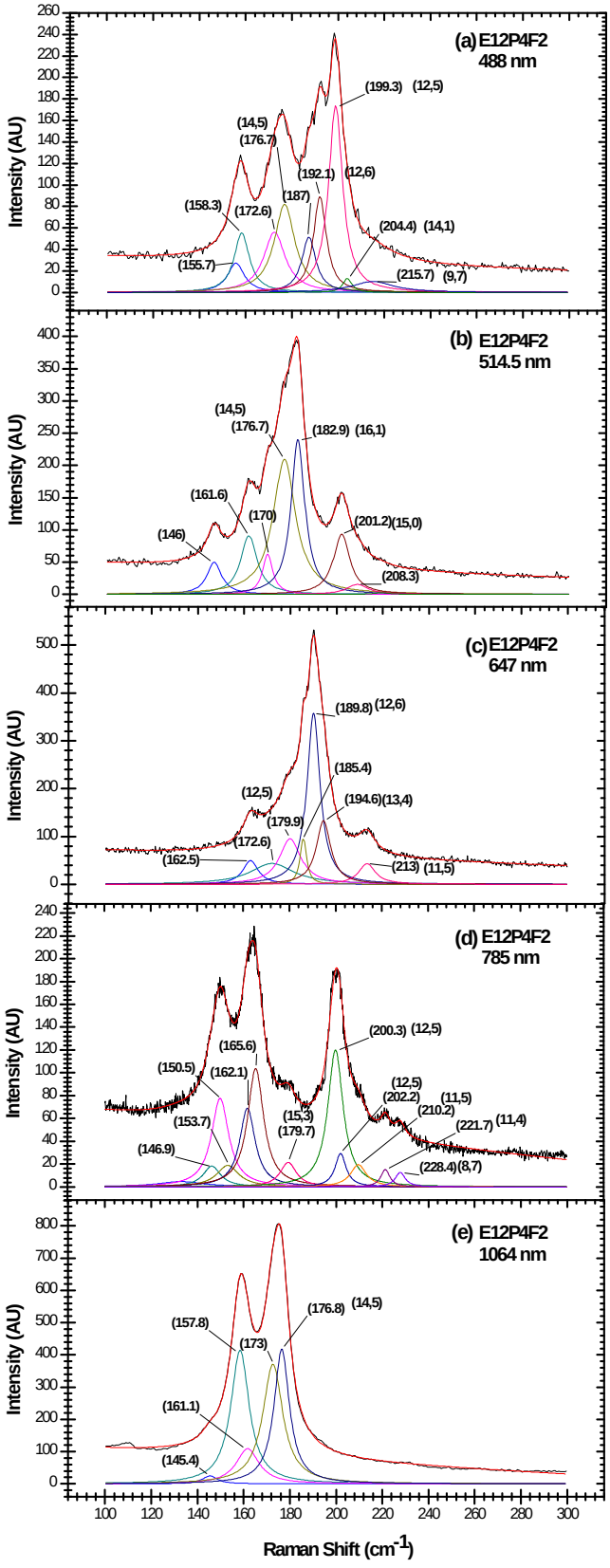


Figure 5.18: Lorentzian fits of the RBM bands of as-prepared SWCNT material obtained by ablating Target E at a furnace temperature of 1273 K.

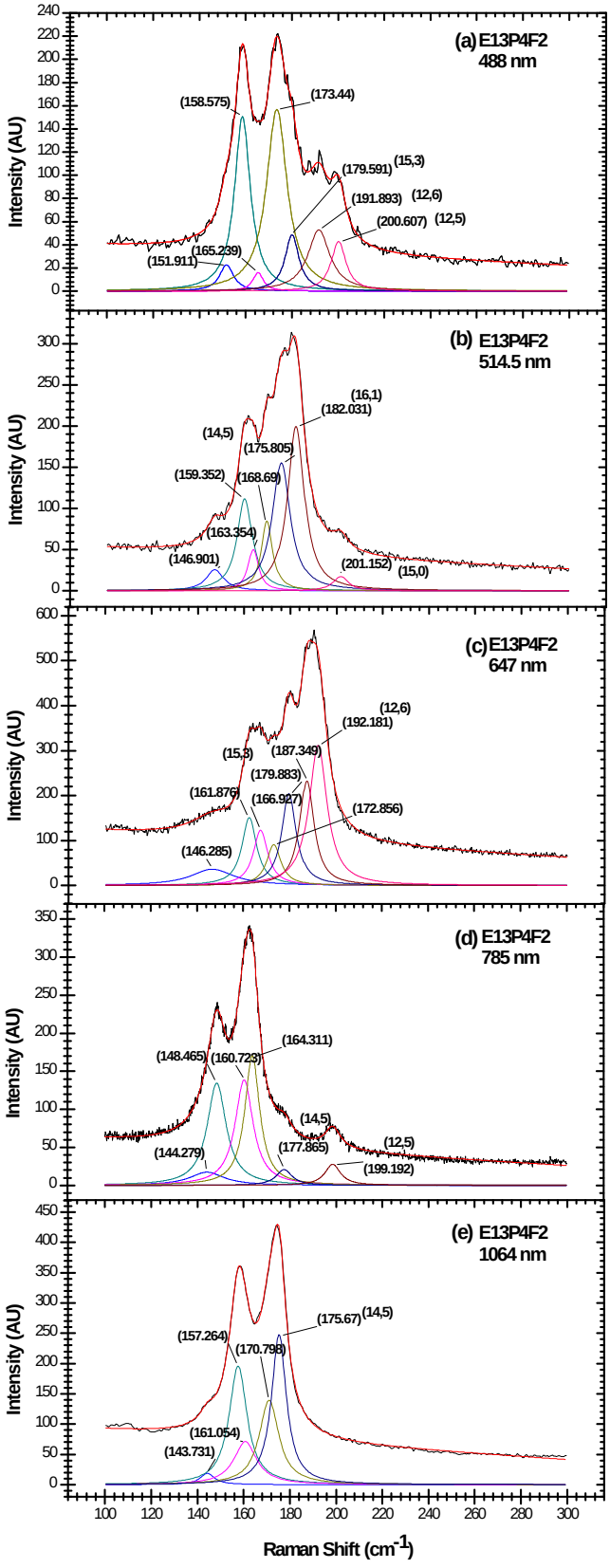


Figure 5.19: Lorentzian fits of the RBM bands of as-prepared SWCNT material obtained by ablating Target E at a furnace temperature of 1373 K.

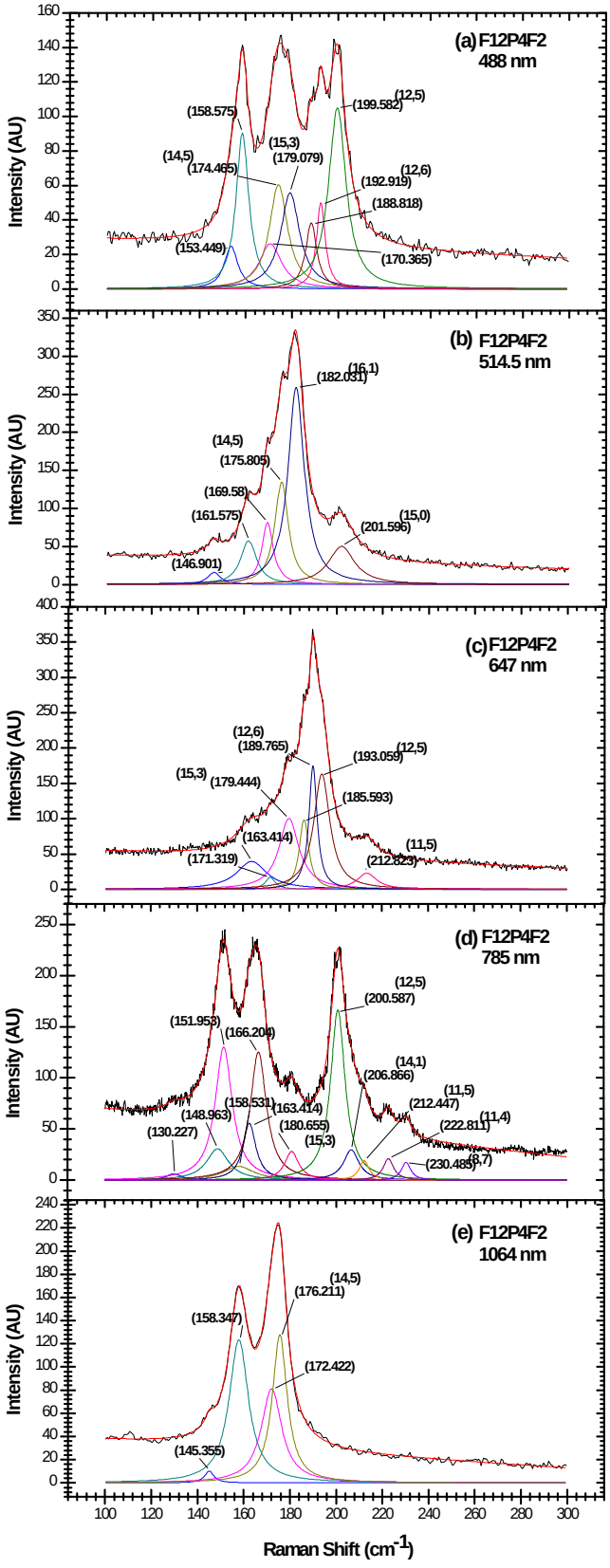


Figure 5.20: Lorentzian fits of the RBM bands of as-prepared SWCNT material obtained by ablating Target F at a furnace temperature of 1273 K.

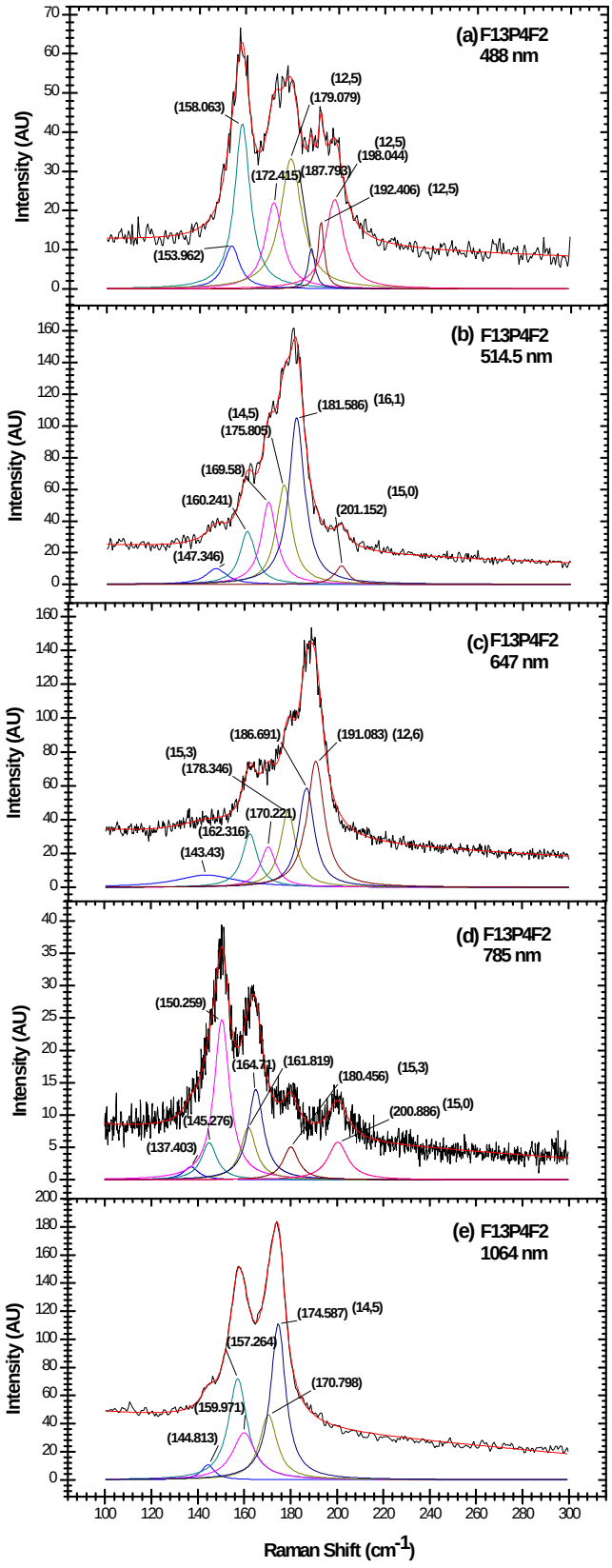


Figure 5.21: Lorentzian fits of the RBM bands of as-prepared SWCNT material obtained by ablating Target F at a furnace temperature of 1373 K.

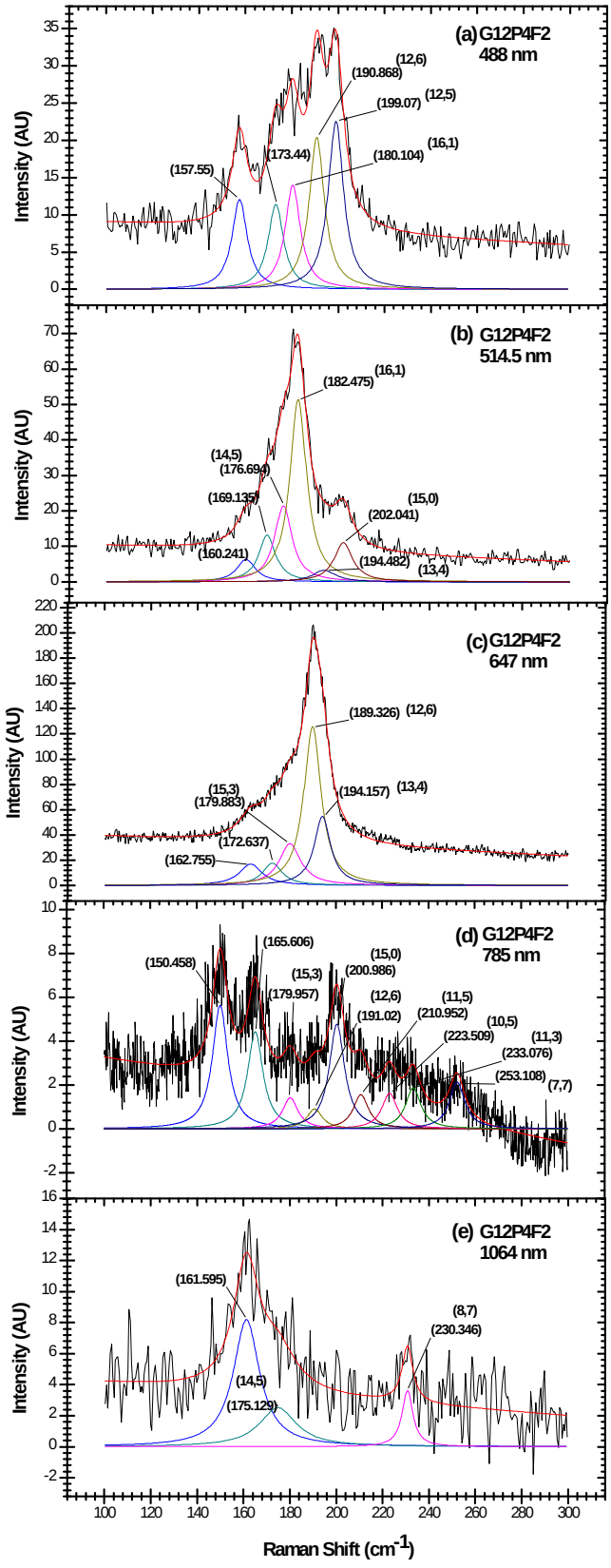


Figure 5.22: Lorentzian fits of the RBM bands of as-prepared SWCNT material obtained by ablating Target G at a furnace temperature of 1273 K.

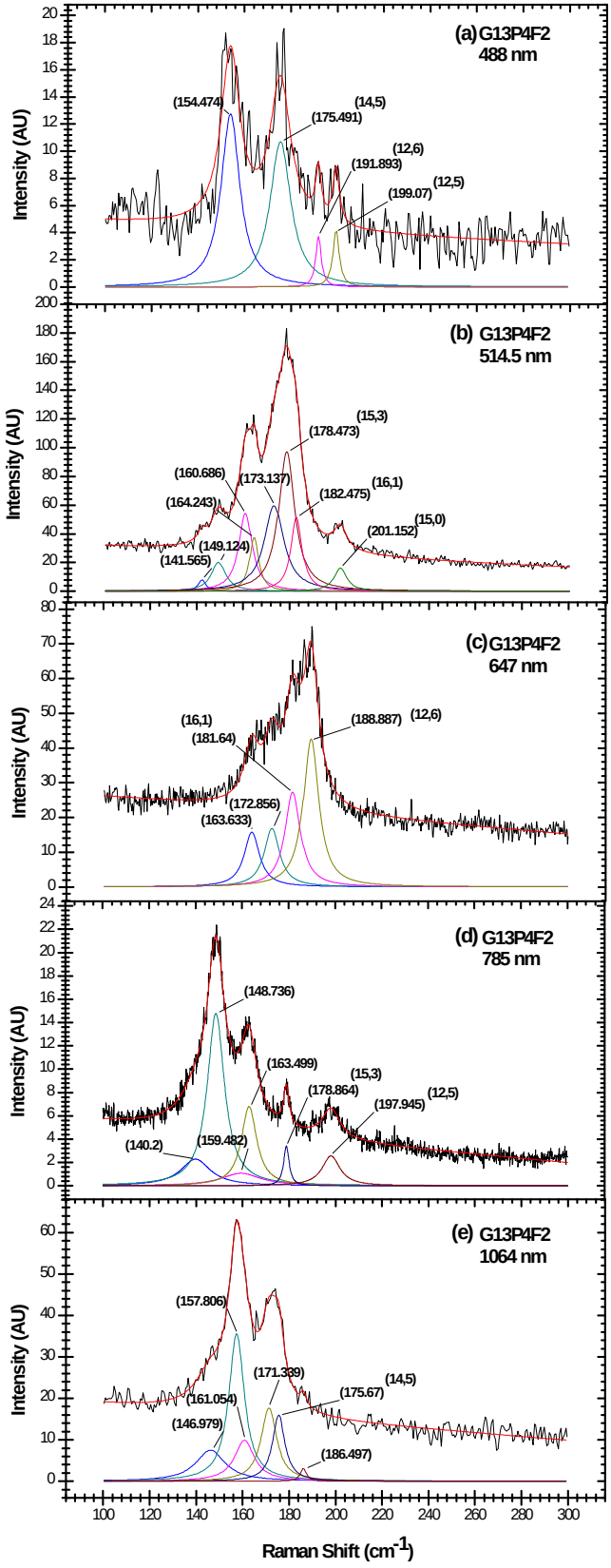


Figure 5.23: Lorentzian fits of the RBM bands of as-prepared SWCNT material obtained by ablating Target G at a furnace temperature of 1373 K.

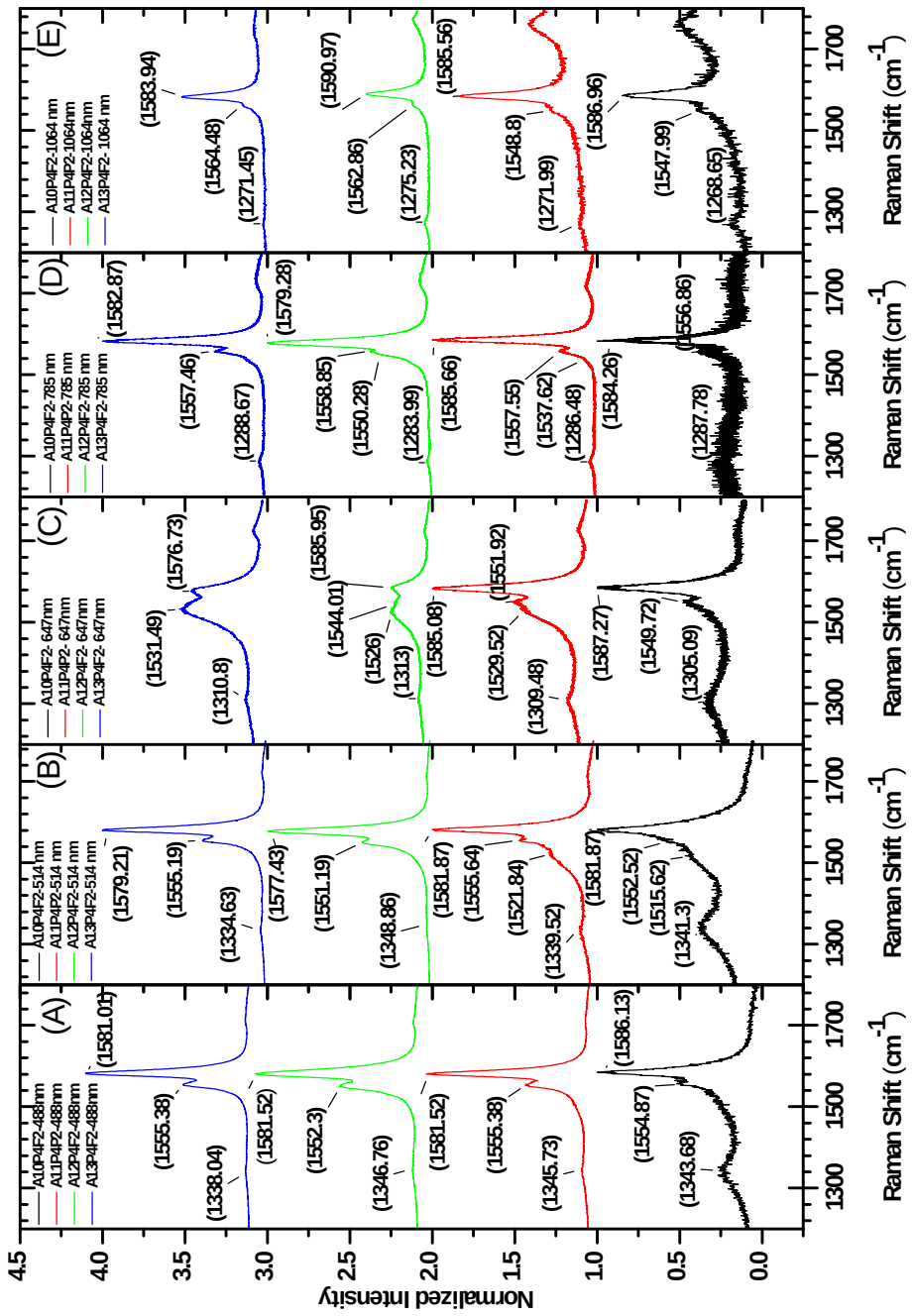


Figure 5.24: Raman spectra showing D and G bands of material synthesized by using Target A at an argon pressure of 400 Torr and flow rate of 200 SCCM.

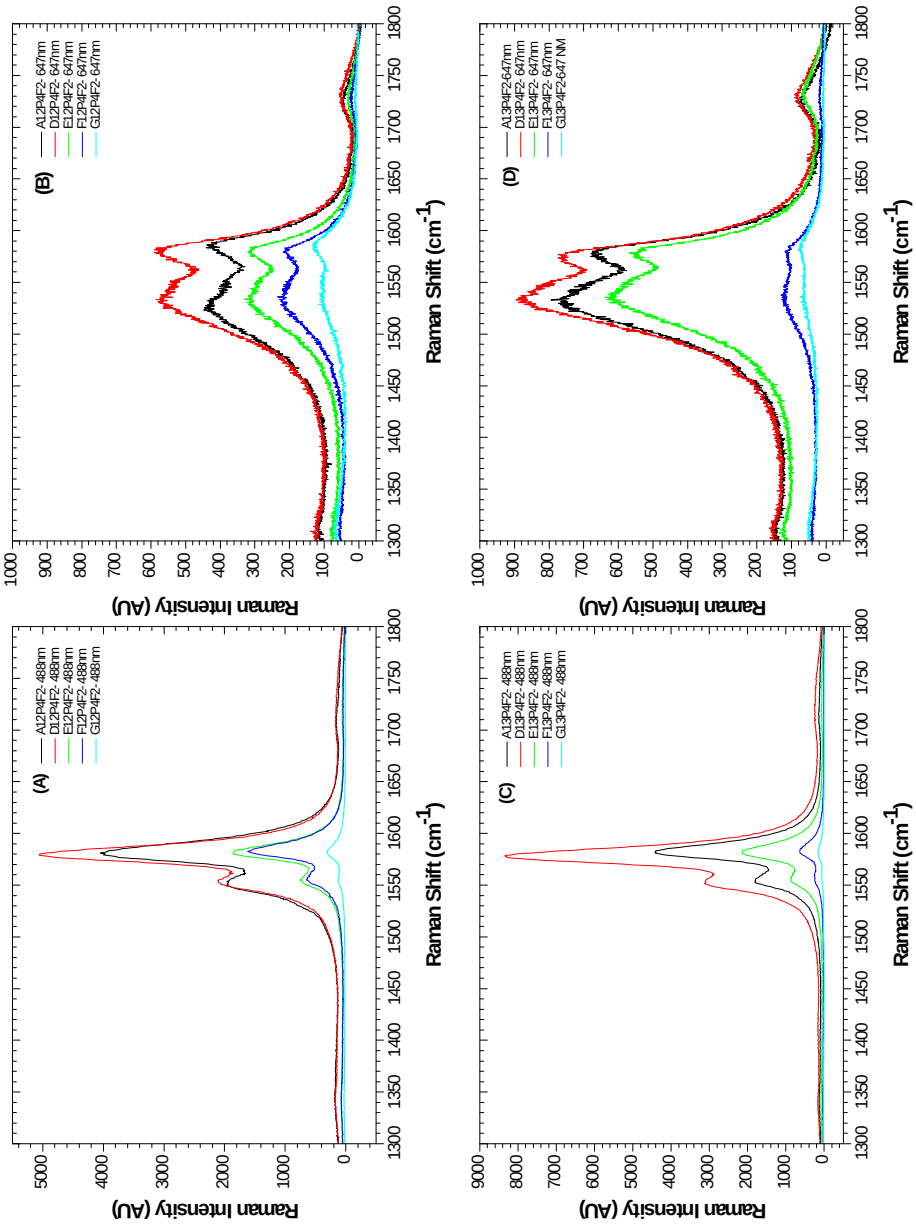


Figure 5.25: A comparison of raw Raman spectra of the D-G bands when excited at 488 and 647 nm. A significant drop in the intensities of the peaks was observed with increasing Fe concentration.

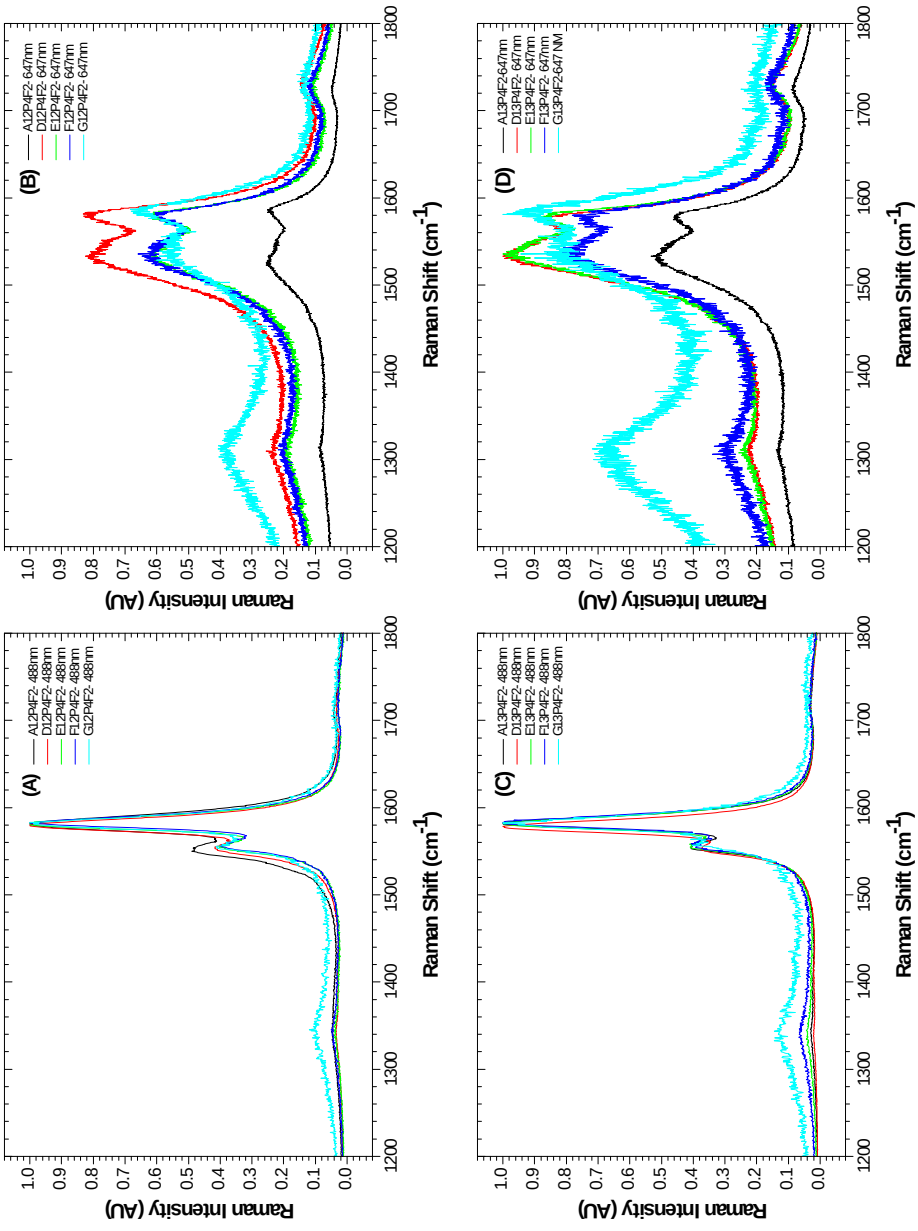


Figure 5.26: A comparison of normalized Raman spectra of the D-G bands when excited by 488 and 647 nm laser excitations. A significant drop in the intensities was observed with increasing Fe concentration. However, no significant change in peaks positions were found.

In Figure 5.25(a-d), the Raman spectra showing only the D and G bands is presented. The spectra for each of the samples were plotted together to illustrate the drop in Raman intensity with increasing Fe concentration. However, it was noted that there was a small increase in intensity after the initial addition of 0.5% Fe; thereafter, a further increase in Fe concentration resulted in a significant drop in the Raman intensity of the G bands with a corresponding increase in the D band intensity, pointing to an increase in disorder with increasing Fe concentration. In Figure 5.26(a-d), normalized spectra of the D and G bands are shown. In these plots, no significant change in the position of the D, G^- or G^+ bands was observed.

5.1.4.1 Analysis of the D* band

The D*-band at around 2700 cm^{-1} was the most intense feature of the second-order Raman spectrum of SWCNTs. It is the second overtone of the D band and has a frequency of $2\varpi_D$. Figure 5.27(a-d) shows the Raman spectra of the D* band for material synthesized using Target A. As with the D band discussed earlier, the peak position of the D*band was observed to be dependent on the laser excitation. The position of the D* shows a shift to higher wavenumbers of the spectrum with the increasing laser excitation energy (488 nm) for all samples.

It was expected that the peak position, $\varpi_{D^*} = 2\varpi_D$. Using the relation:

$$\varpi_D = 1210 + 53 \cdot E_l \tag{5.2}$$

where E_l is in eV [144], a comparison was made between predicted peak positions and measured peak positions for ϖ_D and ϖ_{D^*}. Figure 5.28 shows plots of (a) ϖ_D versus laser excitation and (b) ϖ_{D^*} versus laser excitation. In Figure 5.28(a), an excellent correspondence between experimental and predicted values of the ϖ_D values (using eqn. 5.2) was found. However, in Figure 5.28(b), a significant difference between experimental ϖ_{D^*} and values predicted by eqn. 5.2 was observed. These differences, as large as 26 cm^{-1}, may be explained by bundling effects and the fact that ϖ_{D^*} may also depend on unbundled and individual tube diameters [149].

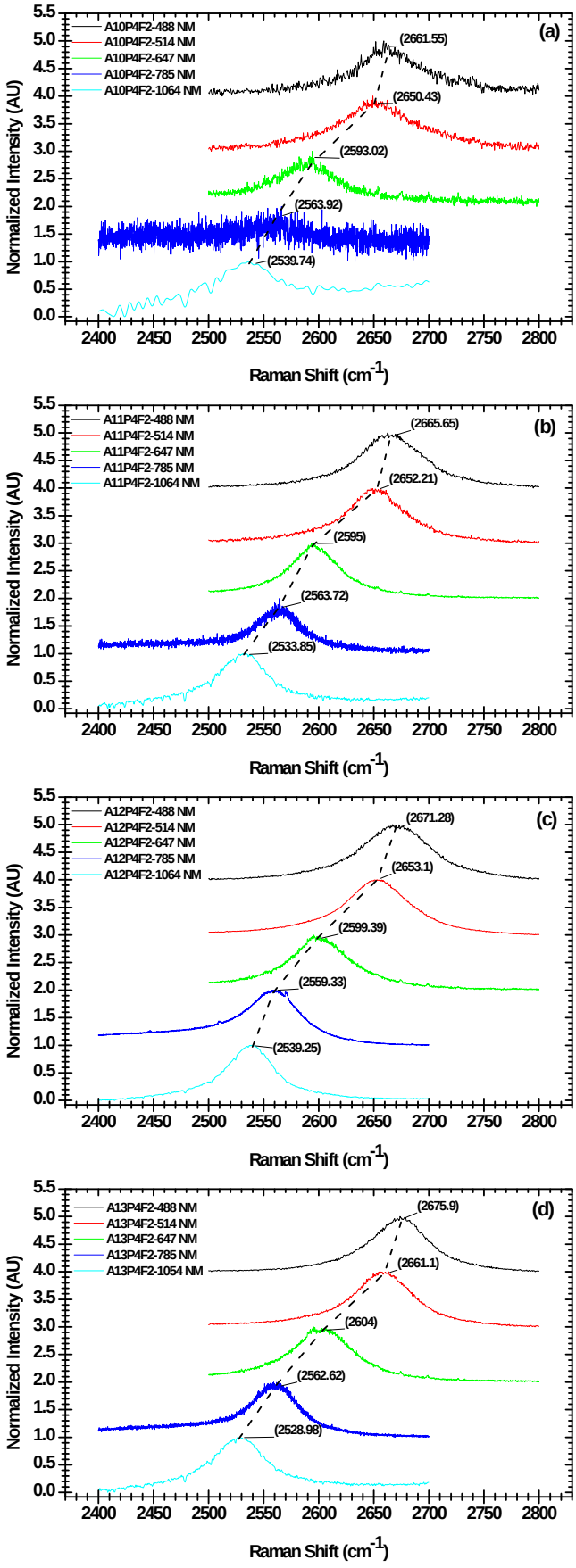


Figure 5.27: Raman spectra of the D* band. The peak postion of the D* band showed a clear dependence on the laser excitation energy for all samples.

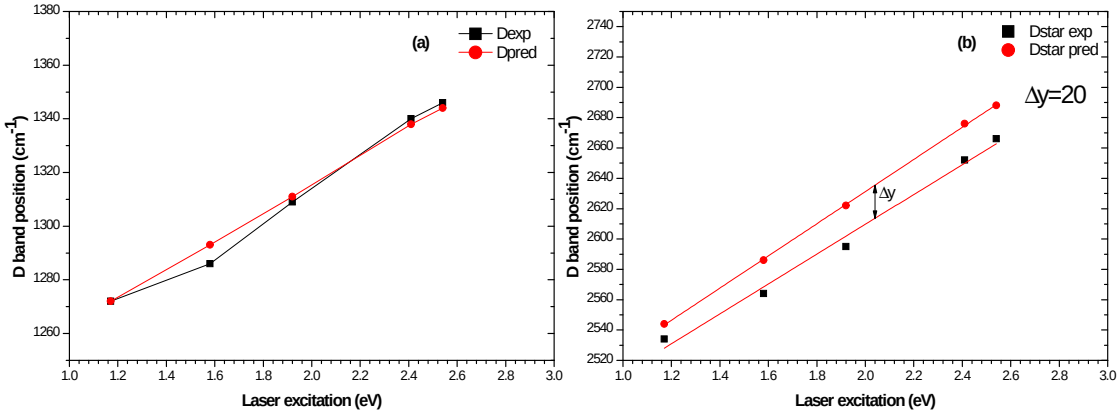


Figure 5.28: A comparison between experimental and predicted Raman peak positions for ϖ_D and ϖ_{D^*}.

5.2 Photoluminescence spectroscopy of SWCNTs

The theory and importance of photoluminescence spectroscopy (PLS) in the characterization of SWCNTs was discussed in section 3.2.9. The methodology employed in the characterization of SWCNTs was discussed in section 4.8.2. Similar to Raman spectroscopy, which was discussed in Section 5.1, a select few as-prepared SWCNT samples were subjected to detailed PLS experiments. These samples are listed in Table 5.7. PLS was used to determine whether furnace temperature and the catalyst composition of the target play a role in influencing the diameter and chirality of as-prepared semi-conducting carbon nanotubes. To do this, two types of plots were presented for each sample that was investigated:

- An excitation versus emission plot which was fitted by several functions relating the excitation-emission photon energies to theoretical calculations, that linked peak positions to chiral assignments.
- A plot of SWCNT diameter vs chiral angle. This was necessary since SWCNTs may have equal $E_{22}E_{11}$ values but have different chiral angles and hence different properties.

These plots allowed for easier evaluation of the effect of experimental conditions on the synthesis process.

5.2.1 Photoluminescence of samples prepared with Target A

Figure 5.29(a-d) shows the PL spectra of SWCNTs prepared from Target A at synthesis temperatures of (a) 1073 K, (b) 1173 K, (c) 1273 K and (d) 1373 K respectively. All samples were made using the same sample preparation method. In comparing the spectra, a striking observation was that the spectra appeared more structured and "cleaner" with reduced background emissions at 1073 K and 1173 K. As the synthesis temperature increased, background emission levels increased making the emission attributed to distinct SWCNTs less discernible. From these spectra we could deduce that the samples made at lower synthesis temperatures were more enriched with SWCNTs than those made at higher synthesis temperatures.

This observation was contrary to the Raman results where disorder was seen to decrease at higher synthesis temperatures. Another interesting observation was that as the synthesis temperature increased, the (n,m) chirality map of the SWCNT with the highest emission intensity shifted towards the top-right of the excitation-emission PL spectrum e.g. $(7,6) \Longrightarrow (8,6) \Longrightarrow (9,7) \Longrightarrow (9,8)$. A plausible explanation of this observation will be made in later sections of this dissertation.

A spectral plot of the diameter versus the chiral angle of SWCNTs for Target A is shown in Figure 5.30(a-d). The following observations could be made based on these plots:

- The SWCNT intensities become lower with increasing synthesis temperature.
- The chiral distribution of SWCNTs increased with temperature.
- A higher synthesis temperature leads to the nucleation of a wider variety of chiral nanotubes. Different chiral tubes appeared to dominate at different temperatures
- The distribution of diameters of the SWCNTs from sample A12P4F2 and A13P4F2 lie in a band between 0.9 and 1.2 nm while for samples A10P4F2 and A11P4F2 the diameter distribution lies between 0.8 and 1.10 nm.

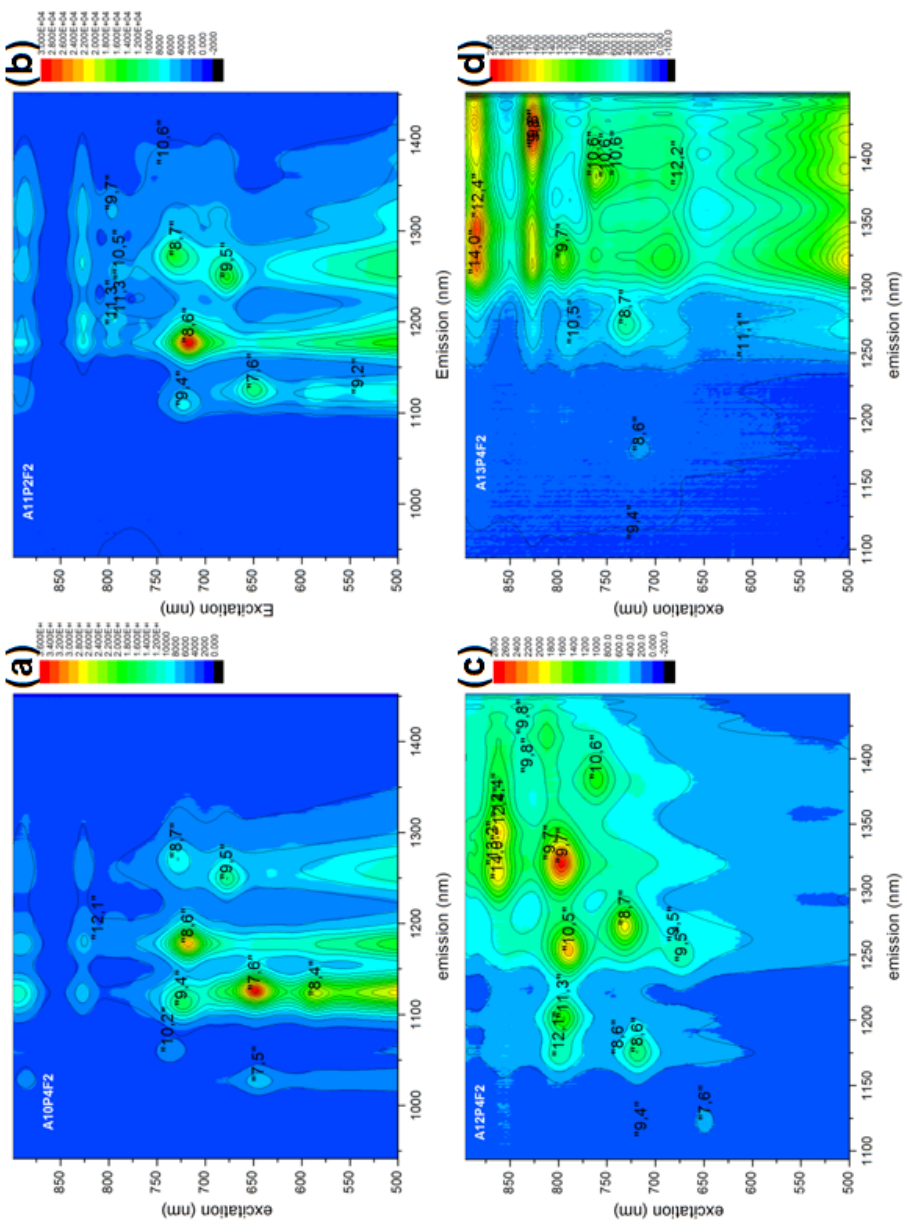


Figure 5.29: Photoluminescence spectra of samples obtained by ablating Target A at (a) 1073 K, (b) 1173 K, (c) 1273 K and (d) 1373 K.

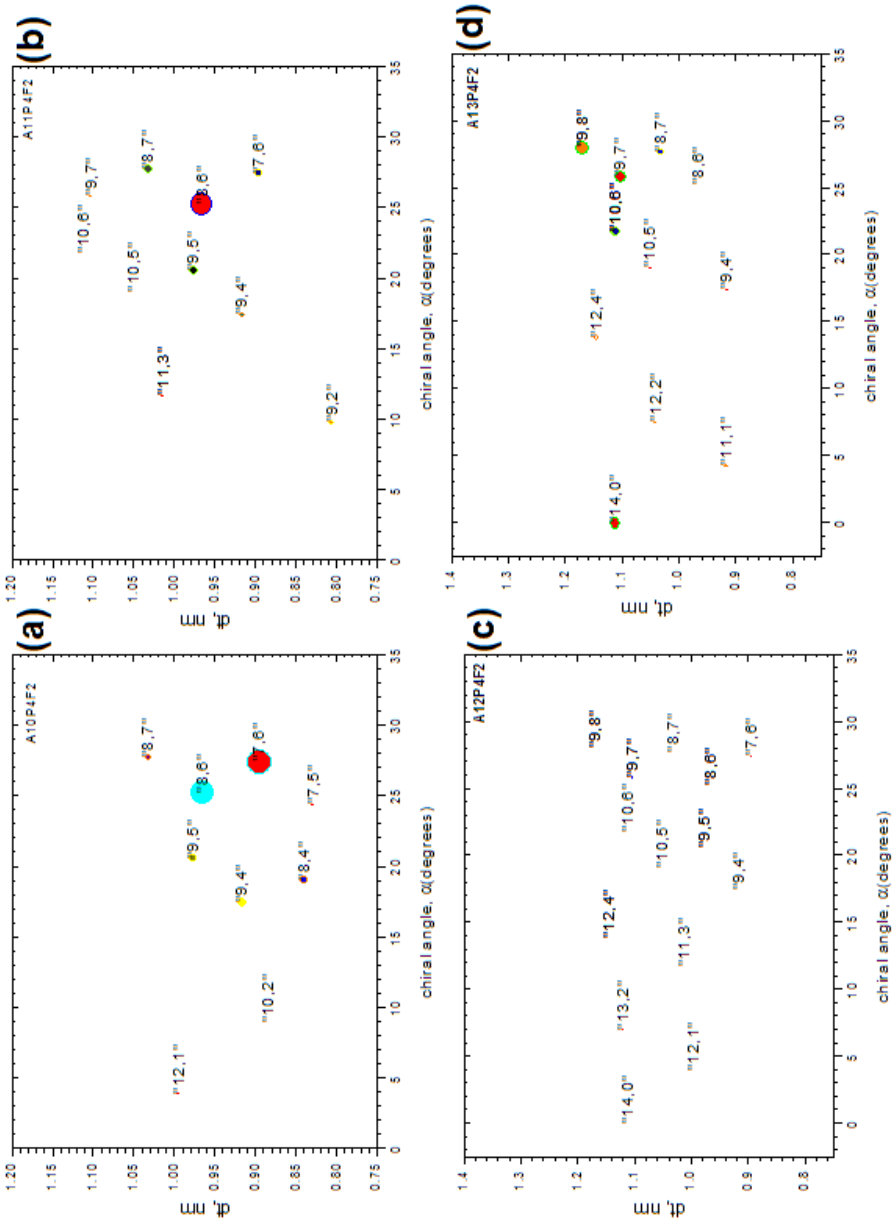


Figure 5.30: Spectral plots of SWCNTs diameters versus chiral angle of samples obtained by ablating Target A at (a) 1073 K, (b) 1173 K, (c) 1273 K and (d) 1373 K.

5.2.2 Photoluminescence spectra of samples prepared with Target D

Figures 5.31(a,b) show the PL spectra of samples synthesized by the use of Target D, which contained 0.5% Ni, 0.5% Co and 0.5% Fe. The pattern of the PL spectra for D12P4F2 (Figure 531(a)) was almost identical to that of A12P4F2 (Figure 5.29(c)) but with slightly higher intensity. While the PL spectra for D13P4F2 was less intense than A12P4F2, the spectra had a reduced "background" noise with an improved peak "fit".

The plots for the diameter versus chiral angle were very similar for D12P4F2 (Figure 5.31(c)) and A12P4F2. However, for sample D13P4F2 (Figure 5.31(d)), fewer chiral nanotubes appear to have been favoured. Furthermore, the diameter range at 1373 K was further reduced to between 1.0-1.20 nm. Nanotubes which dominate at 1273 K, were (14,0), (11,3), 10,5) and (8,7). At 1373 K they were (14,0), (12,4), (9,7) and (11,6).

5.2.3 Photoluminescence spectra of samples prepared with Target E

In Figure 5.32 (a-d) the PL spectra and plots of d_t vs chiral angle are shown for samples E12P4F2 and E13P4F2. As with Target D, significant differences were noticeable between the samples synthesized at 1273 K and 1373 K. At 1273 K the sample E12P4F2 shows that only the (9,7) nanotube dominates while at 1373 K, the sample E13P4F2 shows that (9,7), (12,4) and (11,6) nanotubes dominate. As with Raman intensities (Section 5.1), spectroscopic emission intensities declined as Fe concentration was increased.

5.2.4 Photoluminescence spectra of samples prepared with Target F

In Figure 5.33 (a-d) the PL spectra and plots of d_t vs chiral angle are shown for samples F12P4F2 and F13P4F2. As with other samples obtained from the Targets described above, significant differences were noticeable between the samples synthesized at 1273 K and 1373 K. At 1273 K (F12P4F2), (12,4), (10,6) and (9,7) nanotubes dominates while at 1373 K, (12,4) and (9,7) nanotubes dominate. As with the Raman intensities (Section 5.1), spectroscopic emission intensities declined as Fe concentration was increased.

5.2.5 Photoluminescence spectra of samples prepared with Target G

In Figure 5.34 (a-d) the PL spectra and plots of d_t vs chiral angle are shown for samples G12P4F2 and G13P4F2. As with other samples obtained from Targets described above, significant differences were noticeable between the samples synthesized at 1273 K and 1373 K. At 1273 K (G12P4F2) only the (9,7) nanotube dominates while at 1373 K, only the (11,6) and (9,7) nanotubes dominate. As with the Raman intensities (Section 5.1), spectroscopic emission intensities declined as Fe concentration was increased.

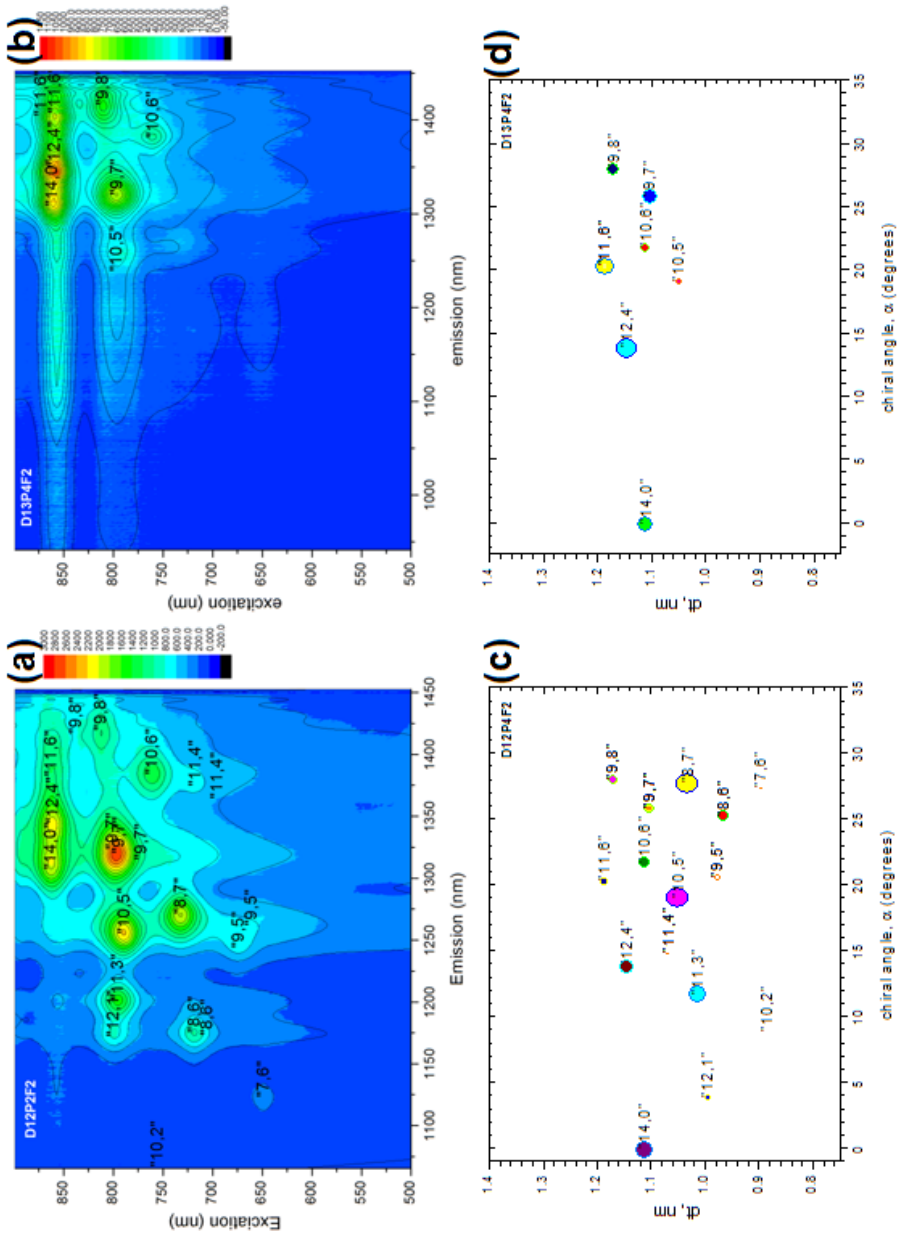


Figure 5.31: PL plots for (a)D12P4F2 and (b)D13P4F2. SWCNT diameter vs chiral angles plots are shown for (c) D12P4F2 and (d) D13P4F2.

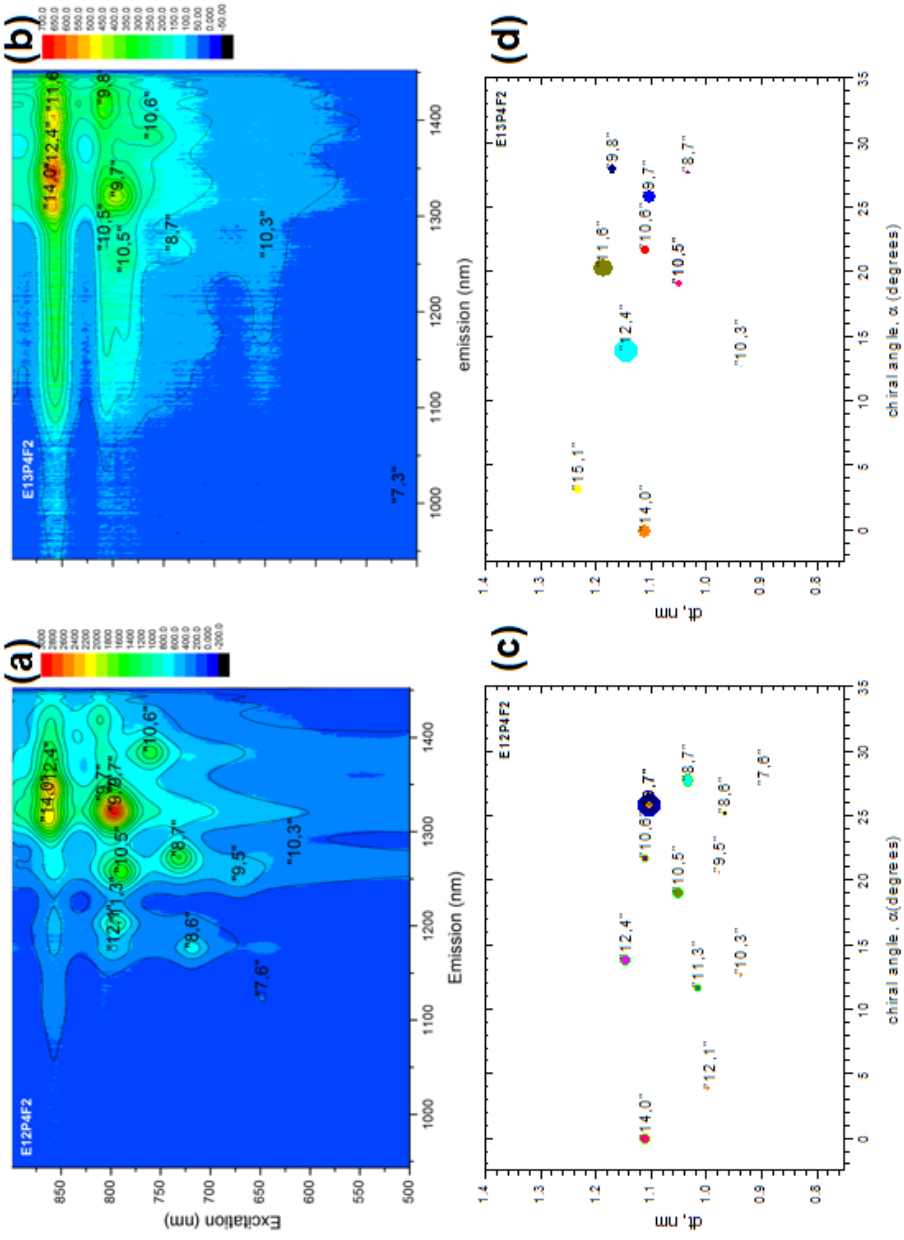


Figure 5.32: PL plots for (a)E12P4F2 and (b)E13P4F2. SWCNT diameter vs chiral angles plots are shown for (c) E12P4F2 and (d) E13P4F2.

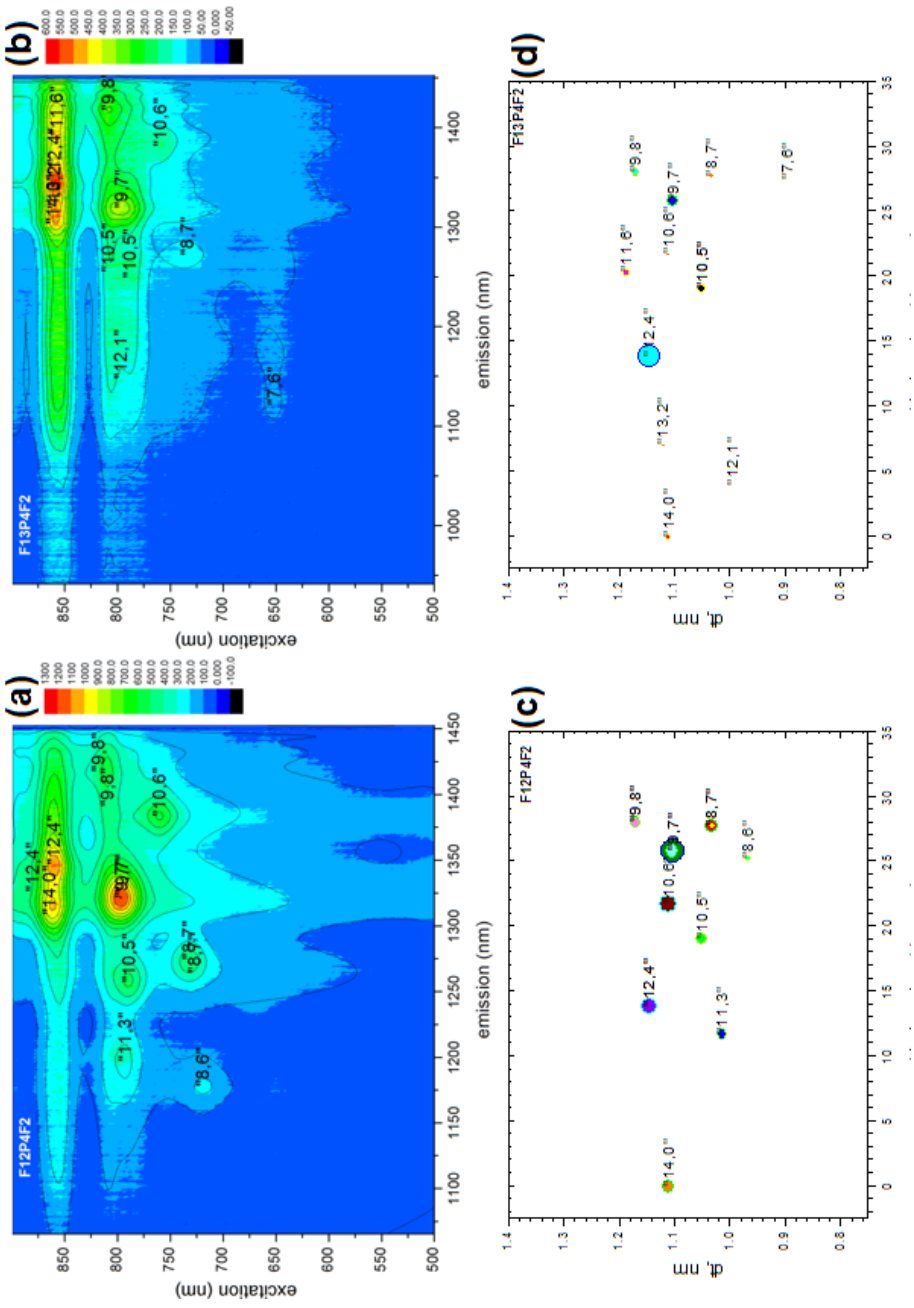


Figure 5.33: PL plots for (a)F12P4F2 and (b)F13P4F2. SWCNT diameter vs chiral angles plots are shown for (c) F12P4F2 and (d) F13P4F2.

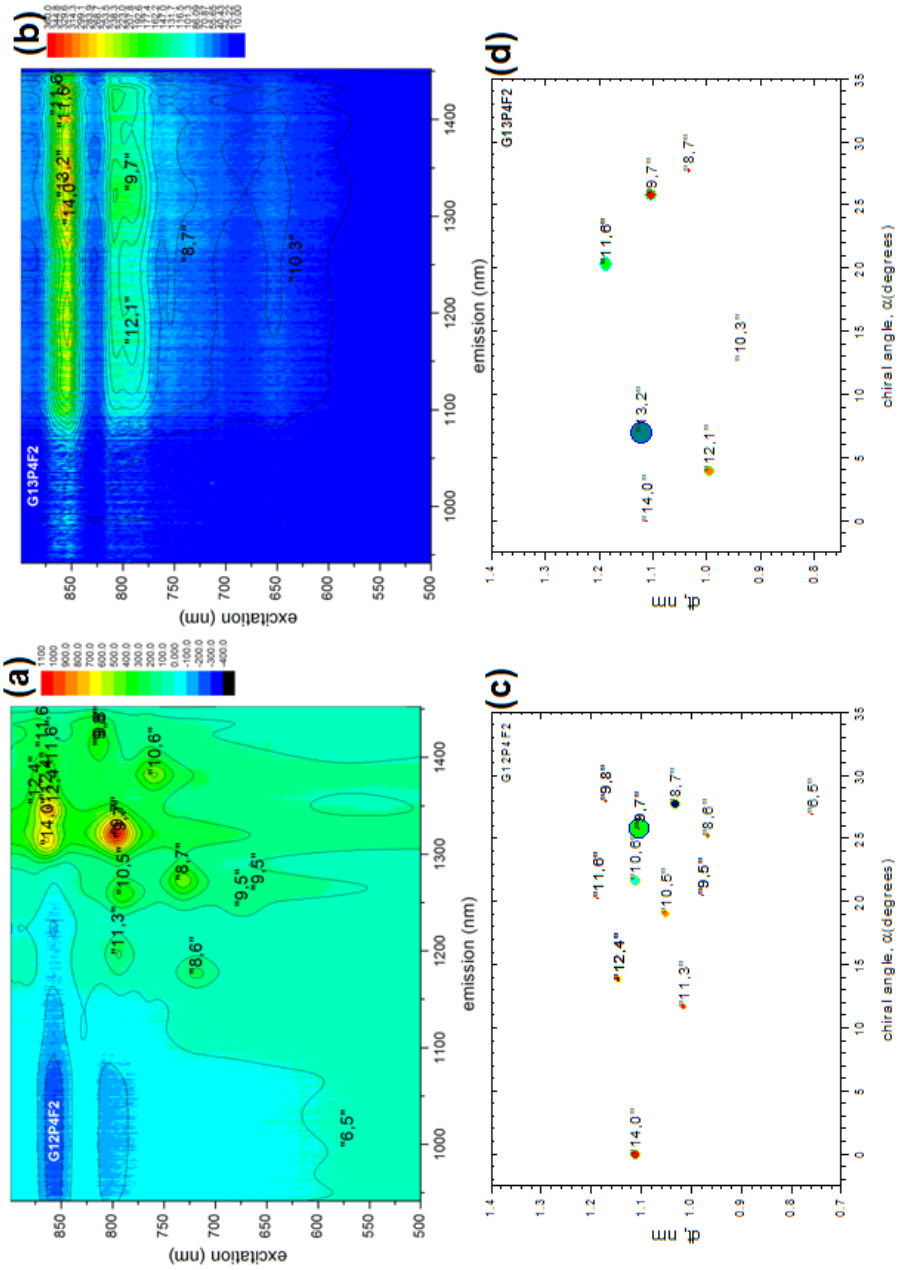


Figure 5.34: PL plots for (a)G12P4F2 and (b)G13P4F2. SWCNT diameter vs chiral angles plots are shown for (c) G12P4F2 and (d) G13P4F2.

5.3 Electron Microscopy studies on the as-prepared SWCNTs

5.3.1 Scanning electron microscopy (SEM)

SEM was used to gauge the quality of the material that was produced (amorphous carbon, carbon nanofibres and nanotubes) under extreme synthesis conditions. These measurements were qualitative in nature since it was not possible to determine with certainty the ability for example, of SEM to differentiate between samples A12P4F2 and D12P4F2 where the synthesis conditions was almost the same except for a small difference in catalyst composition. However, SEM and TEM are the only analytical methods commonly used to visually show the nanotube content.

In Figure 5.35(a-d), SEM images of as-prepared materials synthesized or prepared under various conditions are shown. When no catalyst was used in the laser ablated target, SEM showed the formation of amorphous carbon (Fig. 5.35(a)). SEM analysis of as-prepared material collected from ablating Target A in a 100 SCCM flow of Ar gas, at a pressure of 100 Torr in a furnace operating at 1073 K, showed fibrous carbon nanorods (Fig. 5.35(b)). However, under nearly ideal conditions, SEM analysis of sample A12P4F2 (Fig. 5.35(c)) showed "spaghetti like" nanostructures had formed. When sample A12P4F2 was sonicated in ethanol, then dried, SEM images showed nanotubes covered in a thin film of carbon.

For PL measurements it was necessary to disperse the as-prepared material in a solution of sodium cholate surfactant. In Figure 5.36, SEM images of an air-dried film of surfactant wrapped SWCNTs on top of a holey carbon TEM grid is shown. Tubular structures are clearly visible. The same holey grid was thereafter heated in air at 180 ^0C in an attempt to remove the surfactant. This temperature may not have been high enough to completely remove the surfactant since Wei et al. [150] have suggested 350 ^0C. This high temperature was avoided as this could have destroyed the holey carbon film and hence the sample itself. SEM images of this film are shown in Figures 5.37 and 5.38. The holey carbon films cracked under heating which resulted in the film being pulled apart between the cracks. As the surfactant evaporated (partially), the SWCNT bundles lying over the cracking were exposed and formed bridges between the cracks. With SEM, it was not possible to see individual SWCNTs due to the resolution limit of the instrument. Some SWCNT bundles or SWCNT wrapped in surfactant were measured to be as low as 13 nm in diameter.

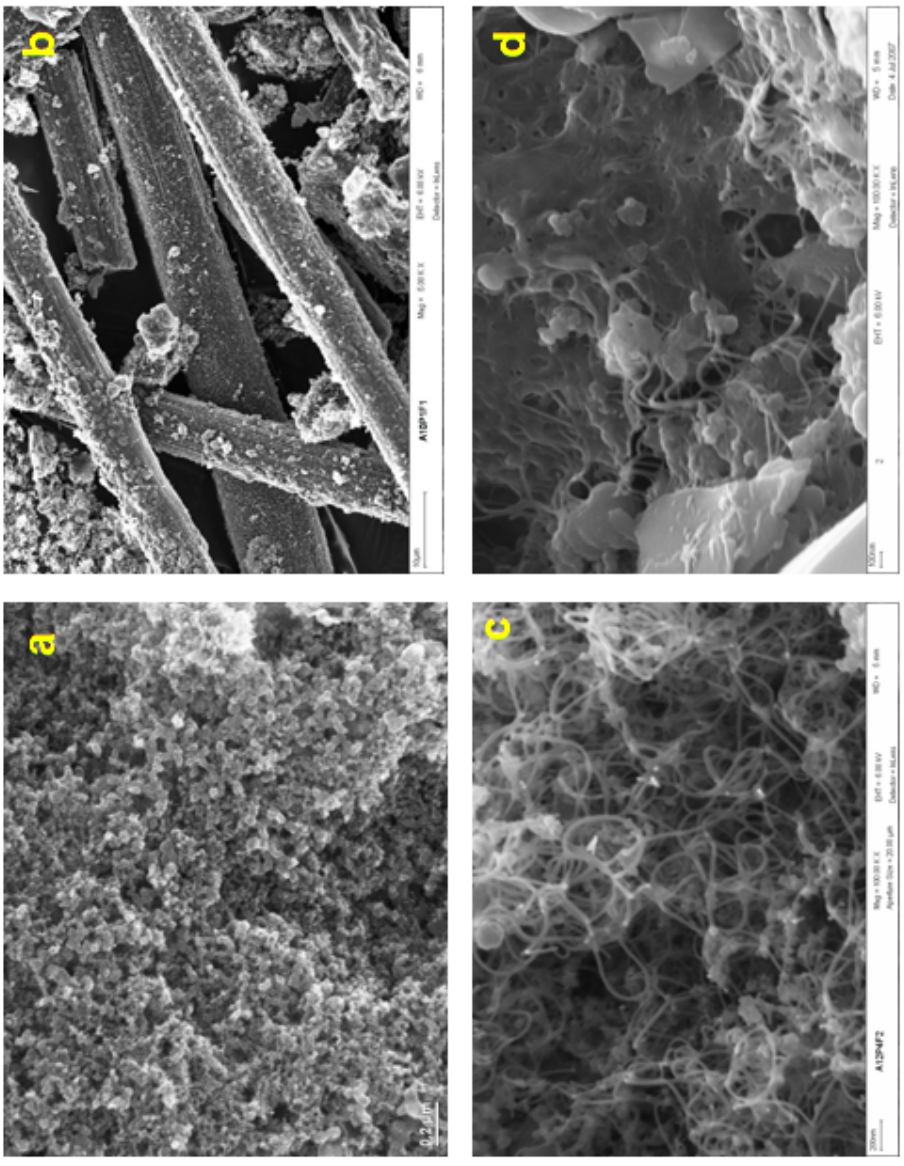


Figure 5.35: SEM images of as-prepared materials synthesized by the laser process under various conditions (a) no catalyst was used, producing amorphous carbon (b) A10P1F1, low temperature, low Ar gas pressure and low flow rate (c) A12P4F2 as-prepared SWCNTs under ideal conditions (d) dried solution of A12P4F2 sonicated in ethanol

5.3.2 Transmission electron microscopy (TEM)

In the hands of a specialist electron microscopist, the resolving power and capability of a high resolution TEM is a very powerful instrument in nanomaterials research. The instrument is far superior to that of a SEM and in carbon allotrope research, it has the ability to distinguish between single-walled, double-walled, multi-walled, graphitic, fibre and other exotic carbon based nanostructures. However, like the SEM, its use as a characterization tool in this dissertation was more qualitative in nature. The sample preparation method used in the TEM investigations was described in Section 4.8.3.

Figure 5.39 shows TEM images of sample A12P4F2 which were recorded at an accelerating voltage of 100 kV at 4 different magnifications. The amount of material typically deposited on a TEM grid is about 10^{-12} g and therefore must be used with caution when suggesting it is a finger print representative of a larger batch sample [151]. As seen in SEM images (Figure 5.35(c)), "spaghetti" like material was also seen in Figure 5.39(a), dispersed together with material that appeared as darker spots. These spots are metallic catalysts and appear dark in contrast to due to a higher intensity of diffracted electrons (EDAX measurements were not done). Under higher magnification as was observed in Figures 5.39(b-d), bundles and individual strands of SWCNTs were clearly observed. The nanotubes were observed to be decorated with what appears to be amorphous carbon. A closer inspection of the area surrounding the catalyst particles, which are typically between 5-20 nm in diameter, showed that in most cases, they were attached to SWCNT bundles.

In Figure 5.40, a SWCNT bundle was seen protruding out of the plane of the TEM grid. The cylindrical ends of the bundle tubes are clearly visible. However, the image is not sufficiently resolved to deduce whether the tube ends are either closed or open.

In Figures 5.41 and 5.42, TEM images of sample A10P4F2 are shown. A closer inspection reveals a significant content of graphitic strands which accounted for the high D peak observed in the Raman spectra of the same sample. Raman spectra of this sample indicated significant disorder.

In Figure 5.42, the results of an analysis at two regions A and B of a TEM image obtained from sample A12P4F100 were made. A measurement of transmitted electrons across the region of interest could be analyzed to reveal lattice spacings of the periodic structures. The region labelled A was a cross section of an individual SWCNT while region B was a cross section of concentric layers surrounding a metal catalyst particle. Two histograms of intensity vs distance were extracted (A12P4F1) and shown adjacent to the

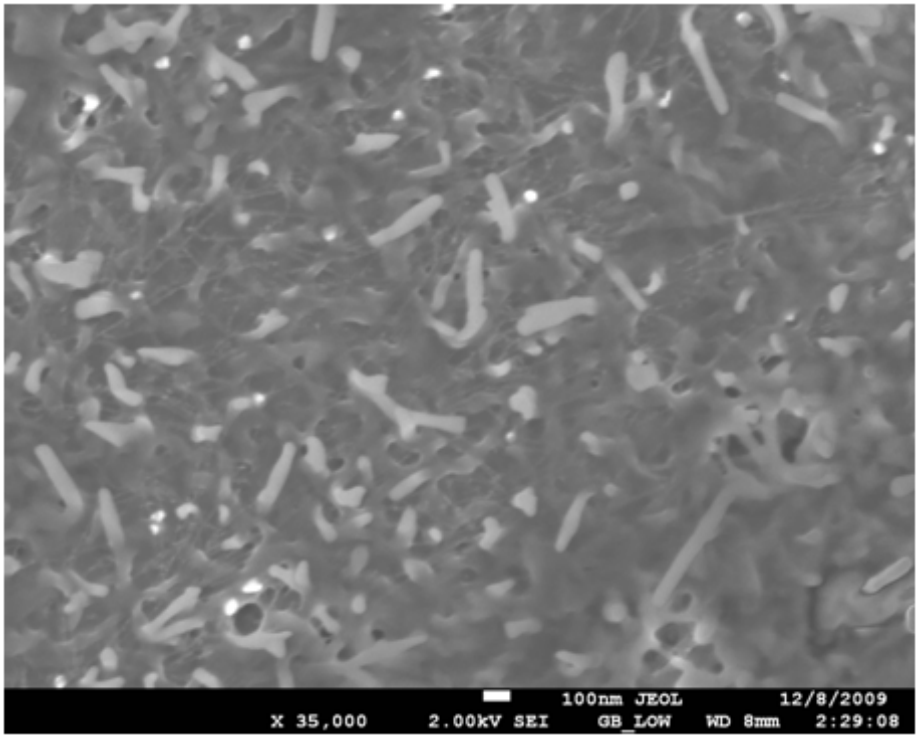


Figure 5.36: SEM of a dried thin film of SWCNT wrapped in 2% sodium cholate solution on top of a holey carbon TEM grid . Tubular structures appear white in contrast due to charging effects.

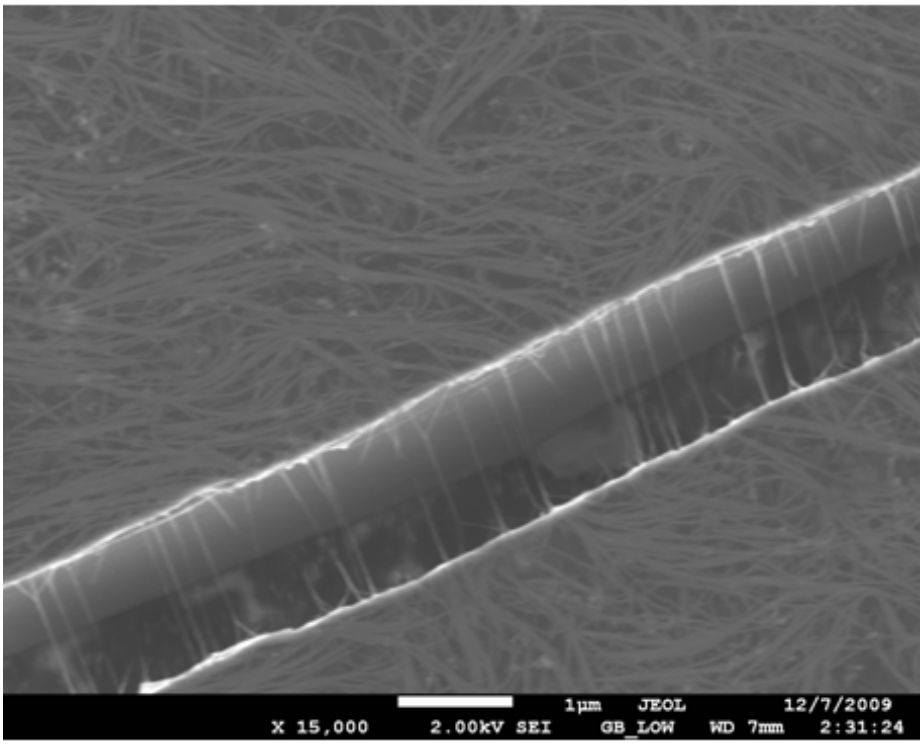


Figure 5.37: SEM of a dried thin film of SWCNT wrapped in 2% sodium cholate solution on top of a holey carbon TEM grid which underwent further heat treatment at 180 ^0C to remove surfactant. Nanotube strands were clearly visible between cracks of the holey carbon film.

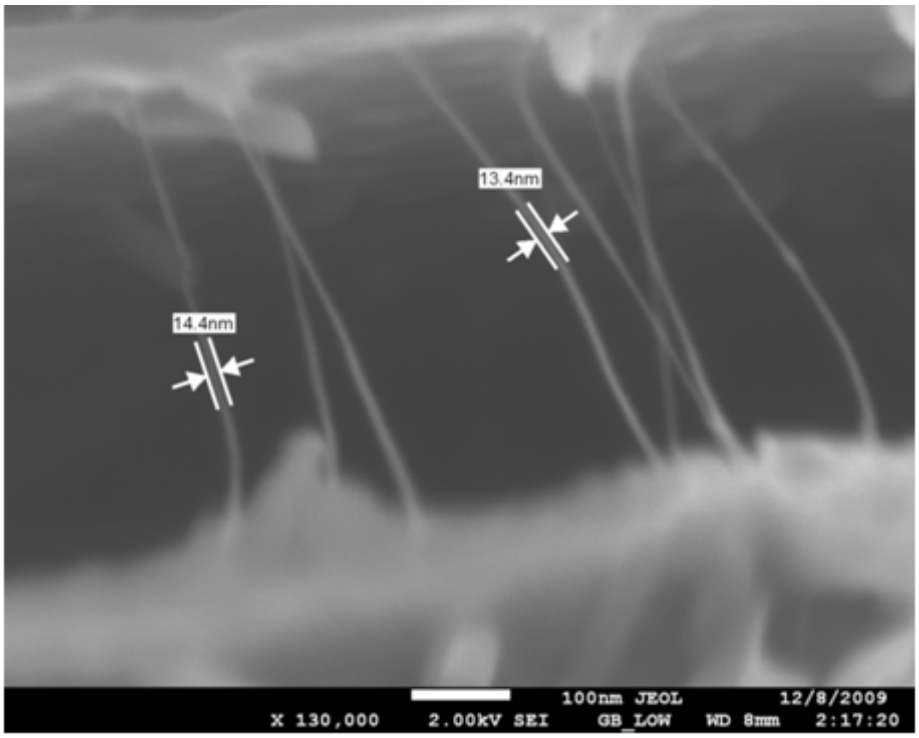


Figure 5.38: A zoomed SEM image of Figure 3.36, showing SWCNT bundles The surfactant "pulled up" at both ends between the crack to reveal the SWCNT bundle.

TEM image of Figure 5.43. From these plots it was determined that the diameter of the SWCNT was 1.22 nm and this is consistent with Raman and PL studies discussed in the earlier sections. The material surrounding the metal particle had a lattice spacing of 0.341 nm which corresponds very well to the interlayer spacing of graphite which is 0.336 nm.

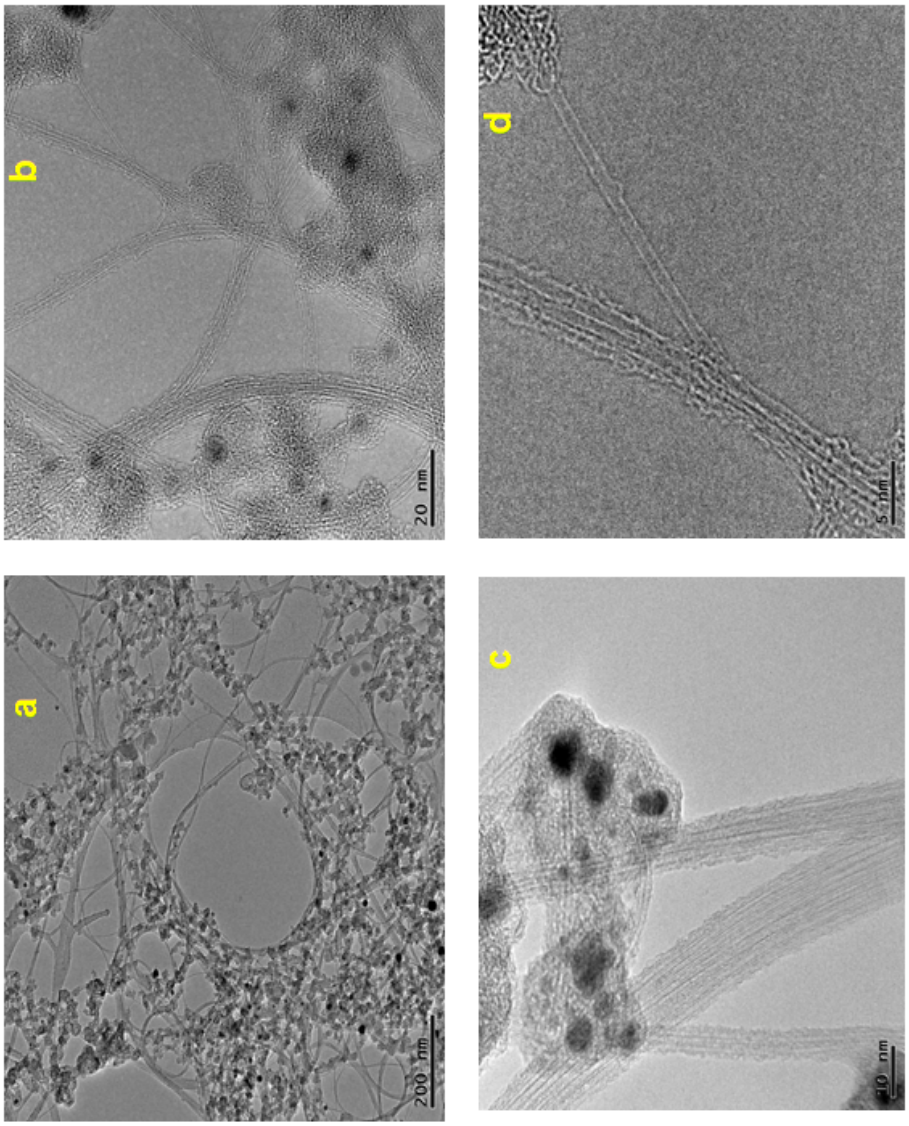


Figure 5.39: TEM images of sample A12P4F2 under increasing magnification from (a) to (d).

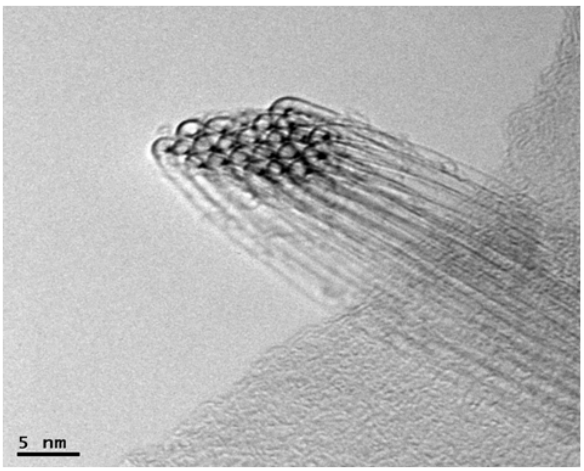


Figure 5.40: A broken end of a SWCNT bundle (A12P4F2) exposing the open ends of individual SWCNTs bonded together in a bundle by van der Waals forces.

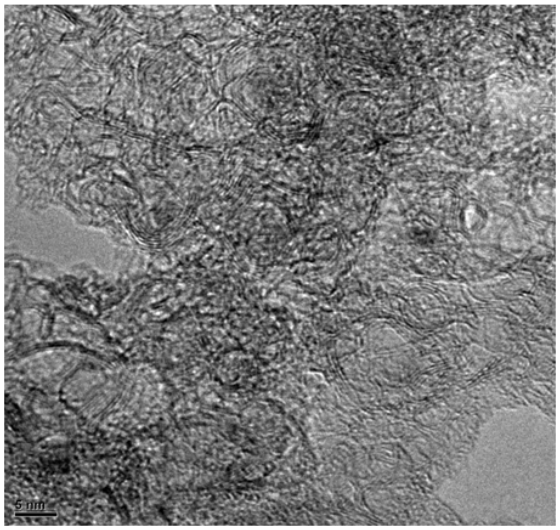


Figure 5.41: A TEM image of sample A10P4F2 showing a high concentration of graphitic ribbons.

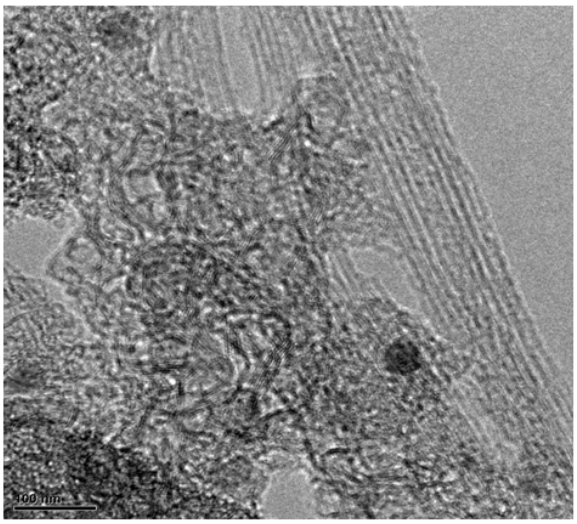


Figure 5.42: A TEM image of a region of sample A10P4F2 showing graphitic ribbons and SWCNTs. The high disorder band in the Raman spectrum of the sample could be attributed to the large concentration of these graphitic ribbons which are made of a few layers of graphene.

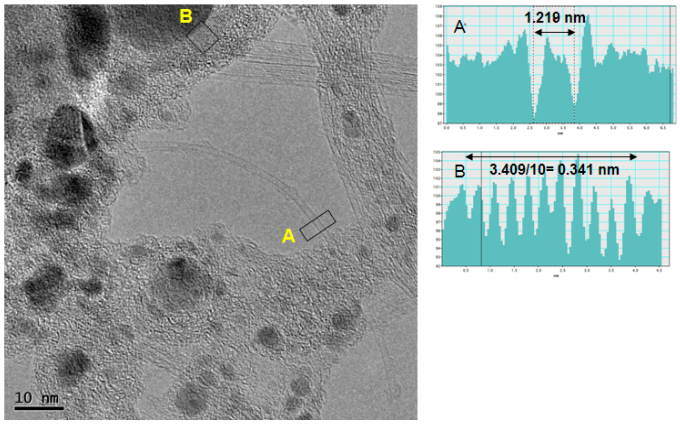


Figure 5.43: A TEM image of sample A12P4F1. Spot analysis at 2 regions A and B were made. The nanotube diameter at A was determined to be 1.219 nm while the layers surrounding the catalyst particle at B was found to correspond to that of graphite.

5.4 Discussions

The laser-furnace method was used to synthesize SWCNTs. As-prepared materials collected from this process method, contained a large fraction of SWCNTs and were characterized to evaluate its content by Raman spectroscopy, photoluminescence spectroscopy, scanning electron microscopy and transmission electron microscopy. These analytical techniques formed the basis to evaluate the effect of experimental parameters on the type of material synthesized (Tables 4.3 and 4.4). Results from the analysis are discussed and proposals made on the physical mechanism responsible for the nucleation and growth of single-wall carbon nanotubes.

5.4.1 Raman Spectroscopy

It is well known that Raman spectroscopy is a standard method to evaluate fullerenes [152] and materials containing SWCNTs [153]. Furthermore, more than one laser excitation is necessary to properly differentiate between the different possible nanotube families which are known to form in the self-assembly process. Thus the as-prepared materials were subjected to five laser excitations so that each of the predominant features of the Raman spectra, which define a SWCNT, were investigated to help understand the influence of process parameters on the nucleation and growth of SWCNTs.

Figure 5.1 shows a 3D graphical plot of the mass of material collected at the centre of the furnace and at the back-end of the quartz tube versus the pressure and argon flow rate. At low pressures and low flow rates of argon gas, more material is deposited in the inner-quartz tube than at the back. On the other hand, at high gas pressures and high flow rates, more material is deposited at the back. This plot shows the dynamical relationship between flow rate, pressure and plasma plume dynamics. Raman analysis of material collected at both regions showed (Fig. 5.2) that the material at the centre had a larger disorder content than material collected at the back end as borne out by the larger I_D/I_G ratio of 0.11 at the centre compared to 0.05 at the back. An explanation of the findings is given below:

- When the laser ablates the surface of the target, material is ejected perpendicular to the surface in the same direction as the incoming pulsed laser. Since the amount of ablated material depends on the energy of the laser, the speed and trajectory of the ablated material will thus depend on the gas pressure and the gas flow rate. In the experiments, the gas flowed in the direction of the incoming laser beam towards the expanding

plasma plume. This would slow the expansion as a result of collisions between argon gas atoms and the constituents of the plasma plume.

- Therefore, a higher flow rate would imply a lower plasma expansion rate. Similarly, the higher the gas pressure, the lower the plasma expansion. This would mean that the use of a higher flow rate and higher gas pressure would restrict the expansion of the plasma plume to a smaller volume. Thus, at a higher gas pressure and flow rate, less material would collect in region B i.e. inside the inner quartz flow tube.

- On the other hand, a combination of low flow rate and low pressure would mean that the expansion rate of the plasma plume would be at its maximum, increasing the amount of material reaching the inner quartz tube.

- At low pressures and low flow rates, the plasma plume has the highest expansion i.e. the least amount of collisions between plasma constituents. In a single laser shot, the ablated material consists of ions, electrons, molecules, clusters of molecules and larger particulates. Due to the different masses of the constituents in the plasma plume, results in a distribution of mass in the plume [128].

- Heavier masses such as carbon clusters and catalysts and other particulates have higher kinetic energies. However, they will experience higher resistance due to collisions with incoming argon gas atoms than lighter components of the plasma such as C_2 and other radicals. At low pressure and flow rates, the collision cross section between lighter and heavier elements will be reduced. Nanotubes that have already nucleated on larger metallic clusters, whilst still in the hot plasma, suffer poor growth since the collision cross section with C and C_2 which are essential for continuous growth, is reduced [154]. Hence, nanotubes found inside the inner quartz tube tend to have higher I_D/I_G values due to limited growth as seen in Figure 5.2

In Table 5.1, the results for the I_D/I_G (or I_D/I_{D*}) ratios for as-prepared materials synthesized using Target A, which contained 1% Ni and 1% Co, are shown. At a furnace temperature of 1073 K, a low pressure of 100 Torr and different flow rates give the best quality of material. A low I_D/I_G values of 0.17 was observed at a flow rate of 200 SCCM. As the furnace temperature increased, the I_D/I_G (or I_D/I_{D*}) ratio at a pressure of 500 Torr were observed to be 0.02. A low flow rate of 100 SCCM appeared to be the best choice across all

pressure and temperatures. This result can be explained as follows. Gas flow plays an important role in enhancing nucleation of SWCNTs by slowing the expanding plasma plume via collisions. However, excessive flow rates introduce instabilities in the plasma plume and rapidly quench it. While it was observed that the quality of nanotubes increased with furnace temperature, a high flow rate of 300 SCCM was seen to be detrimental to the synthesis of SWCNTs producing material with more defects. Collisional quenching [155], reduces the thermal energies of C and C_2 [156] causing these carbon species to quickly form amorphous structures or form structures with high defect ratio's.

The effect of changing the catalyst composition was investigated. The prime objective was to determine if the SWCNT synthesis was influenced, particular in terms of its chirality. Tables 5.2-5.6 shows the results of varying the catalyst composition on the I_D/I_G ratio's. Low I_D/I_G ratio's are important since this would be a requirement if the material is to be used in devices such as chemical sensors. At the same furnace temperature, pressure and gas flow rate, the use of the bimetallic combination of Ni/Fe (Target B) out-performs the traditional combination of Ni/Co (Target A). The I_D/I_G ratio's of material obtained from using Target B, were lower than material obtained from using all other targets (A, D, E, F and G). The use of Fe/Co (Target C) failed to produce any SWCNTs.

The use of the tri-metallic combination as in Target D produced material with I_D/I_G ratio's lower than material obtained from Target A. However, as was observed, a complex relationship between increasing the Fe concentration in the target; synthesis temperature and the resulting I_D/I_G (or I_D/I_{D*}) ratio of the as-prepared materials were found. Figure 5.44 shows graphs of the defect ratio (a) I_D/I_G and (b) I_D/I_{D*} plotted against temperature at different Fe concentrations.

While I_D/I_G is commonly [157] used to reflect defect concentration, it was shown by Maultzsch et al. [142] that I_D/I_{D*} gives a better reflection of the defect concentration. Here, both ratios are presented. Both plots provide similar information. What is noticed is the that the defect concentration decreased with increasing Fe concentrations when the synthesis was performed at 1073 K and a general decrease of I_D/I_G with increasing synthesis temperature was observed. However, a few anomalies in the plots was observed. Between 1273 and 1373 K, I_D/I_G (Figure 5.44(a)) values show a decrease while I_D/I_{D*} values show a marginal increase. Except for material synthesized from Target B, material synthesized from Target G (2% Fe) had the lowest defect value at 1073 K. While the defect values measured at 1073 K was extremely high and point to very poor quality SWCNT for all materials, it would be important to

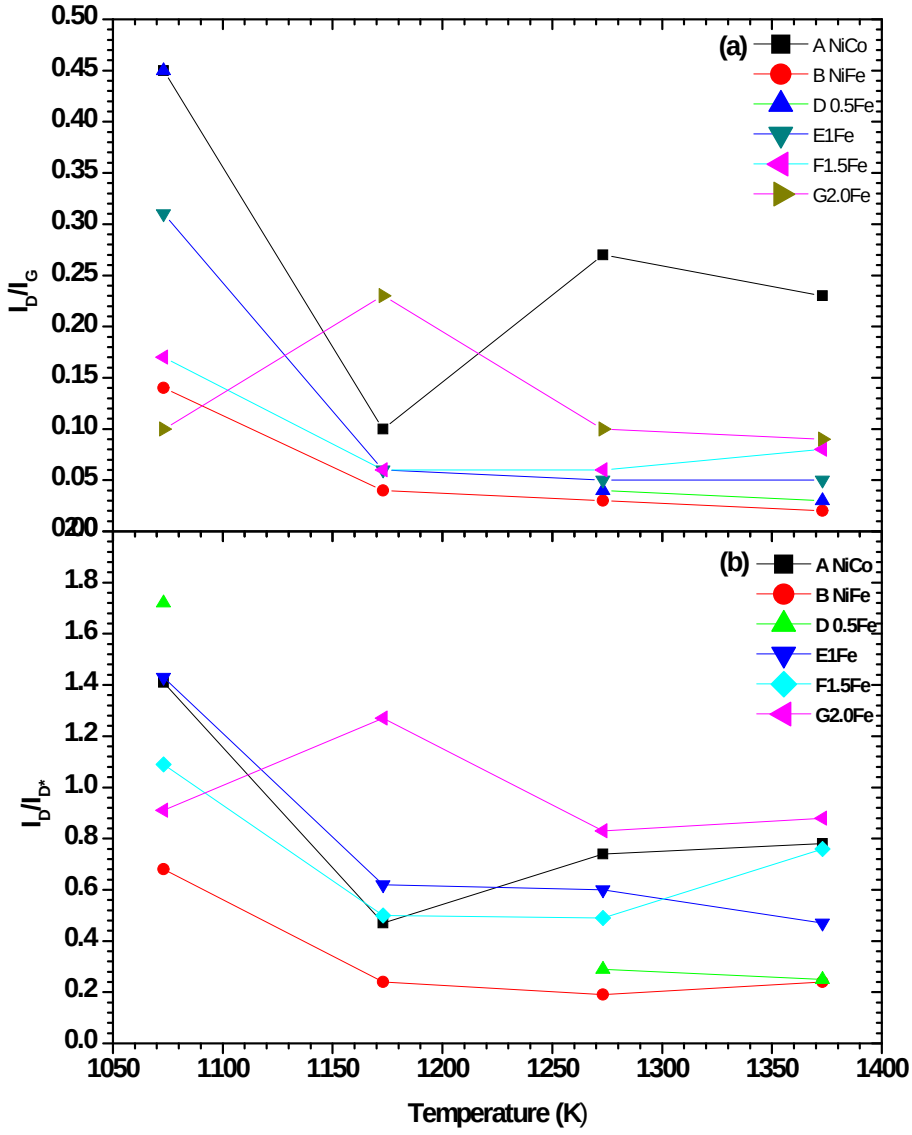


Figure 5.44: Graphical plots of the defect concentration as a function of Fe concentration and synthesis temperature (a) I_D/I_G (b) I_D/I_{D*}.

ask why the further addition of Fe decreased the defect ratio. A plausible and qualitative answer to this question is provided below.

The role of the catalyst in the nucleation of SWCNT involves the interaction of the electronic structure of catalyst and carbon molecules. Furthermore, nucleation and growth mechanisms appear to be different for laser ablation, CVD like methods and arc-discharge [39]. It is important to note that the combination of Co and Fe in this study did not produce SWCNTs and is consistent with the report of Yudaska et al. [139], were it was shown in the laser method, that Fe and Co was not conducive to SWCNT synthesis.

The data show that in the laser process, Ni is the essential element for SWCNT synthesis. However, it is more efficient than when combined with another catalyst such as Fe or Co transition metals as reported in several studies and reviews [39, 134, 158, 139]. The electronic structure of C, Ni, Co, and Fe was presented in Table 2.1. With respect to the outer electrons in the d-orbital, there are 2, 3 and 4 unpaired electrons for Ni, Co and Fe respectively. The reactivity of the metal increases with the number of unpaired electrons i.e. Fe>Co>Ni [1]. Reaction with carbon takes place when the d-orbitals of the transition metals overlaps with the p-orbitals of the carbon atoms [159]. Carbon has a tendency to utilize all unpaired electrons. When Fe is combined with Ni or when it is added to Ni-Co, alloys of these elements form. However, no ternary alloy forms with this combination of elements, only binaries phases of Fe_3Ni and CoFe and individual elemental phases [160, 161, 162]. A low defect value for material synthesized using the Ni/Fe target implied that it was a superior catalyst when compared with material synthesized with Target A (Ni/Co) at all furnace temperatures.

Incremental additions of Fe to the Ni/Co combination increased the Fe/Ni component. Therefore, the low I_D/I_G defect ratio (as was observed with Target B) can be explained by the increasing Ni/Fe component in the catalyst mixture. However, while the Ni/Fe component increased, the FeCo component also increased in the catalyst mixture. We have already stated that a combination of FeCo was ineffective in synthesizing SWCNTs. While I_D/I_G values were seen to decrease with increasing Fe concentration due to Ni/Fe component, it was also seen that the yield in SWCNT dropped. This could be seen from the drop in Raman intensity with increasing Fe concentration due to increasing FeCo content in the catalyst mixture (Fig.5.9-11).

When the synthesis temperature was increased to 1173 K, a decrease in I_D/I_G were observed. An increase in thermal energy of the system, allows increased flexibility in the bond formation between carbon atoms so that structures with reduced strain and lower defect concentration will form, similar to

the effect of annealing. This phenomenon of the reduction of defect concentration with increasing Fe concentration was observed for all samples except Target A. This could not be explained.

At 1373 K, a rise in the defect ratio's was noted. This could be explained by the fact that the catalysts were in a "sea" of carbon reaching the eutectic temperature. The eutectic point is the lowest temperature at which carbon and the catalysts in the hot melt solidifies as a single composition. The temperature of the eutectic point for the individual carbon-catalyst are: 1602 K for C-Ni; 1597 K for C-Co; 1426 K for C-Fe [160, 161, 162]. With increasing synthesis temperature the solubility of C in Fe increases, resulting in the formation of the dominant metal-carbide and a subsequent loss of activity in that catalyst since the formation of the carbide, suppresses the catalytic activity of the metal [139].

The RBM bands of materials synthesized from Targets A, D, E, F and G were analyzed. The RBM spectral region was deconvoluted by fitting Lorentzian curves with each peak corresponding to a unique nanotube family. The results for material synthesized from Target A are shown in Table 5.8 while the fits and chiral assignment for nanotubes produced from Targets D, E, F and G are shown in Figures 5.16-5.23. To determine the composition with certainty, a Raman mapping of the RBM spectral region was required which was not possible in our investigations. From the fitted spectra, it was found that metallic SWCNTs (m-SWCNTs) dominated and also increased in content in all samples as temperature increased from 1073 K to 1373 K. From the five available laser excitations, a rough estimate of at least 90% m-SWCNTs was observed. On the other hand, s-SWCNTs were more prominent at 1073 K and 1173 K than at 1273 K and 1373 K. In the CVD methods of synthesis such as the HiPCo (high pressure CO decomposition) [14] and CoMoCAT [15] (CO decomposition on cobalt molybdenum catalyst), 66% of the as-prepared material were reported to be semi-conducting type. In a recent report by J. Liu and M. Hersam [61], the composition of metallic SWCNT was estimated to be 70% for the laser method.

In general, increasing synthesis temperatures are conducive to increased RBM intensities and correlates well with reduced defect ratios as was discussed earlier. While the width of the RBM spectral region was reduced, more Lorentzian's were required to fit the RBM spectral region at higher synthesis temperatures. This meant that although higher temperatures were responsible for better quality nanotubes, and higher yields, the synthesis of SWCNTs with small variation in chirality became thermodynamically possible. This fact also corroborates very well with PL results (see discussions below).

As observed in the general analysis of Raman spectra, the intensity of the RBM bands showed a decrease in intensity primarily due to the formation of FeCo alloys which inhibited the nucleations of SWCNTs. Small but significant changes were also observed in the RBM bands. There was a distinct shift to lower wave numbers of the RBM spectrum pointing to the synthesis of larger diameter SWCNTs. It is proposed that an increase of the lattice constant on which the SWCNTs nucleate takes place. This change is due to formation of new Ni-Fe alloys. The increase in the lattice constant is from Ni [a= 352.4 pm] to Ni_3Fe [355.2 pm] [162]. The increase in the lattice constant facilitates the nucleation of larger diameter nanotubes. This is consistent with reports by Zhang et al. [163] where studies on Fe concentration was varied from 0.1 to 0.8% wrt 0.3% Ni/0.3%Co. In their report, a drop in I_D/I_G (or I_D/I_{D*}) ratios was not reported.

We have found that incremental increases of 0.5% Fe in the target composition was detrimental to SWCNT synthesis. Significant drops in RBM intensities were observed. This could be attributed to the increase in FeCo catalyst which inhibited SWCNT synthesis. Therefore, we could deduce that by increasing Fe concentration beyond 1.5% increased the reactivity of the catalyst (Fe) to a point where it became detrimental to the synthesis process.

Due to the complexity of understanding the physics of photon-phonon–electron interactions, much of the published reports on Raman analysis of the D and G bands have been performed on individually SWCNTs dispersed and wrapped in surfactant [144]. In our study, only as-prepared bundles were analyzed. Of importance were the shape of the G^- bands. When it could be fitted by a Lorentzian curve, it implied the presence of s-SWCNTs. When it could be fitted by BWF line-shape, it implied m-SWCNTs. While both of these lines-shapes were observed, the BWF lineshape representing metallic nanotubes were only detectable with the 647 nm laser excitation even though RBM analysis from all 5 laser excitations have shown that most of the nanotubes were metallic. So it would have been expected from RBM analysis that the BWF line-shape should have been more prominent in all Raman spectra of the G band instead of only appearing when excited by the 647 laser excitation. Further work is required to understand why this is the case.

The D^* band is the second overtone of the D band. The peak position of the D^* band showed a laser excitation dependence. The band drifted to higher wavenumbers of the Raman spectrum with increasing laser excitation energy. While the position, ϖ_D of the D band was accurately described by eqn. 5.2 (Figure 5.28(a)), the position ϖ_{D*} of the D^*, it was observed that $\varpi_{D*} \neq 2\varpi_{D*}$ (Figure 5.28(b)). The position ϖ_{D*} was offset by about 26 cm^{-1}. We attribute

these differences to bundling effects of tubes of different chiralities. Resolving features of the D* which are rich in information about the chirality which affects ϖ_{D*} due to curvature-induced strain and quantum confinement effects [37], was not possible.

5.4.2 Photoluminescence spectroscopy

PLS is a valuable characterization tool to evaluate semiconducting single-walled carbon nanotubes (s-SWCNTs). The synthesis conditions such as target composition and furnace temperature were varied to evaluate the effect on the type of s-SWCNT that were synthesized. Indeed, we found that the synthesis conditions influenced the nucleation and growth of SWCNTs. For example, it was found that PL from measurements on material synthesized from Target A, that when the synthesis temperature was increased, SWCNTs of larger diameters were promoted i.e. $(7,6)$ (1073 K) $\Longrightarrow$ $(8,6)$ (1173 K) $\Longrightarrow$ $(9,7)$ (1273 K) $\Longrightarrow$ $(9,8)$ (1373 K).

However, contrary to the Raman results, we found that PL intensities of SWCNTs decreased with synthesis temperature. Increasing synthesis temperatures from 1073 K to 1373 K in the laser-furnace method promotes the nucleation of m-SWCNTs. From Raman spectroscopy, fractions as high as 90% in metallic composition were observed. Hence the, PL samples became enriched with metallic nanotubes.

The presence of m-SWCNTs are known to severely quench PL emissions of semiconducting SWCNTs [164]. This may explain the drop in PL intensity at higher temperatures. To strengthen the point that the lower synthesis temperatures favour s-SWCNTs and higher temperature favour m-SWCNTs, RS was measured on samples prepared for PL. In Figure 5.45(a-d), Raman spectra (785 nm laser excitation) of as-prepared and PL samples of (a) A10P4F2, (b) A11P4F2, (c) A12P4F2 and (d) A13P4F2 are shown. It was observed that the Raman intensity of A10P4F2 dispersed in sodium cholate (A10P4F2-NC) was several orders of magnitude stronger than the weak Raman signal emanating from the as-prepared samples. On increasing the synthesis temperature, the strength of the Raman bands intensity of the as-prepared samples increased, and the Raman intensity of the A11P4F2-NC PL samples showed a dramatic increase.

In these cases, the PL measurements, in terms of intensity, correspond well with Raman spectra. It appears that the PL sample preparation method enriched the SWCNT content. However, for A12P4F4 and A13P4F2, the reverse was observed. The Raman signal from the PL samples was relatively

weak when compared to the as-prepared sample. Furthermore, the positions of prominent peaks shifted with temperature i.e., as the synthesis temperature increased, peaks from the lower wavenumber region of the Raman spectra of the PL samples disappeared. At 1373 K (Fig 5.45(d)), hardly any overlap of peaks was observed. Clearly, the sample preparation method has discriminated against larger tubes. To investigate this more clearly, the RBM modes of the Raman spectra of PL samples were fitted with Lorentzian's line-shapes to determine possible tube assignments.

The fitted spectra are shown in Figure 5.45(e-h). From these fitted assignments, the PL spectra shown Figure 5.29(a-d) could be rationalized. s-SWCNT dominate the spectra shown in Fig.5.45(a,b) but on increasing the synthesis temperature, peaks associated with m-SWCNT become dominant. The presence and dominance of metallic tubes with increasing synthesis temperature was the reason for the quenching of PL emission from s-SWCNTs.

Spectral plots of SWCNT diameters versus chiral angle of samples showed no definitive pattern or special features which could be attributed to changes in synthesis parameters. While some s-SWCNTs were prominent at all synthesis temperature, there were many nanotubes that appeared to have formed in a random fashion. Chiral plots showed the presence of a tremendous variety of s-SWCNTs. There was a large spread of chiral angles of SWCNTs between 0^0 and 30^0. However, it was observed that at higher synthesis temperatures, the diameters of the s-SWCNTs were restricted to between 0.9 and 1.2 nm.

PL spectra of samples shown in Table 5.7, showed a lowering of the intensity and resolution of the peaks with increasing Fe concentrations. Decreasing Raman RBM intensities were observed on increasing the Fe concentration. It is proposed that this is due to the increase of FeCo alloy which is detrimental to SWCNT synthesis. The decrease in intensity of the PL spectra can be attributed to PL quenching due to the presence of m-SWCNTs and not the quality or quantity of SWCNTs. This statement can be argued by the fact that the RBM intensities of A10P4F2 were lower than all samples synthesized from targets having increasing Fe content. However, the resolution of the spectra was much better and this was attributed to the synthesis temperature. The population of s-SWCNTs was more significant than m-SWCNTs. Therefore it was not the lack of SWCNTs but an overall excess of m-SWCNTs which caused the deterioration of the PL spectra, as the synthesis temperature was increased.

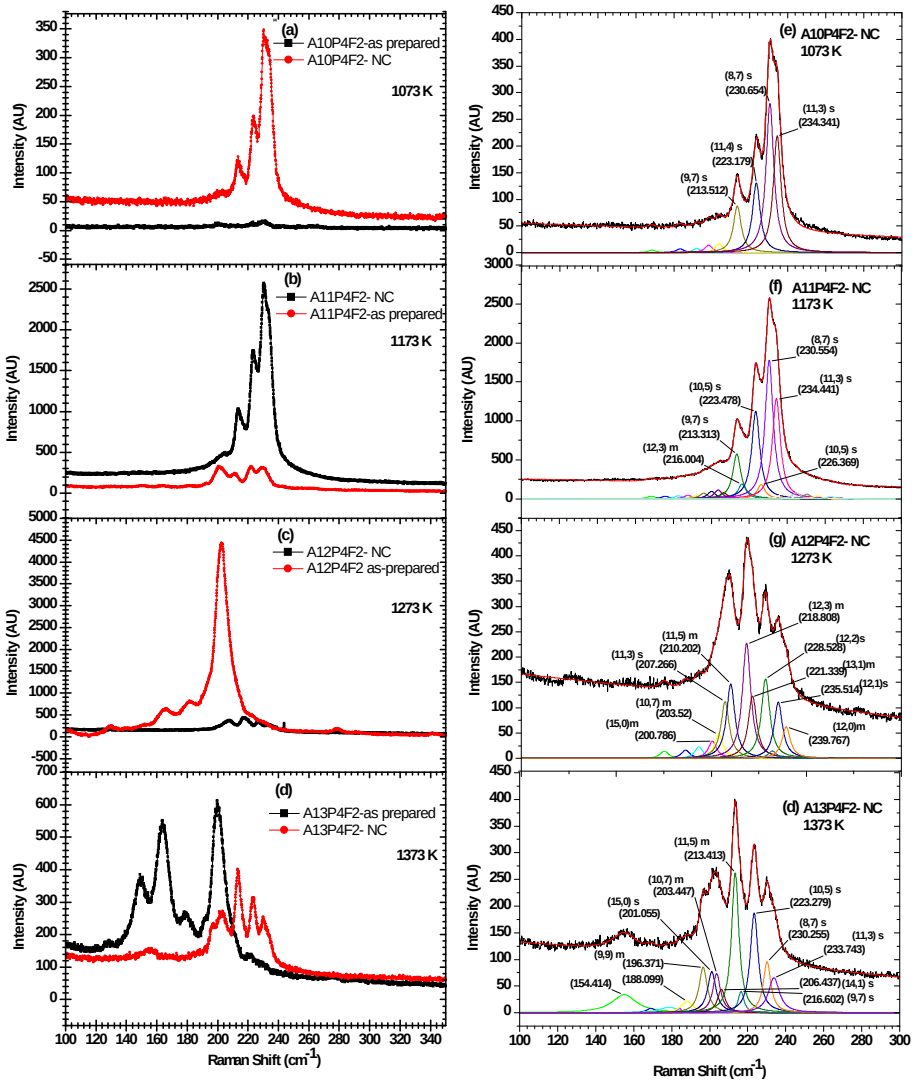


Figure 5.45: A comparison of Raman spectra obtainned from as-prepared materials and samples prepared for PL measurements shown in (a-d) and fitted Raman spectra of PL samples shown in (e-h)

Chapter 6

Optical Emission Spectroscopy (OES) studies applied to Carbon Nanotube Synthesis

6.1 Introduction

In Chapter 4, the experimental set-up for the laser-furnace method in synthesizing SWCNTs was described. In Chapter 5, as-prepared materials synthesized from the laser-furnace method were characterized by Raman spectroscopy, photoluminescence spectroscopy and electron microscopy. The experiments revealed that a variety of SWCNTs (m-SWCNTs, s-SWCNTs and chiral SWCNTs) were found in all as-prepared materials irrespective of which process parameters were chosen. This, was a consequence of the phenomenon of uncontrolled self-assembly. As yet, efforts to control the synthesis of SWCNTs with specific diameters and hence chiralities, the Holy Grail of SWCNTs research, has alluded all research groups. Due to the technological importance and potential of SWCNTs, various separation methods have been adopted from biology and applied to sort and separate SWCNTs. This includes attempts to sort SWCNTs according to their chiralities using density gradient ultracentrifugation (DGU) [68] etc. A recent review on the state and progress in this field was recently published by Lui and Hersam [61]. These efforts bring SWCNTs one step closer in being used in advanced consumer products [22].

The study of growth mechanisms and the control of self-assembly of carbon is not only of importance in carbon nanotube research but is also fundamental to the study and behavior of most materials at the nanoscale. Hence unique insights are learnt in material science from SWCNT studies. In this thesis, an effort was made to understand the dynamics of the laser-induced plasma

environment in which SWCNTs nucleate and grow on metallic catalysts. If optical access to the laser generated plasma is limited to short periods (seconds), a temporal and spatial study of the plasma by optical emission spectroscopy (OES) becomes possible. In this way, the effect of experimental conditions on the plasma characteristics such as electron density, electron or plasma temperature, as well the role of carbon and catalysts in the nucleation of SWCNTs can be made.

In recent times, only a handful of research groups have applied the OES method to the investigation of carbon nanotube synthesis. In the laser-furnace process, these were applied by Arepalli et. al. [136, 165], Ishigaki et al. [166], Puretzky et al. [167] and Nakanishi et al. [168]. OES was applied to the arc-discharge method by Nishi et al. [169]. OES procedures have also been applied in less common synthesis methods which are variations of a combined plasma/CVD methods such as the triode plasma CVD [170], RF thermal plasma [171], pulsed-DC PECVD [172] and the microwave plasma CVD method [173].

In most of these studies, the temporal and spatial behavior of dominant emission bands such as the C_2 Swan bands were investigated. However, no conclusions were made as to the role of C_2 on SWCNT nucleation or, if and when nucleation took place from C_2 or any other carbon species. Furthermore, in applying OES to pursue a temporal and spatial study of the electron density and electron temperature of a plasma, either induced by laser or by high electrical voltage discharge, no group has yet deduced any link or correlation between the changes in electron density, electron or plasma temperature as evidence of the nucleation of SWCNTs.

In this chapter, we have applied *in situ* OES to study the plasma in the laser-furnace method to synthesize SWCNTs. In particular, we have investigated the temporal and spatial behavior of C_2 as well as the electron density and electron temperature. In Chapter 5, the effect of temperature was shown to be most important parameter that influenced the quality of SWCNTs. In this chapter, the role of temperature in influencing C_2 populations, electron density (N_e) and, electron temperature (T_e) was also investigated for targets containing catalysts and without catalysts. In addition, material obtained by single-shot experiments were evaluated by Raman spectroscopy. The results of these experiments are discussed and experimental evidence for the early nucleation and rapid growth of SWCNTs is revealed. Furthermore, using the results and discussions described in Chapter 5, a growth model for SWCNTs is proposed.

6.2 Characterization of laser induced plasmas by OES

The interaction of high-power laser radiation with a target material has been an active topic of research not only in plasma physics but also in the field of material science, chemical physics and particularly in analytical chemistry [174]. The high intensity laser beam (10^7-10^{11} W.cm^{-2}) impinging on a solid target dissociate, excites, and/or ionizes the constituent atomic species from the solid and produce a plasma, which expands either in the vacuum or in an ambient gas. As a result of the laser-matter interaction, various processes may occur such as ablation of the material, high energy particle emission, generation of various parametric instabilities as well as emission of radiation, ranging from the visible to hard X-rays, depending on the intensity of the laser. These processes have been exploited in various applications [123, 174]. In this dissertation, the focus is on the study of optical emissions from laser-induced plasma's which is known collectively as as laser-induced breakdown spectroscopy (LIBS) or laser induced plasma spectroscopy (LIPS) [155]. The basics of a laser interacting with a target surface was covered in Section 4.4 and therefore will not be repeated here. Instead, only the processes taking place within the laser induced plasma and those plasma parameters, which were of vital importance to this work are discussed.

6.2.1 Spectral emission from a laser induced plasma

One of the more important processes, in laser-plasma interactions, are the emission of radiation from the plasma ranging in wavelength from the visible to hard X-rays [174]. This process is very relevant for an understanding of LIPS. It has been found that X-rays are emitted from all parts, during the absorption, interaction and transport regimes. At densities near and slightly above the critical ablation threshold, nearly 70% of the incident laser energy may be re-emitted as X-rays with energies ranging from 50 eV to 1 keV and above. This depends on the temperature of the plasma. However, as the plasma expands away from the target surface adiabatically, its density and temperature decreases. As the plasma temperature decreases, the wavelength of emissions from the plasma increases, i.e., emission shifts from X-rays, to radiation in the visible region.

6.2.1.1 Continuum Emission

The spectral composition of emissions from a plasma has both line and continuum components. The study of characteristic line emissions from the plasma gives information about the composition of target material, i.e., the elements present in the target. The continuum radiation is emitted by the plasma as a result of free-free and free-bound transitions. Free-free transitions (Bremsstrahlung emission) are due to the interaction of electrons with positively charged ions of charge Z and density N_Z. Neglecting the correction factor (the Gaunt factor), the free-free spectral power intensity, for a Maxwellian electron distribution at a temperature T_e is given by [175]:

$$I_v \approx Z_{eff} \frac{N_e N_Z}{T_e^{1/2}} \exp\left(-\frac{hv}{T_e}\right) \tag{6.1}$$

where Z_{eff} is the effective charge for Bremsstrahlung emission, which is generally different from Z due to the partial screening of the nuclear charge Z_N by the $(Z_N - Z)$ electrons [176]. Eqn. 6.1 shows that the logarithmic slope of the spectrum can provide information about the electron temperature, T_e of a plasma. The inverse process is called inverse Bremsstrahlung and is responsible for the absorption of laser radiation at or below the critical density region. When the electron distribution function is not Maxwellian, it is in principle, possible to deconvolute it from the high photon energy non-thermal spectrum (since free-free radiation is very sensitive to high-energy tails). In the case of a laser-produced plasma, the high-energy electrons (usually called supra-thermal electrons) have long mean free paths and can therefore penetrate into the cold solid target. In this case, the Bremsstrahlung spectrum is modified because the electrons, of all energies, are slowed down by their interaction with the cold solid matter [130].

In a free-bound (recombination radiation) transition, a free electron with kinetic energy, ξ_e, is captured by an ion of charge Z in a bound level n of the ion of charge $Z-1$, with ionization energy χ^n. This results in the emission of a photon of energy $hv = \xi_e + \chi^n$. The photon energy is a function of ξ_e, but only photons with $hv > \chi^n$ are emitted. The spectra therefore show discontinuities. These are generally called recombination edges. Above the edges, the spectral dependence is the same as for free-free transition, and T_e can therefore again be deduced from the logarithmic slope. Non-thermal electrons do not contribute to the free-bound spectrum, because the recombination cross-section decreases rapidly for $\xi_e \gg \chi^n$ [130].

6.2.1.2 Line Emission

The emissivity of a spectral line (i.e. number of photons emitted per unit time and per unit volume) is equal to the product of its radiative transition probability times the emitting excited level density. On the other hand, the absorption coefficient for line radiation is obtained from the radiative transition probability by using the Einstein relations. For the interpretation of the line emission, the excited level population should be known [175].

6.2.1.3 Temporal and Spatial Resolution of Emissions

Emissions from a laser produced plasma, in general, and optical emissions in particular, has been extensively studied by using temporally and spatially resolved spectroscopy. It has been observed that initially, after plasma formation, an intense continuum is emitted, which remains close to the target surface [174]. This emission from the dense plasma is like a black body continuum radiation. However, as the plasma expands away from the surface of the target, it cools and the emission is dominated by the spectral lines. During this expansion the spectral lines from highly ionized atoms are observed close to the target surface whereas those from neutral atoms are observed in the plume away from the target. Thus, line emissions are superimposed on the continuum emission.

The line emissions from the multiple ionized species occurs at the time of plasma formation, whereas emission from singly ionized and neutral species are observed nearly 500 ns after the plasma-formation. The rates of decay of the continuum and line emissions are different. The continuum emission due to Bremsstrahlung from the hot plasma decays faster in comparison to the line emission. Thus, it is necessary to record the emission after a certain time delay to get clear information about the line emission from the cold plasma for the purpose of elemental analysis [130, 174, 155].

6.2.2 Theoretical Models for the Plasma

The interpretation of the radiation emitted by the plasmas requires knowledge of both the charge state distribution and the excited level populations of different ions. This is possible by obtaining the solution of a complex system of rate equations, which describe the population and depopulation of all the levels by the processes such as ionization, recombination, collisional excitation and de-excitation, radiative decay and absorption as well as the stimulated emission [128]. Any given charge state is connected with its two neighboring states by the processes of ionization and recombination. Considering the

difficulties associated with solving these equations, approximations are used. These are, in order of increasing electron density are the corona model (CM), the collisional-radiative model (CRM), the local thermodynamic equilibrium (LTE) and models suitable for ultra high electron density ($N_e \geq 10^{24} cm^{-3}$) [176, 177]. Here, the local thermodynamic equilibrium (LTE) is briefly discussed since it is this model which was used to describe the laser induced plasmas generated in this study.

6.2.2.1 Local Thermodynamic Equilibrium (LTE) Model

In the LTE model [176], it is assumed that particle collision processes are mainly determined by the distribution of the population densities of the electrons. The collisions of the electrons are so fast that the electron densities change with sufficient rapidity and the distribution responds instantaneously to any change in the plasma condition. In such circumstances, each process is accompanied by its inverse and these pairs of processes occur at an equal rate. Thus, the distribution of population densities of the energy levels of the electrons is the same as it would be in a system in complete equilibrium. The population distribution is determined by the statistical mechanical law of equipartition among the energy levels and does not require any knowledge of atomic cross sections.

The plasma temperature and density vary in space and time, but the distribution of population densities at any instant and point in space depends entirely on the local values of temperature, density and chemical composition of the plasma. The uncertainty in the prediction of spectral line intensities from the LTE model plasma, depends mainly on the uncertainty in the values of these plasma parameters and atomic transition probabilities. For analytical plasmas, the condition of LTE was considered important for getting any reliable quantitative information. In the case of thermal equilibrium, all the processes in the plasma are collision dominated as discussed above and the plasma can be considered as having a single temperature, i.e. the temperature of the ions is equal to the temperature of plasma, $T_i = T_e$. However, in the expanding plasma, this is possible only locally and for a specific time interval during the evolution. The following criterion must be satisfied by the plasma for it to be in local thermodynamic equilibrium [176, 131]:

$$N_e \geq 1.6 \times 10^{12} \Delta E^3 T_e^{1/2} \tag{6.2}$$

where ΔE in eV is the largest observed transition energy for which the condition holds, and T_e is the electron temperature in Kelvin. It should be

noted that the choice of the time delay is crucial for obtaining the best operating conditions in the laser induced plasma to ensure that LTE prevails during the measurements. However, it has also been found that LTE is not an indispensable condition for qualitative analysis, once the measurement conditions are kept constant and are reproducible.

6.2.3 Measurement of Plasma Parameters

During the experiments, reliable information must be extracted from optical spectral emission data so that the calculations of important plasma parameters such as N_e and T_e (plasma temperature) can be considered to be reliable reflection of the state of the plasma at any instant in time. Some relevant information about the measurement of these parameters is given in below.

6.2.3.1 Line Broadening

In the spectroscopic study of line emissions from the plasma, the intensity of the spectral line as well as its profile is important. The emission line profile is important because it contains information related to the emitter and surrounding plasma environment. An introduction to the theory of line broadening can be found in the books by Griem [176, 177]. Various types of line broadening have been observed in the plasma emission. Natural broadening occurs due to the finite lifetime of excited states and results in the emission intensities having a Lorentzian profile. The Doppler broadening occurs due to thermal or directed motion of the emitting ions and has a Gaussian line shape with a width proportional to the square root of the emitter temperature. This is the dominant broadening mechanism at low electron densities.

Stark broadening which is also known as pressure broadening is observed because the emitting ions experience an electric field due to the presence of plasma electrons and ions around them. This electric field varies statistically for individual emitters and fluctuates in time. The net result is an ensemble averaged line-shape with an overall width related to the average strength of the perturbation in the bound states.

During the early stage of plasma formation, the electron density remains very high ($N_e \sim 10^{15} - 10^{18} cm^{-3}$). As a consequence, the line profiles are dominated by Stark broadening for a considerable period of time [176]. Doppler as well as natural broadening is generally negligible during this period. When the expanded plasma cools and the electron density decreases, the dominance of Stark broadening is reduced, and Doppler broadening starts playing a leading role. It is well known that the final measured line profile normally contains

a contribution from the spectrometer used to measure the width of the line profile. This indicates that measured profiles must be deconvoluted prior to their analysis for the extraction of plasma parameters.

The instrument width needs to be measured experimentally for a given spectrometer. This is dependent on parameters such as slit width, the grating dispersion, and the dynamic behavior of the photon detector. The central peak of the spectrometer slit function can be approximated to a good degree of accuracy by a Lorentzian profile. Since both (the Stark-broadened) spectral line and the spectrometer exhibit Lorentzian shape functions [155], convolution and deconvolution was straight forward. In this case line widths can simply be added or subtracted in the convolution/deconvolution process as given below:

$$\Delta\lambda_{Total} = \Delta\lambda_{line} + \Delta\lambda_{spectrometer} \tag{6.3}$$

6.2.3.2 Electron Density

The width of Stark-broadened spectral lines in plasmas depends mainly on the electron density N_e [176]. Both the linear and the quadratic Stark effect are encountered in spectroscopy. However, only hydrogen atoms and H-like ions exhibit a linear Stark effect, whereas all other atoms exhibit a quadratic Stark effect. This is the reason that in the ideal case, the electron density is extracted from the lines of H or H-like ions, where the half width of the line profile can be calculated easily and with a greater accuracy. However, in this study, hydrogen was not used and does not feature in the measured spectra. In the case of the linear Stark effect, the relation between electron density and the line width is given by a simple relation [177]:

$$N_e = C(N_e, T_e)\Delta\lambda_{FWHM}^{3/2} \tag{6.4}$$

where $\Delta\lambda$ is the "true" full-width half-maximum (FWHM) and the parameter C which has a weak dependence on N_e and T_e, can normally be treated as being constant. The constant C for the H Balmer lines is available in the literature. The first choice for electron density determination in LIPS plasmas containing hydrogen is the H line (with an error of 5%) [176] because of its large intensity and sufficiently large line broadening. These effects can be measured precisely using a spectrometer of moderate resolution. The possibility of self-absorption in this case is relatively small. The second best choice among the Balmer series is the H line. The H line is suitable in cases where the electron density is not too high, $N_e \sim 10^{17} cm^{-3}$. At higher electron densities this strong line is quite susceptible to self-absorption, which severely distorts the

line profile. In the case of non H-like atoms, where the quadratic Stark effect is dominant, the relation between the electron density and the line width is [176]:

$$\Delta\lambda_{FWHM} \approx 2\left[2 + 1.75 \times 10^{-4} N_e^{1/4} \alpha(1 - 0.068 N_e^{1/6} T^{-1/2})\right] \times 10^{-16} w N_e \quad (6.5)$$

The first term in the brackets gives the contribution from electron broadening, and the second term stems from ion broadening. Here w is the electron impact parameter and $N_e = 10^{16} cm^{-3}$, and α is the ion broadening parameter. The parameters w and can be found in the literature [176, 177]. Since the second term in Eqn. (9) is small, the above expression reduces to:

$$\Delta\lambda_{FWHM} \approx 2 \times 10^{-16} w N_e \quad (6.6)$$

which is normally used for calculations in the case of plasmas generated from solid targets.

6.2.3.3 Plasma Temperature

Plasma temperatures are often determined from the measurement of the ratio of the intensity of (a) ion to neutral lines and (b) neutral to neutral lines, usually for the same element. In case (a) the line intensities are combined with the Saha equation and the electron density measurements to determine the ionization temperature of the plasma [176]:

$$\frac{I_{ion}}{I_{atom}} = 2 \times \frac{(2\pi m_e kT)^{3/2}}{N_e h^3} \left(\frac{gA}{\lambda}\right)_{ion} \left(\frac{\lambda}{gA}\right)_{atom} \times \exp\left[\frac{-(V^+ + E_{ion} + E_{atom})}{kT_{ion}}\right] \quad (6.7)$$

where I is the integrated emission intensity of the ion or atom, N_e is the electron density (cm^{-3}), gA is the product of the statistical weight and the Einstein coefficient for spontaneous emission of the upper level (s^{-1}), λ is the wavelength (nm), T_{ion} is the ionization temperature (K), V^+ is the ion potential of the atom (J), E_{ion} is the excitation energy of the ionic line (J), E_{atom} the excitation energy of the atomic line (J), k is the Boltzmann constant (J/K), and h is the Planck's constant ($J.s$). In case (b) the line intensities are combined with the Boltzmann equation to determine the excitation temperature of the plasma and the relation is given by,

$$\frac{I_1}{I_2} = \frac{g_1 A_1}{g_2 A_2} \cdot \frac{\lambda_2}{\lambda_1} \exp\left(-\frac{|E_1 - E_2|}{kT_e}\right) \quad (6.8)$$

where the subscripts 1 and 2 refer to the individual lines in the pair. The accuracy in the temperature determination increases with an increase in energy difference $E_1 - E_2$ in the above equation. The accuracy may be improved by measuring a number of different line pairs and taking the average. However, it should be noted that the accuracy of the measurement largely depends on values of the A coefficients with their error ranging from 5% to 50%.

Values for the product of the statistical weight and the Einstein coefficient (gA) for each element and ionization stage can be found in the NIST database [178]. By applying a natural logarithm operation on both sides of eqn. 6.8, it can be re-written as:

$$\ln\left(\frac{I_{12}}{A_{12}g_2}\right) = -\left(\frac{1}{kT_e}\right)E_2 + \ln\left(\frac{hcN^Z}{4\pi U^Z(T)}\right) \tag{6.9}$$

where Z is the ionization and equals one for singly charged ions, and $U^Z(T)$ is the partition function. Eqn. 6.9 takes the form of a linear equation which can be plotted. By plotting the ordinate, $\ln\left(\frac{I_{12}}{A_{12}g_2}\right)$, versus the abscissa, E_2^Z with its coefficient, $1/kT_e$ can be measured from the gradient of the line from which we can deduce the kinetic electronic temperature. The accuracy of the method is improved if more than several emission lines are plotted and if there is a large range of E_2^Z values.

In this work, the electron temperature was evaluated using six emission lines of CII ions. These lines are given in Table 6.3. The parameters were taken from the NIST spectroscopic atomic database [178].

6.2.3.4 Optical Thickness and Self-absorption

In conditions where the plasma density is very high, the plasma itself absorbs its own emission. This is true mainly for the resonance lines connected to the ground state, but other lines may also be affected. The absorption causes a distortion in the spectral line profile, resulting in a broadened line. This effect is known as self-absorption. During the LIPS experiments, the plasma temperature tends to drop towards the outer parts of plasma plume, and when light passes through these colder parts an effect known as self-reversal can occur. Such lines show a large dip at the center of the ordinarily well-behaved line-shape function, giving doubt as to the presence of two lines.

The above discussion shows that evaluation of the plasma parameters and extraction of quantitative data from the line intensities requires verification that the plasma is not optically thick for the lines being studied. The ratio of emission intensities of resonant and non-resonant lines are verified according to a procedure for the "optically thin" limit described by Cremers and Radziemski

[174]. It is necessary that the observed intensity ratio's are consistent with those predicted by the statistical weights of the upper levels indicating that the plasma is optically thin. Normally during the measurement of major elements in composite solid samples, or in pure samples, severe self-reversal and self-absorption are observed for many lines during the first few seconds after plasma formation.

6.3 Dominant optical emission bands of carbon

The quantum mechanical description of the vibrational properties of diatomic molecules and the consequential emission of radiation corresponding to various signature vibrational modes of C_2 has been extensively studied and reported [33, 179, 180]. These signature vibrational modes have been identified and classified and named after their initial investigators. Figure 6.1 shows a plot of low lying electronic states of C_2 and the observed transitions [181]. Of the nine observed systems of C_2, the most prominent bands in the visible region are the Swan band system ($d^3\Pi_g - a^3\Pi_u$) followed by the Deslandres D' Azambuja (DDA) ($C^1\Pi_g - A^1\Pi_u$) system. The remainder was not detectable since the energies involved in the laser-induced plasma (less than 3 eV) is far less than that needed to excite their vibrational modes or that the measurement was beyond the detectable range of the detector system employed in this study. In Figure 6.2, sample spectra of the Swan and DDA emission bands are shown. In this work, only the Swan bands were tracked as a function of intensity, time and space since the positions of the emission peaks of the DDA band coincided with the emission lines of Ni and Co. For the C_2 Swan bands, peaks associated with the (0,0), (1,1), and (2,2) vibrational bands are prominent at 516.5 nm, 512.9 nm, and 509.9 nm respectively. Of these three peaks, the intensity of the emission line at 516.5 nm was used to reflect the Swan bands.

6.4 Experimental set-up and parameters for *in situ* OES measurements

The experimental setup, description and method to synthesis SWCNTs in large ($\sim$ 160 mg/h) quantities was presented in Section 4.6 of Chapter 4. In that process, the laser was operated continuously at 30 Hz. However, for OES measurements, the laser was operated in single-shot mode. In this dissertation, single-shot actually implies double pulse; one at 532 nm and the other at 1064

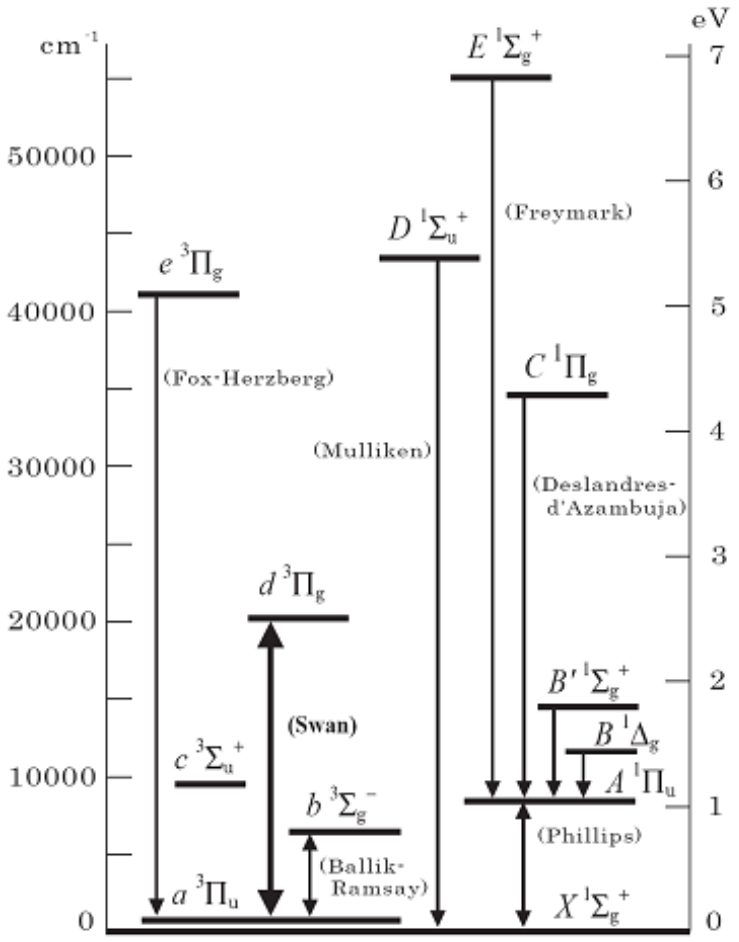


Figure 6.1: Low-lying electronic states of C_2.The direction of arrows indicates emission or absorption. Taken from Tanabashi et al. [181].

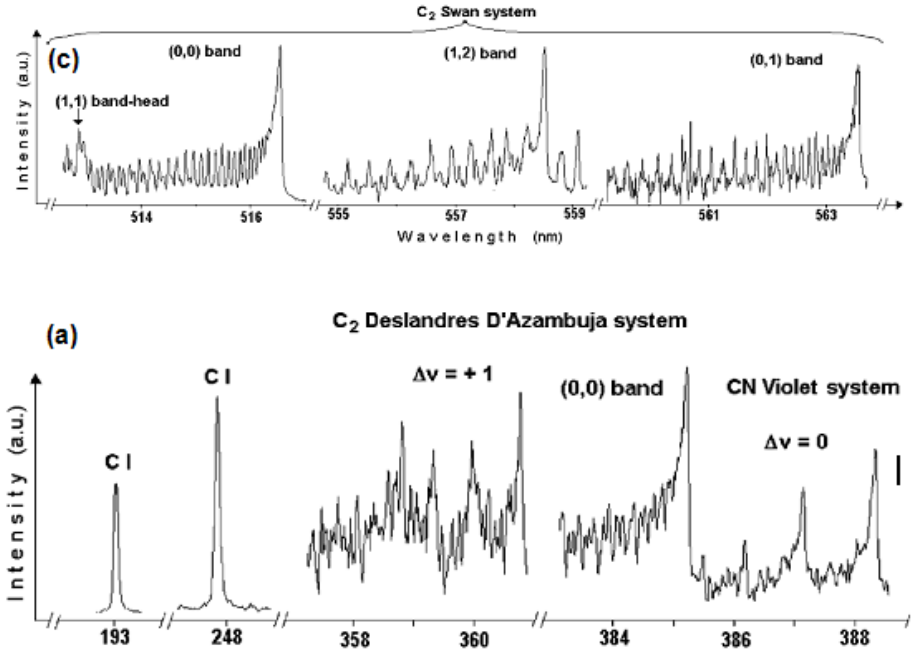


Figure 6.2: Examples of the (a) C_2 Swan band system and (b) The C_2 Deslandres D' Azambuja system. Taken from Vivien et al. [180].

nm. The temporal difference between these two pulses was about 20 ns [154]. It was found that the double pulse enhanced the plasma lifetime and SWCNT yield [182]. In Figure 6.3 the experimental layout for single shot laser synthesis and OES measurements is shown. In Figure 6.4, a schematic of the "close-up" of how the laser-induced plasma was generated and the collection of lights emissions due to ablation is shown. The data was captured by an Andor CC52 optical unit which was mounted adjacent to the centre of the tube furnace on an X-Y-Z mechanical translation stage. The CC52 was linked by optical fibre to the spectrograph. When the target was ablated, the plasma expanded and its movement was primarily in the direction perpendicular to the target surface.

In this setup (Figure 6.2), the target was placed in the same axis as that of the incoming pulsed laser beams, defined as the z-axis. The collection of broad-band spectra was optimized with the aid of a diode alignment laser, built-into the CC52. This allowed regions along the z-axis, through which the plasma plume propagates, to be imaged onto the entrance aperture of the optical fibre connected to an Andor ME5000 Echelle spectrograph. The spectrograph, of focal length 195 mm with f/7, can simultaneously record in a spectral range of 200-950 nm for a single laser ablation event.

The detector attached to the spectrograph was an Andor DH734i intensified charged coupled device (ICCD). The detector has 1024 x 1024 pixels with total

Target composition	**Synthesis temperature** (K)	**Distance** (mm)	**Time** (ns)
A (98%C:1%Ni:1%Co)	1073, 1173, 1273	0, 1, 2 , 3 , 4 , 5	0-10000
graphite (100% C)	1273	0, 1, 2, 3	0-3000

Table 6.1: Experimental parameters under which OES measurements were investigated.

area of 177 μm^2. The detector chip was Peltier cooled to -15^0C for optimum performance. The overall detectable spectral range in a single acquisition was limited to 200-850 nm in a single acquisition. The entire detection system was controlled by a computer loaded with Andor Solis spectroscopic data capture software.

The hinged tube furnace was opened to an approximate angle of 40^0 for periods up to 15 seconds during which time an average of 4 laser ablation events was recorded. Thereafter, the furnace was allowed to regain its temperature setting. This process was repeated three times and the accumulated spectra were averaged to improve statistics.

The ICCD had an internal digital delay generator (DDG) which was connected to the laser output trigger. Firing the laser triggered the ICCD to accept incoming signals. In the initial phase of an ablation event, there is a strong continuum signal due to Bremsstrahlung, emanating from the plasma plume. This period lasted for about 500 ns during which no recombination or emission lines of the atomic species in the plasma were detected. This is our reference point for collecting spectra. We reset this value to 0 ns before each experiment. A fixed gate width of 500 ns was selected in the DDG.

To track the spatial and temporal evolution of the plasma plume, it was possible to increment the delay time from 0 ns to 10 μs in increments of 100 ns. These measurements were then repeated but taken at different distances from the target surface along the z-axis. These were varied from 0 mm (target surface) to 5 mm in increments of 1 mm. The argon gas flow rate and pressure was fixed at 200 SCCM and 400 Torr respectively. For OES, two different targets were used. The first, was Target A which contained 98% C and 1% wt. each of Ni and Co. The second was a pure graphite target (SGL Carbon). OES measurements on Target A was made at (a) 1073 K, (b) 1173 K and (c) 1273 K while for the graphite target the measurement was at 1273 K only. In Tables 6.1 and 6.2, the experimental parameters under which OES was performed are presented.

SpectraPro Quanta Ray Nd:YAG	**1064 nm**	**532 nm**
Pulse energy (mJ)	250	450
Pulse width (ns)	10	8
Spot size, focussed, with lens f_L=1500 mm	3	2
Energy fluenced, focussed beam ($J.cm^{-2}$)	3.5	14
Peak power density, focussed ($MW.cm^{-2}$)	355	1.8×10^3
Beam divergence (mrad)	<1	<1
TEM mode	TEM_{00}	TEM_{00}

Table 6.2: Laser parameters under which OES of in situ SWCNT synthesis were investigated.

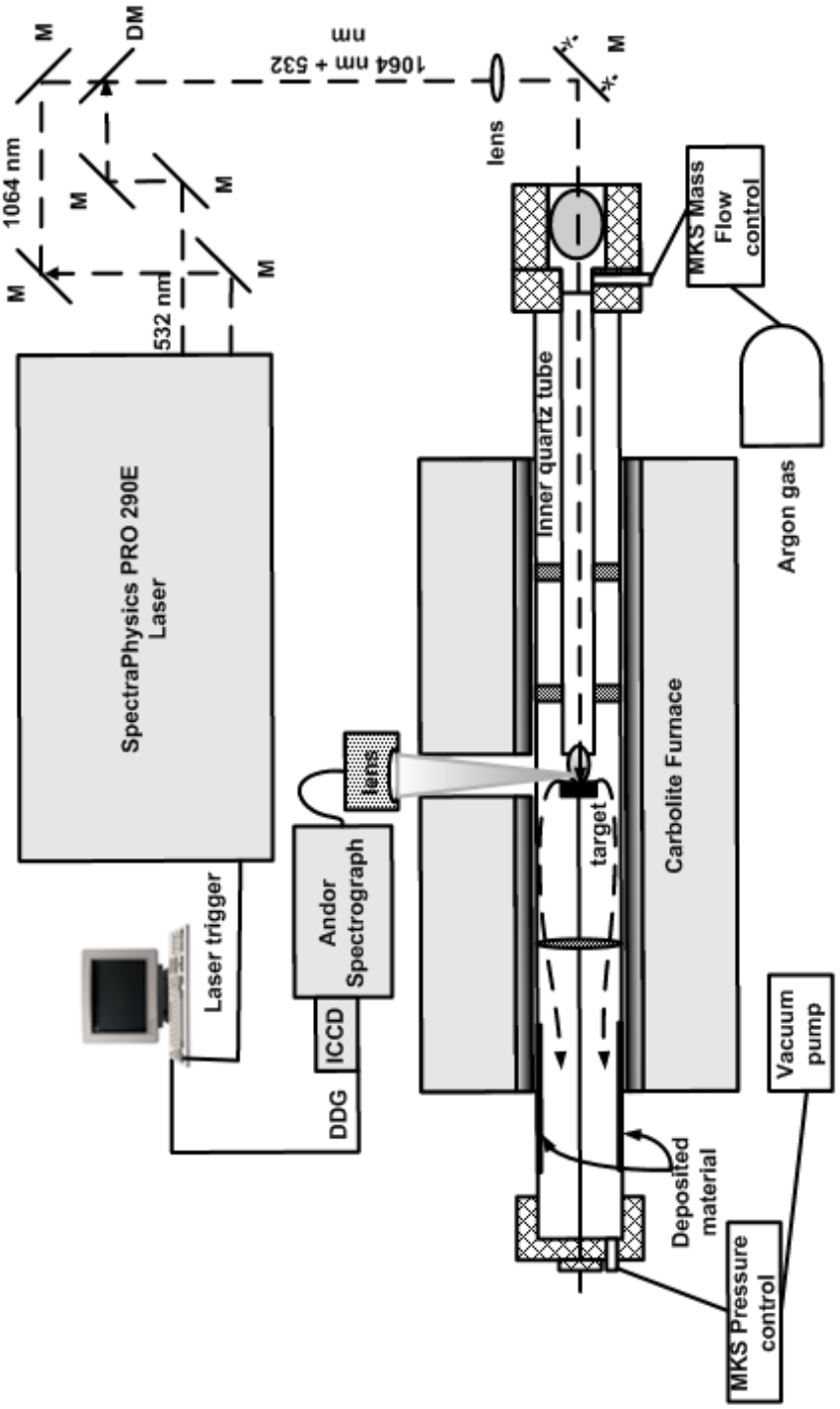


Figure 6.3: Experimental setup for OES measurements and laser single-shot synthesis of SWCNTs.

6.5 Results

6.5.1 Characterization of as-prepared materials by single-pulse laser ablation

In OES investigations, the laser-induced plasma was generated by ablating the target in the furnace with a single-shot (double laser pulse). Optical emissions from the plasma were captured by opening the hinged tube furnace for a few seconds for measurements and was closed thereafter to regain the original temperature setting. After about 4 seconds, a second laser shot was fired at the target to generate a plasma. Again, optical emission data was captured. This process was repeated until all OES measurements were complete. During these measurements, only the furnace temperature was varied. At each furnace temperature setting, a complete set of temporal and spatial measurements were made on the laser induced plasma. Changing the temperature setting to start another set of OES measurements involved:

1. Cleaning of the quartz tube. Over a long period of time, carbon deposits accumulated at various positions in the quartz tube. Cleaning was necessary so that the intensities of the measured optical emissions were not attenuated by the deposits.

2. Polishing of the target to remove pits that had formed over a period of time or replacing with a new outgassed target.

The amount of material ablated due to single-shot ablation events that accumulated at the back-end of the furnace, at zone A, was very minute (<1 μg) and was removed using either lens tissue or a cotton-tipped swab. This material was subjected to Raman spectroscopy analysis. Measurements were made using a HR 800 Raman spectrometer using a 514.5 nm laser excitation. In Figure 6.5, Raman spectra of (a) Target A, 1073 K, (b) Target A, 1173 K, (c) Target A, 1273 K and (d) graphite, 1273 K are shown. From the Raman spectra, it is clear that a single-laser shot at the target, generated sufficient material to nucleate and grow SWCNTs since the time between laser shots was sufficiently long (5 seconds) for material ablated to be carried to the back of furnace without any interference with material from the next laser shot. The results with single-shot are similar to that reported in Chapter 5, when Target A was ablated at a frequency of 30 Hz. At (a)1073 K, the concentration of defects (I_D/I_G) was measured to be 0.46 and the ratio dropped as the furnace temperature increased. At (c) 1273 K, a drop in defect concentration of 0.03 was measured. As a reference for the OES measurements of plasma plumes

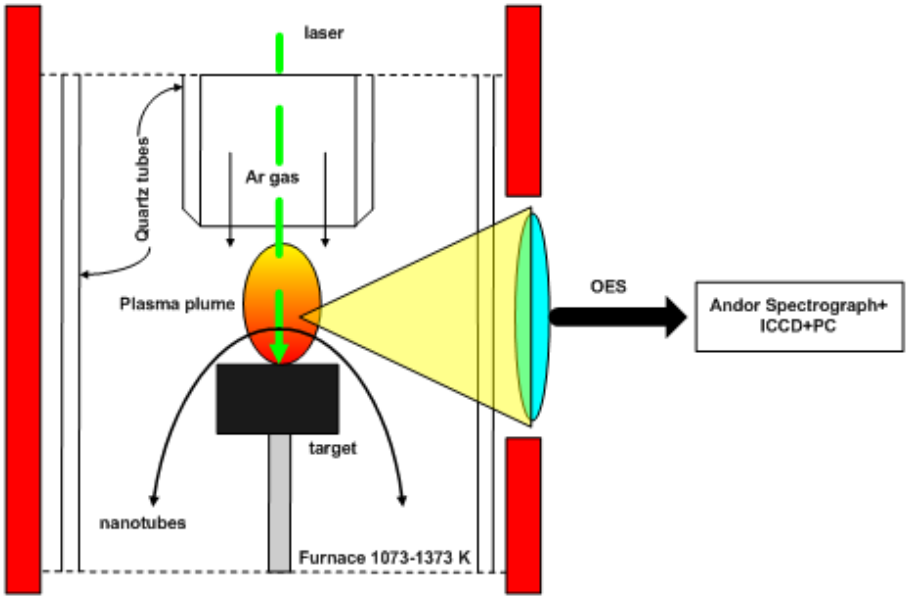


Figure 6.4: A schematic showing a closeup of the laser impinging on the target resulting in the generation of the plasma from which optical emissions were collected. MKMoodley 2010©

emanating from targets containing catalysts, a target which had no catalysts i.e. a pure graphite target was used. In Figure 6.5(d), Raman spectra are shown for material obtained from ablating a pure graphite target continuously and when ablating in single shot mode. Clearly, there was no evidence of SWCNTs. However, there was a distinct difference between the spectra. When the target was continuously ablated, the material collected was amorphous as shown by the absence of the D* peak at around 2700 cm^{-1}. It is known that the D* peak is indicative of a 2D sp^2 bonded hexagonal network. For single shot experiments, the D* peak appeared and was distinct. On the other hand, the D peak was not very clear in the spectrum. Typically this would indicate that the material resembled graphene [183]. This meant that the single-shot method could be used to make graphene. Under continuous ablation, the excess carbon and/or C_2 molecules collide with each other in the absence of a catalyst to form amorphous material.

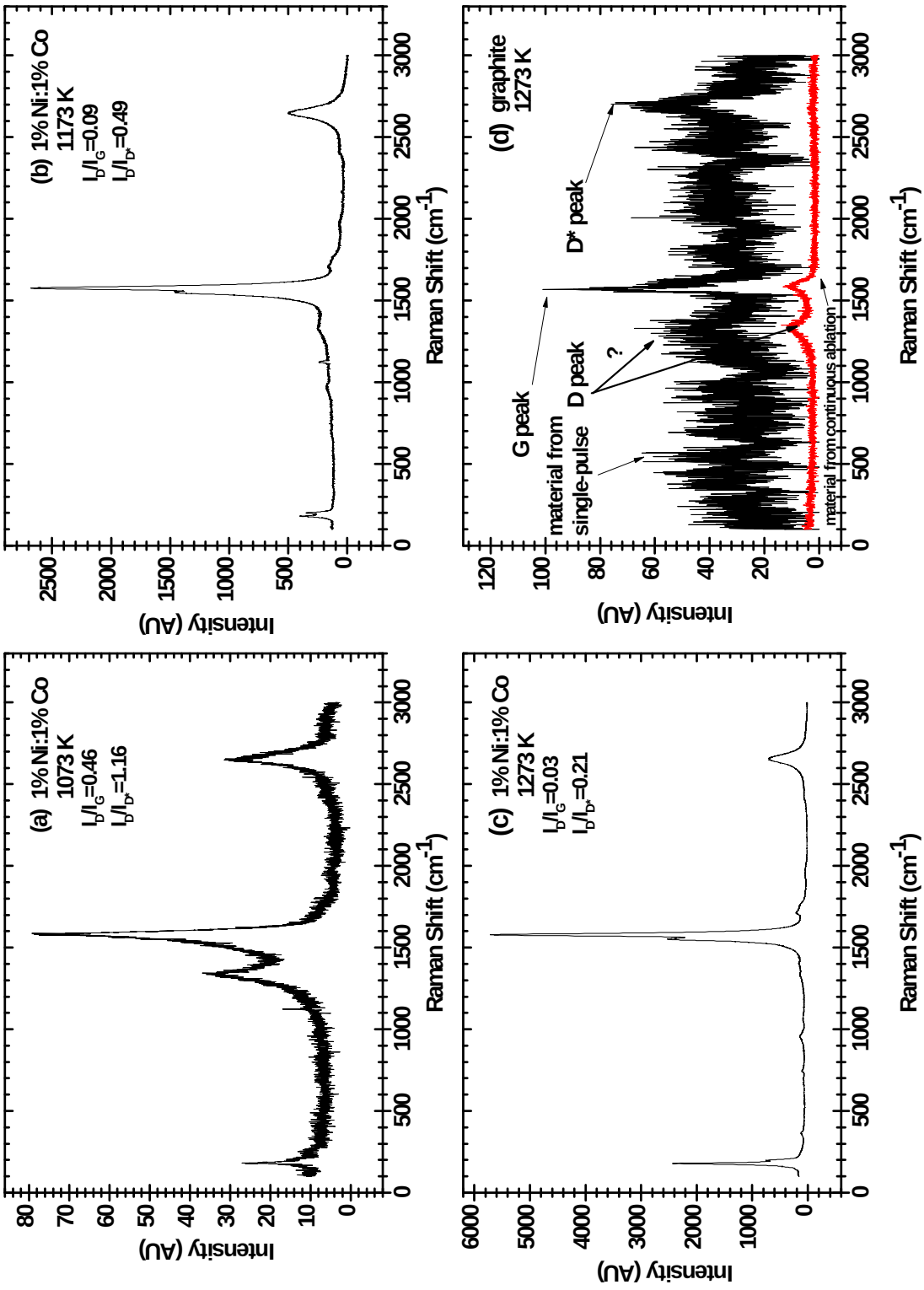


Figure 6.5: Raman spectra of as-prepared material obtained for single laser shot experiments at (a) Target A, 1073 K, (b) Target A, 1173 K, (c) Target A, 1273 K and (d) graphite, 1273 K.

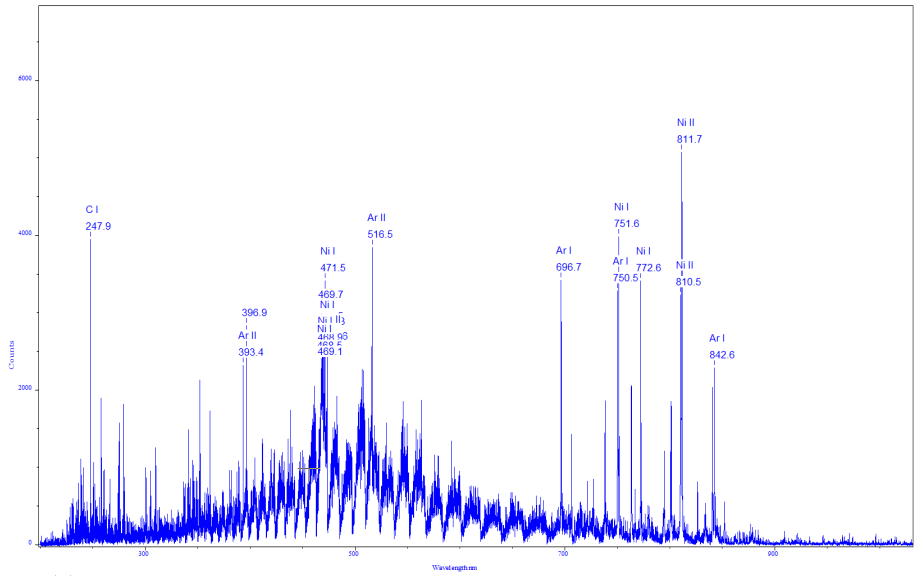


Figure 6.6: A sample of an OES spectrum recorded at a delay time of 1800 ns when a single laser shot was fired at Target A using a furnace temeprature of 1273 K. The gate-width on the DDG was 500 ns.

6.5.2 The temporal and spatial dynamics of C_2

Optical emission spectra emanating from the laser generated plasma were recorded using the experimental parameters given in Table 6.1. All elemental species, neutrals and ions, were identified. In Figure 6.6, a sample spectrum of an ablation event was recorded at a furnace temperature of 1273 K and delay time of 1800 ns using Target A. Built into the software is a database of all known emission lines corresponding to the various elements and its ionization stages. By selecting the element and its ionization stage, peaks in the emission spectra are matched to the database and subsequently gets automatically labelled.

Generally, the emission lines of Ni, Co and Ar dominate the emission spectra while emissions due to carbon are relatively weak. All analysis using selected peaks of carbon emission lines had to be carefully evaluated. In tracking the spatial and temporal behavior of the C_2 Swan bands ($d^3\Pi_g - a^3\Pi_u$), only the intensities of the identified bands was considered. In Figure 6.7, an example of a C_2 Swan band emission was identified and this is shown in Figure 6.6. The vibrational modes of (0,0), (1,1) and (2,2) were identified at the known peak emission positions at 516.5 nm, 512.9 nm and 509.9 nm respectively. In this work, only the peaks associated with the (0,0) vibrational head giving rise to an emission peak at 516.5 nm was recorded and analyzed. The C_2 Deslandres D Azambuja DDA ($C^1\Pi_g - A^1\Pi_u$) emissions were very weak and not easily identified. Furthermore, the peak positions of the DDA bands appeared

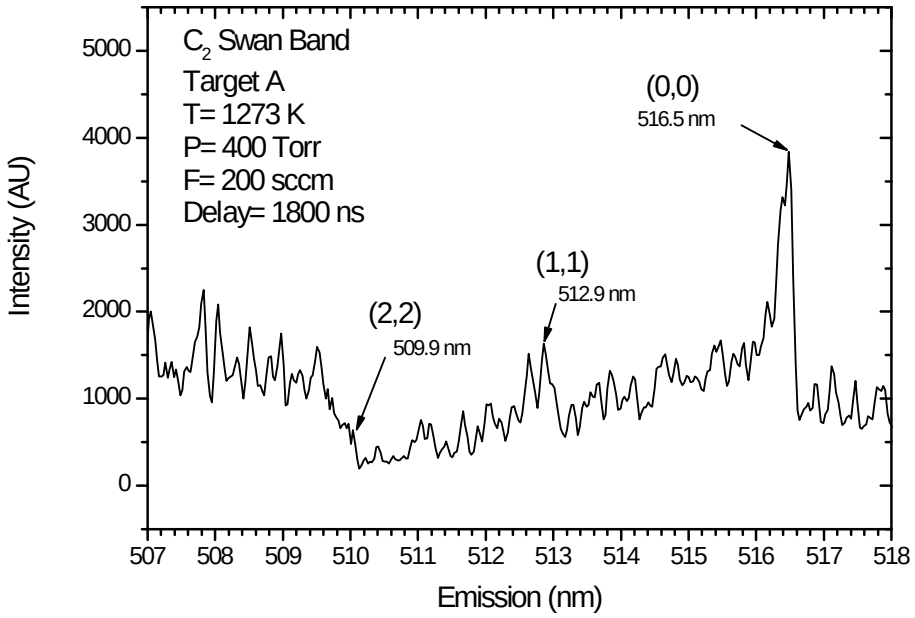


Figure 6.7: A sample of an C_2 Swan bands recorded at a delay time of 1800 ns when a single laser shot was fired at Target A at a furnace temeprature of 1273 K. The gate-width on the DDG was 500 ns. The vibrational bands (0,0), (1,1) and (2,2) and the associated peak emissions were clearly visible.

to coincide with strong emissions of other neutrals and ions and were therefore not used.

In Figure 6.8(a-d), a plot of C_2 intensities as a function of pulse delay time and distance from the target surface are presented. In Figure 6.8(a-c), the temporal and spatial changes of C_2 when Target A was ablated (containing 1% Ni and 1% Co) by firing single laser shots at (a) 1073 K, (b) 1173 K and (c) 1273 K while in Figure 6.8(d), the temporal and spatial behavior of C_2 are shown for when a pure graphite target was ablated. C_2 ($-C=C-$), has been proposed to be a precursor or building block to form carbon nanotubes [184, 185]. Therefore, monitoring the uptake of C_2 with time and space would be helpful in learning about the nucleation and growth of SWCNTs.

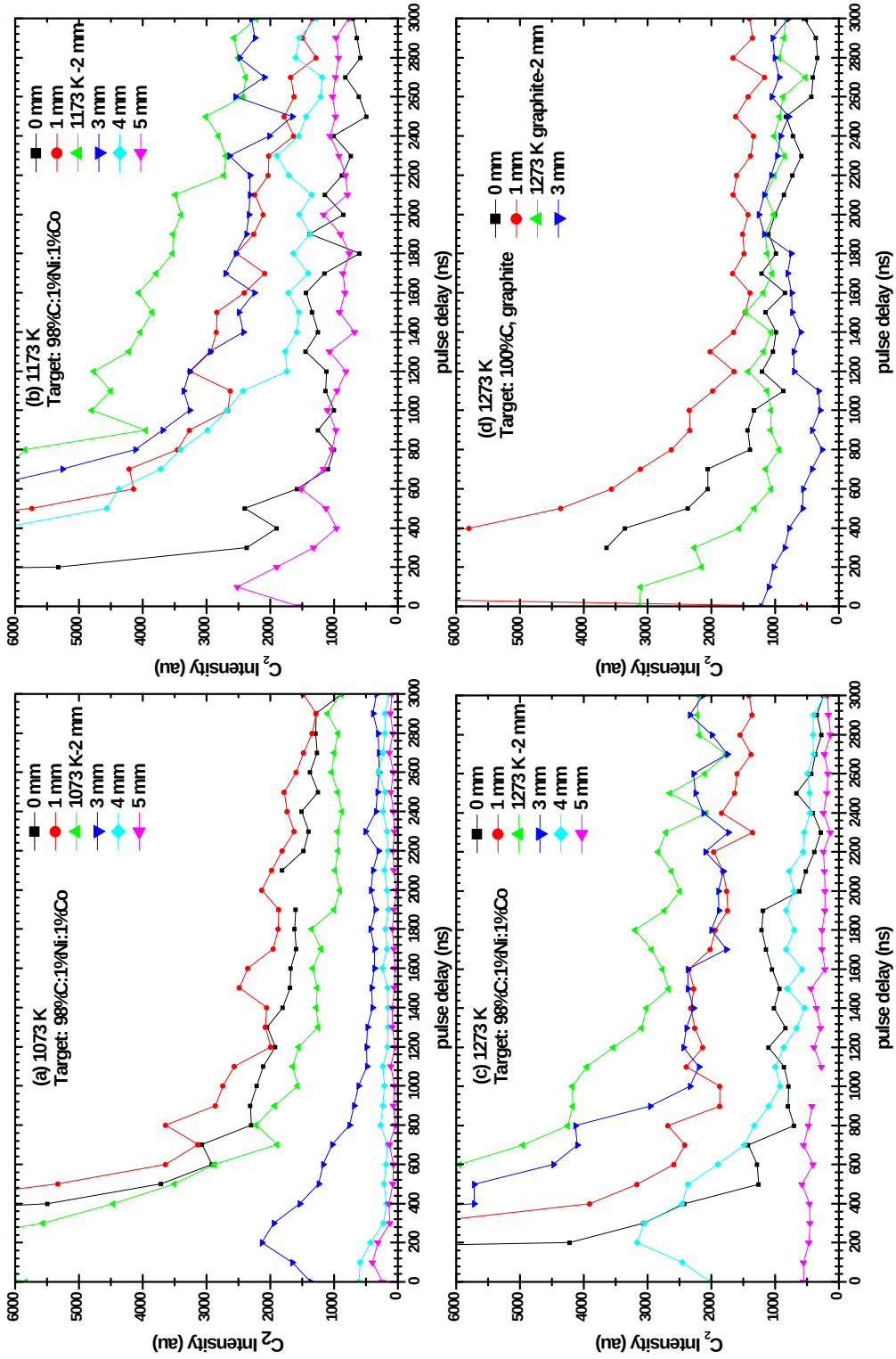


Figure 6.8: Plots of the temporal and spatial dynamics of C_2 Swan (0, 0) band. (a) Target A at 1073 K, (b) Target A at 1173 K, (c) Target A at 1273 K and (d) graphite at 1273 K.

C_2 intensities were found to decrease with distance from the target surface spatially and temporarily for all 4 plots (a-d). It was found that the C_2 intensities increase with increasing temperature. The C_2 dynamics in all the data presented in Figure 6.8 can better be observed in a 3D contour plot or map.

Figure 6.9(a-e), shows the re-plotting of data in the form of contour plots of the temporal and spatial dynamics of C_2 Swan bands. It is clear, that in such a presentation, the C_2 fluctuations in space and time can be clearly seen. Indeed, C_2 was readily detected immediately after the onset of ablation. Its residency time in the furnace increases with temperature from 1073 K to 1273 K. Initially it appears that C_2 emissions are stronger at (b)1173 K than at (a)1273 K. This was probably due to the fact that at the higher temperature of 1273 K, more bond breaking energy was available to destroy the hexagonal lattice network of graphite composite target (Target A) and give higher concentrations of carbon ions than at 1173 K. However, recombination to form C_2 was favoured at the higher temperature where longer periods of residency time were observed (Fig. 6.9(e) versus Fig. 6.9(f)). It must be noted that in Figure 6.9(d), OES measurements were limited to distance of 3 mm from the target surface. The reason for this, was that after 3 mm, the C_2 emission intensities had dropped to the level of background emissions and therefore could not be distinguished. Therefore, while the plots in Figs.6.9(a) and (d) looked similar, at a distance of 3 mm away from the target, the C_2 intensities due to Target A were about 3000 counts higher. Clearly, with reference to Raman spectra shown in Figures 6.5 (a-d), a strong correlation between C_2 lifetimes and nucleation and growth of SWCNTs is seen.

6.5.3 The temporal and spatial dynamics of the electron density

The electron density was determined from the Stark broadening (eqn. 6.6) of the spectral emission line of CII at 283.7 nm, for which $w = 0.074\mathring{A}$ at 20 000 K [177]. The conditions under which changes in the FWHM due to Stark broadening of the CII ion emission occurred, are shown in Table 6.6. To obtain the FWHM, each emission peak(s) at 287.7 nm was deconvoluted and fitted with several Lorentzian line-shapes. From this fitted data, the FWHM associated with the peak at 287.74 nm was used for the electron density measurements. This was a laborious task since each and every emission spectrum measured as a function of distance and time had to be evaluated. However, this was the only way to determine the electron density with reliability and consistency for all OES spectra. The spatial and temporal data for the electron density

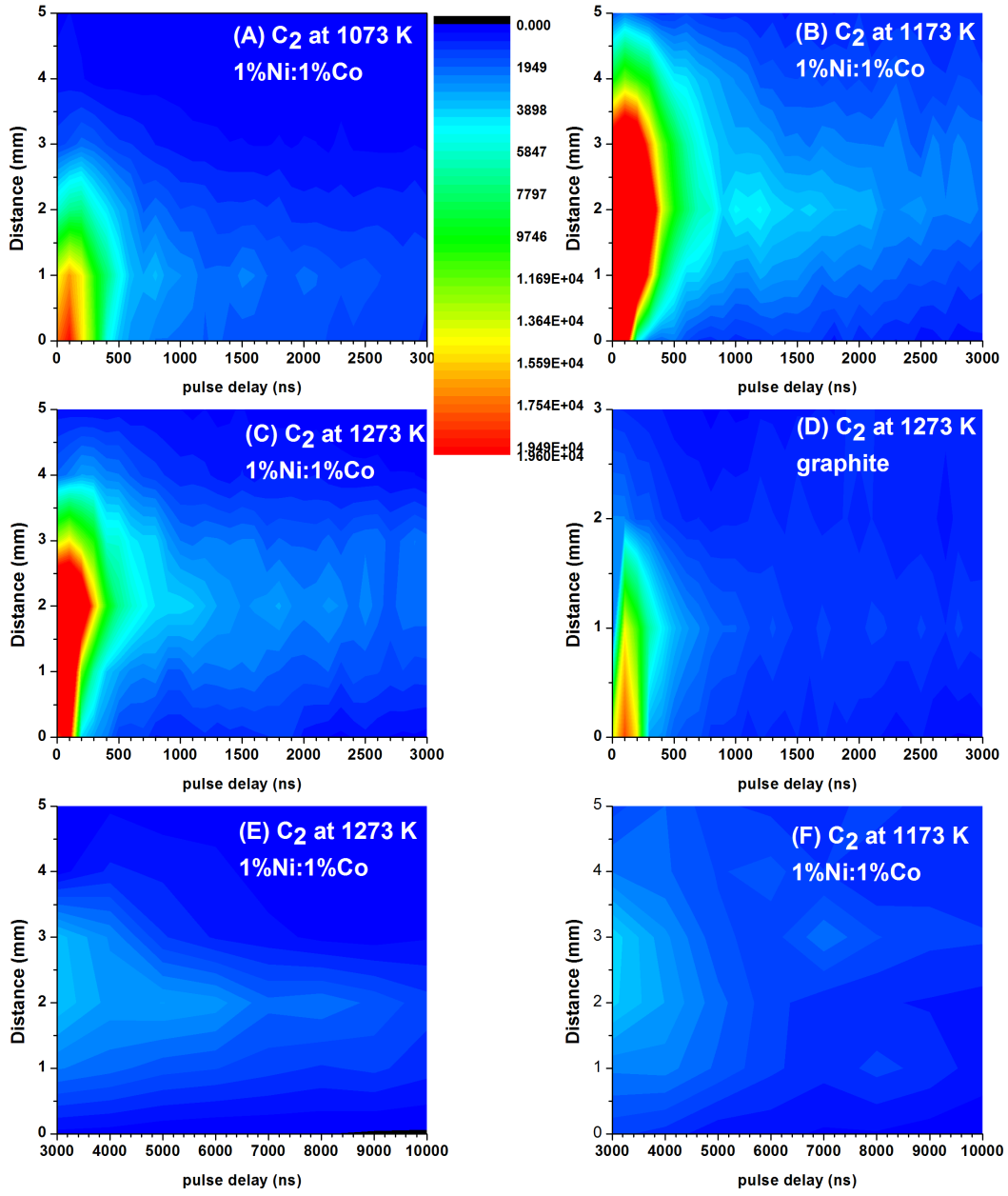


Figure 6.9: A contour plot of the temporal and spatial dynamics of C_2 Swan (0, 0) band. (a) Target A at 1073 K, (b) Target A at 1173 K, (c) Target A at 1273 K and (d) graphite at 1273 K. (e) Target A at 1273 K extended to 10 μs (f) Target A at 1173 K extended to 10 μs.

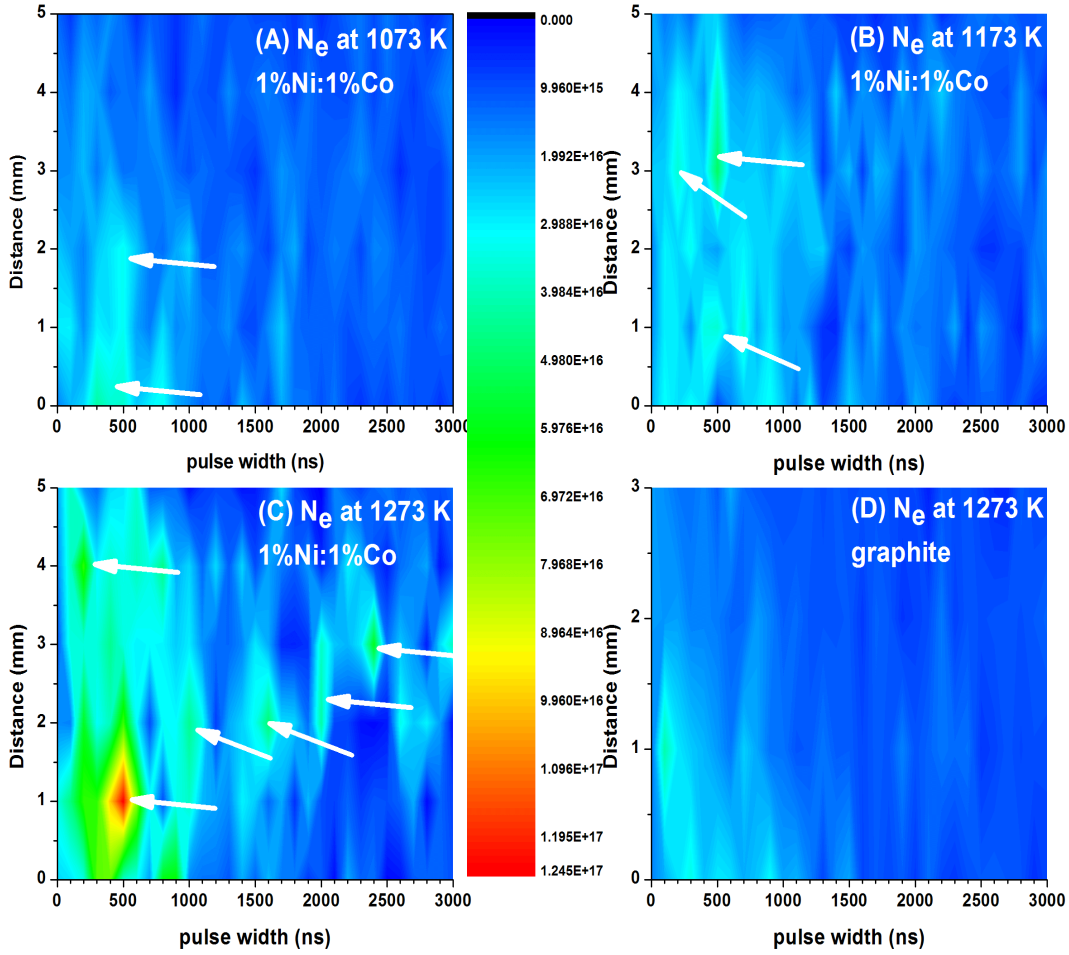


Figure 6.10: Plots of the spatial dynamics of electron density, N_e of (a) Target A at 1073 K, (b) Target A at 1173 K, (c) Target A at 1273 K and (d) graphite at 1273 K. A number of local maxima appearing as hot spots, shown by white arrows, increase with increasing furnace temperature.

measurements were plotted as contour plots or maps and are shown in Figure 6.10(a-d).

Initially, at the instant of ablation, the electron density in the evolving plasma was the same at all pressures and flow conditions. However, as the plasma expands with time, the pressure and flow of argon gas begins to influence the rate of expansion, decay, and eventual extinction of the plume. The electron density was found to vary between $10^{15} - 10^{17}$ cm^{-3}. However, in these experiments, the pressure and flow was kept constant and were set to conditions almost optimal for SWCNT synthesis. Thus, changes in the plasma dynamics, result from the increasing temperature and chemical/physical reactions in the plasma.

With time, the ions and electrons recombine to form neutral elements, C_2 dimers and larger carbon chain molecules. However, the appearance of local maxima or hot spots, where the intensities of electron densities are higher than

surrounding areas, appear to increase with frequency as the furnace temperature was increased. Clearly, the rise in electron density at hot spots was not due the plasma being re-ionized as there was no further energy input into the system after the initial laser pulses. The hot spots could in part be attributed to recombination and clustering phenomena. However, the energy released as a result of these process is insufficient to explain the hot spots. In the plasma when no catalysts involved (Figure 6.10(d)) and where recombination and clustering had taken place, no hot spot activity was observed. The Raman spectra of material formed under these conditions was shown to be amorphous. Hence, the increase in hot spot activity which was seen to increase with temperature must be primarily attributed to another process.

6.5.4 The temporal and spatial dynamics of electron temperature

The Boltzmann plot method [131] was used to evaluate six emission lines of CII [154] (Table 6.3) to determine the electron temperature. The electron temperature was extracted from the gradient of the Boltzmann plot (eqn. 6.9) at each and every point in time and space for which an emission spectrum was captured. From this data, a temporal and spatial map or contour plot of the electron temperature was made (Figure 6.11).

Even though the measurement of the electron temperature is independent of the electron density, similar fluctuations and the appearance of a number of hot spots (white arrows on plots) which increase with furnace temperature, were observed. Again, this was not observed with the graphite target. In comparison, mapping of the electron temperature intensities of the target ablated at 1073 K containing a Ni/Co catalyst (Figure 6.11(a)), showed higher electron temperature intensities than the results from ablating graphite alone at 1273 K (Figure 6.11(d)). Since, the temperature of the plasma was calculated from line intensities, it would imply that the appearance of hot spots can be directly correlated to the release of energy in the plasma primarily due to a process other than recombination and clustering.

6.6 Discussion and conclusions

It is has been suggested in the carbon nanotube research community that C_2 dimers could possibly be the precursors to nanotube growth [184, 185]. Previous reports of *in situ* OES observations in carbon nanotubes synthesis [136, 167, 169, 173, 186, 187, 188] refer mainly to the detection of C_2 species

Wavelength (nm)	$A_2g_2(\times 10^8)$ s^{-1}	**Upper energy level** E_2 (eV)
250.9	1.81	18.67
251.3	3.25	18.85
287.7	1.59	16.33
657.9	1.45	16.33
723.3	1.41	16.33
723.8	2.53	16.33

QTOcaption

Table 6.3: Emission line parameters of CII lines taken from NIST [178].

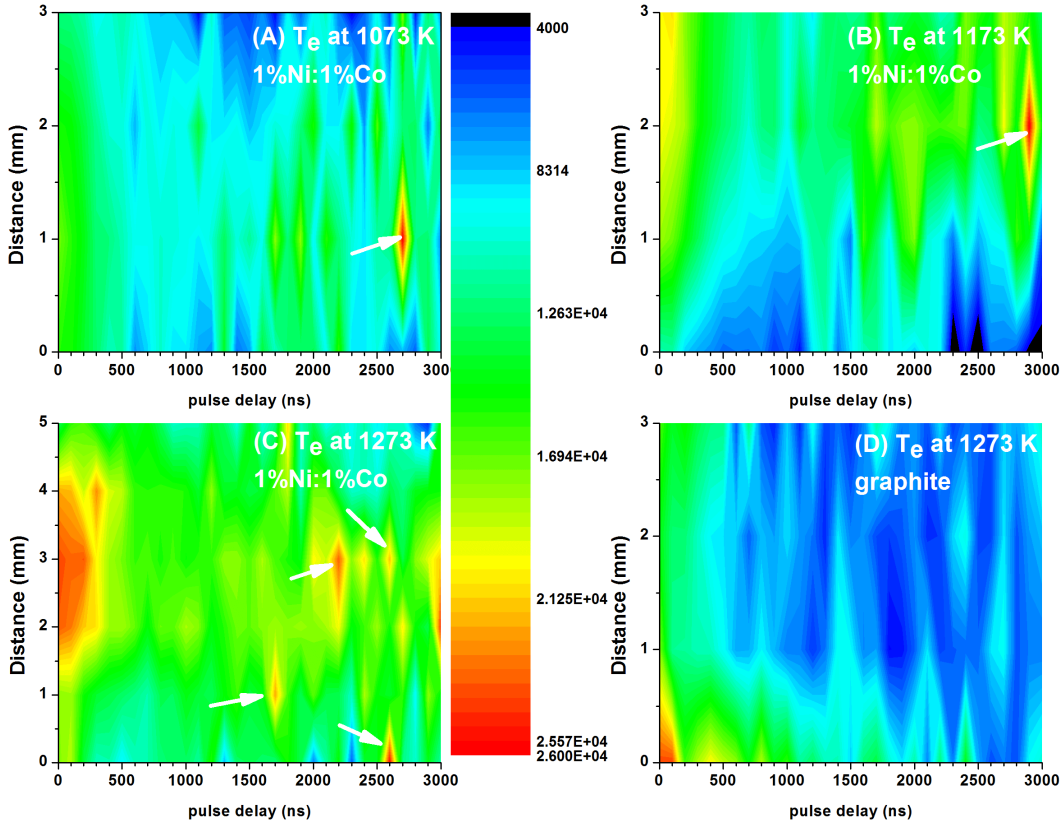


Figure 6.11: Plots of the spatial dynamics of electron temperature, T_e of (a) Target A at 1073 K, (b) Target A at 1173 K, (c) Target A at 1273 K and (d) graphite at 1273 K. A number of local maxima appearing as hot spots, shown by white arrows, increased with increasing furnace temperature.

and the intensity changes observed when external parameters are changed and optical imagery of the plume dynamics was described. No conclusions on the possible nucleation of nanotubes and the role that C_2 have been made. However, a recent study by Marchand et al. [189] reported that the CVD growth of carbon nanotubes could be monitored by *in situ* field emission spectroscopy. From this study, the authors concluded that the SWCNT growth proceeds by a "corkscrew" motion, out of the plane of the catalyst surface via C_2 addition at the interface of the catalyst and the growing nanotube. The source of C_2 was from the dissociation of acetylene gas.

Another recent computational study by Ohta et al. [190], modeled the growth of SWCNTs on a Fe cluster. In this study, a continuous supply of carbon atoms at the Fe–C interface was assumed which resulted in rapid growth rates of 0.043 $\mathring{A}/ps$, equivalent to a growth rate of 4.3 $m.s^{-1}$. Therefore, under favorable conditions, when the carbon feedstock is rapidly available, Ohta et al.[190] suggest that the rapid nucleation at the metal–C interface and growth of nanotubes can be achieved.

The changes in C_2 Swan band intensity as a function of time and distance from the target surface, was described in section 6.5.2 is shown in Figures. 6.9(a-d). The figures show the history of the C_2 in the plasma plume. It was observed that the initial intensity and concentration of C_2 was dependent on the furnace temperature, when pressure, argon gas flow rate and the laser energy was kept constant. Thus, the higher the furnace temperature, the higher the C_2 concentrations and the longer the C_2 persisted in the plasma plume. Since C_2 has been identified as a building block to SWCNTs, a higher C_2 concentration, under the right conditions is expected to promote the growth of SWCNTs. Raman spectra (Figures 6.5 (a-c)) corroborates this picture of C_2 availability and growth of SWCNTs. Another interesting observation, for which we cannot as yet provide any explanation, was why the presence of catalysts such as Ni and Co, play a role in extending the lifetime of C_2 dimers. In the absence of catalysts, C_2 forms small graphene sheets and/or amorphous clusters. Further work is warranted to validate this proposition.

A number of hot spots or local maxima were seen to increase with increasing furnace temperature. They were observed in contour plots of electron density and electron temperature measurements. The electron density and electron temperature were obtained independently of each other and therefore calculation errors can be ruled out. The LTE criterion (eqn. 6.2) was satisfied since with values $\Delta E \sim 4.4$ eV, $T = 24000$ K $\Rightarrow N_e \simeq 1.6 \times 10^{16} cm^{-3}$. The values for Ne measured in this work varies between 1×10^{16} and $5 \times 10^{17} cm^{-3}$ (seen in the plots of Figure 6.10(a-d)). Hence, the LTE criterion was satisfied. In a

single laser shot, electron temperatures near the surface are almost the same (∼24 000 K) when different furnace temperatures were used.

In normal circumstances, the plasma will expand adiabatically and cool off. The electron temperature and density are expected to decrease as a function of 1/distance with time. This was observed when the graphite target was ablated. Hot spot activity was absent for the electron density and electron temperature measurements of the ablated graphite target. However, in the presence of the catalyst, the 1/distance plasma "cool off" was not observed. In fact sharp fluctuations in the form of hots spots were observed. It was shown in Chapter 5, that as the temperature of the furnace increased from 1073 K to 1373 K, the quality and abundance of SWCNTs increased. The formation of an ordered superstructure such as that of a SWCNT from free and energetic C_2 dimers is an exothermic reaction resulting in the release of energy. The total energy of a formed SWCNT (U_2) is lower than the sum of energies of its individual components such as C_2 (U_1), since in nature atoms and molecules tend to bond to achieve a system of lower energy. Therefore, the excess energy Q is : $Q = U_2 - U_1 = \Delta\dot{U}$. The higher rate of nucleation and growth of SWCNTs, mean a higher value of Q, which will be transferred to its surroundings. This energy will be absorbed by the remaining constituents of the plasma, thermally exciting it and this will cause an increase in the optical emission from ions and recombined neutrals. The emission lines become Stark broadened [176] which will give higher electron density values. In the same way, an increase in higher emission intensities would mean higher electron temperatures.

Therefore we attribute the appearance of the hot spots in the electron density maps of Figure 6.10(a-c) and in the electron temperature maps of Figure 6.11(a-c) as being due to the energy released as the result of nucleation and growth of SWCNTs. This argument is strengthened by the fact that under the same experimental conditions, the ablation of a target containing no catalysts showed no hot spot activity and produced no SWCNTs.

These results suggest that the appearance of the hot spots are a direct consequence of the nucleation and growth of SWCNTs. They also confirm results from an earlier study by Moodley et al.[154], where it was reported that when conditions were favorable for the synthesis of SWCNTs, a rise in the electron temperature was noted. In that study the temporal and spatial profile of the electron density was measured at distance of 2 mm from the target surface. The furnace temperature was 1273 K and the argon pressure and flow rate was 400 Torr and 200 SCCM respectively. However, these measurements were for a target containing 4% Ni and 1% Y. Under unfavorable conditions, when the pressure was 100 Torr, a rise in electron temperature was not observed.

Under these conditions, the plasma expanded adiabatically and cooled and the quality of SWCNTs that were synthesized was poor.

Having made the argument that the hot spots are a direct consequence of the nucleation and growth of SWCNTs, the positions in time and space of SWCNT nucleations sites, indicated by the white arrows on the maps were seen to change with furnace temperature. With the data at hand, it was still not possible to establish if the appearance of hot spots was random or if there was a definite physical model that could predict when and where nucleation sites would appear based on a few experimental parameters. This observed complexity demonstrates why it has been difficult to control the synthesis of SWCNTs.

6.6.1 Growth model

We conclude this Chapter by providing a plausible model for the nucleation and growth of SWCNTs based on experimental results, discussions and arguments presented in Chapter 5, 6 and from Refs. [154, 182]. In the laser synthesis of SWCNTs, nucleation and growth takes place on metal catalysts that are ejected from the target surface [135]. Prior to ablation, and due to the manner in which the target was made, the metal catalyst particles (solute) are already covered by polycrystalline graphite solvent . Ramping up the furnace to high operating temperatures promotes the formation of metastable carbides at the graphite–metal interface [191].

X-ray diffraction XRD pattern of the target prior to ablation confirms the presence of Ni_3C [154, 192]. The laser energy deposited at a point at the target surface within 15 ns FWHM, causes the heating rate at this point to rise to an estimated 10^{12} K.s^{-1}. The surface temperature of the target rises to a peak value of approximately 45 000 K [154]. The energy transfer in the target takes place via electronic and vibrational excitation and results in the explosive ejection of target material. The amount of material ejected in a single laser shot was calculated to be between $10^{18} - 10^{19}$ atoms. This material consists of particulates, molecules, ions, and electrons that form the basis of the plasma plume.

The ejected graphite-carbide-metal (GCM) nanoparticles are between 5 and 15 nm in diameter [182]. Due to the high curvature, the interfacial carbide layer is strained as a result of lattice mismatch in the GCM. At high temperatures, the carbide segregates [193] and decomposes into C and Ni [194] causing an increase in electronic activity of Ni. The carbon from the decomposed carbide prefers to increase its coordination number [195]. This results

in the volume, which the segregated carbon at this region occupies to increase causing it to push into the graphite layers above. A fullerene cap may be initiated when stresses in the hexagonal graphite network are relieved by the Stone–Wales rearrangement which results in the transformation of a hexagon into a pentagon, lowering the energy and improving the stability of the lattice. The pentagon formation in a hexagonal-dominated lattice results in a lifting of the C structure out of the plane of the catalyst.

The formation of pentagons has been shown to be energetically favorable. In simulations performed by some groups on the nucleation of fullerenes [196, 197, 198], this process becomes the driving force for the nucleation of a nanotube. The diameter of the resulting tube will depend on the catalyst size, curvature, rims, or edges and other surface contours which result in the minimization of the C–Ni bond energy. In the case of larger spherical catalyst particles, many nucleation sites would be possible leading to multiple tube growth as observed from transmission electron microscopy observations [199, 48].

Chapter 7

Conclusions and Recommendations

7.1 Conclusions

One-dimensional nanostructured materials such as SWCNTs are currently a major focus of research, due to their superior optical, electronic, thermal and mechanical properties and due to the potential applications which could result by exploiting these properties. However, most of the applications are still at the research laboratory stage since challenges relating to the controlled synthesis of type-specific carbon nanotubes have hindered the commercialization of devices based on this material. Although progress has been made on the synthesis of SWCNTs, the control of SWCNT chirality is yet to become a reality. The inability to control the synthesis is due to the lack of a complete understanding of the nucleation and growth process.

In this dissertation, the laser-furnace method was used to study the synthesis of SWCNTs. The investigations revolved around varying process parameters such as gas pressure, gas flow rate, furnace temperature and catalyst composition. A study was made on the effect of varying these parameters on the synthesis of SWCNTs. To quantify these effects, the as-prepared material was characterized by Raman spectroscopy, photoluminescence spectroscopy and electron microscopy. The results to these investigations can be summarized as follows:

1. Variation of the argon gas pressure and flow rate influenced the quantity and quality of as-prepared SWCNTs since these parameters affected the plasma dynamics. Low flow rates and low pressures, reduced the cross section for collisions between plasma constituents, in particular between C_2 and the metal catalysts, which affected the probability of nucleation

and growth of SWCNTs as indicated by high I_D/I_G (or I_D/I_{D*}) values. These values point to high defect concentration in SWCNTs. On the other hand, a high pressure which tends to increase plasma confinement suffered instabilities due to the high flow rate of argon gas. While at these conditions, the amount of as-prepared was significantly large (130 mg/h), the material had a large I_D/I_G (or I_D/I_{D*}) value. The temperature was found to be the critical process parameter in the nucleation and growth of SWCNTs. It was found that as the synthesis temperature was increased from 1073 K to 1373 K, the RBM intensities of Raman spectra increased, indicating an increase in the nucleation and growth of SWCNTs. This correlated with the lowering of I_D/I_G (or I_D/I_{D*}) values with increasing temperature. Furthermore, while higher quality tubes were synthesized with increasing temperature, more Lorentzian's curves were required to fit the RBM data. This pointed to an increase in the number of SWCNTs with small variations in the chirality that became thermodynamically possible. This observation was corroborated by PL results, were it was seen that there was an increase in the number of chiral tubes with increasing temperature. Overall, it was found that an argon pressure of 500 Torr, flow rate of 100 SCCM and temperature of 1373 K, produced SWCNTs at a rate of 80 mg/h with the highest quality and the lowest I_D/I_G (or I_D/I_{D*}) value of 0.02 (0.25).

2. The catalyst composition was changed by adding Fe, in steps of 0.5% to the traditionally used catalyst made of 1% Ni/1% Co. A distinct shift to lower wave numbers of the RBM spectrum was noted. This pointed to the synthesis of larger diameter SWCNTs. We propose that this is due to the increase in the lattice parameter of the catalyst which changed from Ni to Ni_3Fe. The increase in the lattice facilitates the nucleation of larger diameter nanotubes. However, continuously adding Fe to the catalyst mixture gave a significant drop in RBM intensities and hence SWCNT content. We propose that this is due to an increase of FeCo alloy content in the target. FeCo was found to inhibit the synthesis of SWCNTs since it is known, that on their own, these elements are not suitable catalysts in the laser-furnace method of synthesizing SWCNTs. It was found that increasing the Fe concentration beyond 1.5%, increased the reactivity of the catalyst (Fe) to a point where it became detrimental to the synthesis process.

3. It was found that with increasing synthesis temperature, the photoluminescence (PL) intensities of the SWCNTs decreased. This was contrary

to Raman results. It was concluded that as the synthesis temperature was increased from 1073 K to 1373 K, the laser-furnace method promotes the nucleation of metallic SWCNTs. This was determined from the fits of RBM spectra which showed that the peak positions of Lorentzian curves used to fit the data corresponded to positions of known metallic SWCNTs. The presence of m-SWCNTs are known to suppress PL emissions from semiconducting SWCNTs and this is the reason why PL intensities decreased with increasing synthesis temperature. Therefore it was concluded that by controlling the synthesis temperature, either s-SWCNT or m-SWCNT could be promoted.

Optical emission spectroscopy (OES) was used to evaluate the temporal and spatial dynamics of C_2, electron density (N_e) and electron temperature (T_e). The following conclusions were made from this study.

1. We had previously shown that C_2 is a fundamental building block in the nucleation and growth of SWCNTs. In this study the temporal and spatial behavior of C_2, as a function of temperature, was made. It was found that as the furnace temperature was increased from 1073 K to 1373 K in targets which contained catalysts, that the concentration and lifetime of C_2 in the plasma plume increased. Raman measurements on material collected from single-shot OES measurements showed an increase in Raman RBM intensities and a corresponding decrease in I_D/I_G (or I_D/I_{D*}) values with increasing synthesis temperatures. The study showed a direct correspondence between C_2 lifetime and nucleation and growth of SWCNTs. In the absence of catalysts, C_2 formed small graphene sheets or amorphous clusters.

2. Contour plots or maps of the N_e and T_e show a number of hot spots or local maxima which increase in number with increasing temperature. We attribute the appearance of hot spots to the energy released when C_2 is systematically consumed during the nucleation and growth of SWCNTs. Under the same experimental conditions, the ablation of a target containing no catalysts showed no hot spots in either of the N_e or T_e maps and produced no carbon nanotubes. Therefore, it was concluded that the appearance of hot spots is a direct consequence of the nucleation and growth of SWCNTs.

In conclusion, the laser-furnace method for synthesizing SWCNTs was investigated and optimized. Some tunability in the type of SWCNTs which were

synthesized could be achieved by varying process parameters and catalyst composition while investigating the variablity in the type of material that could be synthesized and the application of DGU to separate nanotubes, we have inadvertantly discovered a single experimental system to produce nanotubes. This method could be tested to determine which particular nanotube species would be suitable for a particular application such as gas sensors designed for the detection of methane only.

We have shown that OES is an excellent method to investigate the conditions under which SWCNTs nucleate and grow and can be a useful method to optimize the growth. This knowledge can also be used more effectively i.e. if we know WHEN and WHERE the majority of nanotubes nucleate. With this knowledge, we could devise methods to influence this process by external stimulation such as using a tunable seed laser, whose wavelength is chosen to match a particular vibrational mode of a precursor material such as C_2 or tuned to the bandgap of a particular nanotubes such as a the bandgap of a (9,7) nanotube. In this way, preferential growth of (9,7) nanotubes could possibly be achieved by continuous resonance ensuring the enhanced growth of this nanotube. This procedure could reduce the competitive nature responsible for the many possible nanotubes which are found in the as-prepared material. This line of research may have important implications in achieving the ultimate control in the growth of carbon nanotubes and their use in the electronics industry.

7.2 Recommendations for future work

While, in this dissertation, the plasma properties were determined from the analysis of C_2 and CII emissions, the methods employed could be applied to other constituents of the plasma such as the metal catalysts. A study of temporal and spatial dynamics of the catalysts particles will elucidate their catalytic behavior during the nucleation and growth of SWCNTs. While the Boltzmann plot method was employed to determine electron temperature, the use of the Saha-Boltzmann equation to evaluate emissions from successive ionization stages may prove to be a more accurate method to determine the electron temperature. Further work is also required on high resolution TEM and XRD measurements of catalyst particles in order to accurately determine composition. While it was shown that OES is able to study nucleation and growth of SWCNTs, it could also be applied to other materials systems where significant self-assembly of atoms from the vapour phase into an ordered superstructure occurs, such as in the synthesis of boron nitride nanotubes.

Bibliography

[1] N. Greenwood, A. Earnshaw, Chemistry of the Elements, Pergamon Press, Oxford, England, 1989.

[2] H. W. Kroto, J. R. Heath, S. C. O'Brien, R. F. Curl, R. E. Smalley, C60: Buckminsterfullerene, Nature 318 (1985) 162.

[3] H. Kroto, Symmetry, space, stars and c60, in: Nobel Lecture, Swedish Academy of Sciences, Stockholm, Sweden, 1996, p. 44.

[4] S. Iijima, Helical tubes of graphitic carbon, Nature 307 (1991) 56.

[5] L. Radushkevich, V. Lukyanovic, O strukture ugleroda, obrazujucegosja pri termiceskom razlozenii okisi ugleroda na zeleznom kontakte., Journal of Physical Chemistry (Russian) 26 (1952) 88.

[6] M. Hillert, N. Lange, The structure of graphite filaments, Zeitschrift für Kristallographie 111 (1958) 24.

[7] M. Monthioux, V. L. Kuznetsov, Who should be given credit for the discovery of carbon nanotubes?, Carbon 44 (2006) 1621.

[8] A. Oberlin, M. Endo, T. Koyama, Filamentous growth of carbon through benzene decomposition., Journal of Crystal Growth 32 (1976) 335.

[9] R. Feynman, There's plenty of room at the bottom: An invitation to enter a new field of physics, Engineering and Science Magazine, California Institute of Technology XXIII (1960) 1.

[10] S. Iijima, T. Ichihashi, Single shell carbon nanotubes of 1 nm diameter, Nature 363 (1993) 603.

[11] M. Monthioux, P. Serp, E. Flahaut, M. Razafinimanana, C. Laurent, A. Peigney, W. Bacsa, J.-M. Broto, Introduction to Carbon Nanotubes, Springer, 2007, Ch. 3, p. 43.

[12] T. Guo, P. Nikolaev, A. Thess, D. Colbert, R. Smalley, Catalytic growth of single-walled nanotubes by laser vaporization, Chemical Physics Letters 243 (1995) 49.

[13] H. Dai, A. Rinzler, P. Nikolaev, A. Thess, D. Colbert, R. Smalley, Single-wall nanotubes produced by the metal-catalyzed disproportionation of carbon monoxide, Chemical Physics Letters 260 (1996) 471.

[14] P. Nikolaev, M. Bronikowski, R. K. Bradley, F. Rohmund, D. Colbert, K. Smith, R. Smalley, Gas-phase catalytic growth of single-walled carbon nanotubes from carbon monoxide, Chemical Physics Letters 313 (1999) 91.

[15] B. Kitiyanan, W. Alvarez, J. Harwell, D. Resasco, Controlled production of single-wall carbon nanotubes by catalytic decomposition of CO on bimetallic CoŰMo catalysts, Chemical Physics Letters 317 (2000) 497.

[16] S. Nanotechnologies, Http://www.swentnano.com/tech/cg200.php, online (2010).

[17] Z. F. Ren, Z. P. Huang, J. W. Xu, J. H. Wang, P. Bush, M. P. Siegal, P. N. Provencio, Synthesis of large arrays of well-aligned carbon nanotubes on glass, Science 282 (1998) 1105.

[18] Y. Tseng, P. Xuan, A. Javey, R. Malloy, Q. Wang, J. Bokor, H. Dai, Monolithic integration of carbon nanotube devices with silicon MOS technology, Nano Letters 4 (2004) 123.

[19] M. Dresselhaus, G. Dresselhaus, R. Saito, Carbon fibers based on c60 and their symmetry, Physical Review Letters 45 (1992) 6234.

[20] R. Saito, M. Fujita, G. Dresselhaus, M. S. Dresselhaus, Electronic structure of graphene tubules based on c60, Physical Review B 46 (1992) 1804.

[21] P. Avouris, Carbon nanotube electronics and photonics, Physics Today 34 (2009) 62.

[22] P. Avouris, R. Martel, Progress in carbon nanotube electronics and photonics, in: Beyond Silicon: Carbon-Based Nanotechnology, MRS Bulletin, 2010, p. 306.

[23] M. Fuhrer, C. Lau, A. MacDonald, Graphene: Materially better carbon, MRS Bulletin 35 (2010) 289.

[24] M. Meyyappan, Carbon Nanotubes: Science and Applications, CRC Press, Washington D.C., 2005.

[25] P. Ma, N. A. Siddiqui, G. Marom, J. Kim, Dispersion and functionalization of carbon nanotubes for polymer-based nanocomposites: A review, Composites: Part A doi: 10.1016 (2010) 3.

[26] Q. Cao, J. A. Rogers, Ultrathin films of single-walled carbon nanotubes for electronics and sensors: A review of fundamental and applied aspects, Advanced Materials 21 (2009) 29.

[27] B. Dumé, Hottest topic in physics revealed, http://physicsworld.com/cws/article/news/24845, iOP A website from the Institute of Physics (May 2006).

[28] J. Wood, The top ten advances in materials science, Materials Today 11 (2008) 40.

[29] H. Pierson, Handbook of Carbon, Grapgite, Diamond and Fullerenes, 1st Edition, Noyes Publications, 1993.

[30] B. Brandsden, C. Joachain, Physics of Atoms and Molecules, 1st Edition, Longman, 1983.

[31] H. Palmer, M. Shelef, Chemistry and Physics of Carbon: Volume, Marcel Dekker, New York, 1968.

[32] C. Mantell, Carbon and Graphite Handbook, Interscience, New York, 1968.

[33] A. V. Orden, R. Saykally, Small carbon clusters: Spectroscopy, structure and energetics, Chemical Reviews 98 (1998) 2313.

[34] R. Davis, Diamond Films and Coatings, Noye Publications, New Jersey, 1993.

[35] J. Tersoff, R. Ruoff, Structural properties of a carbon nanotube crystal, Physical Review Letters 73 (1994) 676.

[36] N. Wang, Z. K. Tang, G. D. Li, J. S. Chen, Singlewalled 4 å carbon nanotube arrays, Nature 408 (2000) 50.

[37] M. Dresselhaus, G. Dresselhaus, R. Saito, A. Jorio, Raman spectroscopy of carbon nanotubes, Physics Reports 409 (2005) 47.

[38] J. Lui, S. Fan, H. Dai, Recent advances in the methods of forming carbon nanotubes, MRS Bulletin 29 (2004) 244.

[39] P. Harris, Solid state growth mechanisms for carbon nanotubes, Carbon 45 (2007) 229.

[40] C. Rao, A. Govindaraj, Nanotubes and Nanowires, RSC Publishing, Cambrige, 2005.

[41] D. Bethune, C. Kiang, M. de Vries, G. Gorman, R. Savoy, J. Vazquez, R. Beyers, Cobalt-catalysed growth of carbon nanotubes with single-atomic-layer walls, Nature 363 (1993) 605.

[42] S. Farhat, M. de La Chapelle, A. Loiseau, C. Scott, S. Lefrant, C. Journet, P. Bernier, Diameter control of single-walled carbon nanotubes using argon-helium mixture gases, Journal of Chemical Physics 115 (2001) 6752.

[43] C. Journet, W. Maser, P. Bernier, A. Loiseau, M. DelaChapelle, S. Lefrant, P. Deniard, R. Lee, J. Fischer, Large-scale production of single- walled carbon nanotubes by the electric-arc technique,, Nature 388 (1997) 756.

[44] D. Mann, Carbon Nanotubes: Properties and Applications, Taylor and Francis, 2006, Ch. 2, p. 19.

[45] P. Eklund, B. Pradhan, U. Kim, Q. Xiong, J. Fischer, A. Friedman, B. Holloway, K. Jordan, M. Smith, Large-scale production of single-walled carbon nanotubes using ultrafast pulses from a free electron laser, Nano Letters 2 (2002) 561.

[46] A. A. Puretzky, G. Eres, C. M. Rouleau, I. N. Ivanov, D. B. Geohegan, Real-time imaging of vertically aligned carbon nanotube array growth kinetics, Nanotechnology 19 (2008) 055605.

[47] Y. Saito, M. Okuda, N. Fujimoto, T. Yoshikawa, M. Tomita, T. Hayashi, Single-wall carbon nanotubes growing radially from ni fine particles formed by arc evaporation., Japanese Journal of Applied Physics 33 (1994) L526.

[48] J. Gavillet, A. Loiseau, F. Ducastelle, S. Thair, P. Bernier, O. Stet'phan, J.-C. C. J. Thibault, Microscopic mechanisms for the catalyst assisted growth of single-wall carbon nanotubes, Carbon 40 (2002) 1649.

[49] A. Gorbunov, R. Friedlein, O. Jost, M. Golden, J. Fink, W. Pompe, Gas-dynamic consideration of the laser evaporation synthesis of single-wall carbon nanotubes, Applied Physics A: Materials Science and Processing 69 (1999) S593.

[50] D. Geohegan, H. Schittenhelm, X. Fan, S. Pennycook, A. Puretzky, M. Guillorn, Condensed phase growth of single-wall carbon nanotubes from laser annealed nanoparticulates., Applied Physics Letters 78 (2001) 3307.

[51] R. Sen, S. Suzuki, H. Kataura, Y. Achiba, Growth of single-walled carbon nanotubes from the condensed phase., Chemical Physics Letters 349 (2001) 383.

[52] M. J. OConnell, S. Bachilo, C. Huffman, V. Moore, M. Strano, E. Haroz, K. Rialon, P. Boul, W. Noon, C. Kittrell, J. Ma, R. Hauge, R. Weisman, R. Smalley, Band gap fluorescence from individual single-walled carbon nanotubes, Science 297 (2002) 593.

[53] M. Bockrath, D. H. Cobden, J. Lu, A. G. Rinzler, R. E. Smalley, L. Balents, P. L. McEuen, Luttinger liquid behaviour in carbon nanotubes, Nature 397 (1999) 598.

[54] D. T. S. Berber, Y. Kwon, Unusually high thermal conductivity of carbon nanotubes, Physical Review Letters 84 (2000) 4613.

[55] D. A. Walters, L. M. Ericson, M. J. Casavant, J. Liu, D. T. Colbert, K. A. Smith, R. E. Smalley, Elastic strain of freely suspended single-wall carbon nanotube ropes, Applied Physics Letters 74 (1999) 3803.

[56] B. G. Demczyk, Y. Wang, J. Cumingd, M. Hetamn, W. Han, A. Zettl, R. O. Ritchie, Direct mechanical measurement of the tensile strength and elastic modulus of multiwalled carbon nanotubes, Material Science and Engineering A 334 (2002) 173.

[57] S. C. Tsang, Y. K. Chen, P. J. F. Harris, M. L. H. Green, A simple chemical method of opening and filling carbon nanotubes, Nature 372 (2002) 159.

[58] M. Monthioux, Filling single-wall carbon nanotubes, Carbon 40 (2002) 1809.

[59] W. A. de Heer, A. Châtelain, D. Ugarte, A carbon nanotube field-emission electron source, Science 270 (1995) 1179.

[60] A. Javey, H. Kim, M. Brink, Q. Wangi, A. Ural, J. Guo, P. McIntire, P. McEuen, M. Lunstrom, H. Dai, High-k dielectrics for advanced carbon-nanotube transistors and logic gates, Nature Nanomaterials 1 (2002) 241.

[61] J. Liu, M. Hersam, Recent developments in carbon nanotube sorting and selective growth, MRS Bulletin 35 (4) (2010) 315.

[62] E. S. Snow, F. K. Perkins, E. J. Houser, S. C. Badescu, T. L. Reinecke, Chemical detection with a single-walled carbon nanotube capacitor, Science 307 (2005) 1942.

[63] E. S. Snow, F. K. Perkins, J. A. Robinson, Chemical vapor detection using single-walled carbon nanotubes, Chemical Society Reviews 35 (2006) 790.

[64] Y. Lu, J. Li, J. Han, H.-T. Ng, C. Binder, C. Partridge, M. Meyyappan, Room temperature methane detection using palladium loaded single-walled carbon nanotube sensors, Chemical Physics Letters 391 (2004) 344.

[65] Y. Sun, H. H. Wang, High-performance, flexible hydrogen sensors that use carbon nanotubes decorated with palladium nanoparticles, Advanced Materials 19 (2007) 2818.

[66] H. Hu, A. Yu, E. Kim, B. Zhao, M. Itkis, E. Bekyarova, R. Haddon, Influence of the zeta potential on the dispersability and purification of single-walled carbon nanotubes, Journal of Physical Chemistry B. 109 (2005) 11520.

[67] A. Yu, E. Bekyarova, M. Itkis, D. Fakhrutdinov, R. Webster, R. Haddon, Application of centrifugation to the large-scale purification of electric arc-produced single-walled carbon nanotubes, Journal of the American Chemical Society 128 (2006) 9902.

[68] M. Arnold, A. A. Green, J. Hulvat, S. Stupp, M. Hersam, Sorting carbon nanotubes by electronic structure using density differentiation, Nature Nanotechnology 1 (2006) 60.

[69] H. Czichos, T. Saito, L. S. (Eds.), Springer Handbook of Materials Measurement Methods, Spinger, Heidelberg, 2006.

[70] C. R. Brundle, C. A. Evans, S. Wilson, Encylopedia of Materials Characterization: Surfaces, Interfaces and Thin Films, Butterworth-Heinemann, Sotneham, USA, 1992.

[71] A. Jorio, E. Kauppinen, A. Hassanien, Carbon Nanotubes:Advanced Topics in the Synthesis, Structure, Properties and Applications, Springer-Verlag, 2008, Ch. Carbon-Nanotube Metrology, p. 63.

[72] R. Krishnan, Historical introduction, in: A. Anderson (Ed.), The Raman Effect, Vol. 1, Marcel Dekker, New York, Netherlands, 1971, p. 32.

[73] C. Raman, K. Krishnan, A new type of secondary radiation, Nature 121 (1928) 501.

[74] D. Long, The Raman Effect: A Unified Treatment of the Theory of Raman Scattering by Molecules, Wiley, New York, 2001.

[75] I. Lewis, Handbook of Raman Spectroscopy, Marcel Dekker, New York, 2001.

[76] J. Laserna, Modern Techniques in Raman Spectroscopy, Wiley, New York, 1996.

[77] M. Cardona, Resonance phenomena, Topics in Applied Physics 108 (2007) 115.

[78] C. Hierold, Advanced Micro and Nanosystems: Carbon Nanotube Devices, Vol. 8, Wiley-VCH, 2008, Ch. 8, p. 125.

[79] M. Milnera, J. Kurti, M. Hulman, H. Kuzmany, Periodic resonance excitation and intertube interaction from quasi-continuous distributed helicites in single-wall carbon nanotubes., Physical Review Letters 84 (2000) 1324.

[80] K. Hata, D. Futaba, K. Mizuno, T. Namai, M. Yumura, S. Iijima, Water-assisted highly efficient synthesis of impurity-free single-walled carbon nanotubes, Science 306 (2004) 1362.

[81] P. T. Araujo, I. O. Maciel, P. B. C. Pesce, M. A. Pimenta, S. K. Doorn, H. Qian, A. Hartschuh, M. Steiner, L. Grigorian, K. Hata, A. Jorio, Nature of the constant factor in the relation between radial breathing mode frequency and tube diameter for single-wall carbon nanotubes, Physical Review B 77 (2008) 241403.

[82] M. Cardona, Light Scattering in Solids II, Vol. 50, Springer, Berlin, 1982.

[83] C. Fantini, A. Jorio, M. Souza, M. S. Strano, M. S. Dresselhaus, M. A. Pimenta, Optical transition energies for carbon nanotubes from resonant raman spectroscopy: Environment and temperature effects, Physical Review Letters 93 (2004) 147406.

[84] M. J. Bronikowski, P. A. Willis, D. Colbert, K. A. Smith, R. E. Smalley, Gas-phase production of carbon single-walled nanotubes from carbon monoxide via the HiPco process: A parametric study, Journal of Vacuum Science Technology 19 (2001) 1800.

[85] H. Telg, J. Maultzsch, S. Reich, C. Thomsen, Resonant-raman intensities and transition energies of the e11 transition in carbon nanotubes, Physical Review B 74 (2006) 115415.

[86] R. Saito, T. Takeya, T. Kimura, G. Dresselhaus, M. Dresselhaus, Raman intensity of single-wall carbon nanotubes, Physical Review B 57 (1998) 4145.

[87] A. Jorio, A. S. Filho, G. Dresselhaus, M. Dresselhaus, A. Swan, M. Unlu, B. Goldberg, M. Pimenta, J. Hafner, C. Lieber, R. Saito, G-band resonant raman study of 62 isolated single wall carbon nanotubes, Physical Review B 65 (2002) 155412.

[88] S. D. M. Brown, A. Jorio, P. Corio, M. S. Dresselhaus, G. Dresselhaus, R. Saito, K. Kneipp, Origin of the BreitŰWignerŰFano lineshape of the tangential gband feature of metallic carbon nanotubes, Physical Review B 63 (2001) 155414.

[89] M. A. Pimenta, A. Marucci, S. Empedocles, M. Bawendi, E. B. Hanlon, A. M. Rao, P. C. Eklund, R. E. Smalley, G. Dresselhaus, M. S. Dresselhaus, Raman modes of metallic carbon nanotubes, Physical Review B Rapid 58 (1998) R16016.

[90] A. Jorio, A. G. S. Filho, G. Dresselhaus, M. S. Dresselhaus, A. K. Swan, M. S. Unlu, B. Goldberg, M. A. Pimenta, J. H. Hafner, C. M. Lieber, R. Saito, G-band resonant raman study of 62 isolated single wall carbon nanotubes, Physical Review B 65 (2002) 155412.

[91] D. Kahn, J. Lu, Vibrational modes of carbon nanotubes and nanoropes, Physical Review B 60 (1999) 6535.

[92] J. Maultzsch, S. Reich, U. Schlecht, C. Thomsen, High-energy phonon branches of an individual metallic carbon nanotube, Physical Review Letters 91 (2003) 087402.

[93] O. Dubay, G. Kresse, H. Kuzmany, Phonon softening in metallic nanotubes by a peierls-like mechanism, Physical Review Letters 88 (2002) 235506.

[94] M. Lazzeri, S. Piscanec, F. Mauri, A. C. Ferrari, J. Robertson, Phonon linewidths and electron phonon coupling in graphite and nanotubes, Physical Review B 73 (2006) 155426.

[95] S. Piscanec, M. Lazzeri, J. Robertson, A. C. Ferrari, F. Mauri, Optical phonons in carbon nanotubes: Kohn anomalies, peierls distortions, and dynamic effects, Physical Review B 75 (2007) 035427.

[96] A. Jorio, M. A. Pimenta, A. G. S. Filho, G. G. Samsonidze, A. K. Swan, M. S. Unlu, B. B. Goldberg, R. Saito, G. Dresselhaus, M. S. Dresselhaus, Resonance raman spectra of carbon nanotubes by cross-polarized light, Physical Review Letters 90 (2003) 107403.

[97] M. A. Pimenta, E. B. Hanlon, A. Marucci, P. Corio, S. D. M. Brown, S. A. Empedocles, M. G. Bawendi, G. Dresselhaus, M. S. Dresselhaus, The anomalous dispersion of the disorder-induced and the second-order raman bands, Brazilian Journal of Physics 30 (2000) 423.

[98] A. G. S. Filho, A. Jorio, A. K. Swan, M. S. Unlu, B. B. Goldberg, R. Saito, J. H. Hafner, C. M. Lieber, M. A. Pimenta, G. Dresselhaus, M. S. Dresselhaus, Anomalous two-peak g'-band raman effect in one isolated single-wall carbon nanotube, Physical Review B 65 (2002) 085417.

[99] A. G. S. Filhoa, A. Jorio, G. G. Samsonidzec, G. Dresselhaus, M. S. Dresselhaus, A. Swane, M. S. Unlue, B. B. Goldberg, R. Saito, J. H. Hafner, C. M. Lieber, M. A. Pimenta, Probing the electronic trigonal warping effect in individual single-wall carbon nanotubes using phonon spectra, Chemical Physics Letters 354 (2002) 62.

[100] R. Saito, G. Dresselhaus, M. S. Dresselhaus, Trigonal warping effect of carbon nanotubes, Physical Review B 61 (2000) 2981.

[101] G. Samsonidze, R. Saito, A. Jorio, A. S. Filho, A. Gruneis, M. A. Pimenta, G. Dresselhaus, M. S. Dresselhaus, Phonon TrigonalWarping effect in graphite and carbon nanotubes, Physical Review Letters 90 (2003) 027403.

[102] C. Fantini, A. Jorio, M. Souza, R. Saito, G. G. Samsonidze, M. S. Dresselhaus, M. A. Pimenta, Step-like dispersion of the intermediate frequent

raman modes in semiconducting and metallic carbon nanotubes, Physical Review B 72 (2005) 085446.

[103] V. Brar, G. G. Samsonidze, G. Dresselhaus, M. S. Dresselhaus, R. Saito, A. K. Swan, M. S. Unlu, B. B. Goldberg, A. G. S. Filho, A. Jorio:, Secondorder harmonic and combination modes in graphite, single-wall carbon nanotube bundles, and isolated single-wall carbon nanotubes, Physical Review B 66 (2002) 155418.

[104] H. Kataura, Y. Kumazawa, Y. Maniwa, I. Umezu, S. Suzuki, Y. Ohtsuka, Y. Achiba, Optical properties of single-wall carbon nanotubes, Synthetic Metals 103 (1999) 2555.

[105] C. L. Kane, E. J. Mele, Ratio problem in single carbon nanotube fluorescence spectroscopy, Physical Review Letters 90 (2003) 207401.

[106] C. L. Kane, E. J. Mele, Electron interactions and scaling relations for optical excitations in carbon nanotubes, Physical Review Letters 93 (2004) 197402.

[107] E. Chang, G. Bussi, A. Ruini, E. Molinari, Excitons in carbon nanotubes: An ab-initio symmetry-based approach, Physical Review Letters 92 (2004) 196401.

[108] H. Zhao, S. Mazumdar, Electron-electron interaction effects on the optical excitations of semiconducting single-walled carbon nanotubes, Physical Review Letters 93 (2004) 157402.

[109] V. N. Popov, Curvature effects on the structural, electronic and optical properties of isolated single-walled carbon nanotubes within a symmetry-adapted non-orthogonal tight - binding model, New Journal of Physics 6 (2004) 17.

[110] X. Blase, L. X. Benedict, E. L. Shirley, S. G. Louie, Hybridization effects and metallicity in small radius carbon nanotubes, Physical Review Letters 72 (1994) 1878.

[111] M. Machón, S. Reich, C. Thomsen, D. Sánchez-Portal, P. Ordejón, Ab initio calculations of the optical properties of 4å-diameter single-walled nanotubes, Physical Review B 66 (2002) 155410.

[112] H. Liu, C. Chan, Properties of 4å carbon nanotubes from first-principles calculations, Physical Review B 66 (2002) 115416.

[113] J. Maultzsch, H. Telg, S. Reich, C. Thomsen, Radial breathing mode of single - walled carbon nanotubes: Optical transition energies and chiral - index assignment, Physical Review B 72 (2005) 205438.

[114] P. T. Araujo, S. K. Doorn, S. Kilina, S. Tretiak, E. Einarsson, S. Maruyama, H. Chacham, M. A. Pimenta, A. Jorio, Third and fourth optical transitions in semiconducting carbon nanotubes., Physical Review Letters 98 (2007) 067401.

[115] H. Telg, J. Maultzsch, S. Reich, F. Hennrich, C. Thomsen, Chirality distribution and transition energies of carbon nanotubes, Physical Review Letters 93 (2004) 177401.

[116] S. Bachilo, M. Strano, C. Kittrell, R. Hauge, R. Smalley, R. Weisman, Structure-assigned optical spectra of single-walled carbon nanotubes, Science 298 (2002) 2361.

[117] F. Division, Nanosizer Version 2.0, Horiba (2008).

[118] T. Odom, J.-L. Huang, P. Kim, C. Lieber, Structure and electronic properties of carbon nanotubes, Journal of Physical Chemistry B 104 (2000) 2974.

[119] M. Dresselhaus, G. Dresselhaus, P. Avouris, Carbon Nanotubes: Synthesis, Structure,Prpeorties and Applications, Springer, Heidelberg Germany, 2001.

[120] T. Pradeep, Nano the Essentials Understanding Nanoscience and Nanotechnology, Tata McGraw-Hill Publishing Company Limited, New Delhi, 2007.

[121] B. Fultz, J. Howe, Transmission Electron Microscopy and Diffractometry of Materials, Springer, Heidelberg, 2008.

[122] Http://En.Wikipedia.Org/Wiki/Lasers, Laser, online (2010).

[123] S. Nakai, K. Mima, Development of Inertial Fusion Energy by Lasers, Springer, 2007, Ch. 15, p. 375.

[124] H. Young, R. Freedman, University Physics, Pearson Addison Wesley, San Francisco, 2008.

[125] C. M. Griot, Introduction to Laser Technology, online:http://www.cvimellesgriot.com/products/documents/technicalguide/ Edition, CVIMellegriot.com, USA, 2010.

[126] O. Svelto, Principles of Lasers, 5th Edition, Springer, New York, 2010.

[127] A. Siegman, Lasers, 1st Edition, University Science Books, Sausalito, California, 1986.

[128] C. Grigoropoulos, Transport in Laser Microfabrication: Fundamentals and Applications, 1st Edition, Cambridge University Press, Cambridge, United Kingdom, 2009.

[129] W. Smith, Modern Optical Engineering, 4th Edition, SPIE Press, New York, 2008.

[130] J. Miller, R. Haglund (Eds.), Laser Ablation and Desorption, 1st Edition, Vol. 30 of Experimental Methods in the Physical Sciences, Academic Press, San Diego, 1998.

[131] S. Harilal, C. Bindhu, R. Issac, V. Nampoori, C. P. G. Vallabhan, Electron density and temperature measurements in a laser produced carbon plasma, Journal of Applied Physics 82 (1997) 2140.

[132] J. Lunney, R. Jordan, Pulsed laser ablation of metals, Applied Surface Science 127 (1998) 941.

[133] J. R. Heath, S. C. O'Brien, Q. Zhang, Y. Liu, R. F. Curl, F. K. Tittel, R. E. Smalley, Lanthanum complexes of spheroidal carbon shells, Journal of the American Chemical Society 107 (1985) 7779.

[134] S. Arepalli, W. A. Holmes, P. Nikolaev, V. Hadjiev, C. Scott, A parametric study of single-wall carbon nanotube growth by laser ablation, Journal of Nanoscience and Nanotechnology 4 (2004) 762.

[135] A. Gorbunoff, O. Jost, Laser ablation synthesis of single-wall carbon nanotubes: The SLS model, in: R. Eason (Ed.), Pulsed Laser Deposition of Thin Films: Applications-Led Growth of Functional Materials, Wiley, New York, 2007, Ch. 24, p. 613.

[136] S. Arepalli, P. Nikolaev, W.Holmes, C. Scott, Diagnostics of laser-produced plume under carbon nanotube growth conditions, Applied Physics A 69 (1999) 1.

[137] A. Puretzky, D. Geohegan, X. Fan, S. Pennycook, Dynamics of single-wall carbon nanotube synthesis by laser vaporization, Applied Physics A 70 (2000) 153.

[138] K. Moller, Optics: Learning by Computing, with Examples Using Mathcad, Matlab, Mathematica and Maple, Springer, New York, 2007.

[139] M. Yudasaka, Y.Kasuya, F. Kokai, K. Takahashi, M. Takizawa, S. Bandow, S. Iijima, Causes of different catalytic activities ofmetals in formation of single-wall carbon nanotubes, Applied Physics A: Materials Science and Processing 74 (2002) 377.

[140] M. Rummeli, C. Kramberger, M. Loffler, O. Jost, M. Bystrzejewski, A. Gruneis, T. Gemming, W. Pompe, B. Buchner, T. Pichler, Catalyst volume to surface area constraints for nucleating carbon nanotubes, Journal of Physical Chemistry B 111 (2007) 8234.

[141] J. Maultzsch, H. Telg, S. Reich, C. Thomsen, Radial breathing mode of single-walled carbon nanotubes: Optical transition energies and chiral-index assignment, Physical Review B 72 (2005) 205438–206454.

[142] J. Maultzsch, S. Reich, C. Thomsen, S. Webster, R. Czerw, D. Carroll, S. Vieira, P. Birkett, C. Rego, Raman characterization of boron doped multiwalled carbon nanotubes, Applied Physics letters 81 (2002) 2647–2651.

[143] N. Anderson, A. Hartschuh, S. Cronin, L. Novotny, Nanoscale vibrational analysis of single-walled carbon nanotubes, Journal of the American Chermical Society 127 (2005) 2533.

[144] M. A. Pimenta, G. Dresselhaus, M. S. Dresselhaus, L. G. Cançado, A. Jorio, R. Saito, Studying disorder in graphite-based systems by raman spectroscopy, Physical Chemistry Chemical Physics 9 (2007) 1276.

[145] A. Jorio, C. Fantini, M. S. S. Dantas, M. A. Pimenta, A. G. S. Filho, G. G. Samsonidze, V. W. Brar, G. Dresselhaus, M. S. Dresselhaus, A. K. Swan, M. S. Ünlü, B. B. Goldberg, R. Saito, Linewidth of the raman features of individual single-wall carbon nanotubes, Physical Review B 66 (2002) 115411.

[146] P. T. Araujo, C. Fantini, M. M. Lucchese, M. S. Dresselhaus, A. Jorio, The effect of environment on the radial breathing mode of supergrowth single wall carbon nanotubes, Applied Physics Letters 95 (2009) 261902.

[147] C. Thomsen, S. Reich, Raman scattering in carbon nanotubes, in: M. Cardona, R. Merlin (Eds.), Light Scattering in Solids IX, Springer-Verlag, Berlin, 2007, p. 115.

[148] A. Jorio, P. Araujo, S. Doorn, S. Maruyama, H. Chacham, M. A. Pimenta, The kataura plot over broad energy and diameter ranges, Physics Status Solidi B 243 (2006) 3117.

[149] I. Maciel, M. A. Pimenta, M. Terrones, H. Terrones, J. C.-D. A. A. Jorio, The two peaks g' band in carbon nanotubes, Physica Status Solidi B 245 (2008) 2197.

[150] L. Wei, B. Wang, Q. Wang, L.-J. Li, Y. Yang, Y. Chen, Effect of centrifugation on the purity of single-walled carbon nanotubes from MCM-41 containing cobalt, The Journal of Physical Chemistry C 112 (2008) 17567.

[151] S. Freiman, S. Hooker, K. Migler, S. Arepalli, Measurement Issues in Single Wall Carbon Nanotubes: Practice Guid, National Insitute of Standards and Technology, Washington, USA, 2008.

[152] M. Dresselhaus, G. Dresselhause, P. Ecklund, Raman scattering in fullerens, Jornal of Raman Spectroscopy 27 (1996) 351.

[153] M. Dresselhaus, P. Ecklund, Phonons in carbon nanotubes, Advances in Physics 49 (2000) 705.

[154] D. E. Motaung, M. K. Moodley, E. Manikandan, N. J. Coville, In situ optical emission study on the role of c2 in the synthesis of single-walled carbon nanotubes, Journal of Applied Physics 107 (2010) 044308–044323.

[155] J. Singh, S. Thakur, Laser-Induced Breakdown Spectroscopy, Elsevier B.V., Holland, 2007.

[156] S. S. Harilal, R. Issac, C. V. Bindhu, V. P. N. Nampoori, C. P. G. Vallabhan, Optical emission studies of c2 species in laser-produced plasma from carbon, Journal of Physics D: Applied Physics 30 (1997) 1703.

[157] M. Dresselhaus, G. Dresselhaus, M. Hofmann, The big picture of raman scattering in carbon nanotubes, Vibrational Spectroscopy 45 (2007) 71.

[158] C. L. Pint, G. Bozzolo, R. Hauge, Catalyst design for carbon nanotube growth using atomistic modeling, Nanotechnology 19 (2008) 405704.

[159] C. W. S. Esconjaureguia, K. Maexb, The reasons why metals catalyze the nucleation and growth of carbon nanotubes and other carbon nanostructures, Carbon 47 (2009) 659.

[160] N. Lebrum, P. Perrot, Carbon-iron-nickel, in: G. Effenberg, S. Ilyenko (Eds.), IV/11D2 Ternary Alloy Systems Phase Diagrams, Crystallographic and Thermodynamic Data, Springer, Berlin, 2008, p. 200.

[161] A. Watson, L. Cornish, Carbon-cobalt-iron, in: G. Effenberg, S. Ilyenko (Eds.), IV/11D2 Ternary Alloy Systems Phase Diagrams, Crystallographic and Thermodynamic Data, Springer, Berlin, 2008, p. 482.

[162] J. Tedenac, Cobalt-iron-nickel, in: G. Effenberg, S. Ilyenko (Eds.), IV/11D2 Ternary Alloy Systems Phase Diagrams, Crystallographic and Thermodynamic Data, Springer, Berlin, 2008, p. 497.

[163] M. Zhang, M. Yudasaka, , S. Iijima, Production of large-diameter single-wall carbon nanotubes by adding fe to a NiCo catalyst in laser ablation, Journal of Physical Chemistry B 108 (2004) 12757.

[164] E. Gaufrès, N. Izard, L. Vivien, S. Kazaoui, D. Marris-Morini, E. Cassan, Enhancement of semiconducting single-wall carbon-nanotube photoluminescence, Optics Letters 34 (2009) 3845.

[165] S. Arepalli, P. Nikolaev, W.Holmes, C. Scott, Diagnostics of laser-produced plume under carbon nanotube growth conditions, Applied Physics A 70 (2000) 125–133.

[166] T. Ishigaki, S. Suzuki, H. Kataura, W. Krätschmer, Y. Achiba, Characterization of fullerenes and carbon nanoparticles generated with a laser-furnace technique, Journal of Applied Physics A:Materials and Processing 70 (2000) 121.

[167] A. A. Puretzky, H. Schittenhelm, X. Fan, M. Lance, L. F. Allard, D. B. Geohegan, Investigations of single-wall carbon nanotube growth by time-restricted laser vaporization, Physical Review B 65 (2002) 245425.

[168] T. Ikegami, F. Nakanishi, M. Uchiyama, K. Ebihara, Optical measurement in carbon nanotubes formation by pulsed laser ablation, Thin Solid Films 457 (2004) 7.

[169] M. Nishio, S. Akita, Y. Nakayama, Cooling effect on the growth of carbon nanotubes and optical emission spectroscopy in short-period arc-discharge, Thin Solid Films 464 (2004) 304.

[170] S. H. Lim, H. S. Yoon, J. H. Moon, K. C. Park, J. Jang, Optical emission spectroscopy study for optimization of carbon nanotubes growth by a

triode plasma chemical vapor deposition, Applied Physics Letters 88 (2006) 0331141.

[171] Z. Markovict', B. Todorovict'-Markovic, I. Mohai, Z. Kat'roly, J. Szet'pvoĺlgyi, Z. Farkas, Z. Nikolic, Optical emission study of RF thermal plasma during fullerene synthesis, Fullerenes, Nanotubes, and Carbon Nanostructures, 13 (2005) 215.

[172] J. García-Céspedes, M. Rubio-Roy, M. Polo, E. Pascual, J. Andújar, E. Bertran, Carbon nanotubes grown by asymmetric bipolar pulsed-DC PECVD, Diamond and Related Materials 16 (2007) 1131.

[173] R. K. Garg, T. N. Anderson, R. P. Lucht, T. S. Fisher, J. P. Gore, Gas temperature measurements in a microwave plasma by optical emission spectroscopy under single-wall carbon nanotube growth conditions, Journal of Physics D 41 (2008) 095206.

[174] D. Cremers, L. Radziemski, Handbook of Laser-Induced Breakdown Spectroscopy, John Wiley and Sons, England, 2006.

[175] V. N. Rai, S. N. Thakur, Physics of Plasma in Laser-Induced Breakdown Spectroscopy, Elsevier, 2007, Ch. 4, p. 83.

[176] H. Griem, Plasma Spectroscopy, McGraw-Hill, 1964.

[177] H. Griem, Spectral Line Broadening by Plasmas, Academic Press, New York, 1974.

[178] NIST http://physics.nist.gov/PhysRefData/ASD/linesform.html.

[179] R. Pearse, A. Gaydon, The Identification of Molecular Spectra, Chapman and Hall, :London, 1976.

[180] C. Vivien, J. Hermann, A. Perone, C. Boulmer-Leborgne, A. Luches, A study of molecule formation during laser ablation of graphite in low-pressure nitorgen, Journal of Physics D:Applied Physics 31 (1998) 1263.

[181] A. Tanabashi, T. Hirao, T. Amano, P. F. Bernath, The swan system of c2: A global analysis of fourier transform emission spectra, The Astrophysical Journal Supplement Series 169 (2007) 472.

[182] M. Moodley, N. Coville, B. Holloway, M. Maaza, Synthesis of single-walled carbon nanotubes by dual laser vaporization, South African Journal of Science 102 (2006) 364.

[183] L. Malard, M. Pimenta, G. Dresselhaus, M. Dresselhaus, Raman spectroscopy in graphene, Physics Reports 473 (2009) 51.

[184] R. Saito, G., M. S. Dresselhaus, Electronic structure of double-layer graphene tubules, Journal of Applied Physics 73 (1993) 494.

[185] A. Maiti, C. J. Brabec, C. M. Roland, J. Bernholc, Growth energetics of carbon nanotubes, Physical Review Letters 73 (1994) 2468.

[186] F. Kokai, K. Takahashi, D. Kasuya, M. Yudasaka, S. Iijima, Growth of single-wall carbon nanotubes dependent on laser power density and ambient gas pressure during room-temperature CO2 laser vaporization, Applied Physics A 73 (2001) 401.

[187] F. Kokai, K. Takahashi, D. Kasuya, M. Yudasaka, S. Iijima, Growth dynamics of single-wall carbon nanotubes and nanohorn aggregates by CO2 laser vaporization at room temperature, Applied Surface Science 197-198 (2002) 650.

[188] G. Radhakrishnan, P. Adams, L. Bernstein, Plasma characterization and room temperature growth of carbon nanotubes and nano-onions by excimer laser ablation, Applied Surface Science 253 (2007) 7651.

[189] M. Marchand, C. Journet, D. Guillot, J.-M. Benoit, B. I. Yakobson, S. Purcell, Growing a carbon nanotube atom by atom: "and yet it does turn", Nano Letters 9 (2009) 2961.

[190] S. I. Y. Ohta, Y. Okamoto, K. Morokuma, Rapid growth of a single-walled carbon nanotube on an iron cluster: Density- functional tight-binding molecular dynamics simulations, acsNANO 2 (2008) 1437.

[191] A. Wiltner, C. Linsmeier, Formation of endothermic carbides on iron and nickel, Physica Status Solidi (a), 201 (2004) 881.

[192] I. C. for Diffraction Data (ICDD), File (00-06-0697), xRD data file (2008).

[193] D. Laplaze, L. Alvarez, T. Guillard, J. Badie, G. Flamant, Carbon nanotubes: Dynamics of synthesis processes, Carbon 40 (2002) 1621–1634.

[194] Y. Leng, L. Xie, F. Liao, J. Zheng, X. Li, Kinetic and thermodynamics studies on the decompositions of Ni3C in different atmospheres, Thermochimica Acta 473 (2008) 14.

[195] S. Esconjauregui, C. Whelan, K. Maex, The reasons why metals catalyze the nucleation and growth of carbon nanotubes and other carbon nanostructures, Carbon 47 (2008) 659.

[196] X. Fan, R. Buczko, A. A. Puretzky, D. B. Geohegan, J. Howe, S. Pantelides, S. J. Pennycook, Nucleation of single-walled carbon nanotubes, Physical Review Letters 90 (2003) 145501.

[197] S. Khan, S. Ahmad, Modelling of c2 addition route to the formation of c60, Nanotechnology 17 (2006) 4654.

[198] S. Lair, W. Herndon, L. Murr, S. Quinones, End cap nucleation of carbon nanotubes, Carbon 44 (2006) 447.

[199] S. Lebedkin, P. Schweiss, B. Renker, S. Malik, F. Hennrich, M. Neumaier, C. Stoermer, M. Kappes, Single-wall carbon nanotubes with diameters approaching 6 nm obtained by laser vaporization, Carbon 40 (2002) 417.